COMPOSITION AND MICROSTRUCTURE EVOLUTION IN SEMI-SOLID CAST Al-Zn ALLOYS

By

Sarah Louise George

A thesis submitted to the Faculty of Engineering and the Built Environment,
University of Cape Town, in the fulfilment of the requirements for the degree of
Doctor of Philosophy

CENTRE FOR MATERIALS ENGINEERING
DEPARTMENT OF MECHANICAL ENGINEERING
UNIVERSITY OF CAPE TOWN

APRIL 2010

ABSTRACT

COMPOSITION AND MICROSTRUCTURE EVOLUTION IN SEMI-SOLID CAST Al-Zn ALLOYS

By: Sarah Louise George

Semi-solid metal casting produces a low porosity, globular microstructure, which makes it an attractive competitor to wrought parts. This research explores the suitability of utilising heat treatable, Al-Zn-Mg-Cu alloys for the production of high strength parts for the automotive and aerospace industries, using the semi-solid metal rheocasting process. The process results in segregation, arising from non-equilibrium solidification, thus placing high demands on the post-solidification homogenisation and solution heat treatments, in order to derive optimum strength during subsequent ageing treatments. If the semi-solid metal castings can be age hardened to the same extent as the equivalent wrought competition, then this process could replace the machining of parts from conventional wrought stock.

The semi-solid cast microstructure was investigated with the aid of light microscopy, scanning electron microscopy, elemental dispersive x-ray spectroscopy and electron backscatter diffraction, in order to establish the extent of segregation associated with the as-cast condition. Evolution of the as-cast structures of AA7075 and A713 composition alloys was investigated during subsequent heat treatments, with the view to achieving a fully homogenised structure prior to solution treatment and age hardening. *In situ* SEM heating experiments were performed, in order to document the evolution of the microstructure during homogenisation treatments. The results from the heating experiments and thermal analysis were used to evaluate the possibility of effective homogenisation processes for removal of the as-cast segregation.

Owing to its negative effect on the homogenisation process, incipient melting of the solute-rich phases, identified using differential scanning calorimetry, had to be avoided during heat treatments. It was determined during *in situ* heating experiments that the interaction between the eutectic and the porosity in the semi-solid cast structure during overheating caused the agglomeration of and morphological changes to the isolated porosity, resulting in the formation of large pores within the previously interglobular regions. This could potentially have a negative impact on the structural integrity of a part in service.

The evaluation of the as-cast condition provided insight into the mechanisms involved in the formation of the globular microstructure that is characteristic of SSM processing. Evidence showed that the mechanism was one of alternating planar and cellular growth, and that dendritic growth did not occur during the semi-solid metal rheocasting. This was highlighted by the absence of inter-dendritic liquid and the presence of internal crystallographic misorientations in many of the grains in the as-cast condition.

ACKNOWLEDGEMENTS

I would like to thank the following people for their assistance and support during the duration of this thesis:

My supervisor, Prof. Rob Knutsen for his support, encouragement and advice over that last few years;

Prof. Candy Lang, Penny Park-Ross and Leizl Matthews for their understanding and support through the emotional ups and downs and for making me laugh when I was taking things too seriously;

The National Research Foundation and the Centre for Materials Engineering for their financial assistance;

Sagren Govender at the Centre for Scientific and Industrial Research (CSIR) in Pretoria, for giving me the opportunity to base my research on the rheocasting technique established there, and for manufacturing the samples for this investigation;

Phil Prangnell, of the University of Manchester, for giving me the amazing opportunity to visit and study in Manchester in 2008/2009, and for giving me support during my stay;

Prof. J. Humphreys, Ian Brough and Michael Faulkner for their unfailing support and their assistance with the microscopes during my time at the University of Manchester;

Miranda Waldron at the Electron Microscope Unit at the University of Cape Town, for teaching me how to use the SEM and assisting me whenever the need arose;

Glen Newins and the workshop staff for their continued assistance in sample preparation;

My family and friends for their endless support and tolerance when the going was tough;

My mother for helping me with the editing of my document and for teaching me the difference between defining and non-defining clauses.

TABLE OF CONTENTS

TABLE OF FIGURES

SYMBOLS

V_S	Volume of a solid sphere
V_L	Volume of liquid
A_{SL}	Solid-liquid interfacial area
G_V^L	Gibbs free energy per unit volume of liquid
G_V^S	Gibbs free energy per unit volume of solid
γ_{SL}	Solid-liquid interfacial free energy
r^*	Critical radius
ΔG^*	Activation energy for the formation of a nucleus with a critical radius size
ΔT	Undercooling
L_v	Latent heat of fusion per unit volume
T^*	Critical temperature
k_B	Boltzmann's constant
f_S	Volume fraction solid
λ_2	Secondary dendritic arm spacing
$\dot{\gamma}$	Shear rates
at%	Atomic percent
BEI	Backscattered electron image
BSE	Backscattered electron
CSIR	Council for Scientific and Industrial Research
DSC	Differential scanning calorimetry
EBSD	Electron backscatter diffraction
EDS	Energy dispersive x-ray spectroscopy
GDT	Globular-to-dendritic transition
G_L	Gibbs free energy of the liquid
HAGB	High angle grain boundary
HCP	Hexagonal close packed
HPDC	High pressure die casting
HV	Vickers Hardness
LAGB	Low angle grain boundary
PLOM	Polarised light optical microscopy

RDC	Rheo-die casting process
SE	Secondary electron
SEI	Secondary electron image
SEM	Scanning electron microscopy
SS	Semi-solid
SSM	Semi-solid metal
T_E	Eutectic melting temperature
T_m	Melting temperature
TMP	Thermo-mechanical processing
wt%	Weight percent
X_0	Final average composition

CHAPTER 1: INTRODUCTION

Aluminium alloys are used extensively in the aerospace and automotive industries. The most common of these alloys are the heat treatable, high strength alloys that are used for primary structural components. These components can either be machined or cast. Machined parts are produced through extensive thermo-mechanical processing routes before the final shaping, this resulting in high mechanical strength properties. However, the multiple steps involved in the machining of parts make them expensive to manufacture. On the other hand, the casting of parts is an inexpensive, single-step manufacturing route that produces parts with low mechanical strengths and low structural integrity, making them undesirable for high strength applications. Semi-solid metal (SSM) casting is a relatively new process that offers an attractive near-net shape manufacturing route for precipitation hardenable aluminium alloy components, potentially resulting in a component with mechanical properties that could be a competitive alternative to the processing routes used for wrought or machined parts, but with the benefit of the rapid processing route of casting.

The key to the potential for high strength using the SSM casting technique is the as-cast microstructure that develops as a result of the production process. The SSM microstructure differs from the dendritic microstructure that is associated with traditional casting, in that it consists of a globular grain morphology that originates from the turbulent mixing characteristic of the semi-solid slurry production process. Agitation during slurry production also assists in limiting segregation in the semi-solid volume prior to casting. Notwithstanding the advantages of mixing in the semi-solid state, further segregation still occurs during the solidification of the cast product, such that the inter-globular regions have a distinctly different composition from the average globular grain composition.

SSM casting has two different casting techniques, thixocasting, which includes a billet preparation step, and rheocasting, which is a single step process. Since the 1970s, many researchers have concentrated on the thixocasting route and have had success with the SSM casting of conventional casting alloy compositions. More recently, the thixoforming of wrought composition alloys has been investigated, as these alloys are better suited to high strength applications. However, there are some disadvantages to thixoforming, the most significant being the high costs involved for industrial implementation. Consequently, considerable research is currently focused on rheocasting, a more economically viable technique.

The emphasis of this investigation is on the SSM rheocasting technique, designed by the Council for Scientific and Industrial Research (CSIR) of South Africa. The technique consists of a slurry production process, where the thixotropic properties are exploited by the use of induction stirring during controlled cooling of the liquid metal in order to maintain the viscosity of the melt. Once the slurry has reached a 50% solid fraction it is transferred to a standard industrial High Pressure Die Casting (HPDC) facility.

The mechanisms involved in the slurry production step lead to the formation of globular solid particles in the melt. The morphology of these particles allows for an increased viscosity with increasing solid fraction. The slurry is transferred to the HPDC at approximately 50% solid fraction, which is made possible by the flow characteristics of the slurry at lower temperatures and higher solid fractions. The temperature and viscosity of the slurry allows for the non-turbulent filling of the die that results in a marked reduction in the amount of entrapped gas porosity in the final part. Owing to the reduction in the actual casting temperature, there is a positive effect on the shrinkage porosity that results during casting. This dramatic reduction in overall porosity has the effect of improving the structural integrity of the part, thus making it an attractive alternative for the manufacture of high strength parts.

If SSM rheocasting is to be a viable commercial production process the final properties of the part need to be comparable to the wrought parts that are currently used. Owing to these strength requirements, the use of alloy compositions that result in higher strengths is necessary. These high strength compositions are generally the wrought composition alloys, such as the Al-Zn-Mg-Cu composition alloy AA7075, which are not typically designed to suit casting processes. These SSM cast parts, using traditionally wrought composition alloys, will undergo post production precipitation hardening treatments to improve their mechanical properties. The ability to harden these SSM cast parts will hinge on the removal of segregation, an artefact of the casting process itself, and the homogenisation of the as-cast structure prior to solution treatment and subsequent precipitation hardening treatments.

The main advantage of using a high strength, heat treatable alloy such as AA7075 is to exploit the heat treatability and age hardening characteristics. By selecting an alloy of this complexity for the SSM manufacturing technique, the implication is that the part is intended for high load applications where structural integrity, in conjunction with strength, is important. For this reason, the integrity of the part must be monitored. Generally, the porosity is located within the interglobular regions, surrounded by solute-rich eutectic that has a lower melting temperature than the bulk. This low temperature is within the solution treatment temperature range. Solution treatment at high temperatures is necessary for the production of a supersaturated solid solution prior to ageing in the post production heat treatment. Therefore, it is important to ensure that heating of the structure is not detrimental to the structural integrity of the part.

Over the years the main focus of development for these SSM processes has been on manufacturing techniques, equipment and technological development. Little focus has been directed at understanding the mechanisms causing the characteristic globular microstructure, such as: nucleation rate, growth morphology and others that affect the morphological development of the globular grain structure. The characterisation of the as-cast SSM microstructure will aid in determining the effectiveness of particular heat treatments and homogenisation practices. These practices and treatments directly affect the maximum achievable mechanical properties attainable from the SSM cast parts.

1.1. AIMS OF THIS RESEARCH

The main aim of this investigation was to determine whether SSM casting, or more specifically the CSIR Rheocasting process, is a viable alternative for the production of high strength parts for the automotive and aerospace industries. In order to recognise this aim, key objectives needed to be met. These objectives included:

- Investigation into the extent of segregation associated with the SSM cast microstructure.
- Identification of the key features that are an integral part of the SSM cast microstructure.
- Identification of the mechanisms involved in the production of the characteristic globular structure of SSM casting.
- Comparison of the distribution and extent of segregation between an AA7075 alloy, traditionally used for wrought applications, and an A713 casting alloy.
- Investigation into the effect of heat treatments on the porosity morphology and the structural integrity of the casting.
- Investigation into the suitability of the standard T6 heat treatment for use on SSM cast samples in order to maximise the strength, focusing on the homogenisation of the segregation.

CHAPTER 2: LITERATURE REVIEW

2.1. THE MANUFACTURE OF ALUMINIUM PARTS

High strength aluminium parts are used extensively in the aerospace and automotive industries. As technology advances, the trend is to move towards the production of more lightweight parts, but with an aim to maintaining the cost effectiveness of those parts. The use of aluminium for high strength parts is becoming fairly common, but, in the interest of decreasing costs, the use of casting as the manufacturing technique is being investigated as a cheaper, more rapid production process, as opposed to the wrought process most often employed in the industry.

Complex shaped aluminium components used in the automotive and aerospace industries are generally manufactured in one of two ways; machined or cast, essentially solid-state or liquid-state processing routes[1]. The machining of a part is the last step in a series of processes to produce the final product, whereas casting is a more rapid single-step processing route. Both casting and machining processes have their advantages and disadvantages, and different components with specific property requirements may demand a specific manufacturing route.

Aluminium alloys are divided into casting and wrought alloys, where the compositions are tailored for the different manufacturing processes. The alloy systems generally used for high strength parts are the Al-Zn system, or the 7000 series alloys. These are heat treatable alloys and their strengths can therefore be increased using various post production heat treatments. The Al-Zn system is most commonly used for wrought processing, although there are some casting alloys in use, such as the A713 Tenzaloy alloy.

Traditionally, casting alloys have a relatively high silicon content, as silicon expands during transformation from liquidus to solidus, thus reducing shrinkage. The presence of silicon also aids the flow of the melted alloy in the die cavity. The Al-Zn series of alloys have a low silicon content, and are therefore not as-castable, but they do have the potential for strengthening through precipitation hardening.

2.1.1. PRODUCT MANUFACTURE TECHNIQUES

All aluminium components originate from a casting process of some sort. Wrought products begin as-cast ingots. These ingots are very large and the solidification process associated with this type of large ingot is very specific and different from the casting of near-net shaped parts, although the basic principles associated with the solidification process are the same. Namely, liquid metal is transferred to a mould where the temperature of the metal decreases and the metal begins to solidify – by the formation and growth of nuclei into grains and the growth of these grains, until the metal is fully solid.

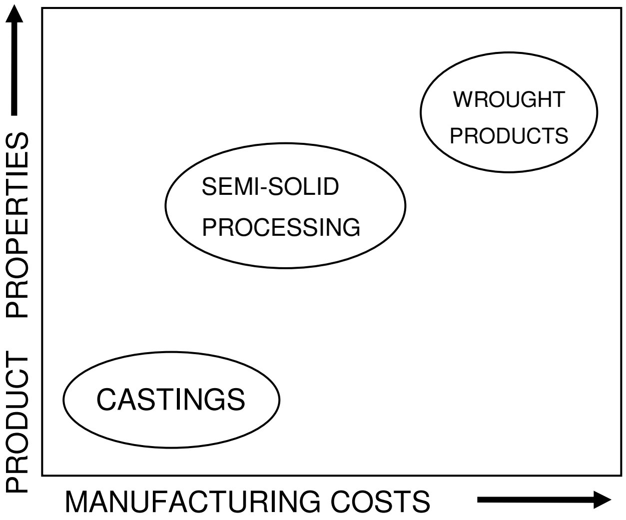

Figure 2.1: *Cost vs. properties relationship for cast and wrought products*[1]**.**

The most commonly-used casting techniques for aluminium are sand casting, permanent mould casting and high pressure die casting. The major problem with aluminium castings is the relatively high shrinkage that occurs during solidification. Also, problems such as hot tearing/cracking, residual stresses and shrinkage porosity need to be minimised or avoided. As with the wrought alloys, there are some casting alloys that are heat treatable, although imperfections that arise in the casting/solidification process may cause blistering and distortion on subsequent heat treatment. Another problem with castings is that they generally have worse mechanical properties than a similar wrought product[2].

Die casting involves injecting liquid metal under pressure into a permanent metal mould. The mould is made up of two pieces, or dies, that are clamped together prior to the injection of the liquid metal, and are opened rapidly after solidification.

It would be ideal to have a process that were as rapid as liquid-state casting, where the final properties of the product would be comparable to a solid-state machined product. Semi-solid metal casting is a technique that comes close to these requirements[1].

2.1.2. MICROSTRUCTURE OF TRADITIONALLY CAST PARTS

In the casting of metals, molten metal is poured (using gravity) or pushed/forced (using low or high pressure) into a die. The molten metal then undergoes a solidification process, where, on cooling, solid nuclei form and grow into grains. These grains continue to grow until solidification is complete.

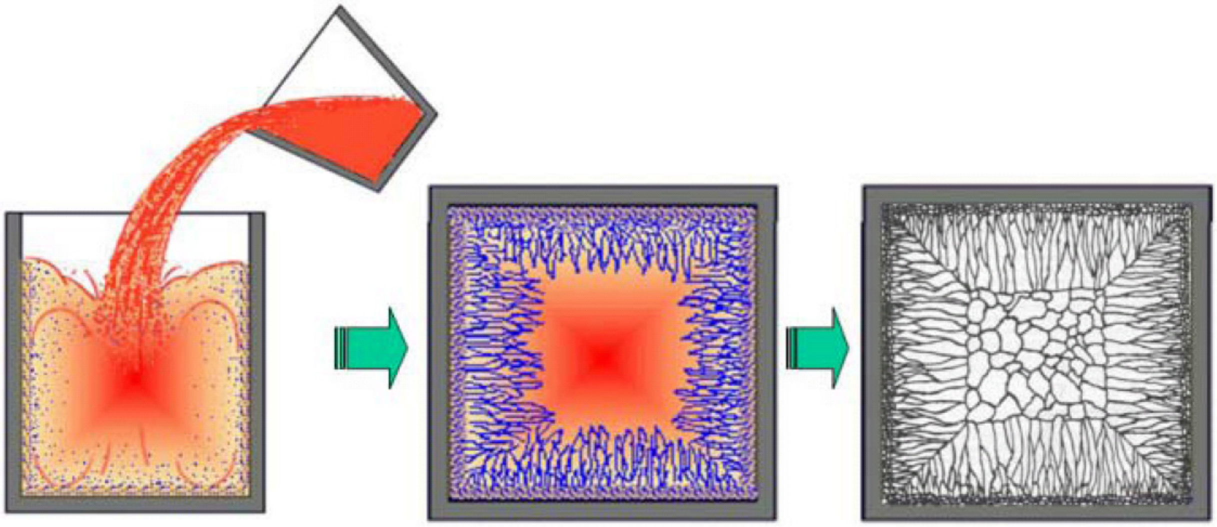

Figure 2.2: *Typical solidification structure of a cast ingot*[3].

During casting, a solidification microstructure forms, the structure of which is determined by the relative temperature gradients between the liquid and the die interface, and the number of solid nuclei that form within the liquid metal. In the final microstructure, each grain is the result of individual nuclei that originated during solidification. The nucleation of solid material often begins at the mould wall and randomly-oriented grains form. These grains form the outer equiaxed zone of the microstructure.

Dendrites begin to form and grow in a direction parallel to that of the heat flow. These dendrites form when the nuclei, originally spherical, grow and become unstable. Their shape changes from that of a sphere to a “tree-like” shape with branches that grow into the liquid.

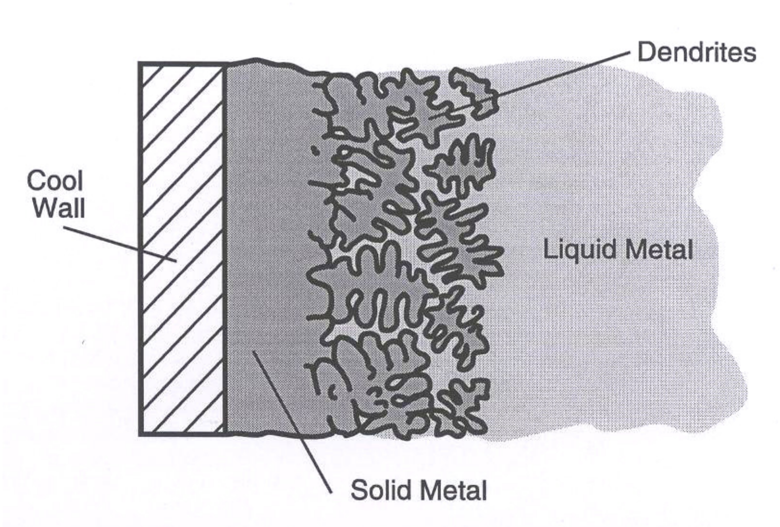

Figure 2.3: *Dendritic solidification of molten metal originating at a cool wall or die surface*[4].

The dendrites grow inwards from the surface forming a columnar zone. During this stage, dendrite branches may break off and can grow independently. These new nuclei grow in the centre of the casting and form a central equiaxed zone[5].

2.1.3. CASTING DEFECTS

There are disadvantages to casting, the most significant of which are the inherent casting defects that result from the process. These will affect the quality of the final product, but the extent of the defects can be minimised by good casting practices and the selection of the correct casting technique for a particular alloy and for a particular product.

Typical casting problems are: shrinkage during solidification (resulting in shrinkage porosity and dimensional instability), hot tearing/cracking, residual stresses, inclusions and segregation.

2.1.3.1. SHRINKAGE POROSITY

Shrinkage porosity is a result of volumetric shrinkage of the metal during solidification. This shrinkage porosity often forms cavities between the dendritic branches of a cast structure. This is caused by over-rapid cooling of the cast metal[6]. The extent of the porosity may vary from a few large voids to many small holes distributed throughout the casting. The extent of shrinkage is maximised with higher pouring temperatures – since metal contracts as it cools and solidifies. The morphology of shrinkage porosity is usually irregular with rough edging, and corresponds to the shape of the eutectic region around the pores[7]. This is in contrast to the porosity associated with entrapped gas, which results in smooth, spherical pores.

The presence of porosity is problematic in a casting, because cracks can easily propagate from these pores, especially from the irregularly-shaped pores within the eutectic region that result from shrinkage.

2.1.3.2. INCLUSIONS

Non-metallic particles can be created by oxidation of the liquid metal, or particles from slag or dirt may be found in the metal prior to casting. These particles will have different properties to the metal and will not deform in the same way during casting or during post-production operations. The presence of inclusions can be minimised by various casting practices, such as preventing exposure of the liquid metal to the air, and the effective use of gates in the mould design.

2.1.3.3. SEGREGATION

Solidification produces a variation in composition within the cast structure. This phenomenon is termed segregation. Segregation occurs in all castings, although the degree of segregation may vary, depending on the complexity of the alloy composition, the casting parameters and the casting technique. Composition variation over large distances, of the order of centimetres or more, is referred to as macrosegregation, whereas composition variation over small distances is microsegregation.

The driving force for any segregation is the difference in composition between the first and the last metal to solidify during the casting process. The first nuclei will have a purer composition and the last to solidify will be rich in solute. The specifics of this process will be discussed in detail in **Chapter 2.3.1**.

The segregation that is associated with ingot casting is most often successfully removed during subsequent thermo-mechanical processing (TMP), which involves extensive deformation and heating. However, some cases of macrosegregation cannot ever be fully removed, and artefacts of this will remain after TMP. In net shaped castings, the segregation can only be removed to some extent through heat treatment, which is generally not as efficient as processes that include deformation and heat.

The presence of a high degree of microsegregation in a casting will affect the extent of the effectiveness of homogenisation heat treatments, and subsequently will have a dramatic effect on any precipitation hardening processes, thus limiting the final mechanical properties of a cast part.

2.2. SEMI-SOLID METAL CASTING

Semi-solid metal (SSM) processing is a relatively new manufacturing route. The principle behind it was first discovered by Spencer, Mehrabian and Flemings at MIT in 1972[8,9], who were investigating the hot-tearing in the casting of steels. They ascertained that if the dendritic structure is broken up during the solidification process, the partially solidified metal alloy begins to flow with the fluidity of machine oil and exhibits thixotropic behaviour[8]. The SSM process is based on the thixotropic properties of metals, where, in the semi-solid state, the viscosity of the metal decreases when the shear rate is increased. (If metals are sheared just below their melting points, they take on the appearance of a shear-thinning liquid, which is described as thixotropic[10]). Spencer *et al* determined that when metal alloys are vigorously agitated during solidification, the solid that forms has a non-dendritic structure. Another attribute is that these non-dendritic, partially solidified metals, behave as fluid slurries at solid fractions as high as 60%[9]. This type of viscous slurry can then be cast successfully at lower temperatures and will produce a non-dendritic final structure from the non-dendritic nuclei present in the slurry.

There are several advantages to the semi-solid process, but from a casting technology point of view, one of the main advantages is the non-turbulent filling of the die, owing to the viscosity of the slurry, which in turn eliminates the air entrapment that is often associated with conventional filling of the die, giving high integrity and better mechanical properties to the cast part[11]. Other advantageous characteristics associated with semi-solid metals are: the lower heat content than liquid metal upon casting; the presence of solid nuclei at the time of die filling; the higher and more controllable viscosity as compared to liquid metals; and the lower flow stresses.

2.2.1. RHEOLOGY AND THIXOTROPY

Rheology deals with the simultaneous deformation and flow of materials. Shear flow that is associated with stirring and the production of semi-solid slurries is an inter-relationship between rheology and the mechanical properties of materials, and is of particular importance in the assessment of the viscosity and deformation behaviour of a material within a mushy (semi-solid) state[12].

The key to semi-solid processing is the phenomenon of thixotropy. Here, the viscosity of a material changes (lessens) as it is stirred (sheared). The word *thixotropy* is derived from the Greek words *thixis*, meaning stirring or shaking and *trepo*, meaning turning or changing[1]. This thixotropic nature is seen in non-Newtonian fluids, where the viscosity is a function of the physical properties of the fluid and the external conditions[12]. In thixotropic fluids, the shear stress is not proportional to the shear rate, and the viscosity is dependent on the shear rate, pressure, temperature and time[1].

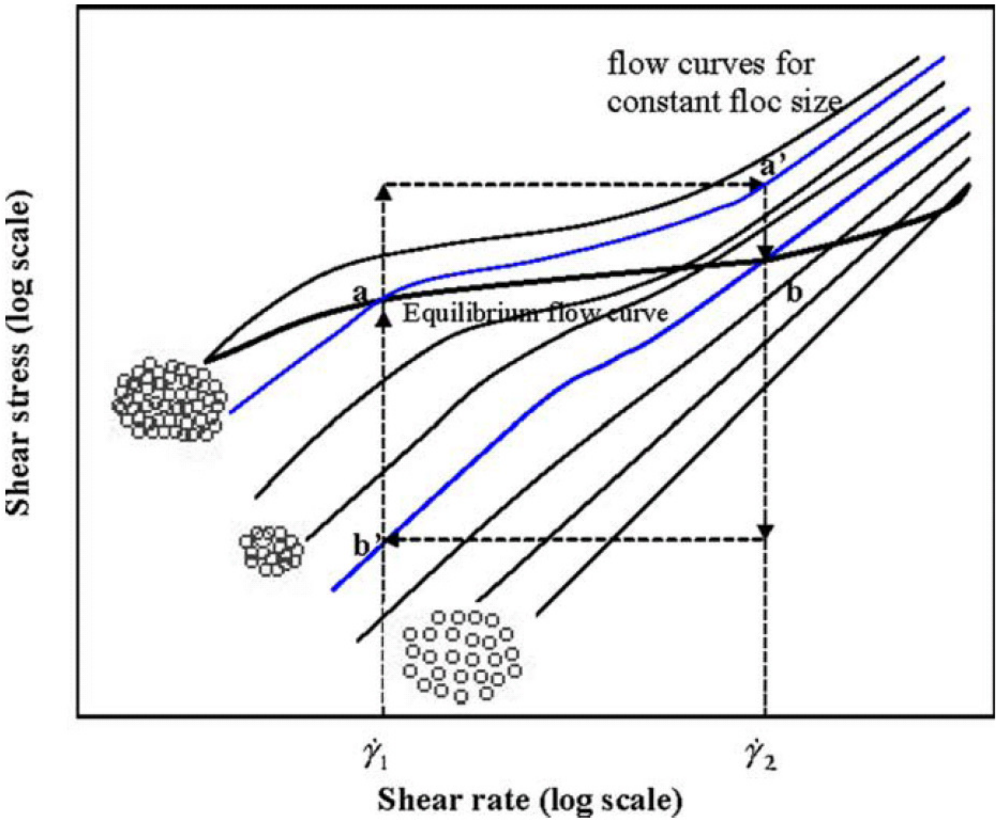

Figure 2.4: *Flow curves of a flocculated suspension*[10, 13].

A semi-solid metallic system can be likened to a flocculated suspension and considered as a microstructure consisting of a series of large flocs, or particles in a suspension. **Figure 2.4** shows that, by increasing the shear rate from $\dot{\gamma}_1$ to $\dot{\gamma}_2$, the flocs break up and separate until their size corresponds to the flow curve that passes through *b*. If the shear rate is then reduced back to $\dot{\gamma}_1$, the particles begin to collide and agglomerate, until an equilibrium size is reached that is appropriate to the new shear rate. In semi-solid metallic systems, the agglomeration occurs because particles are colliding and, depending on their orientations, new boundaries are formed. Metallic semi-solid slurries are thixotropic for volume fractions of solid higher than 30%[13].

The viscosity of the thixotropic material during shearing depends on the particle morphology. The more spherical the particle, the lower is the steady state viscosity[14]. In semi-solid metallic alloy systems, the particles evolve in both shape and size during shearing, with their structural evolution tending towards a more spherical shape with the change in viscosity. The various mechanisms of this morphological change during shearing will be discussed in **Chapter 2.3.3**.

2.2.2. MICROSTRUCTURAL MORPHOLOGY

Nearly all commercially-important alloys solidify dendritically, with either a columnar dendritic structure originating from a mould wall, or an equiaxed dendritic structure, where solidification occurs in a free liquid and dendrite arms grow in the major axial directions (often simplified to a six-arm floating solid growing in a free liquid). During dendritic solidification of castings and ingots, a number of processes take place simultaneously within the semisolid region. These include crystallisation, solute redistribution, ripening, interdendritic fluid flow and solid movement[15, 17]. **Figure 2.5** shows the transition from dendritic type solidification to a more favourable spherical structure, with the increase in the shear rate and turbulence intensity during cooling/solidification. These mechanisms occur prior to casting in the semi-solid metal casting techniques.

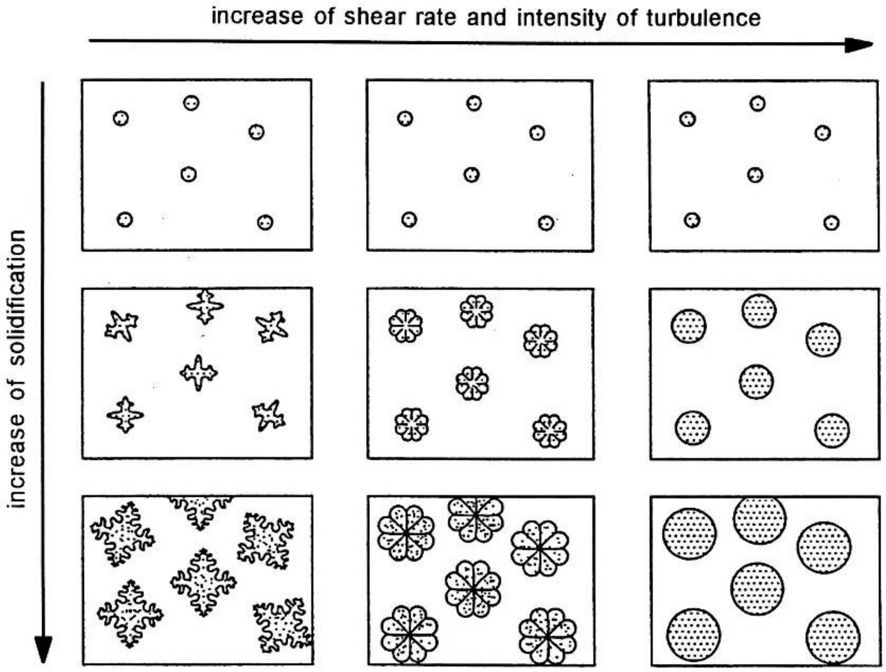

Figure 2.5: *Schematic illustration of morphological transition from dendritic to spherical via rosette with increase in shear rate and intensity of turbulence*[15].

It is clear that for a fully globular microstructure, high shear intensity is needed to create the desired morphology. There are various schools of thought as to the true mechanisms for this transformation from dendritic to globular morphology. These mechanisms will be discussed in more detail in **Chapter 2.3.3.**

2.2.3. VARIOUS SSM PROCESSING TECHNIQUES

The semi-solid metal processes can be divided into two different classes, namely thixo-processing, which is a feedstock producing process, and rheo-processing, which is a single step process. Under the umbrella of each process are different manufacturing techniques, such as-casting, forging and extrusion. For simplicity, these processes will be discussed only in conjunction with high pressure die casting (HPDC) as the final forming step.

2.2.3.1. THIXOCASTING

Thixocasting was the first SSM technique to be implemented. **Figure 2.6** shows a schematic of the two steps of the thixocasting process. This method involves the use of a feed stock material that has been produced with a fine, globular grain structure [most commonly by the continuous casting technique, where the metal is magneto-hydrodynamically (MHD) stirred during solidification]. These pre-conditioned billets can then be used as the source material for a forming process, where they are heated to the semi-solid temperature range and then formed[16].

Figure 2.6: *A schematic of the thixocasting technique*[16]**.**

The resulting microstructure is globular in morphology and has a consistent material composition and quality.

The main drawbacks to this process are: the high feedstock costs, owing to the pre-conditioning; the non-recyclable scrap; and the oxide formation during the re-heating step.

2.2.3.2. RHEOCASTING

The rheocasting process eliminates the need for feedstock material and produces semi-solid slurry directly from the liquid metal[16]. A schematic of the steps involved in the rheocasting process is shown in **Figure 2.7**. The liquid metal undergoes a shearing process during cooling and solidification to produce a non-dendritic semi-solid slurry, which, when it reaches a solid fraction of approximately 50%, is then transferred directly into a mould or die[17]. The advantage of this method is that the actual casting for this technique can be carried out using standard High Pressure Die Casting (HPDC) machinery, which for industry would mean lower capital costs.

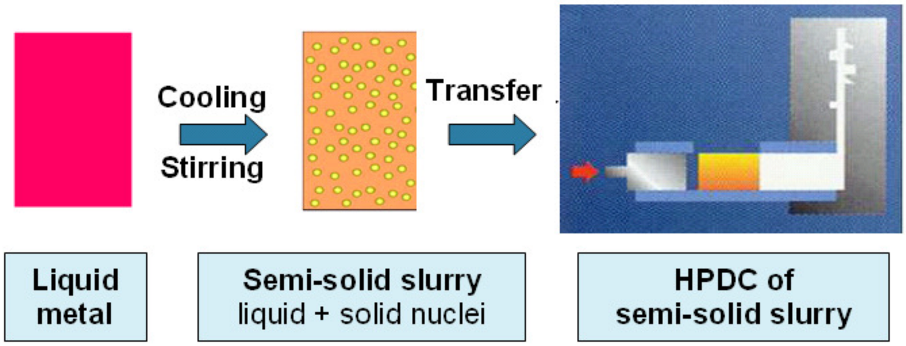

Figure 2.7: *A schematic of the rheocasting technique*[16]*.*

The main disadvantage of this process is the narrow temperature range for the slurry production.

2.2.4. THE *CSIR* RHEOCASTING FACILITY

The Council for Scientific and Industrial Research (CSIR) in South Africa developed a rheocasting process with a novel rheo-processing unit.

Molten metal, at a temperature as close to the liquidus as possible, is poured into a stainless steel cup. The cup is mechanically transferred to the rheo-processor, where it is moved upwards within the coils of the processing unit. During this slurry production process, the cup proceeds stepwise through three conditioning units, each consisting of an AC induction coil and air cooling coils.

The induced electromagnetic field supplied by these induction coils, and the air-cooling system that operates simultaneously, cools and stirs the slurry until the metal reaches the desired semi-solid temperature and structure. The CSIR Rheo-processing unit is shown in **Figure 2.8**, illustrating: in **Figure 2.8 (a)**, a computer rendered model of the experimental prototype, and in **Figure 2.8 (b)**, a photograph of the commercial unit.

The slurry is processed until it reaches a target temperature where the solid fraction is 50%. The rate of cooling and the target temperature are material specific. The temperature control within the system is within Δ4°C[16,18]. The slurry is then transferred to the shot sleeve of a 130 ton HPDC machine for casting.

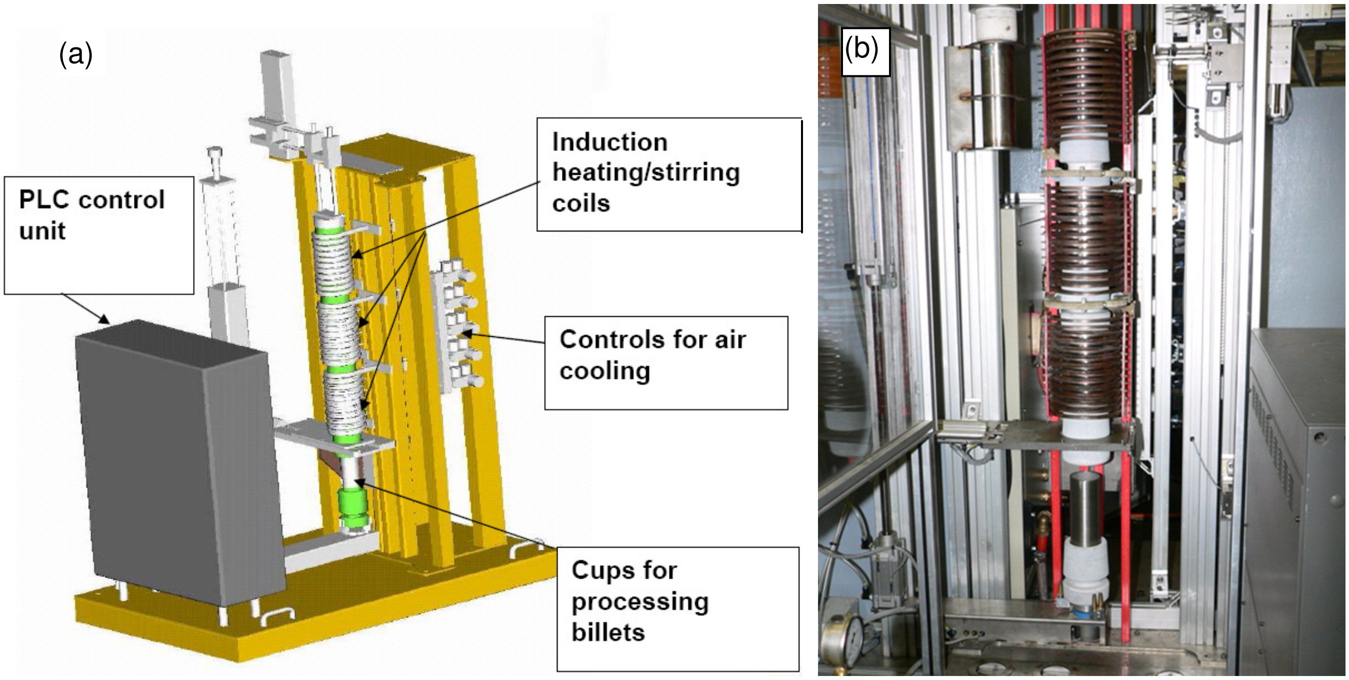

Figure 2.8: *The Rheo-processing unit from the CSIR rheocasting facility, (a) schematic of the experimental prototype and (b) the commercial unit.*

2.3. SOLIDIFICATION AND MICROSTRUCTURE

All solidification starts with the formation of nuclei within the melt. Crystals then begin to grow from these nuclei[19]. This growth process proceeds until all of the melt has been transformed into solid. The nucleation type and growth process will determine the type of microstructure that results. And the microstructure, in turn, will determine the mechanical property limitations.

2.3.1. SOLIDIFICATION DURING TRADITIONAL CASTING

2.3.1.1. NUCLEATION AND GROWTH

At the onset of the solidification of an alloy, solid nuclei form when the forces of attraction that are present between atoms or ions in the melt cause them to bind together to form a solid crystalline phase[19]. The forces of attraction are always present but when the binding together results in a decrease in the free energy of the system, this becomes the driving force for the onset of solidification. The stability of the individual nuclei is not guaranteed, as the conditions need to be ideal for the critical stability of these nuclei, even locally within the melt. If these conditions are not met, the nucleus will re-melt or dissolve and disappear.

If a liquid is cooled below its equilibrium melting temperature (T_m), there is a driving force for solidification. Solidification will only initiate if the undercooling (the cooling of a metal below the transformation temperature without the occurrence of a transformation) is great enough to cause a decrease in the free energy of the system and a shift to a more stable state, in this case, the formation of a solid nucleus with a critical radius. The degree of undercooling required to cause the onset of solidification is dependent on the presence of impurities, which act to catalyse the nucleation of the solid[20]. As a solidification front advances, solute is redistributed at the interface. Commonly, solute is rejected into the liquid, where it accumulates into a solute boundary layer.

Depending on the temperature gradient, such liquid may be undercooled below its freezing temperature, even though it is hotter than liquid at the front. This is termed ‘constitutional undercooling’, to emphasize that it arises from variations in liquid composition. Once constitutional undercooling occurs, the plane front becomes unstable. A bump on the interface penetrates into the undercooled liquid, where the unstable front causes it to grow more quickly[21].

The impurities and the presence of a mould wall act as sites for heterogeneous nucleation of the solid phase. Without these sites, homogeneous nucleation is possible, but the conditions for the onset of homogeneous nucleation require much larger undercoolings than the more common, heterogeneous nucleation.

The process of homogeneous nucleation can be used to understand nucleation in general. For a given volume of liquid at a temperature of ΔT below T_m, with a Gibbs free energy of G_1, when a small sphere of solid forms by the clustering of atoms, the Gibbs free energy of the system will change to G_2. This change in energy is described by:

$$G_2 = V_S G_V^S + V_L G_V^L + A_{SL}\gamma_{SL} \qquad \textit{Equation 2.1}$$

where V_S is the volume of the solid sphere, V_L is the volume of the equivalent liquid, A_{SL} is the solid-liquid interfacial area, G_V^L and G_V^S are the free energies per unit volume of liquid and solid respectively, and γ_{SL} is the solid-liquid interfacial free energy[20]. The free energy of the system without any solid present is given by:

$$G_1 = (V_S + V_L)G_V^L \qquad \textit{Equation 2.2}$$

The formation of solid therefore results in a free energy change $\Delta G = G_2 - G_1$ where:

$$\Delta G = -V_S \Delta G_V + A_{SL}\gamma_{SL} \qquad \textit{Equation 2.3}$$

Depending on the amount of undercooling, there is a critical nucleus radius (r^*) size that is associated with a maximum excess free energy. If $r < r^*$, the system can lower its free energy by dissolution of the solid, whereas when $r > r^*$, the free energy of the system is decreased as the solid grows[20].

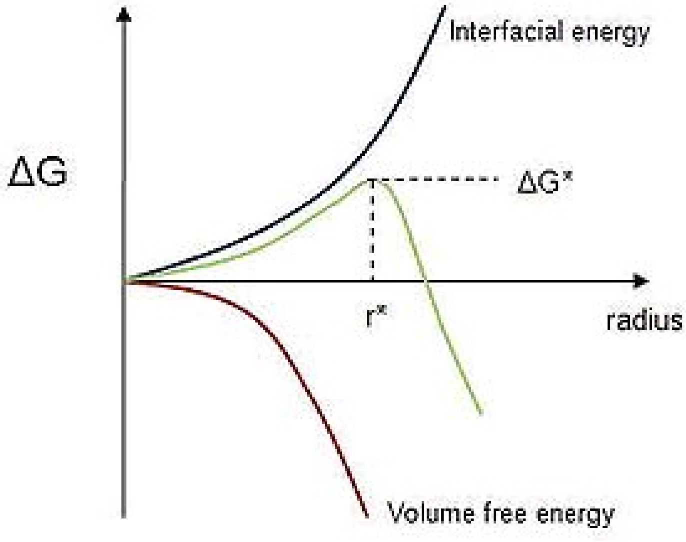

Figure 2.9: *The free energy change associated with homogeneous nucleation of a sphere of radius r[20].*

These unstable nuclei with $r < r^*$ are called embryos or clusters. These embryos consist of several atoms that are ordered in a crystalline way. They arise spontaneously and at random and there is a constant exchange of atoms between the embryos and the melt, and in many cases these embryos will dissolve and disappear[19].

The energy required to form a stable nucleus, with a critical radius size r^*, is:

$$\Delta G^* = \frac{16\pi\gamma_{SL}^3}{3(\Delta G_V)^2} \qquad \textit{Equation 2.4}$$

and

$$r^* = \frac{2\gamma_{SL}}{\Delta G_V} \qquad \text{Equation 2.5}$$

where ΔG^* is the activation energy for the formation of a nucleus with a critical size r^* and ΔG_V is the Gibbs chemical free energy change per unit volume from the liquid to the solid.

Using Boltzmann's statistical mechanics in combination with the laws that describe the capacity of the nuclei to grow rather than dissolve (as described in the **Equation 2.4** and **Equation 2.5**), it is possible to determine information regarding the number of nuclei per volume, the time that it takes for the clustering to occur and activation energy for critically-sized nuclei to form[19]. Results from these types of calculations show that there is a temperature range within which falls a critical temperature (T^*) where a large number of nuclei per unit volume are formed. The average activation energy for forming a nucleus at this temperature is:

$$\Delta G^* = 60 k_B T^* \qquad \textit{Equation 2.6}$$

where k_B is Boltzmann's constant.

2.3.1.2. SOLID-LIQUID INTERFACE INSTABILITY AND HEAT FLOW

Solidification is controlled by the rate at which the latent heat of solidification can be conducted away from the solid-liquid interface[20]. If the growth of the solid is into a superheated liquid, [referring to the heat directions shown in **Figure 2.11 (a)**], there is a positive temperature gradient and heat is conducted away from the liquid into the solid, with the interface remaining stable. In this way, planar growth is the result. However, if the liquid is supercooled, there is a negative temperature gradient [referring to the heat directions shown in **Figure 2.11 (b)**], and the interface becomes unstable. The resulting growth of the interface is protrusional, leading to dendritic morphology.

As solidification progresses in a two-phase alloy, a solute-rich boundary layer builds up ahead of the planar liquid-solid interface[22]. The solute composition is at a maximum at the interface and the concentration then decreases with increasing distance from the interface. This can be seen in **Figure 2.12 (b)**. Owing to the fact that the liquidus temperature, based on the phase diagram in **Figure 2.12 (a)**, increases as the solute content decreases, the equilibrium liquidus temperature increases with distance from the interface, as indicated in **Figure 2.12 (c)**. If protrusions do begin to form from this planar interface, they will extend into a superheated liquid ahead of the interface and will melt back. **Figure 2.12(d)** shows the situation where the liquid ahead of the interface is at an actual temperature that is below the equilibrium liquidus temperature, i.e. supercooled. Because the supercooling is a direct result of composition change, this type of supercooling is termed ‘constitutional supercooling’. Under these conditions, the interface is unstable and any protrusion that forms will extend into the supercooled liquid and will not disappear[22]. During the initial stages of the destabilisation of the solid-liquid interface, the formation of a cellular growth structure is seen. This can be seen in **Figure 2.10** (a) – (e), where in (b) as a protrusion forms, solute is rejected laterally and piles up at the root of the protrusion, this lowers the equilibrium solidification temperature in that area, causing depressions to form, as indicated in (c). This in turn triggers the formation of other protrusions. Eventually the protrusions develop into cells growing parallel to the direction of heat flow[20], as shown in **Figure 2.10** (e).

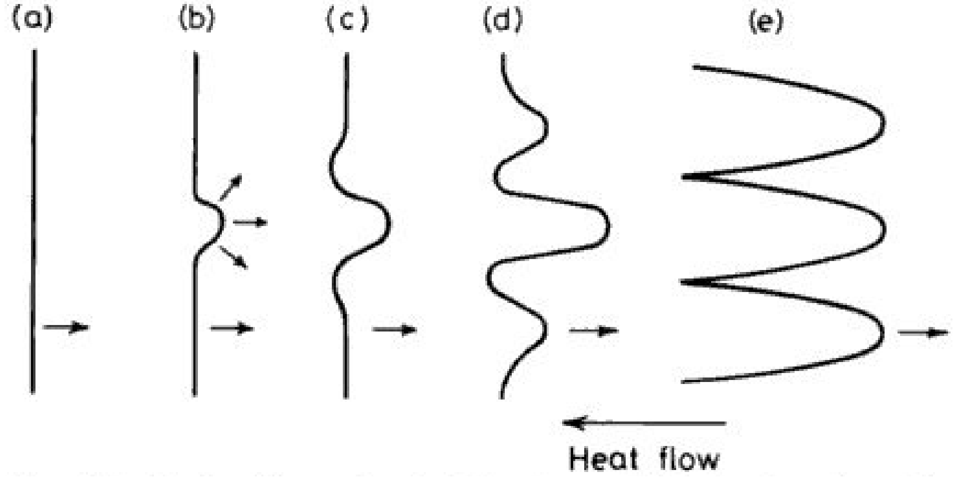

Figure 2.10: *Breakdown of a planar solidification front into cells[20].*

Cellular growth occurs at low growth rates and planar interface grows perpendicular to the solid-liquid interface regardless of crystal orientation of the interface[22]. The transition from cellular to dendritic growth occurs when there is a shape change during increased velocity. The length increases in relation to the radius of the tip, and the growth direction aligns itself with the <100> dendrite direction. In addition, the cross-sectional area of the protrusion changes from that of a circular shape to one where side branches begin to form and grow. In this way cellular growth is a precursor to dendritic growth, if the conditions are correct, as seen in **Figure 2.12** (d).

The solid-liquid interface of a metallic system is referred to as having an atomically-rough or diffuse interface. At this interface, the transition from liquid to solid occurs over a few atomic layers. The migration of this type of solid-liquid interface takes place by continuous growth[20]. This continuous growth or solidification is a diffusion-controlled process that is generally accepted to occur at approximately the equilibrium melting temperature (T_m) with minute or no undercoolings. For pure metals, the rate is controlled by heat conduction or, more specifically, the rate at which latent heat of solidification can be conducted away from the solid-liquid interface. For alloys, the growth is controlled by solute diffusion.

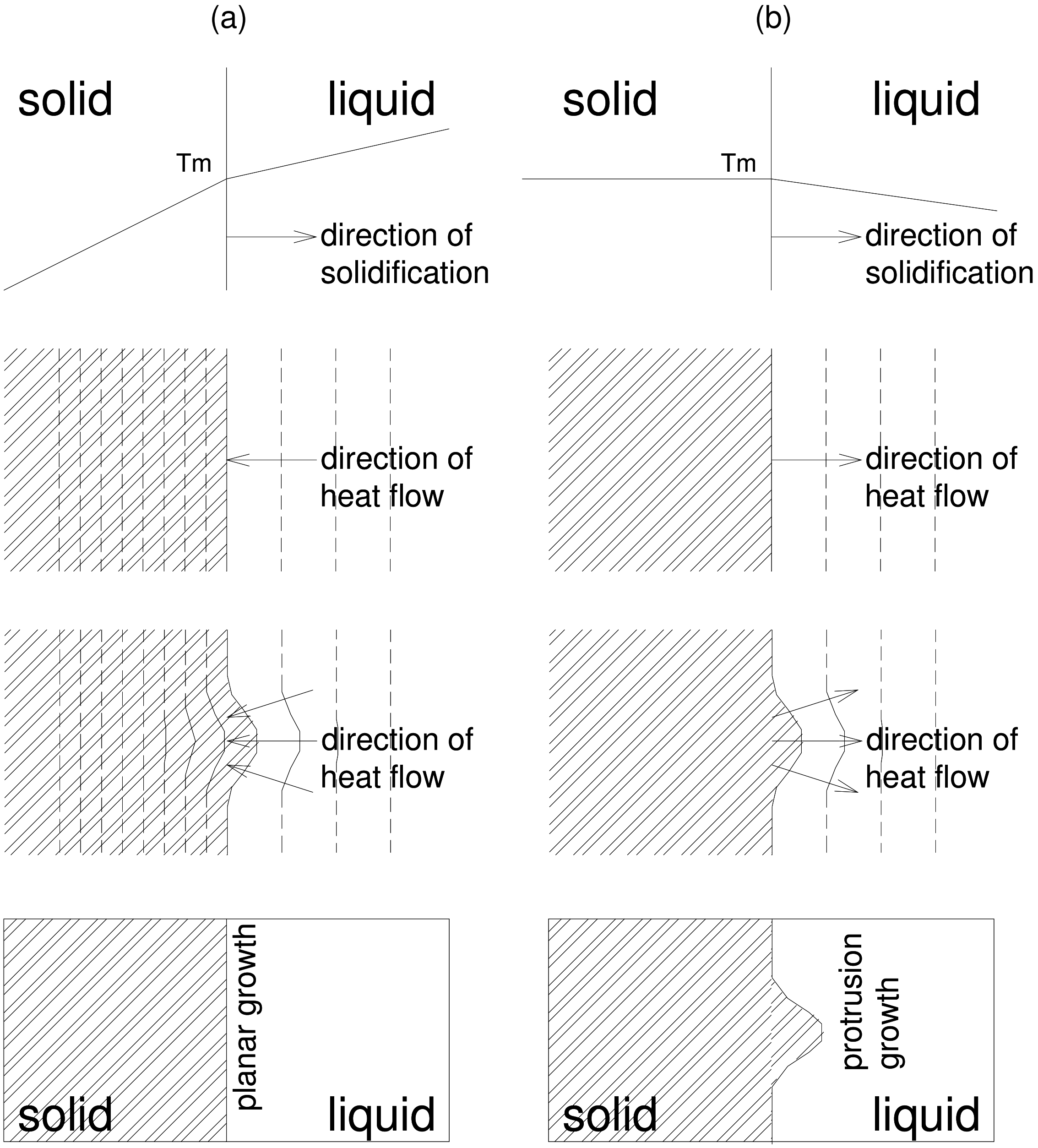

Figure 2.11: *Temperature distribution, and direction of heat flow effects on the solid-liquid interface stability; (a) planar growth; (b) protrusional growth*[20]*.*

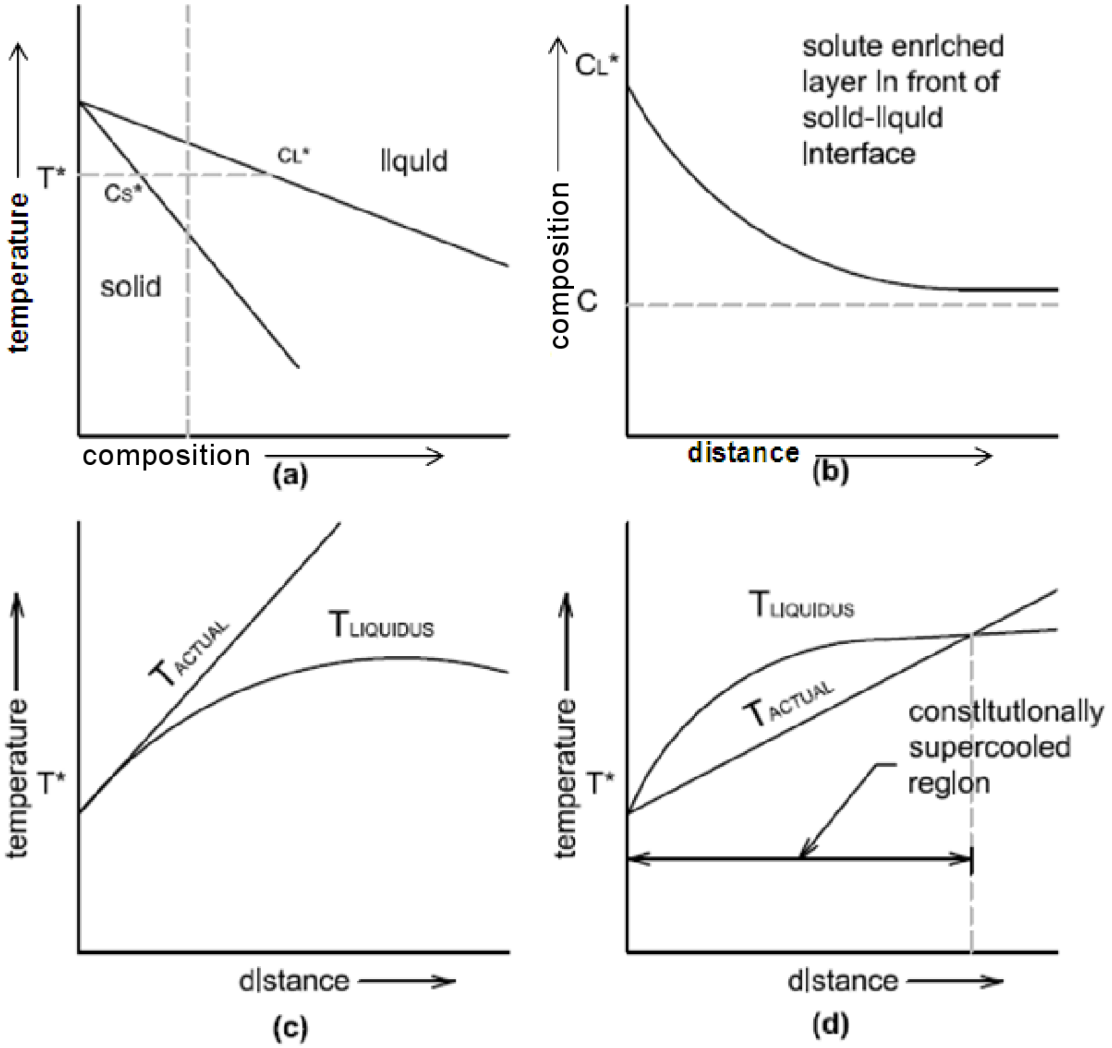

Figure 2.12: *Constitutional supercooling in alloy solidification. (a) Phase diagram; (b) solute enriched layer in front of solid-liquid interface; (c) stable interface; (d) unstable interface.*

2.3.1.3. PLANE FRONT SOLIDIFICATION AND THE SCHEIL EQUATION

To understand the fundamentals of solidification it is easier to look first at single-component alloys under normal solidification conditions (plane front solidification from one end) and progress from that point.

The solidification pattern of alloys depends on temperature gradients, cooling rates and growth rates. There are three cases that are used to describe the typical modes of solidification when considering a planar solid-liquid interface along a bar with unidirectional solidification. These are:

(i) infinitely slow (equilibrium) solidification;
(ii) solidification with no diffusion in the solid but perfect mixing in the liquid;
(iii) solidification with no diffusion in the solid and only diffusional mixing in the liquid[20].

For each of these simple solidification paths, a typical compositional gradient will result. Case (i) will give a homogeneous distribution, with compositions following the solidus and liquidus lines. Case (ii) occurs when the cooling rate is too rapid to allow substantial diffusion in the solid phase, giving the first solid to form a purer composition than the subsequent solid that forms. This causes an even enrichment of the mixed liquid. The solid-liquid interface in (iii) will always have a rapid build-up of solute just ahead of the solid, resulting in a rapid increase in the composition of the solid formed in the initial transient phase. There is then a phase of solid-state solidification with no variation of composition. The last to solidify is the extremely solute-rich liquid that forms an eutectic.

Although these three cases are described individually, solidification of an alloy will generally exhibit features from all three cases.

Figure 2.13 shows that, when considering a bar cooled from one end, the first solid to form at T_1 will have composition $k_0 X_0$, which has a lower solute concentration than the alloy, where k_0 is the equilibrium distribution coefficient. This means that the first solid to form will be purer than the liquid from which it is formed, so that solute is rejected into the liquid, thus raising its solute concentration[20].

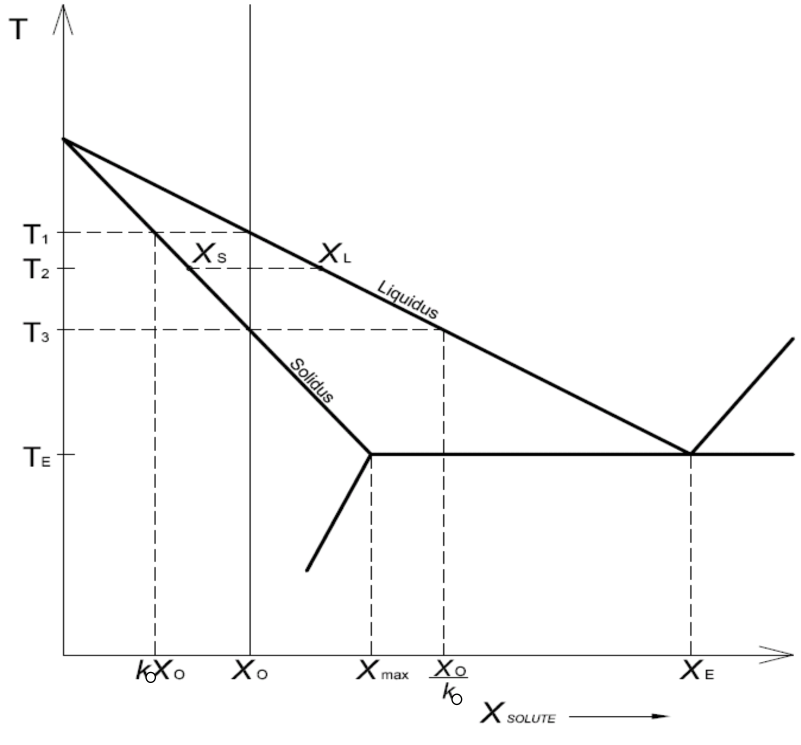

Figure 2.13: *A hypothetical phase diagram. The equilibrium distribution coefficient K_o = Xs/Xl is constant*[20].

In order to achieve equilibrium solidification, crystal growth needs to be infinitely slow. In addition, there needs to be complete diffusion in the liquid state and complete diffusion in the solid state. The composition of the solid and the liquid are always homogeneous, following the liquidus and solidus lines of the phase diagram, as shown in **Figure 2.13.** The final composition of the whole will be X_0. Only if the conditions of solidification satisfy these parameters will equilibrium solidification be achieved.

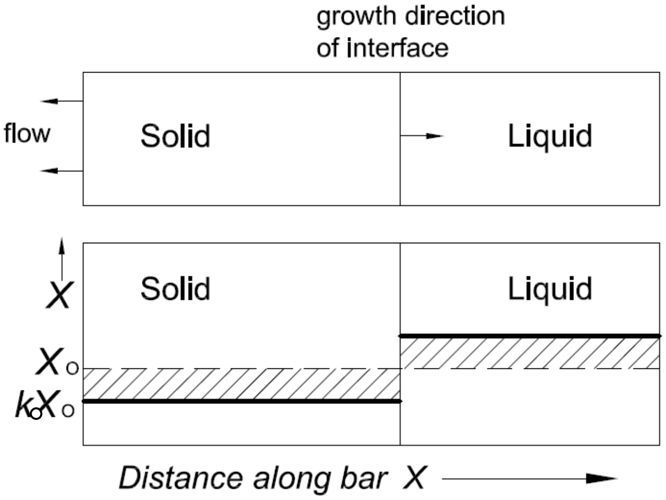

Figure 2.14: *Unidirectional/equilibrium solidification of alloy X_0 and corresponding composition profile at T_2*[20]*.*

Generally, equilibrium solidification does not occur, owing to the fact that the concentration of solute within a melt will usually be unevenly distributed. Therefore, complete diffusion in the solid is unlikely and the composition of the first solid to form will be of a purer concentration and will consequently affect the concentration of the remaining melt. This variation in composition in both the solid and the melt during the solidification process leads to what is referred to as micro-segregation (a separation of the solute elements on a micro scale).

Figure 2.15 shows the composition solidification path that occurs when there is no diffusion in the solid and complete mixing in the liquid. This case also results in an overall composition of X_0, but there are composition variations over micron-scale distances within the structure.

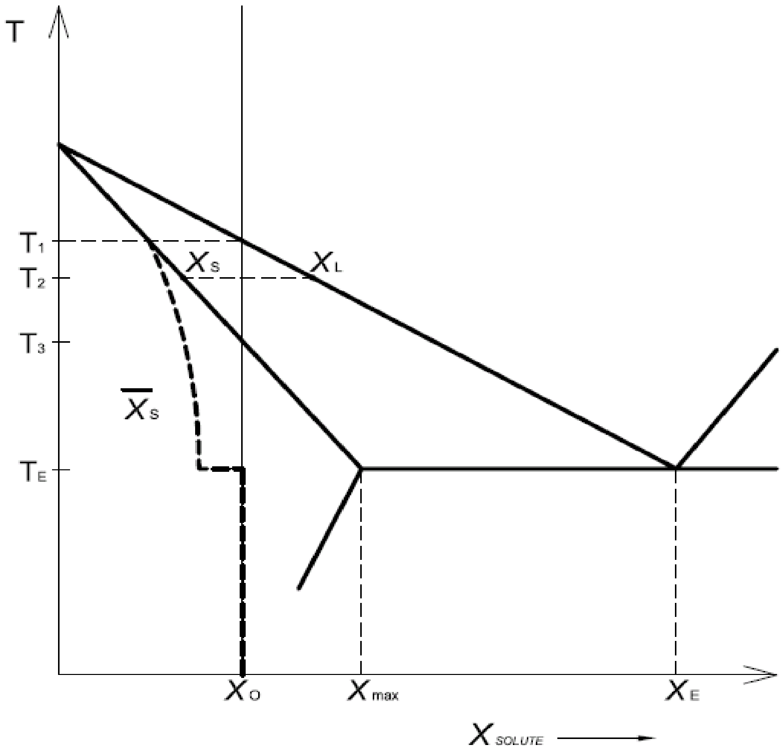

Figure 2.15: *Planar front solidification of an alloy X_o assuming no diffusion in the solid, but complete mixing in the liquid, showing the mean composition of the solid $\overline{X}_S$* [20].

Case (ii) follows the composition line illustrated in **Figure 2.15**, where there is no diffusion in the solid and complete mixing in the liquid. This case occurs when the rate of cooling is too rapid to allow significant diffusion in the solid phase. As a result, the first solid to form will have a purer composition than any subsequent solid. The remaining liquid has a homogeneous concentration distribution, owing to the mixing, but the solute content will increase as solute is rejected from the solid during the progression of the solidification process. The final solid will have a compositional gradient with increasing solute content from the first to the last liquid that solidifies. This is referred to as 'coring', which is a type of micro-segregation across distances of the order of a single grain diameter. The composition along a bar that has solidified from one end under these conditions can be determined by following the solid-liquid interface progression shown in **Figure 2.16**.

The first solid to form is always purer than the liquid, with a concentration of k_0X_0, according to **Figure 2.13** when equilibrium conditions exist, and solute is rejected into the liquid just ahead of the solid-liquid interface, causing a solute rich boundary layer. During non-equilibrium conditions *k*, the non-equilibrium distribution coefficient should be considered, where the relationship between k/k_o is given by:

$$\frac{k}{k_o} = \frac{1}{\left\{ k_o + (1-k_o)\exp(\frac{-\delta_c G_R}{D_1} \right\}} \qquad \text{Equation 2.7}$$

where δ_c is the thickness of the boundary layer, G_R is the growth rate and D_1 is the diffusion rate in the liquid. These parameters will be affected in situations where the liquid is stirred.

As the sequence of solidification and solute rejection continues, the liquid becomes progressively richer in solute. In case (ii) there is perfect mixing in the liquid, resulting in a homogenous distribution within the liquid. If there is only diffusional mixing in the liquid, as described in case (iii), the solute-rich liquid is situated just ahead of the solidification front, with diffusion alone being insufficient to distribute the solute homogeneously throughout the liquid. This solute-rich boundary layer results in further solidification taking place at progressively lower temperatures[20]. With decreasing temperature, the next layer of solid will be slightly richer in solute than the previous layer. However, since there is almost no diffusion in the solid, the separate layers of solid retain their original composition. Thus, the mean composition of the solid is always lower than the composition of the solid-liquid interface[23]. Solidification will then end close to $T_{E,}$ with the formation of an eutectic structure.

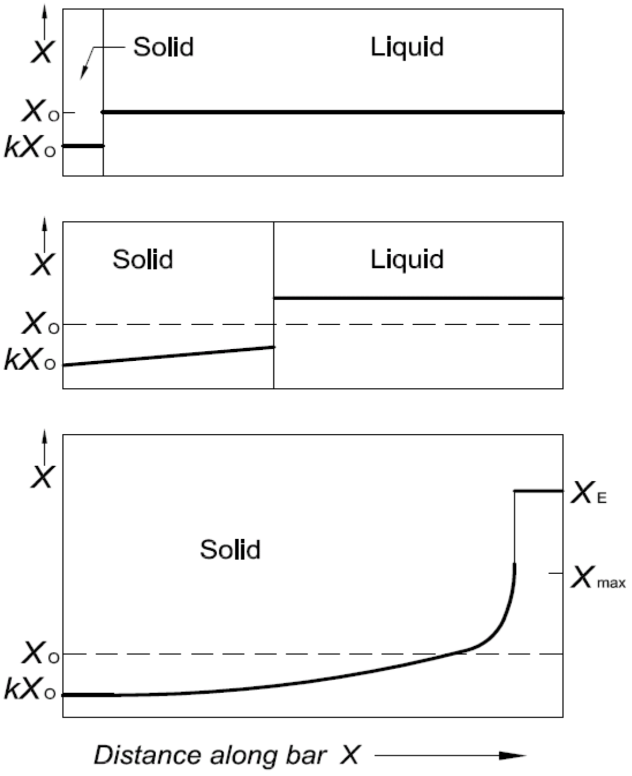

Figure 2.16: *Composition profile corresponding to* ***Figure 2.15****.*
(a) Composition just under T_1, (b) composition profile at T_2 and (c) composition profile at the eutectic temperature, T_E, and below.

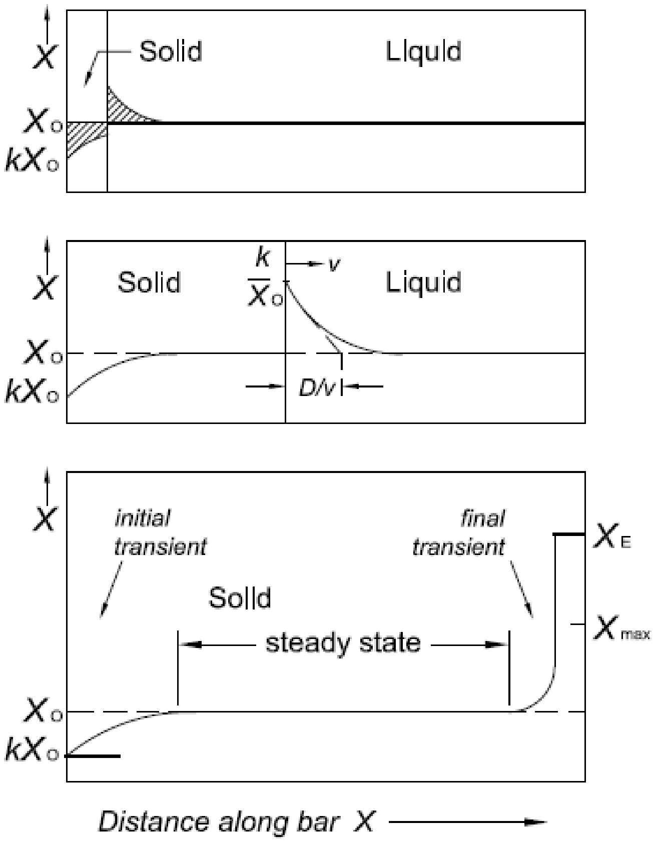

Figure 2.17 : *Solidification along a bar with no diffusion in the solid and only diffusional mixing in the liquid*

The change in composition along the solidified bar can be obtained by equating the amount of solute rejected into the liquid with the resulting solute increase in the liquid. This is described by

$$(X_L - X_S)df_S = (1 - f_S)dX_L \qquad \textit{Equation 2.8}$$

where f_S is the volume fraction solidified. The integration of this equation, using the boundary condition, $X_S = kX_O$, when $f_S = 0$, gives

$$X_S = kX_O(1 - f_S)^{(k-1)} \qquad \textit{Equation 2.9}$$

and

$$X_L = X_O f_L^{(k-1)} \qquad \textit{Equation 2.10}$$

These equations are known as the *non-equilibrium lever rule* or the *Scheil equations*. For *k<1*, these equations always predict that when there is no diffusion in the solid there will always be some eutectic in the last drop of liquid to solidify[20].

2.3.1.4. EQUIAXED DENDRITIC GROWTH IN A FREE LIQUID

The formation of dendrites arises owing to the solidification mode, as discussed in **Chapter 2.3.1.3**, and to the rate of cooling. Various models have been developed to describe equiaxed (6-primary arm) dendritic solidification in a free liquid scenario. The guidelines of these models can be used to describe the transition from nucleation to the equiaxed growth of dendritic grains in a free liquid during solidification.

Wu and Ludwig[24] have developed a modified volume-averaged equiaxed solidification model (WL model), which takes into account nucleation, globular grain growth, globular-to-dendritic transition, dendritic growth, formation of extra- and interdendritic eutectic, grains transport and convection. This model was based on a combination of other models in order to develop a model that described equiaxed dendritic solidification by modifying and combining previous globular and dendritic models. Some of these models were:

- The Rappaz and Boettinger[25] model, which considered an environment where the concentrations of the interdendritic liquid regions were different from the concentrations at the dendrite tips.
- The Rappaz and Thévos[26] (RT) model, which considered uniform and equal concentration of the interdendritic liquid and the liquid around the dendrite tip.
- The Wang and Beckermann[27] model, which incorporated the growth of the dendrite tips and the coarsening of the dendrite arms, in order to consider solute diffusion over different length scales.

An equiaxed dendrite is simplified to a volume equivalent sphere (seen in both the RT model[26] and, in more detail, in the WL model[24]), as shown in **Figure 2.18**. The equivalent sphere has the same volume as the natural contour around the primary and secondary dendrite arm tips of the grain. This natural grain contour is represented by the dotted line in the figure. The dendrite itself is considered as a 6-arm equiaxed dendrite, where the diameter of the equivalent sphere is determined by the length of the primary and secondary dendrite arms. The sphere enclosing the dendrite is called the grain envelope.

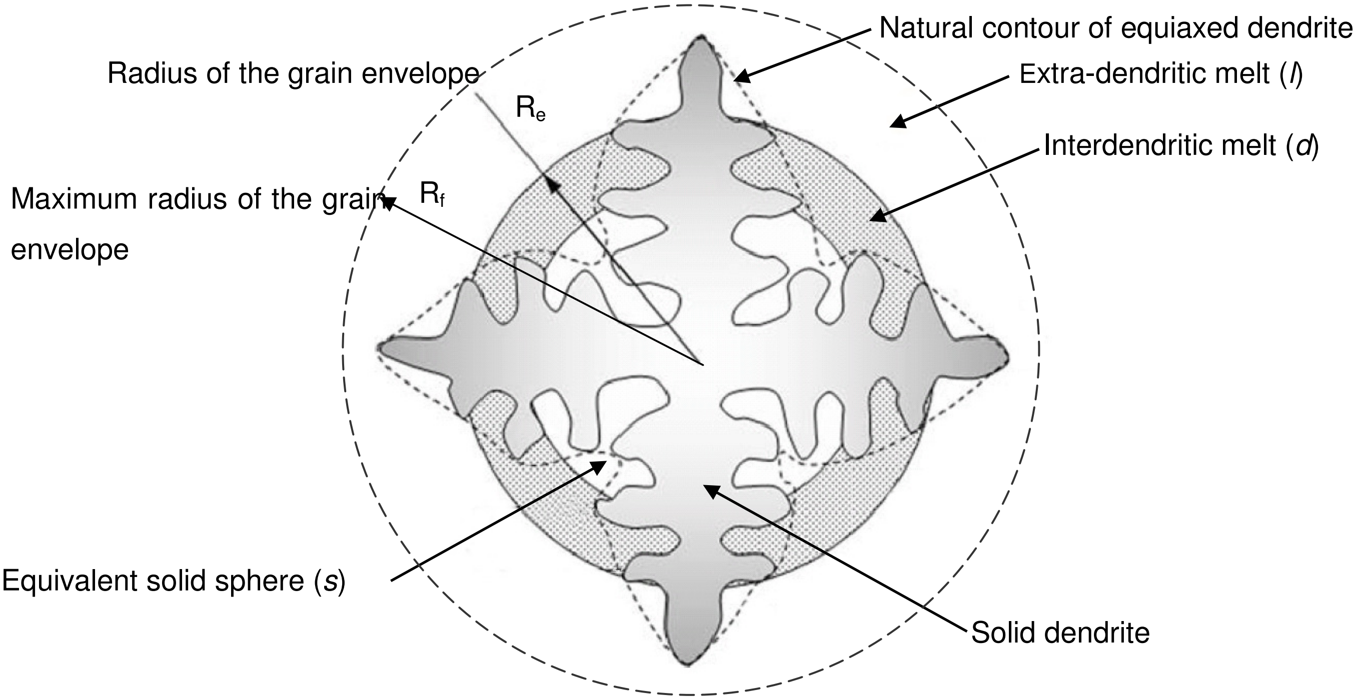

Figure 2.18: *The shape of a dendritic grain is simplified by an 'equivalent sphere', as illustrated in the WL-model [24].*

The spherical volume is divided into three regions: the solid dendrite (*s*); the interdendritic melt (*d*) within the envelope of the grain; and the extra-dendritic melt (*l*), outside the envelope. According to the RT model, the concentration profile is characterised by these three regions. In the solid dendrite, back-diffusion is neglected (i.e. the Scheil-type model). The main distinction between the RT model and the WL model is that, contrary to the RT model, the WL model suggests that there is incomplete mixing in the interdendritic melt, resulting in a non-uniform solute distribution where the diffusion length of the solute is related to the secondary dendritic arm spacing, λ_2.

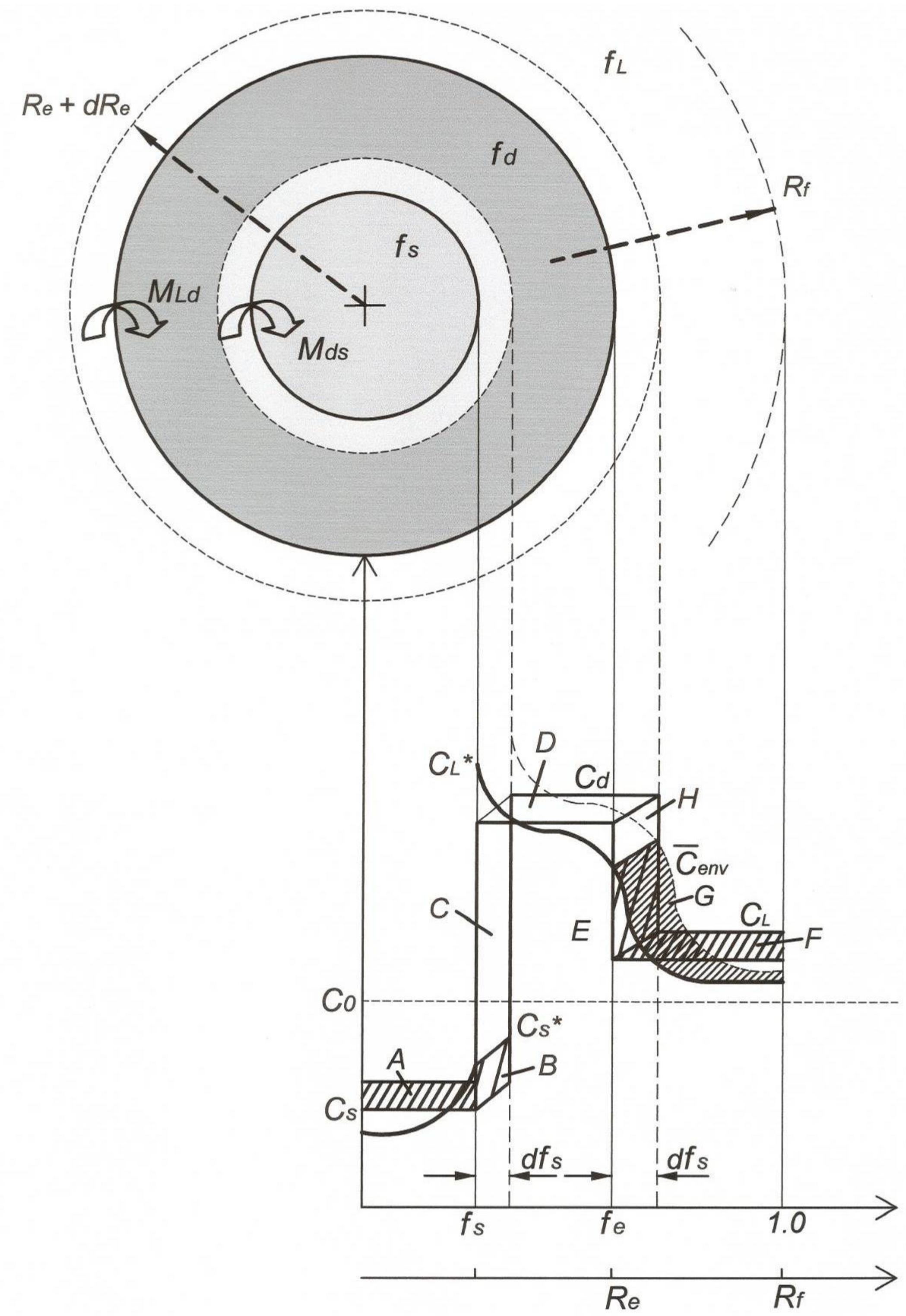

Figure 2.19: *Showing the solute redistribution, owing to grain growth and interdendritic melt solidification*[24]*.*

Figure 2.19, taken from the WL model, shows the solute concentration variations across the three different regions as the radius of equivalent sphere increases by a distance dR_e in a time interval *dt.* The figure includes the mass transfer across the different regions, taking into account mass and solute conservation[24]. As the volume fraction of the solid (f_s) increases, solute is rejected at the s-d interface.

Immediately on nucleation, when the local temperature drops below the liquidus temperature, an equiaxed grain begins to grow with a globular morphology. At this point, there is no interdendritic melt and only mild solute enrichment at the solid-liquid interface. At a particular stage, the growth velocity of the grain envelope increases, and when it exceeds the growth velocity of the globule, a globular-to-dendritic transition (GDT) is reached, beyond which free dendritic growth begins[28]. The evolution of the equiaxed microstructure can be described in four stages, shown in **Figure 2.20** (a). The first stage is globular growth.

The second stage is beyond the GDT point, where the dendritic morphology can now be simplified into an equivalent sphere, as per the WL model. At this stage, interdendritic melt is incorporated into the grain envelope. The interdendritic melt has a non-uniform solute distribution and this composition imbalance acts as a driving force for the solidification of the interdendritic melt. This, in turn, causes solute rejection from the new solid into the melt, resulting in further enrichment of the interdendritic melt concentration. This increase in concentration as the sphere radius increases by dR_e can be seen in the schematic **Figure 2.19**. During stage II, large amounts of latent heat are released during the solidification of the interdendritic melt. At some point, this release of latent heat causes the cooling rate to decrease and there is an onset of recalescence, which is the sudden increase in temperature of the solid caused by the release of latent heat as the metal undergoes a change in crystalline structure. This is the start of stage III.

Owing to the recalescence and local rise in temperature, there is a decrease in the growth velocity of the grain envelope and growth rate slows. Thus, the concentration difference between the interdendritic melt and the average concentration of the grain envelope decreases. Stage IV begins when the grain envelope can no longer grow significantly, owing to impingement.

This stage is characterised by confined dendritic growth, where there is coarsening or thickening or the dendrite arms. The differences in the concentration of the inter- and extra-dendritic melt decrease, and the enrichment of extra-dendritic melt increases and approaches an eutectic concentration. The composition variations across the four stages can be seen in **Figure 2.20**.

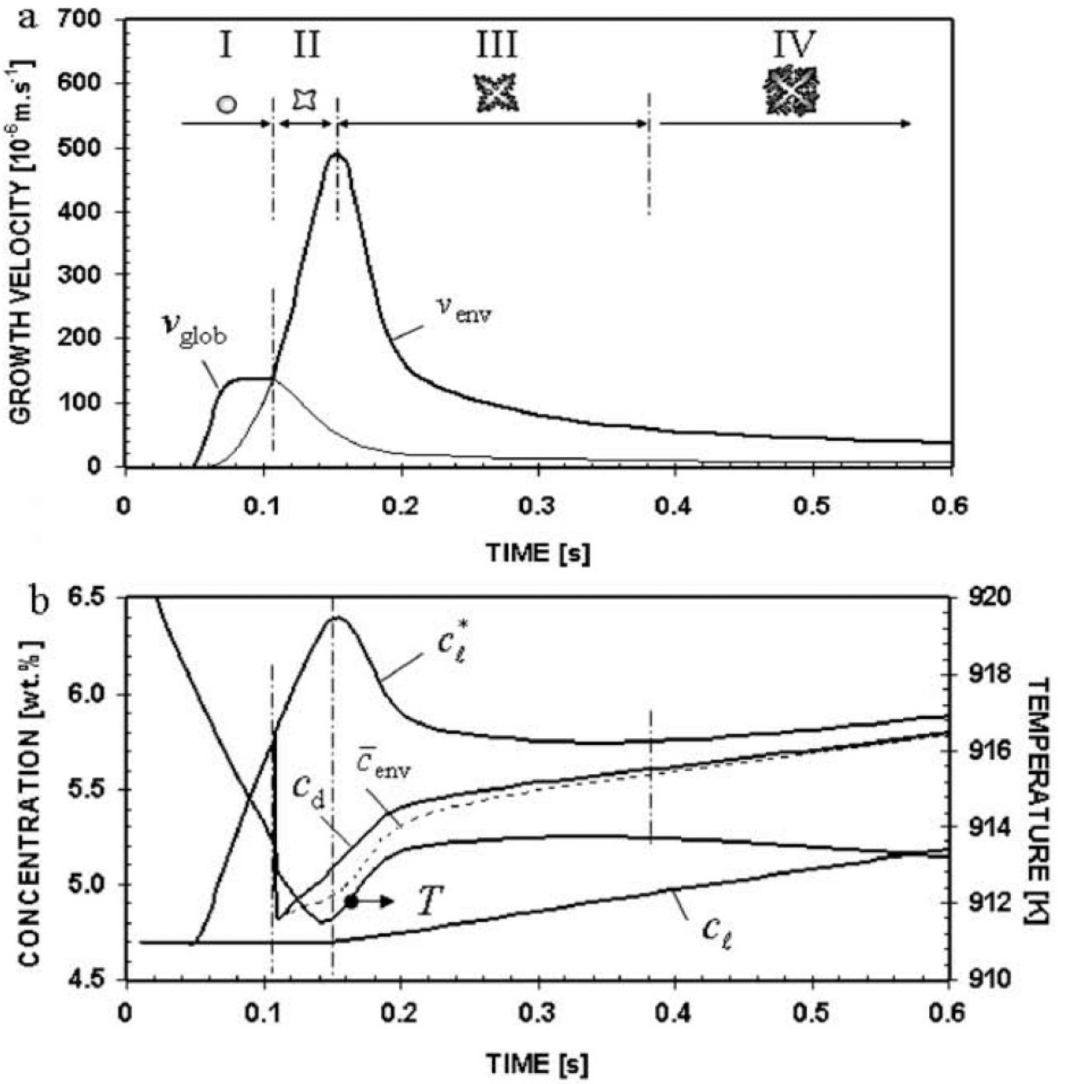

Figure 2.20: *Phase evolution for an Al-Si alloy during casting, showing (a) grain growth velocity and (b) concentrations in different phase regions*[28].

2.3.2. SOLIDIFICATION DURING STIRRING / TURBULENCE

2.3.2.1. EFFECT OF STIRRING ON NUCLEATION AND GROWTH

In addition to the consideration of free energy and temperature for the stability of the embryos and nuclei, it is necessary to examine the effect of kinetic motion, or stirring, on the stability of the nuclei, the critical radius size and changes in the morphology.

In conventional casting, liquid metal is poured into a mould and heterogeneous nucleation begins in the undercooled liquid on the cool mould walls. During casting in the presence of turbulence some solidified crystals will break away from the mould walls, a large portion of the solid crystals are transferred by convectional currents to the overheated regions of the mould. They soon dissolve. Therefore, only a small portion of the nuclei survive and this results in a non-uniform, coarse structure. An ideal situation would be for all of the nuclei to survive the casting process. This can be achieved under the following conditions: uniform temperature and composition distribution throughout the liquid volume; well-dispersed heterogeneous nucleation sites; and rapid extraction of latent heat to prevent recalescence. If these conditions are satisfied, the nuclei formed will survive and be evenly distributed, resulting in a fine and uniform microstructure[15, 29].

During semi-solid casting, the most significant processing step is the slurry production process, where the liquid metal undergoes a controlled cooling and stirring process, causing a high shear rate and turbulence within the melt during the nucleation process. In light of the importance of the above, it is necessary that the effect of stirring on the nucleation process and the changes in the critical conditions associated with nucleation be fully investigated.

The stirring process causes dispersive mixing in the melt and this results in an even distribution of temperature and composition and, once cooling begins, nuclei.

For nuclei to be stable in the melt during solidification, the temperature has to be such that there is a driving force for solidification. As nucleation occurs and solid clusters begin to form and grow in the melt, these clusters are only stable once they reach a critical radius, where growth, rather than re-melting, will decrease the free energy of the system. After the onset of heterogeneous nucleation at the mould walls, seen in conventional casting, only a small fraction of these nuclei that are formed will remain intact. This is due to the convection currents transferring them to areas where the temperature of the bulk liquid is higher. The heat causes the nuclei to remelt[15]. In contrast, during solidification under turbulent and shear conditions, the onset of heterogeneous nucleation on these nuclei, which are now floating in the free liquid owing to convection, takes place rapidly throughout the melt. This is due to the uniform temperature and composition distribution associated with a stirred melt. In these circumstances, the nucleation rate is no different from that of conventional casting. However, the survival rate of the nuclei is much higher in the stirred melt, leading to an increase in the effective nucleation rate. This in turn has a significant impact on the resulting microstructure, whereby the greater the quantity of nuclei that survive and grow, the finer will be the resulting microstructure.

There are three distinct zones within a solidification system, when the Scheil conditions are considered[22,23]:

(i) non-homogeneous solid, wherein solute distribution is controlled by diffusion that is dependent on the concentration gradient and heat flow, i.e. temperature;

(ii) solid-liquid interface or the ‘boundary layer’, which is highly enriched owing to the solute rejection from the growing solid phase;

(iii) bulk liquid, where solute is expected to be uniformly distributed, owing to convection and diffusion.

The main consideration when stirring is introduced is its effect on the boundary layer of the solid and on the solute distribution within the melt. These factors affect the diffusion, back into the solid and also into the liquid, as the solid-liquid interface progresses during solidification. This, in turn, affects the composition distribution in the solid and the resulting degree of segregation.

Vogel and Cantor[30] investigated the stability of spherical particle growth in a stirred melt, focusing on the effect of the thermal and solutal flow and the boundary layer thickness on the stability of the solid-liquid interface. It was determined that for a given bulk liquid undercooling, stirring led to an increase in the average rate of particle growth. Secondly, stirring destabilised the solidifying interface. Thirdly, stirring led to a decrease in the critical radius size of the nucleus for relative stability. In addition, if there were a decrease in the amount of undercooling, and the heat and solute at the interface were efficiently removed, causing a reduction in the boundary layer thickness, then both the increased rate of growth and the decrease in stability would be counteracted.

Forced convection, owing to shear forces during stirring, has the effect of enhancing both mass and solute transport within the melt. The consequence of this is a reduction in the thickness of the solutal diffusion boundary layer and a reduction in the degree of constitutional undercooling around floating solid particles[15]. Thermal and mass transport are dominated by diffusion in the boundary layer, and outside the boundary layer they are transported by convection. When there is shear and rotation in the fluid because of stirring and turbulence, the flow penetrates into the regions between the dendrite arms. This stimulates growth in the region of the dendrite tip in both axial and lateral directions, giving rise to a rosette morphology. Turbulence also stimulates the growth rate at the root of the dendrite when the diffusion boundary layer is very thin, resulting in a sphere-like growth morphology. If the turbulence is such that the boundary layer eventually disappears, then the thermal and mass transports will be solely controlled by convection, in which case a sphere will be the stable growth morphology[15, 31].

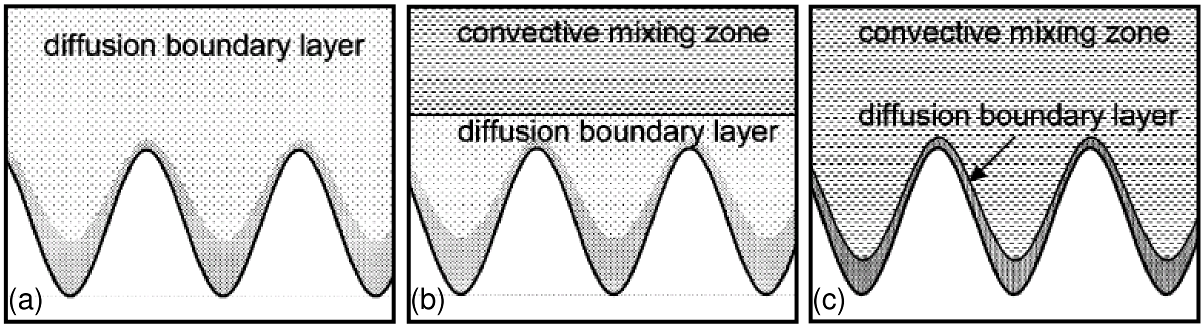

Figure 2.21: *Schematic illustration of the effect of fluid flow on the diffusion boundary layer geometry around a growing solid[31].*

Figure 2.21 shows a schematic of various boundary layer thicknesses and geometries around a growing solid. **Figure 2.21 (a)** shows an infinite diffusion boundary layer that is the consequence of solute transfer by diffusion throughout the entire volume of liquid. This results in a purely dendritic growth structure. A finite diffusion layer is illustrated in **Figure 2.21 (b)**. This finite layer is caused by the presence of low and intermediate shear rates, categorised as laminar flow. A finite boundary layer is located around the growing particle and beyond that is a convective mixing zone, with homogeneously-distributed solute in the melt, arising from convection. Solute transport within this finite boundary layer is still diffusive, and, consequently, dendritic growth still occurs if the thickness is such that the dendrites within the layer are unaffected by the laminar flow. This confirms the theory of destabilised solid-liquid growth fronts in convection and laminar flow (Vogel and Cantor[30]). At high shear rates, such as those experienced during slurry production in semi-solid metal casting, flow is characterised as turbulent and there is an increased likelihood that liquid will penetrate into the interdendritic region. This results in an extremely narrow boundary layer, as shown in **Figure 2.21 (c)**. Mixing inside this narrow boundary layer is diffusive and, beyond this layer, convective mixing takes place[15, 31].

2.3.3. DENDRITIC TO GLOBULAR GROWTH MORPHOLOGY IN SSM PROCESSING

Spencer and Flemings ascertained that when metal alloys were agitated vigorously during solidification, the viscosity of the liquid was maintained, while the temperature decreased and the solid fraction increased. In addition, after a controlled cooling to a 50% solid fraction, the solid that formed after casting was “non-dendritic” in structure[9]. The stirring process had the effect of globularising the morphology of the grains that formed and grew during the process. Spencer *et al* stated at the time that the non-dendritic structure was caused by the breakdown of the initially dendritic grains as a result of the shear stresses introduced by stirring[8]. This statement was based on 1971 observations of a Sn-15%Pb alloy in a Couette viscometer with various shearing and cooling rates.

Research into semi-solid metal processing and the resulting globular microstructure and the mechanisms that make it so, has been on-going for more than 30 years. Over this time, various researchers have used different techniques and have come to varying conclusions as to the true mechanism behind the morphological changes that occur during stirring. These can be divided into two general categories: dendrite fragmentation and spherical growth[32, 17]. Within each of these categories there are various theories that claim to explain the globularisation mechanisms.

2.3.3.1. DENDRITE FRAGMENTATION MECHANISM THEORY

At first it was believed that fragmentation of the initial dendrites was as a result of the shear experienced during forced convection[33]. These detached dendrite arms would then undergo a non-equilibrium growth process to provide nucleation sites for the observed globular particles. **Figure 2.22** shows the breaking off of dendrite arms when flow is introduced, and the floating of the detached arms in the surrounding melt[33]. This theory does provide a mechanism for grain multiplication under the conditions of forced convection, but it has been stated that, based on the toughness of the material, the dendrite arms would be more likely to bend than fracture when exposed to turbulent flow[34].

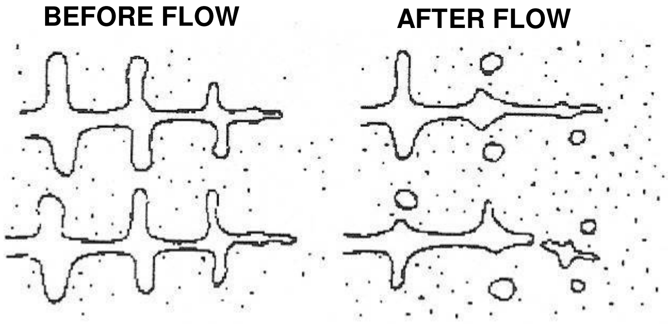

Figure 2.22: *Schematic of the breaking of dendrite arms with the introduction of shear.*

Vogel, Doherty and Cantor[34] proposed a model to describe the mechanism of dendrite fragmentation by grain boundary-induced melting. Based on experimental evidence, the model depended on the premise that, if a dendrite arm were bent through an angle θ with respect to the dendrite stem, the extra dislocations required to achieve this rotation would rearrange (by recovery and recrystallisation processes at high temperatures) to form a grain boundary with a misorientation angle θ. The energy of this boundary was proportional to the angle of misorientation. The formation of a highly bent dendrite arm would lead, after a short time delay, first to the formation of a grain boundary, followed by solute-rich liquid attacking the grain boundary, and finally, to the separation of the dendrite arm from the main dendrite.

This theory was supported by Doherty, Lee and Feest[35]. It was determined that the globular morphology was the result of dendritic fragmentation (breaking off of dendrite arms at their roots) during shearing, as shown in **Figure 2.23**. This illustrates the mechanism of grain boundary fragmentation.

Other experimental evidence for dendrite arm bending under large, externally-applied strains during stir casting was observed by Vieira *et al*[36], and commented on further by *Doherty*[37]. Ananiev *et al*[38] supported the experimental evidence that even normal solidification conditions could cause dendrites to mechanically bend[37] and found that there existed a critical loading level, which, if exceeded, resulted in the re-melting of the dendrite neck/root cross-section. This was a mechanism very similar to mechanical fragmentation.

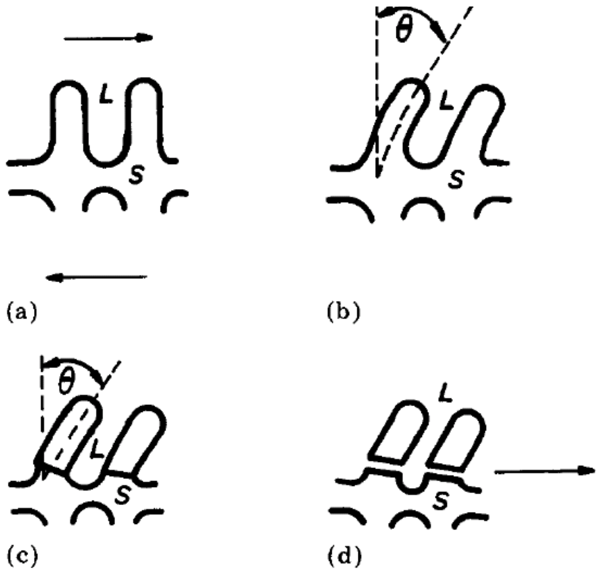

Figure 2.23: *Schematic model of the grain boundary fragmentation mechanism: (a) an undeformed dendrite arm; (b) a dendrite arm after bending; (c) the reorganisation of the lattice bending to give grain boundaries; (d) the grain boundaries have been "wetted" by the liquid phase*[35].

Hellawell[39,40] suggested that the shear stresses were not enough to cause massive fragmentation, but the cause of the globularisation was the re-melting of the dendrite arms at their roots. This type of fragmentation was a two-step process. Firstly, there was thinning of the secondary dendrite arms as a result of localised solute accumulation. This was due to the solute rejection from the dendrite arms during growth, in the area between the dendrite arms. Secondly, detachment occurred, owing to local melting at these positions. This melting was induced by decreases in growth or temperature gradients, or by a local rise in temperature. A schematic of this process, as determined by Campanella *et al* can be seen in **Figure 2.24**[41], which shows: (a) the growth of a protrusion into a developed dendritic side arm: (b) the thinning of the dendrite side arms, caused by the presence of a solute-rich boundary layer; and (c,) if the conditions were conducive, the fragmentation of the dendrite side arm by dendrite root re-melting. After detachment, these side arm fragments could be transported by thermo-solutal convection into the open liquid for the formation of rosette structures under low shear. The survival of these fragments depended on a favourable environment.

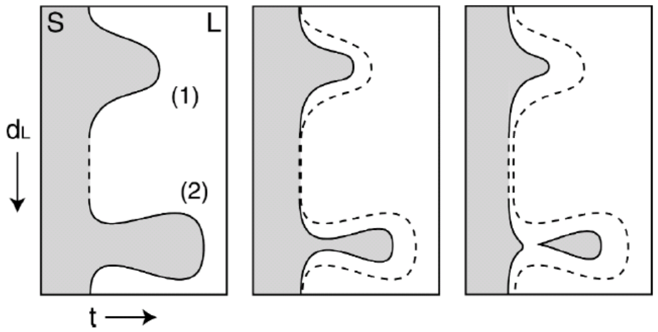

Figure 2.24: *Schematic of (a) dendritic growth, (b) thinning of dendrite arms and (c) fragmentation of secondary dendrite arm by dendrite root re-melting*[41]*.*

This mechanism of melting at the dendrite root for fragmentation of side arms has been investigated by others[41, 42] and the theory has been verified by modelling. An example of these results can be seen in **Figure 2.25**.

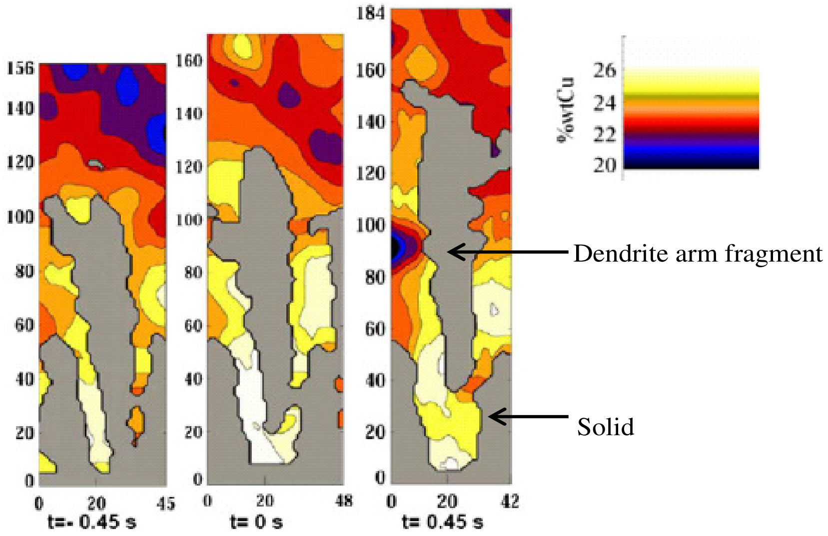

Figure 2.25: *Model of an Al-20wt%Cu alloy*[42]*. Contours show the solute enrichment between the dendrite arms during solidification, causing dendrite arm fragmentation by melting.*

These melted-off dendrite arms are re-distributed by the fluid flow and act as further nuclei within the melt, this adding to the overall grain refinement of the structure. These fragmented dendrites are expected to grow dendritically in the melt in their initial period of growth until there is an effect or impingement on the diffusion fields[17]. The mechanism of globularisation by this type of fragmentation can be described by the following steps[43]: (i) dendrite arm fragmentation by the re-melting of dendrite roots; (ii) transportation of these fragments by interdendritic convection; (iii) survival of the fragments in the liquid; and (iv), growth into rosette structures under low shear, and into spheroids at increased shear rates. This morphological progression after detachment, as described by Flemings[33], is shown in **Figure 2.26**.

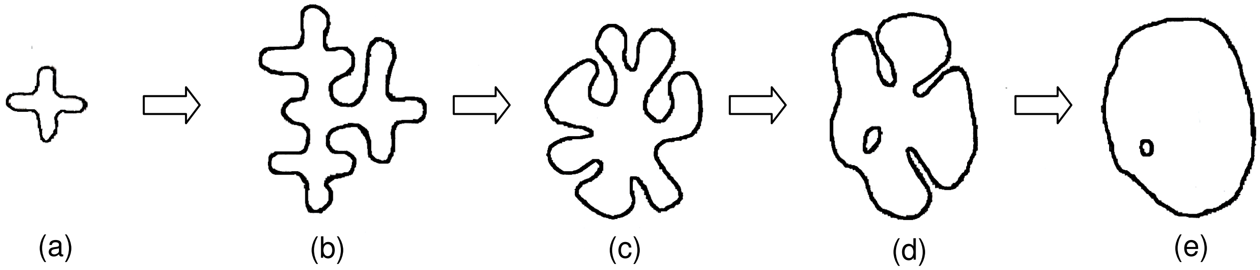

Figure 2.26: *The evolution of a structure during solidification with increasing shear rate, increasing shear time and decreasing cooling rate: (a) initial dendritic fragment, (b) dendritic growth, (c) rosette, (d) ripened rosette and (e) spheroid.*

Mullis[44] presented a model for dendritic growth in a non-stationary flow and predicted the bending of dendrite arms into a rosette formation. This theory was not a fragmentation theory, but neither was it a spherical growth theory. Instead, it described the change in morphology of the resulting grains by deformation of dendritic growth. This theory was based on a Cellular Automaton programme that was used to trace the locus of the dendrite tip within an equiaxed crystal, growing in a free liquid, and to approximate the shape of the resultant crystal. The locus was determined by the growth rate, the flow velocity and the deflection of the tip. A schematic for this growth is shown in **Figure 2.27**.

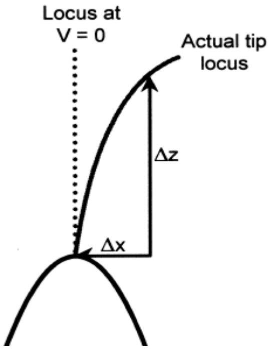

Figure 2.27: *Schematic of locus of the growing tip bending into the cross flowing undercooled melt.*

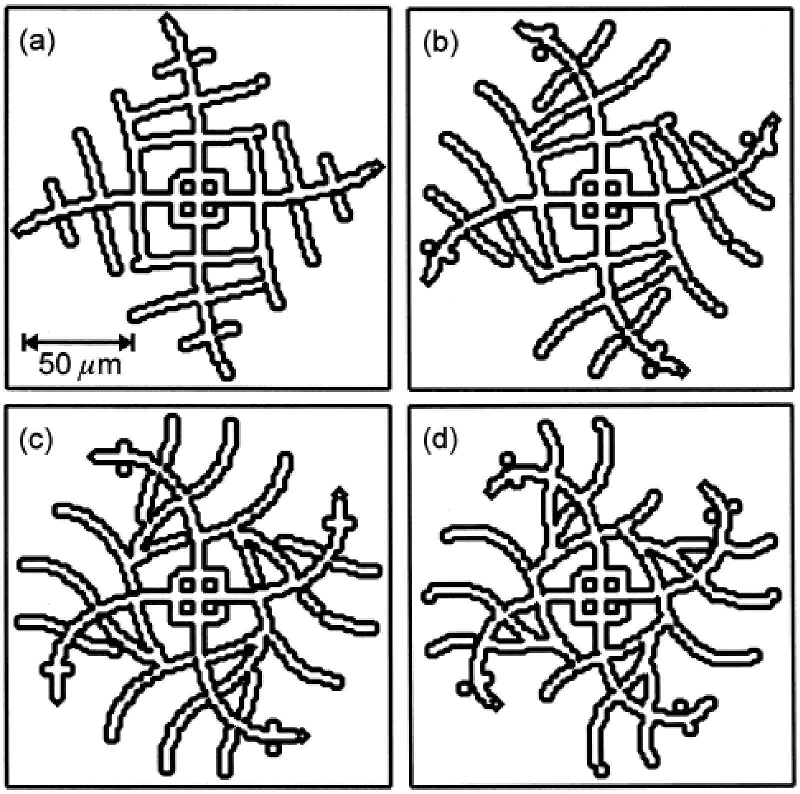

Figure 2.28: *Cellular automaton simulations by Mullis. Showing bending of dendrite tips as a result of increased shear rates: (a) $\dot{\gamma}$ = 200/s; (b) $\dot{\gamma}$ = 400/s; (c) $\dot{\gamma}$ = 600/s and (d) $\dot{\gamma}$ = 800/s.*

The limitation of this model is that it ignores dendrite trunk thickening and ripening during growth, but merely traces the loci of the tips. Secondary arms are considered to grow until they collide with primary or other secondary grains and then their growth is terminated. **Figure 2.28** shows the cellular automaton prediction for various shear rates. It can be seen that the magnitude of the bending, determined by shear rate, defines the maximum size of the dendritic crystal, prior to full spheroidisation.

2.3.3.2. SPHERICAL GROWTH MECHANISM THEORY

The more recent theories tend towards the view that the globular morphology seen in semi-solid metal processing is as a result of spherical growth under forced convection[32].

Molenaar, *et al*[45,46] suggested that the rosette-type growth originated from cellular growth during solidification under shearing, owing to the thermal gradient in the liquid at the interface and the boundary layer, and to a decreased growth rate that resulted from the morphological type of growth becoming cellular. **Figure 2.29** (b) shows that the growth morphology changes from dendritic to cellular before stability of the interface is achieved for conventional solidification (unidirectional), while **Figure 2.29** (a) shows that the interface is stable when G_L = 0, and it is suggested that the growth of a solid in a stirred free liquid will be cellular when G_L has become sufficiently small.

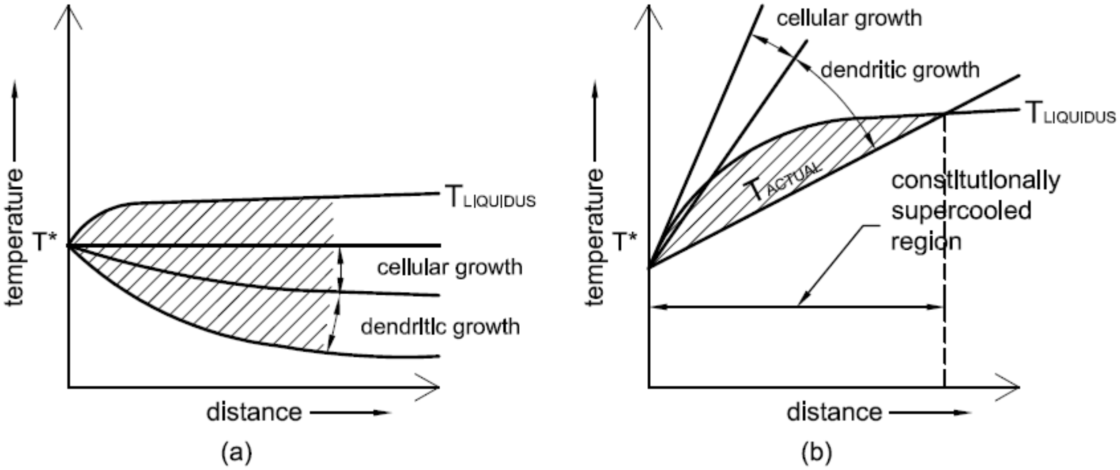

Figure 2.29 : *Constitutional supercooling at the solid-liquid interface, showing the temperature profile where there is a transition between dendritic growth and cellular growth for (a) a floating particle in a free liquid, and (b) in conventional solidification.*

Molenaar also determined that stircast/rheocast structures were typically non-dendritic, and that the growth of the primary particles, even at early stages of solidification, is cellular rather than dendritic. A stircast structure is made up of rosette-type particles and particles consisting of radially grown cells. The radially grown cells are considered to have grown with a cellular growth morphology owing to their associated cell-spacing (defined as the measure of the cell-tip diameter) which is large when compared to that of dendritic growth. This increased cell-spacing is a more stable morphological type of growth. Another characteristic that was viewed was the decrease in the amount of entrapped liquid with increasing solidification time (longer stirring times with slower solidification rates), until a point where the structure was made up of agglomerated cells.

Ji and Fan[15] experimentally investigated the effect of turbulent flow on growth morphology and determined that increased shear rate and the intensity of stirring stabilised the liquid-solid interface. The growth morphology changed from rosette to spherical. This can be seen in **Figure 2.30** and, in more detail, in **Figure 2.5**.

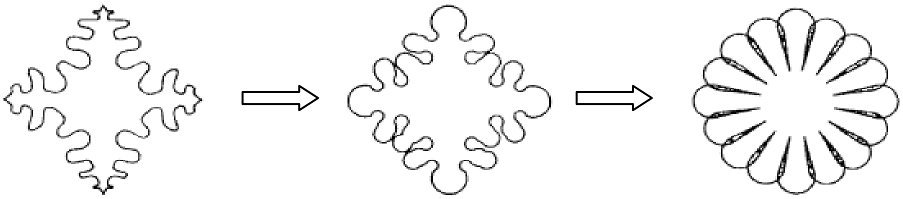

Figure 2.30: *Schematic illustration of the evolution of a rosette with from equiaxed dendrites under pure shear flow.*

This theory of morphology change was used in conjunction with stability analysis and the boundary element method in a Monte Carlo simulation by Das *et al*[31,47]. From this it was concluded that a laminar type of fluid flow destabilised the solid-liquid interface of particles growing from a fixed substrate, and promoted dendritic growth. This was due to the rotational motion under turbulent flow. The periodic stabilising and destabilising effect promoted a rosette-type growth morphology. A turbulent flow that penetrated into the interdendritic region prevented dendritic growth and stabilised the solid-liquid interface.

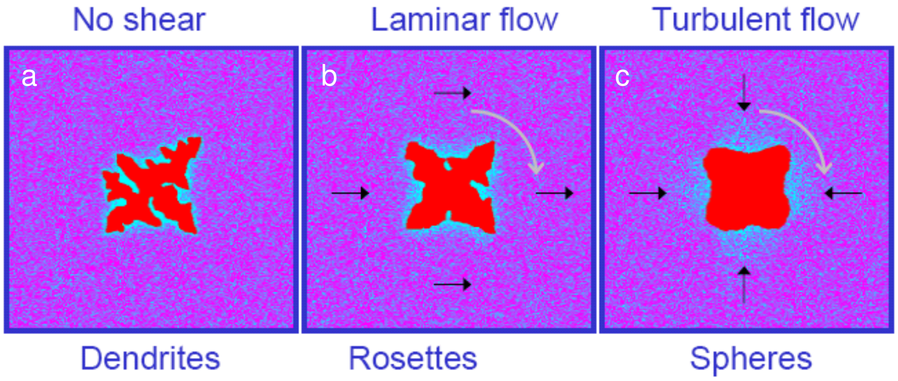

Figure 2.31: *The effect of shear and fluid flow on the morphology of solidification structures. (a) Pure diffusion; (b) and (c) increase of the flow turbulence, stabilising the liquid-solid interface and promoting rosette and spherical growth morphology, this corresponding to the decrease in the diffusion boundary layer thickness.*

The various theories focussed on growth morphology and largely ignored the nucleation process within a stirred melt. Investigations into the nucleation process are problematic, owing to the impossibility of observing the microstructural formation at the early stages of the process[17]. Nucleation was generally treated as heterogeneous, as there was no indication that stirring induced homogeneous nucleation. If dendrite fragmentation were a globularisation method, the fragments would act as further nuclei for continued solidification.

During the continuous cooling stage in primary solidification during SSM processing the volume fraction increases with shearing time, as shown in **Figure 2.32**[32]. At the same time, the particle density also increases, which cannot be explained by the dendrite fragmentation theory. This evidence supports a theory of a continuous heterogeneous nucleation mechanism during the continuous cooling stage, with a high nucleus survival rate that is due to uniform temperature and composition distributions in a stirred melt. Fan and Liu[32] propose that these nuclei grow spherically with an extremely fast growth rate, and that the coarsening rate is much slower during the isothermal shearing stage.

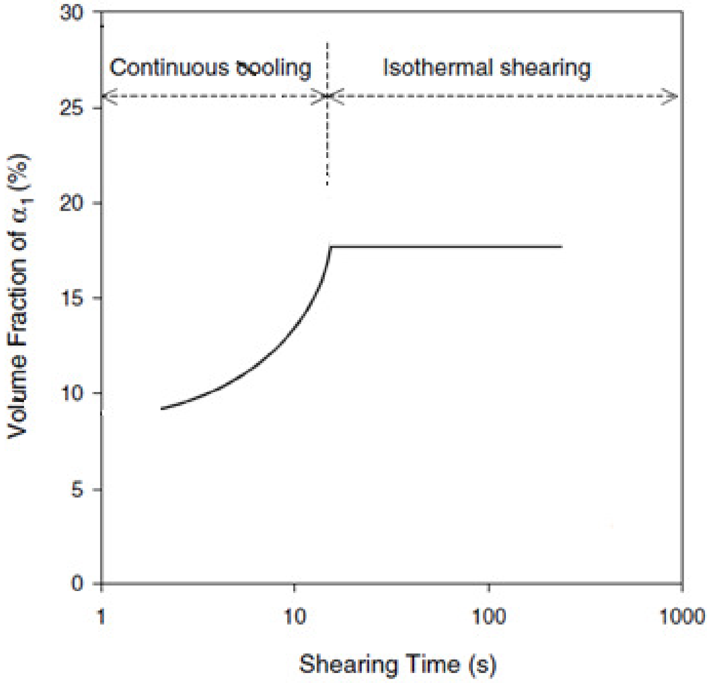

Figure 2.32: *Volume fraction of primary particles formed in the twin-screw slurry maker in the RDC process.*

Niroumand and Xia[48] have shown that, after semi-solid slurry production, the primary particles do not originate from dendrites that break up during the turbulent flow. Instead, they are pseudo-particles that group together and form pseudo-clusters in 2D. However, 3D analysis shows that they are, in fact, connected to one another and are not individual primary grains, but are large, agglomerated 3D primary grains, which may have been disfigured by the shearing process. A 3D render of this type of globule is shown in **Figure 2.33**.

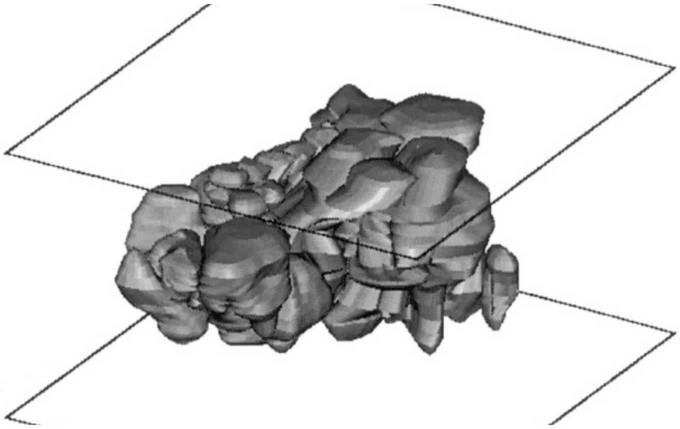

Figure 2.33: *A 3D rendered pseudo-cluster, or single primary grain, after semi-solid slurry production.*

2.3.4. SECONDARY SOLIDIFICATION DURING SSM PROCESSING

There is a general acceptance of the fact that there are both primary and secondary solidification stages that occur during SSM processing. Primary solidification occurs during the slurry production step of the process. This primary solidification stage can be divided into two sub-stages: continuous cooling and isothermal shearing[32, 49]. This can be seen in **Figure 2.32**. Heterogeneous nucleation occurs in the continuous cooling stage, and particle coarsening occurs through Ostwald ripening, the consumption of the smaller particles, during the isothermal shearing stage. Secondary solidification refers to the solidification of the remaining liquid during transfer of the slurry to the shot sleeve and inside the die cavity during the casting process itself.

Hitchcock *et al*[49] devised a labelling system, with terminology for grains of different average sizes within the standard SSM cast structure (produced by the RDC process). α_1 were large α-Al grains that formed inside the slurry maker, α_2 were slightly smaller α-Al grains that formed during transfer into the shot sleeve prior to casting, and α_1 were the fine grains that made up a large portion of the structure and were delineated by eutectic. The α_2 grains were formed by heterogeneous nucleation of the remaining liquid during slurry transfer. It was suggested that these grains grew dendritically in the absence of turbulence and that they fragmented when they were forced through the narrow gates of the die during HPDC. The rate of cooling during the secondary solidification stage would affect the final α-Al grain size, as the α_1 and α_2 grains would continue to grow during this stage. Therefore, a rapid cooling rate would result in smaller α_1 grains[50].

2.4. HIGH STRENGTH ALUMINIUM ALLOYS

Alloys in the Al-Zn-Mg (7xxx series) are referred to as high-strength aluminium alloys, owing to their heat treatability and precipitation hardenability. They are used extensively in the automotive and aerospace industries. There are a few drawbacks to this series of alloy: they are susceptible to stress corrosion cracking (although the extent of this can be minimised with the addition of copper as an alloying element)[51]; and the presence of course particles (greater than 1µm), such as Fe-rich or Cu-rich phases, will lead to deterioration of the alloy series' toughness and fatigue properties[52].

The Al-Zn-Mg-Cu quaternary system is the basis of one of the strongest aluminium alloys, of which AA7075 and A713 alloys are part. The phase diagram is shown in **Figure 2.34**. There are three domains of continuous solid solutions that are formed by the phases of Al-Mg-Zn and Al-Cu-Mg ternary systems (between Al_6CuMg_4 and $Al_2Mg_3Zn_3$, between $MgZn_2$ and AlCuMg, and between $Al_5Cu_6Mg_2$ and Mg_2Zn_{11}). The major alloy phases that are present are based on $\eta(MgZn_2)$, $T(Al_2Mg_3Zn_3)$, $S(Al_2CuMg)$ and $\theta(Al_2Cu)$. Generally, this type of alloy can be homogenised substantially by a 35-hour homogenisation treatment at 450℃, but undissolved phases present will remain at the end of the treatment. These phases are a combination of Cu-bearing T and Zn-free S. The latter implies that zinc diffuses out of the S phase during annealing[53]

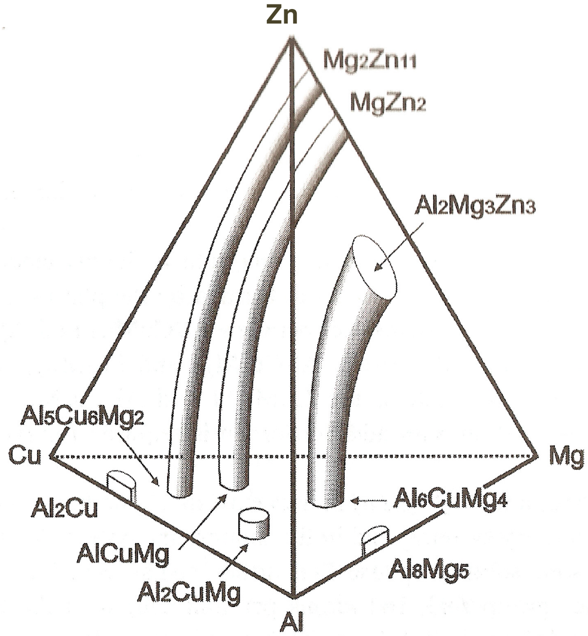

Figure 2.34: Phase diagram of the Al-Cu-Mg-Zn system showing the compositional ranges of single phases in a 3D diagram[54].

The strength of these alloys is controlled by the ageing process of precipitation and growth of fine precipitates of the ή phase, which is a semi-coherent metastable form of the equilibrium $MgZn_2$ phase[55]. Prior to any strengthening treatments, it is necessary to homogenise the as-cast structure in order to remove the segregation that results from the solidification process. Homogenisation of cast ingots is usually carried out to mitigate the effects of both micro- and macro-segregation by allowing the time at temperature to dissolve the Zn, Mg and Cu-rich eutectic intermetallic phases shown in the above phase diagram.

2.5. POST SOLIDIFICATION HEAT TREATMENTS

Heat treating is a term that is used to describe the heating and cooling operations that have the effect of altering the mechanical properties, the metallurgical structure or the residual stress state of a metal product. The heat treatment of aluminium alloys generally refers to the treatments involved in the increasing of strength and hardness of the precipitation-hardenable wrought alloys, such as AA7075[56,57]. The heat treatment of casting alloys, such as A356 and A357, is very similar to those designated for wrought alloys. The main difference is that cast products are not strained or cold worked at any stage, owing to their near-net shape after casting[56].

The heat treatment of aluminium alloys has three steps[58]:

- Solution treatment: a high temperature soak, where the maximum quantity of soluble hardening elements are dissolved until a homogeneous solid solution is achieved;
- Quenching: a rapid cooling, in order to preserve the solid solution and to produce a super saturated solid solution at room temperature
- Age hardening: a moderate temperature soak, where the solute atoms precipitate in the structure, either at room temperature (RT), the natural ageing process, or at elevated temperature, the artificial ageing process.

This process is shown schematically in **Figure 2.35**. The inserts of the general microstructure configurations show the change from heterogeneous and segregated at the start, to homogeneous and single phase after solution treatment, and with fine precipitates evenly distributed after ageing.

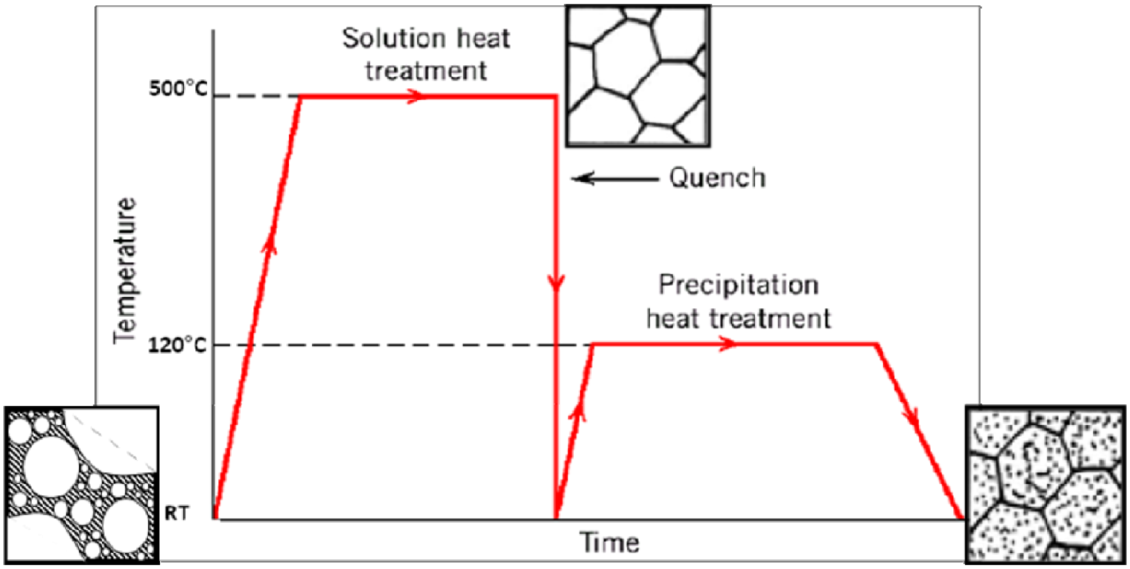

Figure 2.35: *Typical temperature-time profile for a precipitation strengthening heat treatment, with schematics of typical microstructures at RT, after solution treatment and after ageing.*

2.5.1. SOLUTION HEAT TREATMENT / HOMOGENISATION

For heat treatable aluminium based alloys, the best balance of properties is obtained if the solution treatment is carried out to a point where the maximum quantity of alloying elements is dissolved, while no melting occurs. Hence, solution treatment is carried out just below the start temperature of incipient melting[59], approximately 460℃ for AA7075, within the single phase, equilibrium solid solution range, and holding the temperature until such a time as the soluble hardening elements in the alloy are in solid solution and there is a nearly homogenous solution. Temperature control is essential, as any overheating will cause subsequent adverse effects on the ductility and other mechanical properties[60]. Immediately after solution heat treating, the product is quenched. This is done to preserve the solid solution that was formed in the previous step. In this stage a supersaturated solution is produced at room temperature. This offers the most favourable conditions for precipitation hardening.

2.5.2. AGEING TREATMENT

Ageing is the final stage in the heat treatment process for the modification of the mechanical and microstructural properties of a product. The main precipitation sequence that dominates the hardening in most of the commercially used AA7XXX alloys is:

SSSα → GP zones → $\acute{\eta}$ → η

where SSS*α* represents the super saturated solid solution, GP zones are the Guinier-Preston zones, *η* is a quaternary phase that contains Al, Zn, Mg and Cu[61]. The ageing treatment of Al-Zn-Mg alloys starts, in most cases, with a natural ageing process, after solution treatment and quenching[62]. The decomposition of the supersaturated solid solution near room temperature takes place by the formation of Guinier-Preston (GP) zones, which are ordered, solute-rich groups of atoms that may be only one or two atom planes in thickness. At higher temperatures other metastable phases form preferentially, and at even higher temperatures there is the formation of stable (equilibrium) phases. *ή* particles form in the early stages of artificial ageing and are metastable. *H* is the stable quaternary phase that contains Al, Zn, Mg and Cu based on the solid solution of $MgZn_2$ with AlCuMg components[63]. The structure and composition of the metastable and stable precipitates are strongly dependent on the alloy composition and on the ageing temperature. The Al-Zn-Mg-Cu alloys are quench sensitive after homogenisation and solution treatment, and low quenching rates will reduce the hardening after ageing[64]. The reduction in mechanical strength associated with the quench sensitivity is due to the non-hardening precipitation formed at high temperatures [typically S (Al2CuMg) and T (a quaternary phase based on Mg3Zn3Al2) which are sequences that form at temperatures in excess of 200℃] which lowers the supersaturation of the solid solution, and consequently, the hardening capability of the alloy during any subsequent ageing treatments.

The ageing process involves heating the aluminium alloy to a moderate temperature (between approx. 90 and 230℃). At this temperature, there is a decomposition of the supersaturated solid solution, which was created by the quench from the solution heat treatment, into a finely dispersed precipitate which occurs in the sequence SSS*α* → GP zones → *ή* → *η*[2]. At the onset of ageing, the solute atoms will form clusters near vacancies, and coherent precipitates will begin to form once a sufficient number of atoms have diffused into these vacancy clusters. The start of these precipitates is the formation of GP zones which retain the structure of the matrix where they produce elastic strains on the surrounding matrix[2]. Semi coherent precipitates form when the lattice can no longer withstand the growing mismatch created by these clusters as they grow. These semi-coherent precipitates continue to grow until an equilibrium precipitate forms[58] that has no coherency with the parent lattice. For complete decomposition, the ageing process may have to be made up of several stages.

The morphology of stages of the precipitation process of Al-Zn-Cu alloys is as follows[2]:

- *GP(I) zones*: spherical and ordered
- *GP(II) zones*: thin zinc disks, 1-2 atom layers thick and are partly ordered
- *ή*: hexagonal, disk shaped, semi-coherent with a composition close to MgZn
- *η*: hexagonal $MgZn_2$, forms at or from *ή.*

The temperature-time cycle is critical for the ageing process. These parameters must be selected with the desired final properties in mind. The optimum size and distribution of precipitates may maximise one property, but have a negative impact on another. For this reason, ageing can be performed in stages, in order to arrive at a compromise that will offer a desired combination of properties[57].

2.6. SUMMARY OF LITERATURE REVIEW AND SCOPE OF THESIS

The literature review offers a broad range of information pertaining to manufacturing techniques used for the production of aluminium parts, the different stages of the solidification that are experienced during casting, when both equilibrium and non-equilibrium conditions are dominant, and the history of the semi-solid metal casting technique and the non-dendritic microstructure associated with the technique.

The motivation behind this work was to determine whether SSM casting could be used as a viable alternative for the production of high strength parts. Before this outcome could be determined, a series of various more focused results need to be ascertained, each of which are critical pieces in the broader scope of the project.

In order to create a viable alternative part, the part itself needs to be successfully heat treated to maximise its age hardening characteristics, and this should be verified by extensive mechanical testing. The age hardenability hinges on the achievement of a supersaturated solid solution after solution treatment. This in turn hinges on the homogeneity of the part prior to post solidification strengthening heat treatments. The literature review touches on the occurrence of segregation in cast parts and the composition variations that result from non-equilibrium solidification parameters. Therefore, the main focus and scope of this investigation was on the extent of segregation that results from the SSM casting process when alloys that are more suited to wrought processing routes are used, and the possibility of the removal of this segregation through homogenisation treatments. An effective homogenisation step is critical for the successful use of post solidification heat treatments.

Focus was also placed on the review of the theories that have recently been used to describe the mechanisms responsible for the characteristic globular microstructure of SSM cast parts. These mechanisms will dictate not only the morphology of the final grains, but also the composition distribution within the globular grains and consequently the final composition distribution throughout the casting.

CHAPTER 3: EXPERIMENTAL APPROACH

The experimental approach for this investigation was divided into two sections. First, a full characterisation process of the as-cast microstructure was needed in order to understand fully both the casting process itself and the effect of any subsequent strengthening treatments. Once the characterisation process was completed, an investigation into the effect of heat treatments on this structure could then begin, with the aim of strengthening the final part through heat treatment.

3.1. THE MATERIAL

The purpose of this project was to investigate the use of a high strength Al-Zn alloy for a novel casting/manufacturing technique, semi-solid metal casting. The main emphasis was to determine whether comparable strengths associated with wrought products were achievable with the semi-solid rheocasting technique, when the same alloy composition was used.

The alloy selection was based on the high strength, precipitation hardenable Al-Zn alloys, namely AA7XXX wrought and A7XX.0 casting alloys.

‘Wrought’ is a term applied to alloys produced in ingot or billet form and subsequently worked by thermo-mechanical processing to produce a semi-finished product, from which the final products can then be made.

Cast alloys are those generally used in parts cast to final or near-final shape. Casting alloys are designed for parts where no subsequent thermo-mechanical processing (such as rolling, forging, extruding etc.) will take place, meaning that the only method of segregation reduction is through simple heat treatments.

These 7XXX and 7XX.0 series alloys have zinc as their main alloying element, often with significant amounts of copper and magnesium[65]. They are heat treatable. Zinc-bearing aluminium alloys, especially those with copper and magnesium, provide the highest strengths of any of the wrought commercial series (typical UTS range: 220 to 610 MPa)[65].

The main alloy under consideration was AA7075, a complex Al-Zn-Mg-Cu wrought composition alloy that produces extensive segregation on casting, which is successfully removed during thermo-mechanical processing, prior to machining to final dimensions. Post production, this alloy gains its strength by the precipitation of a Zn-based second phase during ageing heat treatments.

Owing to the nature of the segregation associated with AA7075, a second alloy was also used. A7XX.0 series aluminium casting alloys are not extensively used, owing to their relatively poor castability, when compared with the A2XX and A3XX series Cu and Si alloys. Notwithstanding the castability factors, there are several well-established Al-Zn casting alloys. One such alloy is A713, which is an Al-Zn casting alloy with an extremely low silicon content, which in itself is very unusual for casting alloys, as Si reduces the shrinkage during solidification, owing to its expansion during transformation from liquidus to solidus.

The AA7075 composition alloy was supplied by the CSIR. The alloy based on the A713 alloy was made to order by Metlite (Metlite Alloys (Pty) Ltd, P.O. Box 430, Eppindust, 7475). The final composition could not be exactly matched to the A713 alloy standard. The compositions of the alloys were determined using spectrographic spark erosion at the CSIR, and are shown in **Table 1**.

Table 1: *Chemical composition (in weight percent) of the Al-Zn alloys used in this investigation.*

	Zn	Mg	Cu	Fe	Si	Cr	Mn	Al
AA7075	5.56	2.45	1.55	0.24	0.24	0.18	0.15	balance
*AA7075	5.1-6.1	2.1-2.9	1.2-2.0	0.50	0.40	0.18-0.28	0.30	balance
A713	7.62	0.52	2.58	0.26	0.31	---	0.03	balance
**A713	7.6	0.4	0.8	0.55	0.12	0.06	0.2	balance

* Alcoa standard for AA7075 wrought alloy

** Alcoa standard for A713 casting alloy

3.2. MANUFACTURE OF THE SEMI-SOLID METAL CAST PLATES

The cast plates were manufactured by the CSIR in Pretoria. The rheocasting process was developed by the CSIR, the mechanics of which was described in **Chapter 2.2.4**. Samples that were investigated were produced from both the AA7075 and the A713 alloys. Samples for each alloy were supplied in various states; namely, semi-solid metal cast and liquid cast, as well as in the form of a slurry slug. The parameters for the sample preparation for this investigation were as follows:

RHEOCASTING PROCEDURE

- Blocks of each alloy were melted in an electrical resistance furnace. The molten metal at a temperature of 700℃ was poured into a stainless steel cup, which was then transferred to the rheo-processing cell of the casting facility.
- The liquid metal was simultaneously air cooled and stirred, via an induction electromagnetic field coil, for approximately 100-120 seconds (A typical temperature distribution curve for the stirring operation is shown in **Figure 3.1**.), until a semi-solid temperature of 625℃ was reached (the temperature corresponding to approximately 50% solid fraction, determined by DSC results, shown in **Figure 3.2**)
- The slurry in the mushy state was dropped into a shot sleeve of a 130 ton high pressure die casting (HPDC) machine and cast into a die.
- The die dimensions were: 4mm x 60mm x 100mm.
- The casting parameters were:
  - Die temperature: 270℃
  - Shot sleeve temperature: 170℃
  - Piston speed: 500mm/s
  - Consolidation time: 45 seconds

LIQUID CASTING PROCEDURE

- Blocks of each alloy were melted in the same electrical resistance furnace. The molten metal, at a temperature of 700℃, was poured into a stainless steel cup, followed by transfer to the shot sleeve and pressure cast according to the same method as was described for the rheocasting procedure.
- The die dimensions were: 4mm x 60mm x 100mm.
- The casting parameters were:
  - Die temperature: 270℃
  - Shot sleeve temperature: 170℃
  - Piston speed: 200mm/s
  - Consolidation time: 45 seconds

SLUG CASTING PROCEDURE

- Rheocast semi-solid slug: The first two processing steps of the casting procedures above were performed. The cup containing the semi-solid mixture was dropped into a cold water quench bath. After full solidification and cooling, the slugs were removed from the cups.
- Liquid cast slug: The molten metal at a temperature of 700℃, was poured into a stainless steel cup. The cup was then dropped into a cold water quench bath. After full solidification and cooling, the slugs were removed from the cups.

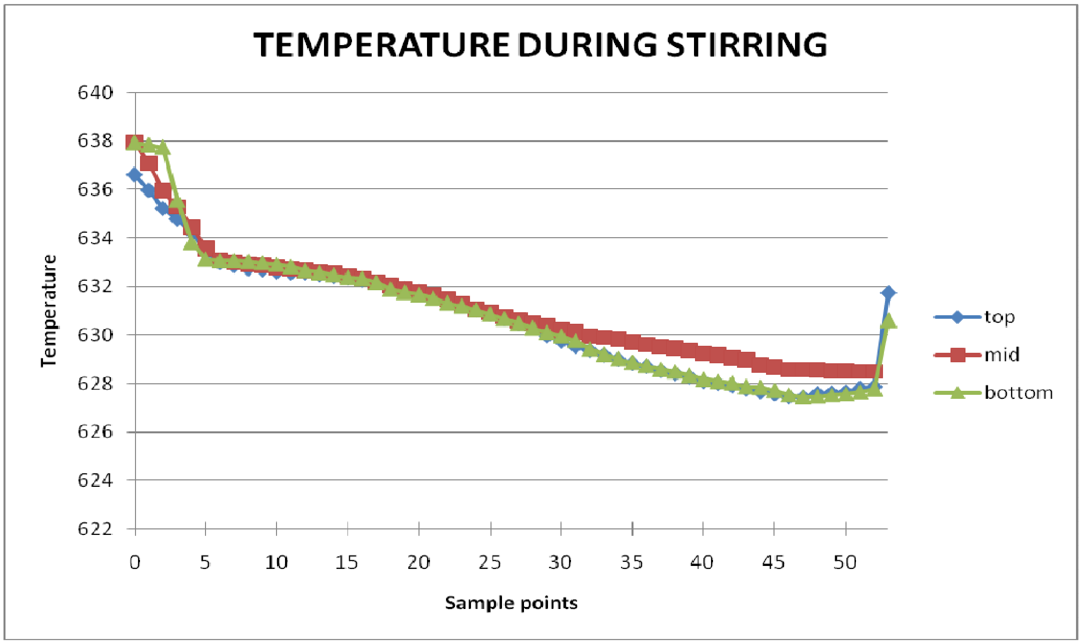

Figure 3.1: *Temperature distribution within melt of a AA7075 composition alloy during stirring in the Rheocasting facility.*

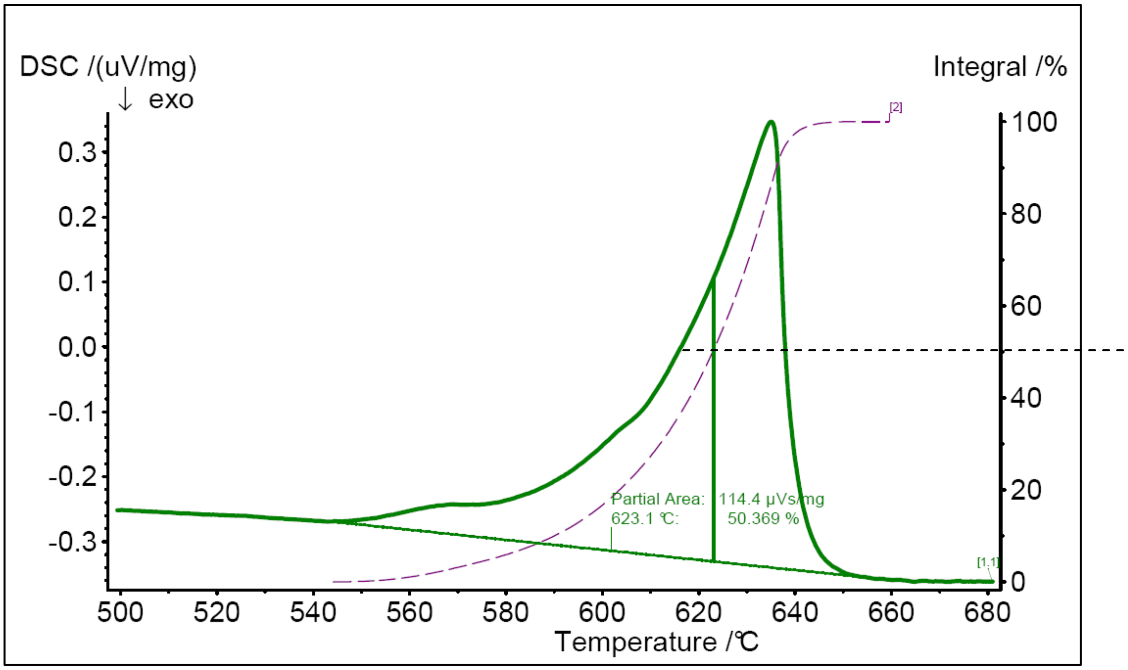

Figure 3.2: *DSC curve of homogenised A713.0 sample, showing partial area for 50% solid fraction.*

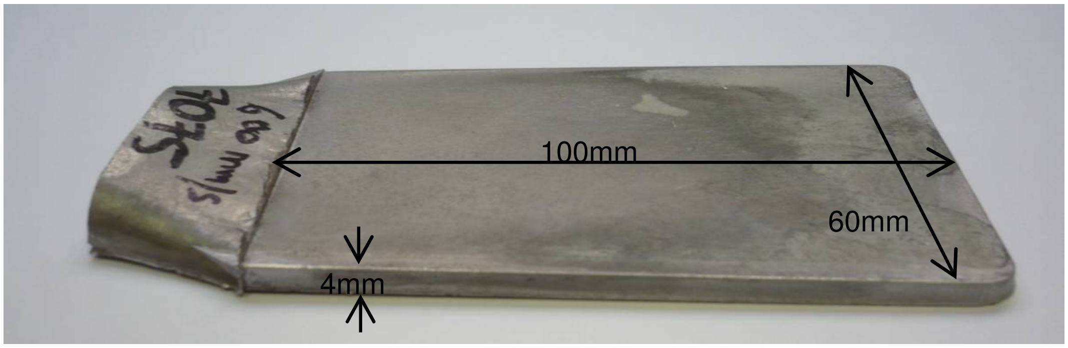

Figure 3.3: *SSM cast plate (dimensions: 4 x 60 x 100mm).*

The cast plates that were used for the investigation are shown in **Figure 3.3**. The plates were x-rayed for porosity prior to sectioning. Samples where the x-ray images showed evidence of porosity were deemed unacceptable and were discarded.

3.3. METALLOGRAPHY

The first step in the experimental procedure was to complete a full evaluation and characterisation of the as-cast condition of semi-solid metal (SSM) cast plates from both the AA7075 and A713 type alloys. These were then compared to liquid cast plates that were cast under the same casting conditions.

For this process, a variety of metallographic techniques were utilised. Only after the characterisation process had been completed could there be any evaluation into the effect that homogenisation practices and further strengthening heat treatments would have on the as-cast structures.

The macro-differences in the microstructure across the manufactured plates, from the inlet point to the end of the plate, were not a main focus in this investigation. Focus was placed on the typical globular microstructure rather than the variation of grain size and distribution along the length of the casting that would be the result of die temperature and casting speeds. The morphology of the primary grains and the segregation surrounding the primary grains was the main objective.

3.3.1. SAMPLE SECTIONING AND PREPARATION

The cast plates were sectioned along the centre line of the length of the plates, based on the assumption that the flow of metal during casting would create a structure mirrored about the centre line. Samples were cut from one half of the plate and the other half was left intact in the event that a corresponding sample would be needed for verification at a later date. The half plate was divided into 10mm x 10mm squares with positions numbered according to their location. Samples from the edges of the plate were avoided, as the degree of heterogeneity within these regions was extremely high. The sectioning layout is shown in **Figure 3.4**.

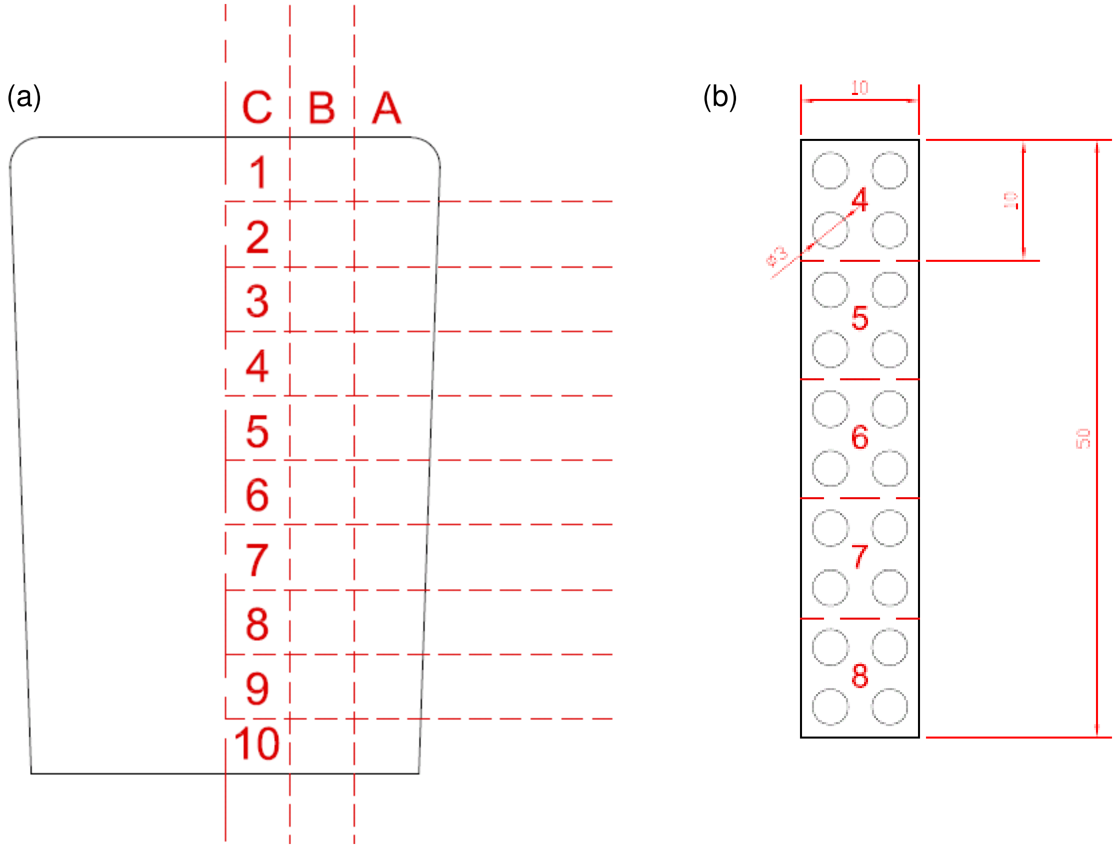

Figure 3.4: *Sectioning layout of a typical SSM cast plate. (a) 10 x 10mm square areas for microscopy, and (b) the location and layout for the wire-cutting of samples for DSC.*

From these squares, different size samples were used, depending on the type of experiment or equipment used. For light microscopy the samples were cut into 5mm samples and viewed on edge (through the thickness). For SEM samples 2mm samples were cut and again viewed on edge. For thermal analysis, using Differential Scanning Calorimetry (DSC), four 3mm diameter cylinders were wire cut from each 10mm x 10mm square through the thickness of the plate. These were then sliced into 1mm-thick disks. This was carried out in order to maintain a common surface area and volume for the various DSC experiments.

Samples for microscopic investigation were mounted using a Struers automatic hot-mounting facility, and when heat during mounting would affect the microstructure, they were cold mounted, using Specifix-20 cold mounting resin. They were then ground and polished, using a Struers automatic polishing facility. They were ground with 1200 grit SiC paper until plane, and then polished using a three-step polishing regime: firstly, 6μm diamond suspension lubricant (DiaDuo) on a MD-Dur cloth disk, followed by 3μm diamond suspension lubricant (DiaDuo) on a MD-Mol cloth disk, and finally polished to a mirror finish, using a colloidal silica OP-S solution on a MD-Nap polishing disk. This mirror finish was deemed sufficient for both light and electron microscopy. It was determined that electro-polishing (using a 105ml methanol - 45ml nitric acid mix at -30℃) should not be utilised for these samples, owing to the topographical surface finish created with the semi-solid cast microstructure.

Samples prepared for viewing, using polarised light optical microscopy (PLOM), were anodised, using Barker's solution, comprising a 2% solution of 4ml HBF_4 (tetra fluoro-boric acid) and 200ml of distilled water. It was an electrolytic reaction, where the sample was immersed in the solution at room temperature, using direct current at a voltage of 30V for 60-90 seconds. This process was performed using an aluminium cathode. Stirring was not strictly necessary, but it did aid in ensuring an even reaction across the surface of the specimen.

3.3.2. LIGHT MICROSCOPY

The microscope used was a Reichart MeF3 A, fitted with a Leica DFC320 camera and the relevant software. The specimens were prepared using electrolytic anodising (The method is discussed in the previous chapter.). The process of anodising deposited a film of Al_2O_3 on the surface of the sample. The thickness of the film varied over each grain. The layer thickness was dependent on the crystallographic orientation of each grain, relative to its neighbouring grain. When the sample was viewed through plane polarised light, the contrast effects were converted to striking colour contrasts. Each colour represented an area of different crystallographic orientation[66]. In a cast structure, the dendritic grains would have primary, secondary etc. arms that were the same orientation, which allowed for the distinction of grain networks/agglomerates, using polarised light optical microscopy. The information gleaned from this technique was purely qualitative, and gave no quantitative information as to the actual orientation of the grains. This technique was a useful precursor to the more quantitative orientation mapping technique, namely the electron backscatter diffraction (EBSD) technique.

3.3.3. SCANNING ELECTRON MICROSCOPY (SEM)

The surface preparation of a sample is dependent on the type of information that is needed from that sample, either topographical information from a rough surface or microstructural information and fine detail from a well-polished smooth sample. Sample preparation for this investigation was described in **Chapter 3.3.1**. The mirror-finished polished samples were placed on stubs with conductive paste to avoid charging during microscopic investigation.

Various SEM systems were used during this investigation, and are listed below with a brief description of the primary reason for their specific uses.
LEICA 440 (University of Cape Town) with a LaB_6 filament: Conventional SE and BSE imaging, and EDS point and mapping analysis.

Leo1525 SmartSEM (National Metrology Institute of South Africa (NMISA) at the Council for Scientific and Industial Research (CSIR) in Pretoria) with a Tetra/Vangaurd EBSD detector and the INCA suite: EBSD mapping.

ZEISS EVO 60 (School of Materials, University of Manchester, UK) with a tungsten filament and Oxford INCA x-sight EDS: Conventional SE and BSE imaging, and high resolution EDS.

CAMSCAN MX2500 (School of Materials, University of Manchester, UK) with a field emission gun source: Conventional SE and BSE imaging, high resolution EBSD, *in situ* heating experiments with SE, BSE and EBSD mapping

The beam current in all instances was set to 20keV and the working distance varied, depending on whether other applications were being used during the SEM investigations, such as EBSD and EDS (which will be discussed later).

3.3.3.1. SECONDARY AND BACKSCATTERED ELECTRON IMAGING

The two SEM modes that were used in this investigation were secondary electron (SE) mode and backscattered electron (BSE) mode. Backscattered electrons were produced by single large-angle or multiple small-angle elastic scattering events[67], whereas secondary electrons were formed by interaction with the primary electrons with loosely-bound atomic electrons.

The yield of backscattered electrons depended on the atomic number of the material hit by the incident beam. The higher the atomic number, the greater the yield of backscattered electrons, the brighter that area would look in an image, as compared to areas in the same image with lower atomic number elements. This meant that a backscattered electron image (BEI) gave information regarding material composition.

Secondary electrons had a lower voltage than backscattered electrons, but the resolution of the imaging was much higher, owing to the smaller interaction volume of these electrons. The yield of secondary electrons depended strongly on the surface tilt and weakly on atomic number and crystal orientation. Secondary electron images (SEI) gave surface topography information, as well as showing material contrast and crystal orientation contrast.

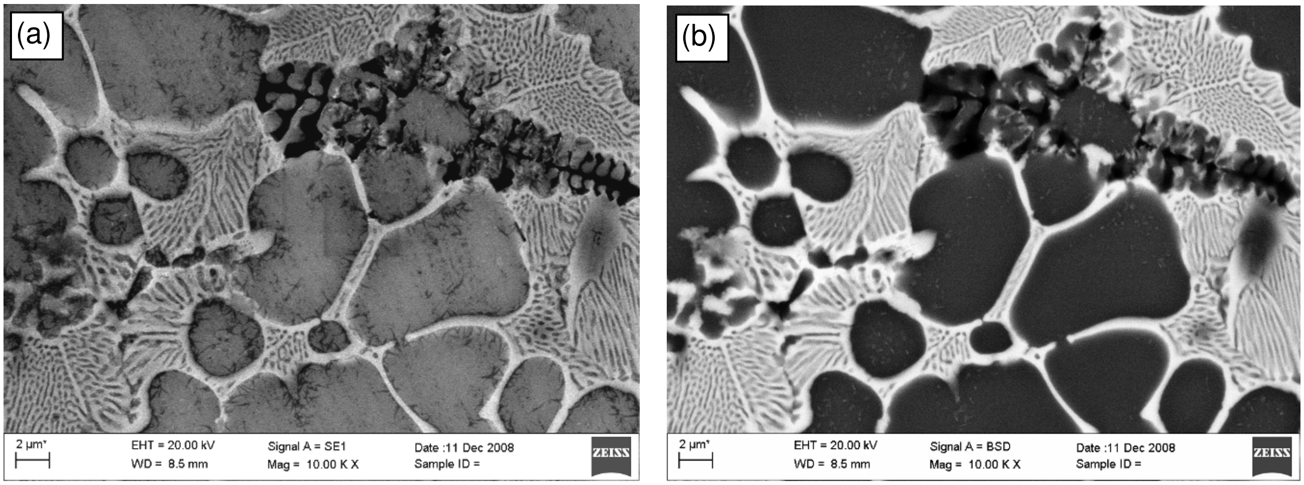

Figure 3.5: *Images of a semi-solid cast AA7075 sample, showing grains, porosity and a lamellar eutectic, images in (a) secondary electron mode and (b) backscattered electron mode.*

Figure 3.5 shows the differences in information that are seen between SE and BSE images. The SE image in (a) shows the topography of the sample, as well as residual defects from the polishing procedure, while the BSE image in (b) shows the contrast between the light grey aluminium alloy grains (atomic number of 13) and the white of the zinc (atomic number of 30) in the lamellar eutectic. Each mode offered different information, which could have been pertinent to an investigation, such as the precipitates seen in the BSE image in **Figure 3.5** (b), which could not be identified in the SE image in (a).

For this investigation, areas were examined in both secondary and backscattered modes, in order to determine whether information was purely topographical (resulting from the metallographic polishing preparation on the two-phase semi-solid cast structure), or whether there were compositional effects stemming from the segregation introduced by the casting process itself.

This evidence was used to determine which areas needed further compositional investigation, using energy dispersive x-ray spectroscopy analysis.

3.3.3.2. ENERGY DISPERSIVE X-RAY SPECTROSCOPY (EDS)

EDS is often referred to as a semi-quantitative method of composition determination. This is due to the interaction volume that is associated with an electron beam when it strikes a sample. During EDS of a small feature on the surface of a sample, the interaction volume may penetrate to a depth beyond that of the feature, thus the results will be accumulative of the feature in question and the substrate beneath, giving inaccurate results. Therefore, interaction volume and the composition of the bulk must always be taken into consideration. Another limitation of this method is the inability to detect the lightest elements, as well as energy peak overlaps among different elements, particularly the x-rays emitted from the different energy level shells (K. L and M shells) in different elements.

The EDS facilities used in this investigation were mentioned in **Chapter 3.3.3.** The average EDS interaction volume had a maximum penetration depth of the order of 2.5um to 3um and a beam diameter of approximately 10nm, depending on the spot size of the beam. The analysis software was INCA and spot/point analyses were used, in conjunction with elemental area mapping.

EDS was used to identify the extent of segregation in the as-cast structure, with the main emphasis on:

- the coring in the larger primary and secondary grains;
- any significant concentration or compositional variations in the smaller interglobular grains;
- the eutectic compositions and any inter-metallics in the structure.

The extent of the coring was evaluated by identifying the changes in composition from the centre to the edges of the globular grains, continuing into the cellular protrusions that extended into the eutectic regions. In addition, elemental line scans and area maps were completed to further identify any trends in the compositional distribution in the as-cast structure.

The same areas and analyses were completed on semi-solid cast samples of both the AA7075 composition alloy and the A713 composition alloy. The extent of segregation associated with each alloy was compared. The extent and degree of segregation was then compared to that of conventionally cast (HPDC) samples and semi-solid slug samples of each alloy.

3.3.3.3. ELECTRON BACKSCATTER DIFFRACTION (EBSD)

Electron backscatter diffraction (EBSD) is a technique carried out in the SEM, which is used to generate orientation maps by obtaining crystallographic orientation information for every point over an area of sample[68]. This orientation information can be displayed on a map according to

Euler angles, where each point is coloured, according to their orientation, with red, green and blue levels proportional to the Euler angle position on the Cartesian axis. Areas of similar orientation make up the grains. A grain boundary can be identified when neighbouring areas have a misorientation separating them. When this misorientation is of the order of less than 15°, the grain boundary is termed a low angle grain boundary (LAGB), which is a sub-grain or internal type boundary. A misorientation of greater than 15° is typically a high angle grain boundary (HAGB), which demarcates the boundary between neighbouring grains of different crystallographic orientations.

The acquisition software used in Pretoria was the INCA suite, and in Manchester the Channel 5 suite. The orientation data collected from both EBSD systems were then analysed, using the custom-written software package, VMAP 8[69].

The EBSD technique was used as part of the characterisation process, whereby large-area maps were generated to identify general orientation and boundary information, while smaller- area maps, with higher resolution were generated to focus on the smaller inter-globular grains and their interaction with the surrounding larger primary dendritic agglomerated grains.

3.4. THERMODYNAMIC CALCULATIONS

The calculation of phase diagrams was achieved using the CALPHAD (**CAL**culation of **PHA**se **D**iagrams) method, where the phase diagram gave a representation of the thermodynamic properties of a system. Therefore, if the thermodynamic properties were known, it was possible to calculate the multi-component phase diagrams[70,71]. The model is based on the Scheil-Gulliver scenario, and assumes that solute diffusion in the solid phase is small enough to be considered negligible and that diffusion in the liquid is extremely fast and can be considered to be complete throughout the liquid[72].

3.4.1. JMaTPro

JMatPro (Java-based materials properties) was used to calculate the thermo-physical and physical properties of the liquid and solid phases that were critical components in casting simulations. JMatPro creates curves of properties, such as: the fraction solid transformed, enthalpy release, thermal conductivity, volume and density, all as a function of temperature[73].

The elemental composition was entered into the programme, which then calculated the solidification path at a selected temperature interval until a final remaining liquid of 0.01%. The phases that formed for the particular alloy compositions were graphed, and phase details were viewed in the form of solid fraction *vs.* temperature curves for solidification. In addition, temperature phase information could be determined by viewing a wt% phase *vs.* temperature curve. The information produced by this programme is based on the occurrence of equilibrium conditions, which are not experienced during SSM casting. Therefore the information gained from this programme was used as a guide for the interpretation of the phases present in the as-cast condition.

This phase information could then be compared to the ratios of elements determined during EDS compositional analysis.

3.5. DIFFERENTIAL SCANNING CALORIMETRY (DSC)

DSC is a thermal analysis technique that measures the heat evolution of a substance under a controlled temperature programme. This technique is used to determine temperatures of incipient melting and for solidification studies[59].

A **NETZSCH STA409** Thermal Analyser was used, fitted with an S-type thermocouple, with a maximum operating temperature capability of 1500℃. The samples were approximately 20mg in weight (The sectioning and preparation was discussed in **Chapter 3.3.1**.). An alumina crucible (Al_2O_3) was used, with a lid, in both the reference and sample positions. The temperature profile was: RT – 700℃, at a heating rate of 10°/min, followed by an isothermal holding time of ten minutes, and finally a cool down from 700℃ – RT, at a cooling rate of 10°/min. The heating curves of heat flow *vs* temperature were plotted, and the endothermic peaks were analysed, by determining peak onset temperature, maximum peak temperature and peak area. The results for the different alloys in the various casting conditions were compared.

3.6. HEAT TREATMENTS

A standard T6 heat treatment was used, which comprised: 500℃ solution/homogenisation treatment for six hours, followed by a rapid quench to room temperature, a 12-hour natural ageing process at 30℃, and then an artificial ageing treatment at 120℃ for 12 hours.

Solution/homogenisation heat treatments were performed in a salt bath with AS 135 tempering salt, with an operating temperature range of 160-550℃ and a melting point of 135℃. A salt bath was used to ensure an even temperature distribution and temperature control of ±1℃.

The natural ageing process was performed in an immersion heated water bath at 30℃ to ensure good temperature control.

The artificial ageing process was performed in an oil bath with silicon-based oil. The temperature was 120℃ and samples were aged to different times, in order to determine the peak ageing conditions. Therefore, the ageing times varied from six hours to 14 hours, where samples were removed at hourly intervals.

3.7. *IN SITU* HEATING

In situ heating experiments were performed at the School of Materials at the University of Manchester, in the CamScan MX2500, on a custom designed and built hot stage. The set-up is shown in **Figure 3.7**.

Figure 3.7 (a) shows the general set-up, with the power source, the SEM and the thermocouple. The temperature of the sample was controlled via voltage control of the DC power source. The sample temperature and stage temperature were monitored via thermocouples embedded in the stage and just below the sample. The temperatures were viewed on a temperature gauge and the voltage was controlled manually.

The hot stage is located on a mounting plate inside the large chamber of the CamScan SEM. The mounting plate can move in the x- and y-directions and can rotate to the 70° angle required for the EBSD. The location of the hot stage on the plate and its position in the SEM can be seen in **Figure 3.7** (c) and (b) respectively. The sample preparation was discussed in **Chapter 3.3.1**. The sample was mounted on the top of the hot stage, using carbon paste, and was surrounded by a heat shield, to limit the amount of heat radiating from the top of the hot stage, in order to minimise the deterioration in the detection process as a result of heat.

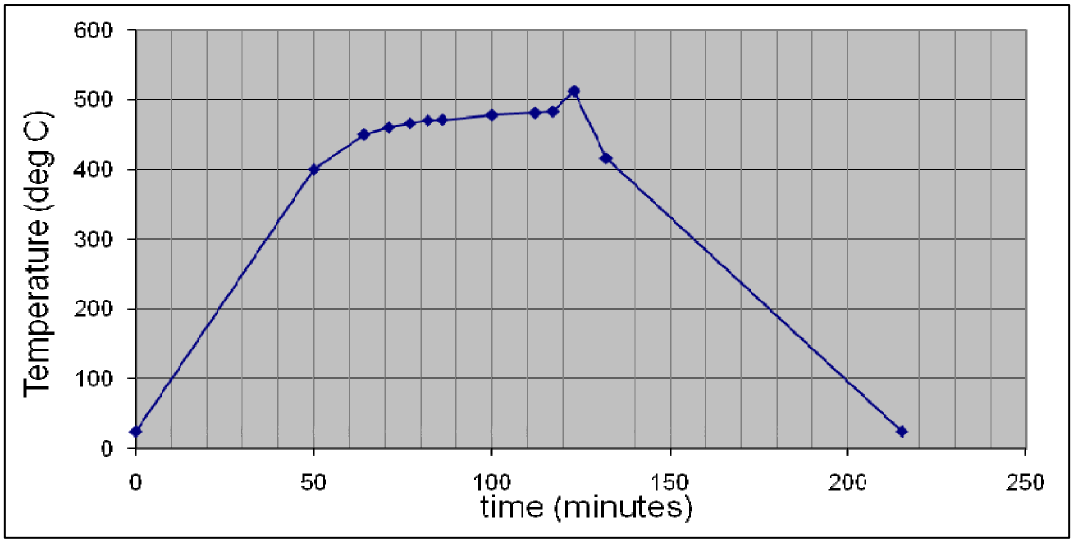

Figure 3.6: *Temperature profile of typical in situ experiment.*

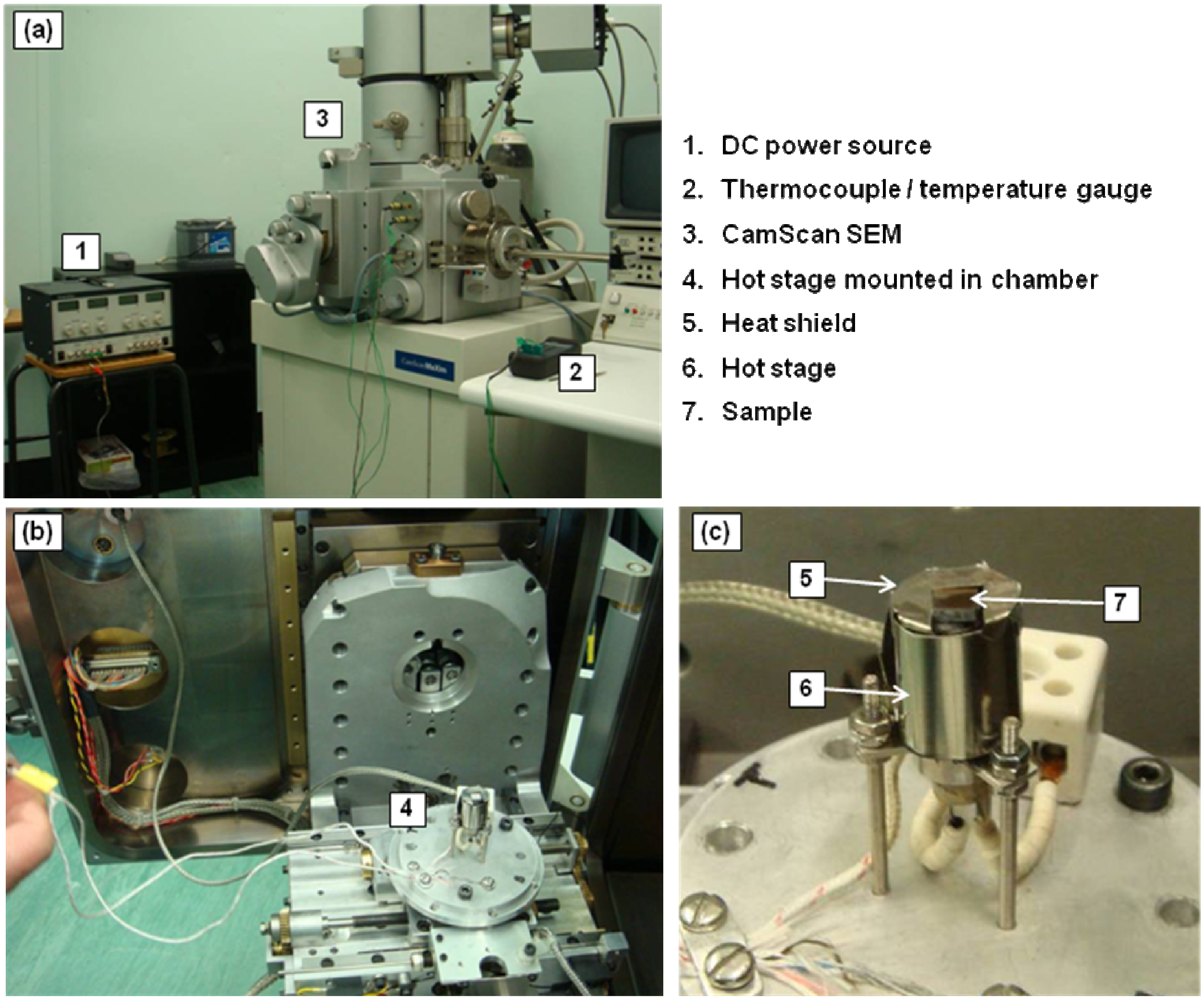

1. DC power source
2. Thermocouple / temperature gauge
3. CamScan SEM
4. Hot stage mounted in chamber
5. Heat shield
6. Hot stage
7. Sample

Figure 3.7: *In situ heating hot stage showing: (a) general set-up, (b) the hot stage inside the SEM chamber; and (c) the sample position on the hot stage, with key labels 1-7 as indicated.*

The *in situ* experiments used conventional SE and BSE imaging and EBSD mapping to track the microstructural changes that occurred during heating. The temperature profile of a typical experiment is shown in **Figure 3.6**. Images were taken at 10℃ increments from 400℃ to a maximum temperature of 510℃, after which the sample was cooled. Another image was taken at 420℃ and again at room temperature.

3.8. TESTING MATRIX

The testing matrix for the experimental procedure involved the characterisation of the microstructure of the two alloys under investigation, namely AA7075 composition alloy and A713 composition alloy. The structures of the semi-solid metal cast samples were the main emphases of the investigation, but in order to better understand the process, these SSM samples were compared to equivalent high pressure die cast (HPDC) samples, which originated from liquid alloy (excluding a slurry production step), and samples that had been quenched immediately after the slurry production step. This was described in more detail in **Chapter 3.2**.

Table 2 : *General testing matrix for experimental procedure.*

	SSM CAST		**LIQUID HPDC**		**SSM SLUG**	
	AA7075	**A713**	**AA7075**	**A713**	**AA7075**	**A713**
Charaterisation						
PLOM	✓	✓				
SEM	✓	✓	✓	✓	✓	✓
EDS	✓	✓	✓	✓	✓	✓
DSC	✓	✓	✓	✓	✓	
JMatPro			✓	✓		
Heating						
Standard T6	✓					
SEM of T6	✓					
in-situ SEM	✓	✓		✓		
in-situ EBSD	✓	✓		✓		
post heating SEM	✓	✓		✓		
post heating EDS	✓	✓		✓		

CHAPTER 4: RESULTS AND DISCUSSION
CHARACTERISATION PROCESS

The primary aim of this investigation was to determine whether semi-solid casting of high strength, heat treatable, Al-Zn alloys could achieve similar strengths to a wrought equivalent after post solidification heat treatments (T6). The first step in the investigation was to perform a typical T6 heat treatment on wrought and semi-solid cast samples and to assess the results.

4.1. T6 HEAT TREATMENT

The T6 heat treatment typically used for the age hardening of Al-Zn alloys, such as AA7075, involves a solution treatment, a rapid quench to room temperature, a natural ageing step and an artificial ageing step. To determine the property variation resulting from the SSM casting process, a wrought sample and a SSM cast sample of the AA7075 composition were heat treated according to the T6 plan:

(i) Solution treatment: 500℃ for 6 hours or 460℃ for 15 hours
(ii) Natural ageing: RT for 12 hours
(iii) Artificial ageing: 120℃ for 10 hours to 14 hours

The final properties were evaluated using hardness testing, and are shown in **Table 3** (with error values). The hardness values in **Table 3** show that, for the AA7075 alloy, the wrought samples hardened to the highest value, and the trend seen in **Figure 4.1** indicates that after 14 hours the hardness was either at a maximum or was still increasing. (The maximum value for the AA7075 alloy after the T6 heat treatment is accepted to be 175HV.) For the same alloy in the SSM cast condition, the maximum hardness within this range was found in the sample where the solution treatment temperature was at 460℃ (below the incipient melting temperature of the solute-rich eutectic phase). This value was lower than the normal solution treatment temperature range for this type of alloy (480-500℃).

The results in **Table 3** for the A713 alloy show that the maximum achievable strengths for the fully homogenised ingot sample, which had undergone a solution treatment step at 500℃, were well below that of the AA7075 alloy. The same trend was seen in the SSM cast samples, whereby the A713 samples solution treated at 460℃, below the incipient melting temperature, showed a higher hardness value at shorter times than those solution treated at 500℃, where incipient melting occurred during heating. The values for these T6 treatments are given in **Figure 4.1**.

Table 3: *Hardness values in HV for wrought and SSM cast AA7075 and A713 alloys after solution treatment at different temperatures and a range of ageing times.*

Alloy	Condition	Soln treat T	Hardness after ageing at 120 for:									
			10hrs		11hrs		12hrs		13hrs		14hrs	
AA7075	wrought	500℃	163.3	+3.2 -3.0	161.8	+1.7 -3.6	164.3	+1.2 -1.3	168	+2.2 -2.2	171.4	+1.2 -0.8
	SSM	500℃	143.2	+6.4 -6.0	138	+9.8 -8.4	135.2	+1.7 -4.6	138.8	+4.2 -3.2	149.2	+1.8 -1.8
	SSM	460℃	145.1	+4.5 -3.0	139.5	+3.9 -5.5	142.7	+4.9 -5.2	155.8	+4.2 -4.2	149.3	+3.7 -3.3
A713	homog. Ingot	500℃	112.7	+5.2 -8.3	111	+6.3 -5.8	118	+6.2 -3.6	109.3	+11.2 -6.3	114.3	+5.3 -3.8
	SSM	500℃	94.4	+2.0 -2.7	89.6	+2.8 -4.6	91.1	+2.1 -3.6	91.6	+2.1 -3.2	95.5	+2.1 -2.2
	SSM	460℃	90	+3.2 -7.0	93.1	+3.4 -5.4	94.8	+5.2 -3.0	96.5	+4.1 -4.7	93.5	+6.7 -9.5

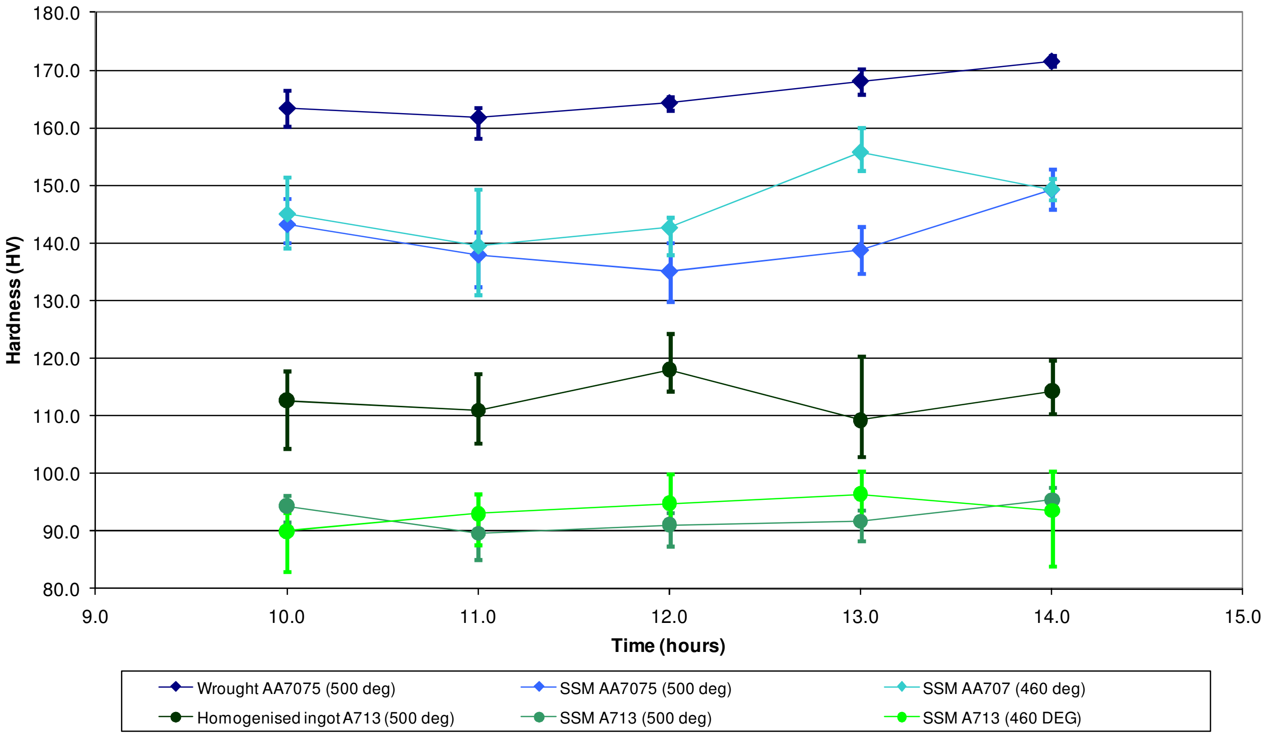

Figure 4.1: *Hardness curves for the T6 heat treatments for AA7075 and A713 alloys, comparing starting condition and solution treatment temperature. Results correspond to those in Table 3.*

Using the T6 heat treatment regime, the A713 alloy produces much lower hardness values when compared to the AA7075 alloy. The composition of the A713 alloy is less complex than that of the AA7075 alloy, therefore the temperature and time requirements in order to maximise the achievable strengths for the alloy through heat treatment of the A713 alloy may vary from the T6 treatment used in this investigation.

The microstructures of a SSM cast AA7075 alloy and a wrought AA7075 sample are shown in **Figure 4.2** (a) and (b) respectively. **Figure 4.2** (c) and (d) show the same samples after solution treatment at 480℃ for six hours. The solution-treated wrought sample in (d) shows a homogenous structure, with an even grain size distribution. The solution-treated SSM sample in (c) exhibits heterogeneous grain size distribution. The grains that have grown from the previous interglobular region are still very small when compared to the large globular grains.

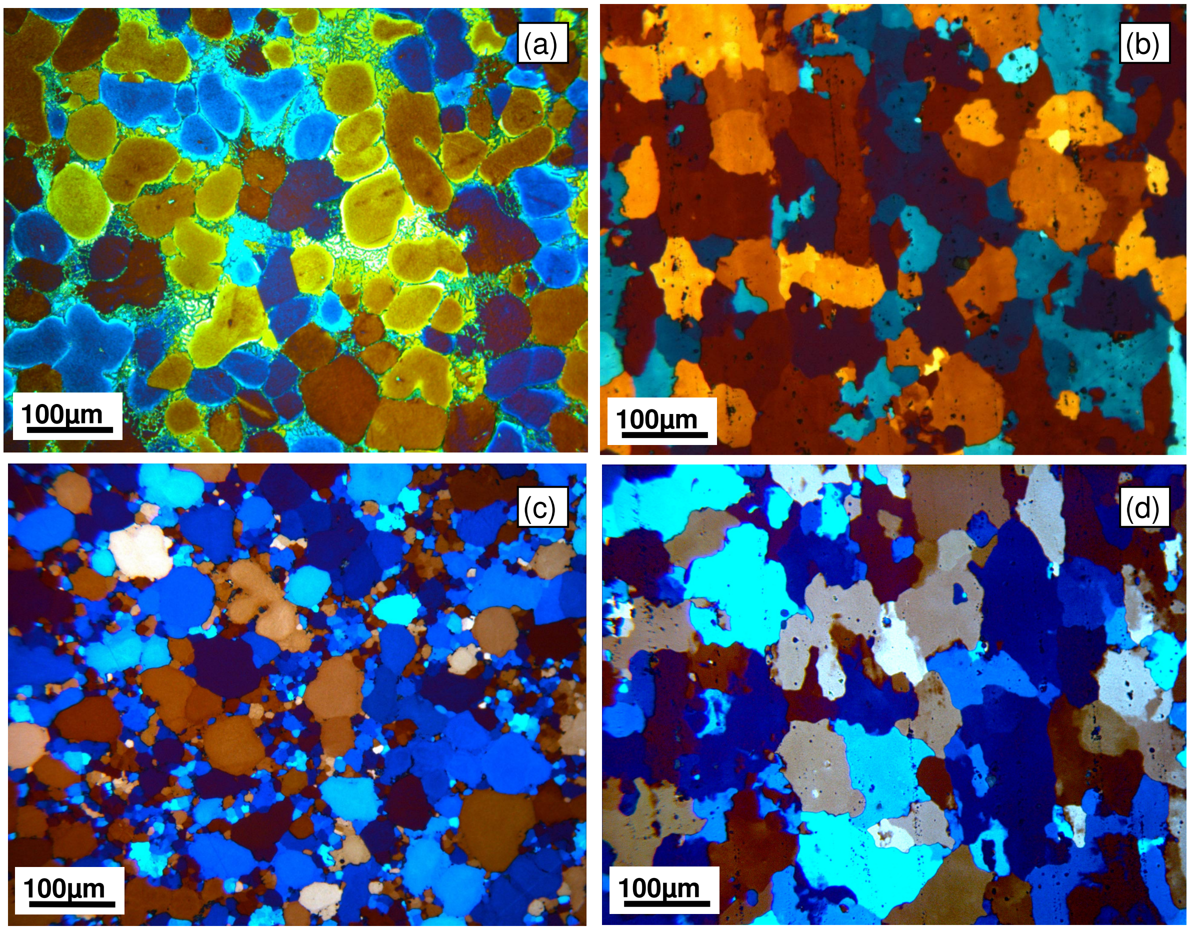

Figure 4.2: *(a) SSM cast AA7075 alloy in the as-cast condition and (c) after solution treatment at 480℃ for 6 hours; (b) Wrought AA7075 in the as received condition and (d) after solution treatment at 480℃ for 6 hours.*

If the solution treatment had been insufficient to homogenise the grain size distribution to a higher degree, it would also not have been sufficient to homogenise the elemental segregation. This homogenisation would have been further hindered by the melting of the segregated phase during solution treatment, as is shown by the DSC curves which are presented later in **Figure 5.4**.

Figure 4.3 shows the typical shrinkage porosity associated with the SSM as-cast condition. It is located within the interglobular regions and often surrounded by the lamellar eutectic, or bounded by grain edges. The morphology of this type of shrinkage porosity is irregular and is defined by the surrounding structure. The lamellar eutectic edge, that borders the porosity, is smooth and ends abruptly.

These DSC results show that incipient melting occurs below the solution treatment temperature of 480℃. Therefore, the solution treatment of the SSM cast structure is not an effective homogenisation process prior to ageing. Thus, it is important to evaluate the microstructural changes that occur at temperatures slightly higher and slightly lower than the incipient melting temperature of approximately 465℃. In order to evaluate further the solution treatment process, heat treatments were performed on samples in the salt bath at 476℃(+-2℃) for differing times: 30, 60 and 120 seconds. Each sample was quenched to room temperature within one second of removal from the salt bath. The micrographs that were generated can be seen in **Figure 4.4**.

Figure 4.4 (a) shows the general microstructure of a SSM cast AA7075 alloy after heating to 476℃ for 30 seconds, and **Figure 4.4** (b) shows a higher magnification of the interglobular area of the same sample. The eutectic in this area is no longer perfectly lamellar in structure. There is an exposure of porosity, which may be the result of the eutectic volume having decreased, owing to incipient melting occurring below the heating temperature. In (a), the coring rings can be clearly seen on the larger globular grains, with a distance of approximately 5µm or less from the edges of the grains.

Figure 4.4 (c) and (d) show the general and higher magnification images, respectively, of a SSM cast AA7075 alloy after heating to 476℃ for one minute. The general microstructure in (c) shows that the coring rings have shrunk in the direction of the centre of the grain, with the contrast being much clearer as solute from the eutectic-containing interglobular regions diffuses towards the centre of the globular grains. The micrograph in (d) shows the breakdown of the definition of the lamellar eutectic, with a portion of the eutectic now appearing smooth, with no lamellae.

Figure 4.4 (e) and (f) show the general and higher magnification respectively of a SSM cast A7075 alloy after heating to 476℃ for two minutes. The structure is very similar to that of the one-minute samples in (c) and (d), indicating that there is little effect on the structure of the eutectic after the initial change to it at this temperature, and that the process has slowed down. There is contrast between the outer edges of the globular grains and their centres. There is more diffusion from the zinc-rich interglobular region towards the middle of the grains, seen in the further increase in distance from the grain edges of the coring rings.

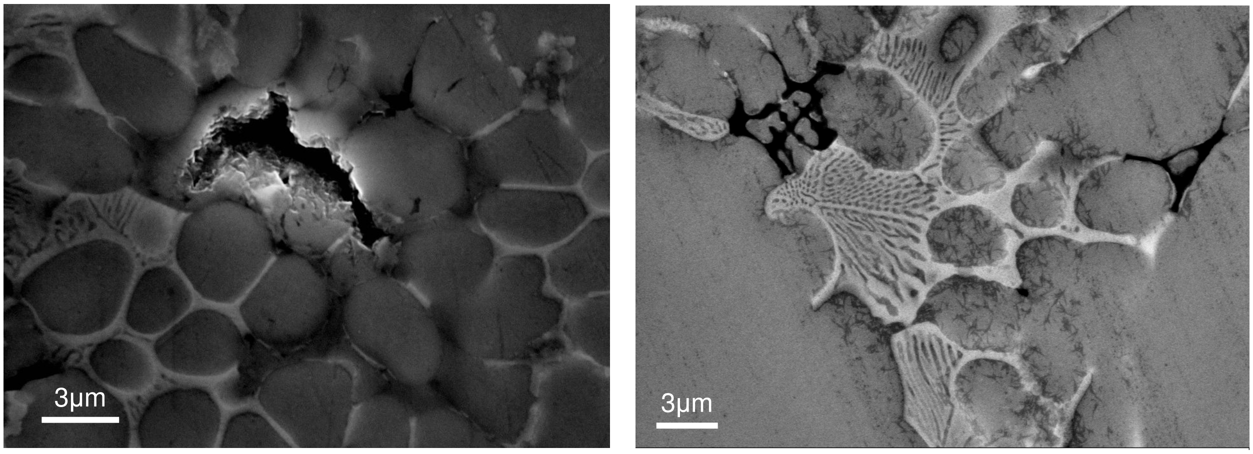

Figure 4.3: *SEM SE images of shrinkage porosity in the SSM as-cast AA7075 alloy, located within the interglobular regions and with irregular morphology.*

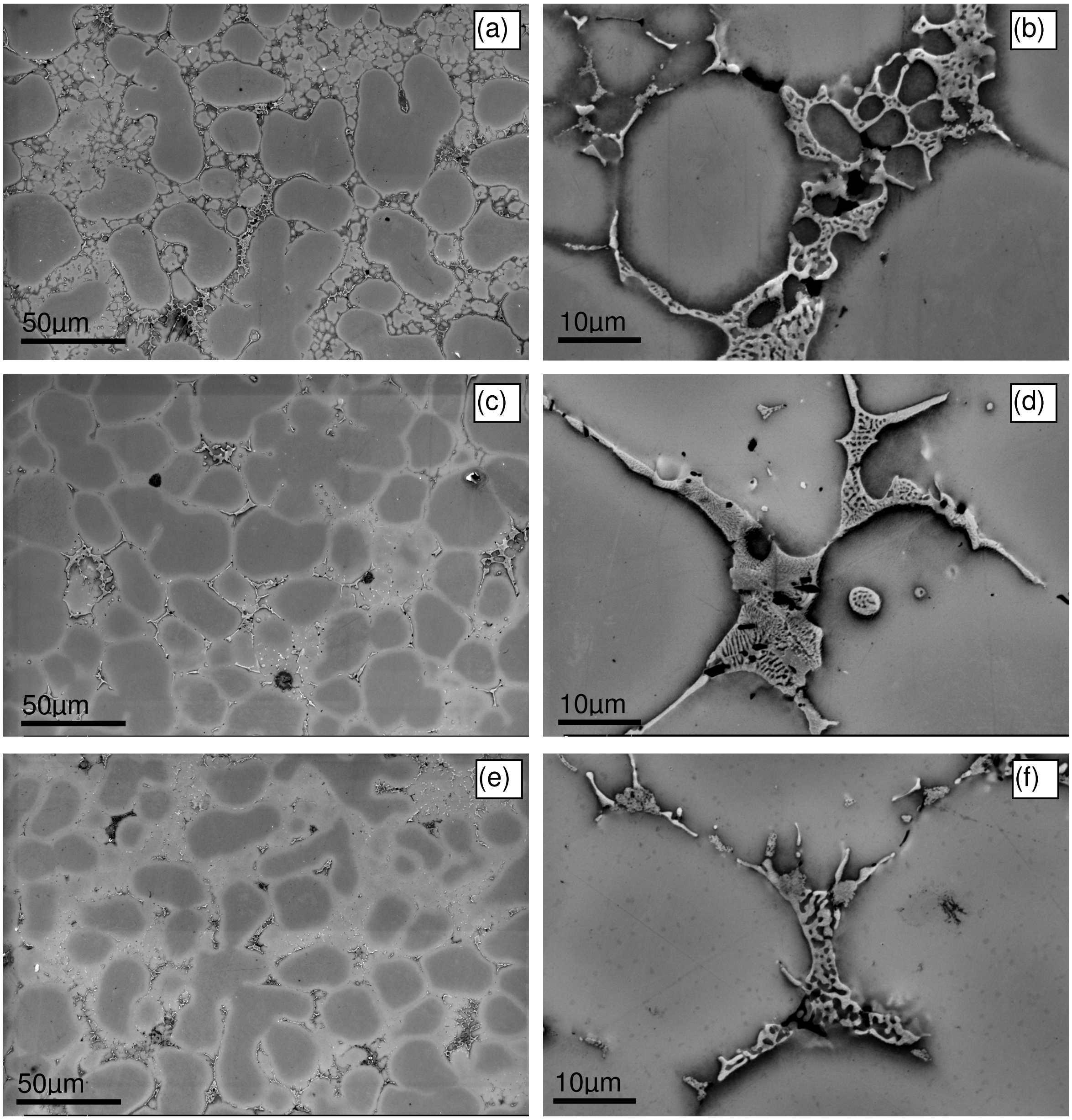

Figure 4.4: *Microstructure of SSM AA7075 alloy after heat treatment at 476°C, showing (a) the general structure and (b) eutectic are after 30 seconds; (c) the general structure and (d) eutectic are after 1 minute; and (e)the general structure and (f) eutectic are after 2 minutes holding times before quenching.*

Figure 4.5 shows the effect of heating at 476°C for 2 minutes on the porosity located within the interglobular regions. The eutectic surrounding the porosity evident in **Figure 4.5** no longer has clean edges, such as those seen in **Figure 4.3**, and the lamellar structure is no longer discernable. The change in the edge characteristics may be as a result of smearing of the non-lamellar phases during the polishing procedure. The porosity exposure is circled in **Figure 4.5**.

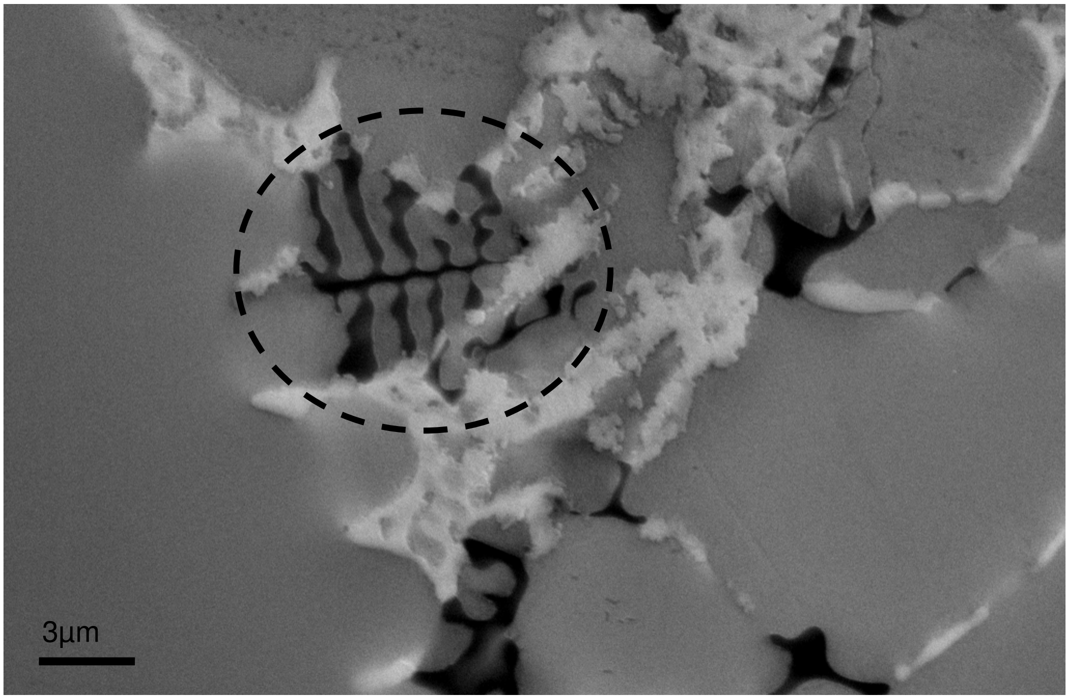

Figure 4.5: *SSM cast AA7075 alloy after heating to 476°C for 2 minutes, showing the exposure of porosity.*

The hardness results indicated that the SSM samples did not reach the same strengths as those achievable from the wrought equivalent. The lower strength values, coupled with the microstructures of the solution treated SSM samples in **Figure 4.2** (c), indicated that the SSM cast microstructure requires a more complex homogenisation process prior to ageing in order to maximise the strength of the structure after heat treatment. Before a custom heat treatment plan could be designed, the as-cast structure needed to be fully characterised. The characterisation process would help to gain an understanding as to how the structure would be affected by different temperature ranges and heat treatments.

4.2. THE AS-CAST CONDITION

The starting point of this investigation was the completion of a thorough examination of the typical microstructure produced by the semi-solid casting process, specifically the structure produced using the semi-solid metal rheocasting process developed by the CSIR. This characterisation process aimed to describe the quality and features of the microstructure in general, both on a macro scale, and, in detail, on a micro scale.

4.2.1. MORPHOLOGY

Semi-solid metal casting produces a globular microstructure. An example of the semi-solid microstructure can be seen in **Figure 4.6**. The microstructure is made up of large globular grains, with grain sizes proportional to their growth time within the solidification process and the effect of growth impingement from surrounding grains. Between these globular grains is the interglobular region, which is made up of small grains and an eutectic or second phase.

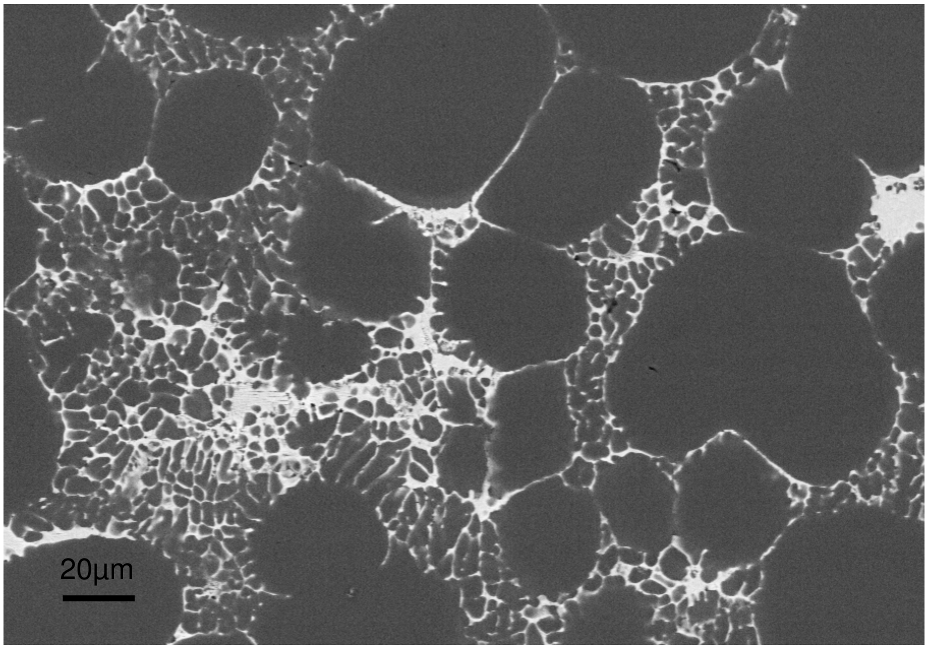

Figure 4.6: *General semi-solid cast microstructure, indicating primary, secondary and interglobular grains.*

The semi-solid cast plates were sectioned and samples were viewed at intervals along the length and through the thickness of the cast plate, in order to determine the extent of the microstructural variation, with respect to grain size and distribution along those axes.

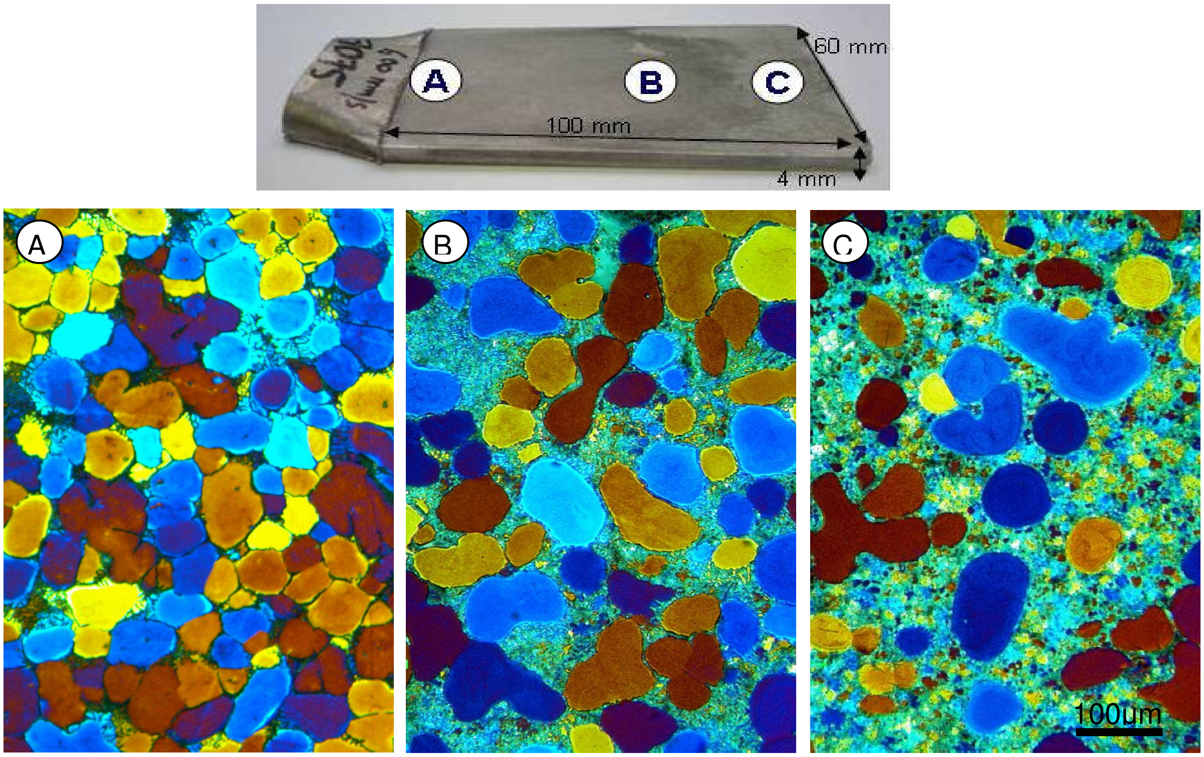

Figure 4.7: *Polarised light optical micrographs, showing the microstructural variation along the length of the SSM cast plate, from (a) to (c).*

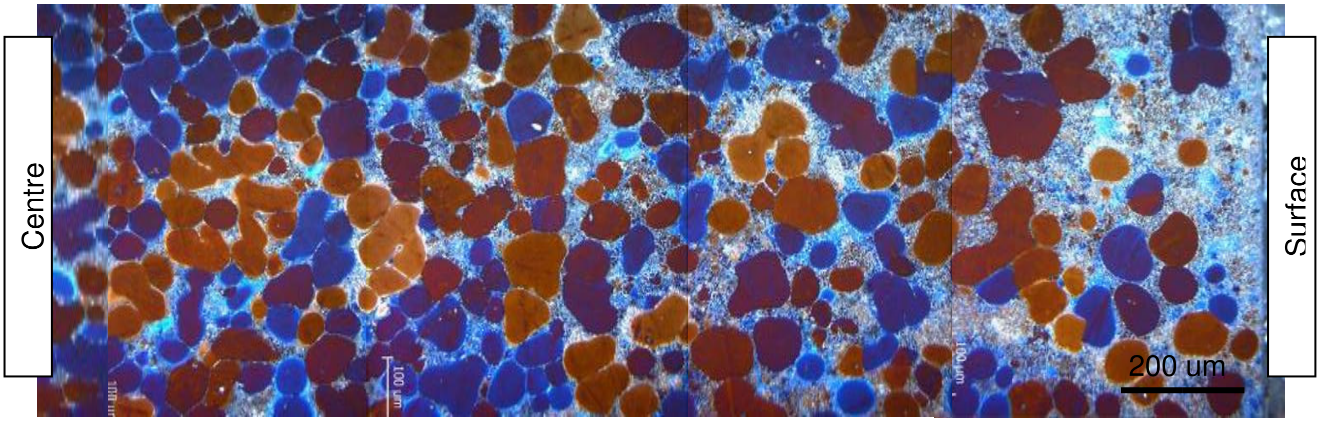

Figure 4.8: *Polarised light optical micrographs, showing the microstructural variation through the thickness of the SSM cast plate, from the centre of the thickness to the outer surface.*

The micrographs in **Figure 4.7** illustrate the grain size variation across the length of a typical semi-solid cast plate. The micrographs show that the ratio of primary globular grains to the smaller interglobular regions decreases as the structure progresses from the inlet point of the casting to the end of the plate. The area at the inlet has many primary grains of similar size, with very little interglobular region between, whereas the area at the end of the cast plate is predominantly interglobular region, with few primary and secondary grains. The grain size within the interglobular region in this area (at the end of the plate) has a larger diameter when compared to those at the middle of the length of the plate. **Figure 4.8** shows a similar trend through the thickness of the plate. With the centre of the thickness, seen on the left edge of the Figure, having a greater concentration of primary grains, with interglobular grains that are barely distinguishable at that magnification; the surface edge, seen on the right of the figure, has few primary and secondary grains, but the size of the small grains within the interglobular region has increased and these grains are now discernable in the image.

Further investigation into the morphology of the grains within the structure was achieved through higher magnification polarised light optical microscopy (PLOM) and scanning electron microscopy (SEM), using both backscattered and secondary electron imaging. The two alloys that were investigated were an AA7075 alloy and an A713 alloy.

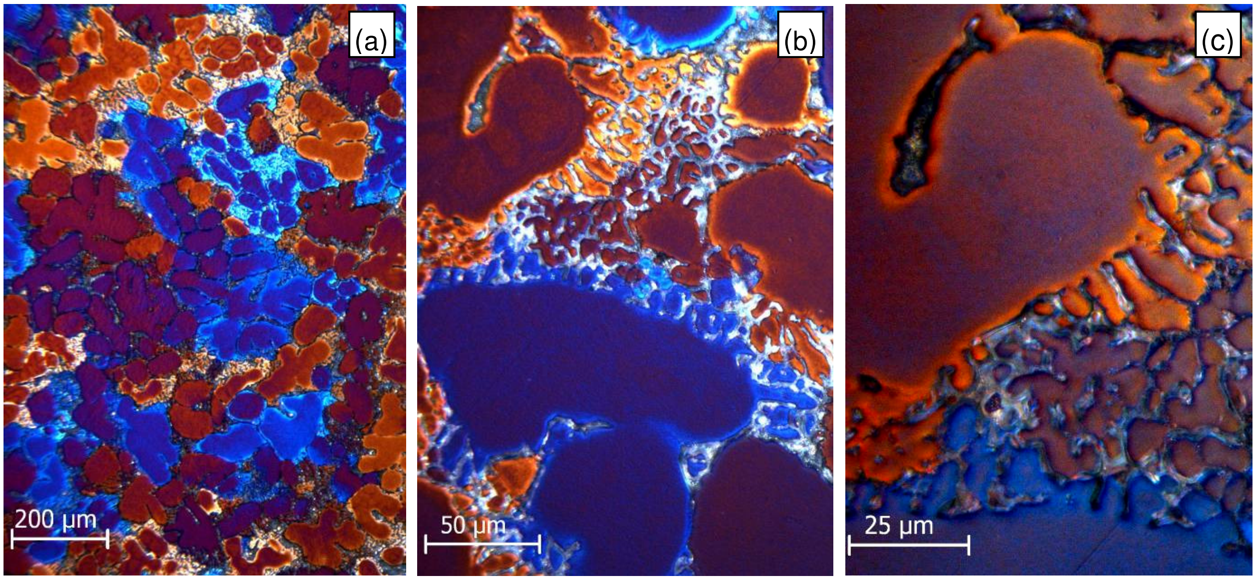

Figure 4.9: *Polarised light micrographs for SSM cast AA7075 alloy in increasing magnification from (a) - (c).*

Figure 4.9 shows a SSM cast AA7075 alloy in increasing magnifications, to illustrate the general morphology of the globular grains and their situation within the structure as a whole, as well as the interaction between the larger grains and the surrounding interglobular regions. In PLOM images, the variations in colour represent qualitative differences in relative orientation. From **Figure 4.9** (a), it can be seen that the globular grains are often clustered together in groups with similar colours. This supports the premise discussed by Niroumand and Xia[48] and Reisi and Niroumand[74], where the morphology of the globules is described as a grouping of agglomerate particles that are viewed as clusters of grains. **Figure 4.9** (b) and (c) show that the interglobular region is also comprised of clusters of small grains with similar colours, when viewed with polarised light, indicating similar orientations and connection to parent surrounding primary grains, whether visible or below the surface. **Figure 4.9** (c) focuses on the cellular protrusions that extend from the outer edges of the larger primary and secondary grains into the interglobular regions. Many of the protrusions show dendrite root thinning, indicating that, during processing, there may have been root thinning to an extent as to cause detachment of these dendrite arms into the liquid, allowing them to become nuclei for further solidification.

It can be seen that light microscopy is insufficient for viewing this type of microstructure at higher magnifications, as the second phase, or eutectic, between the grains is not defined. For more detailed evaluation, SEM was used.

This investigation focused on two different Al-Zn alloys, namely, an AA7075 alloy and an A713 alloy (actual compositions shown in Table I in Chapter 3). The characterisation process was performed on samples from both alloys under the same conditions, after the same processing steps.

In comparing the microstructures seen in **Figure 4.10** and **Figure 4.12**, it can be seen that the typical globular microstructure, incorporating primary, secondary and interglobular grains, was maintained for both alloys. By examining the structures at a higher magnification, as shown in **Figure 4.11** and **Figure 4.13**, it could be seen, qualitatively, that there were morphological differences in the cellular protrusions between the two alloys. The AA7075 alloy generally exhibited increased cellular protrusion length when compared to the A713 alloy samples.

Another feature that was noticeable in both alloys was the presence of a higher contrast ring around the outer edges of the globular grains. This was attributed to variations in the atomic number and, consequently, in the composition of these areas in contrast to the centre of the grains. These are referred to as coring bands, and are discussed in more detail in the **Chapter 4.2.2**.

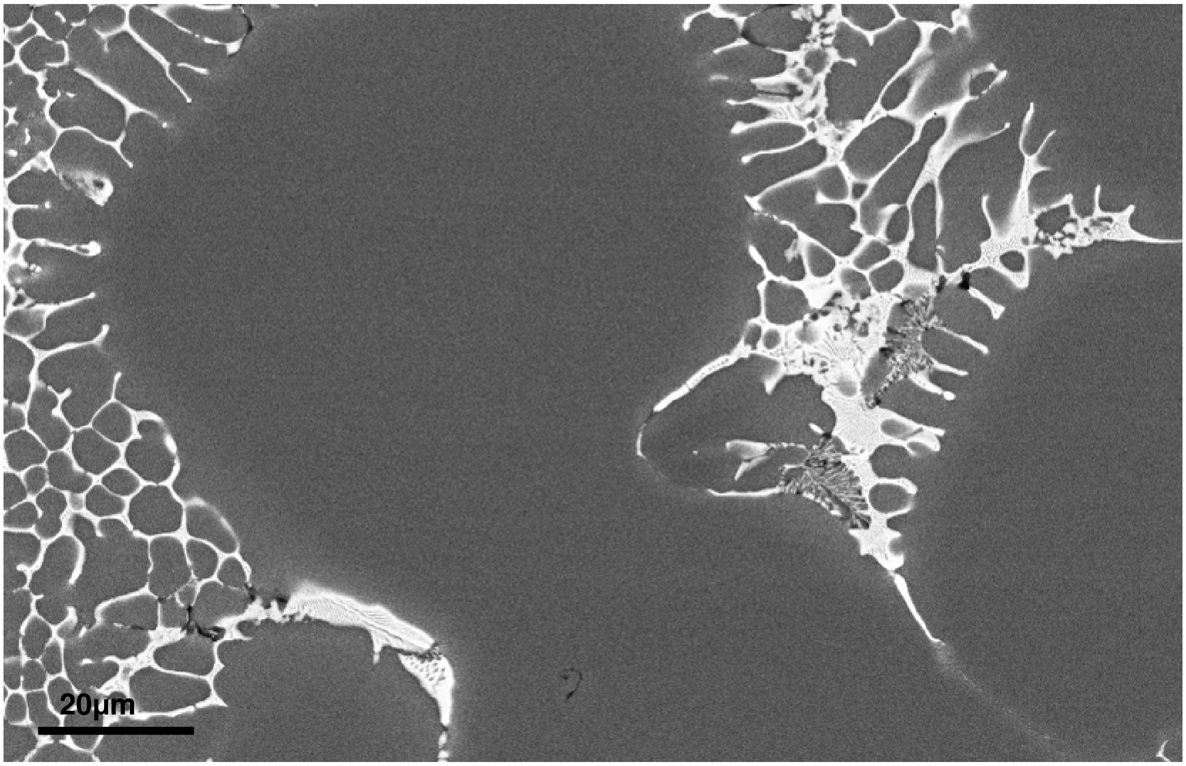

Figure 4.10: *SEM image of SSM cast AA7075 alloy, showing a primary grain surrounded by interglobular region, the second phase between the interglobular grains.*

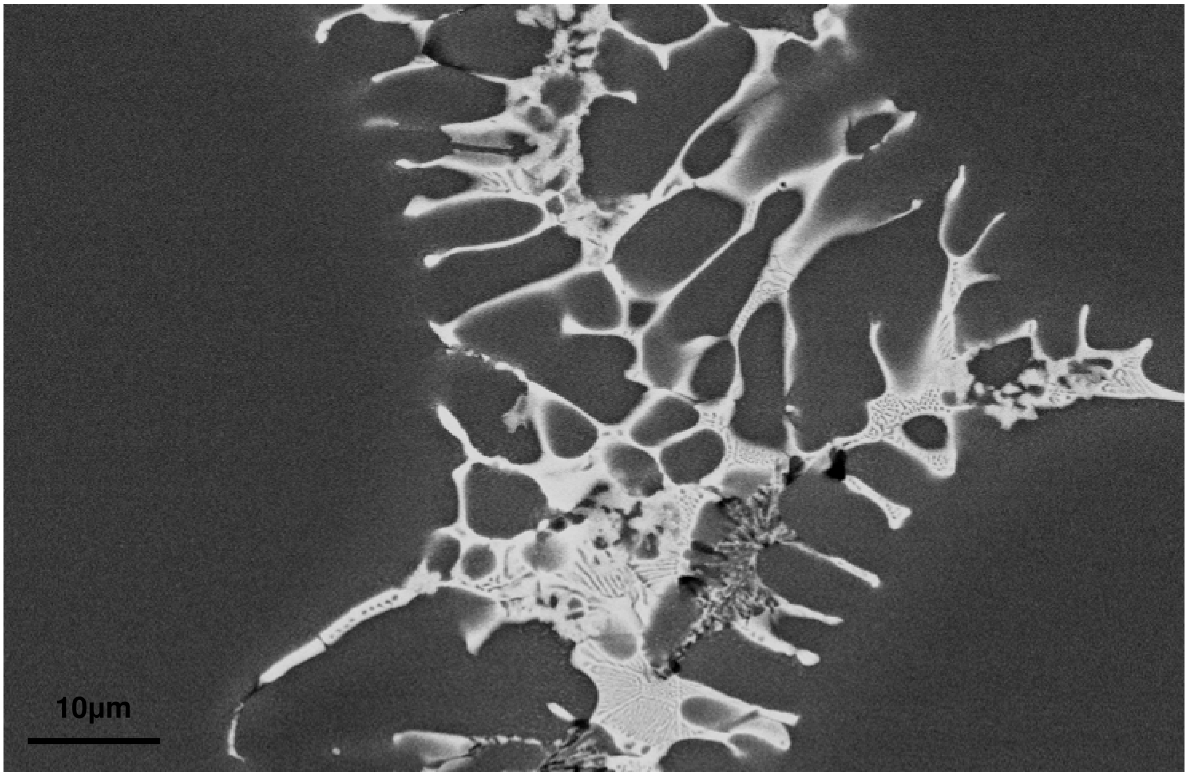

Figure 4.11: *SEM image of SSM cast AA7075 alloy interglobular region and cellular protrusions, showing the lamellar eutectic between the grains, porosity and iron inter-metallic in detail.*

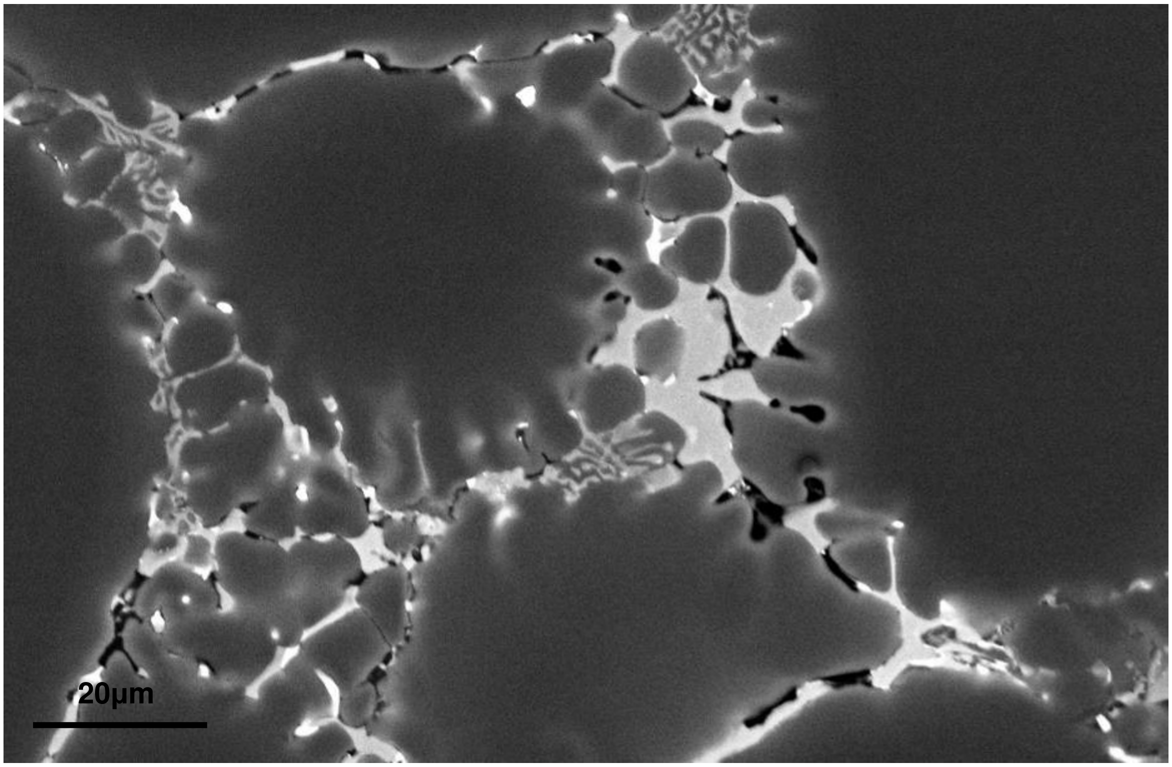

Figure 4.12: *SEM image of SSM cast A713 alloy, showing a primary grain surrounded by interglobular region, with second phase between the interglobular grains.*

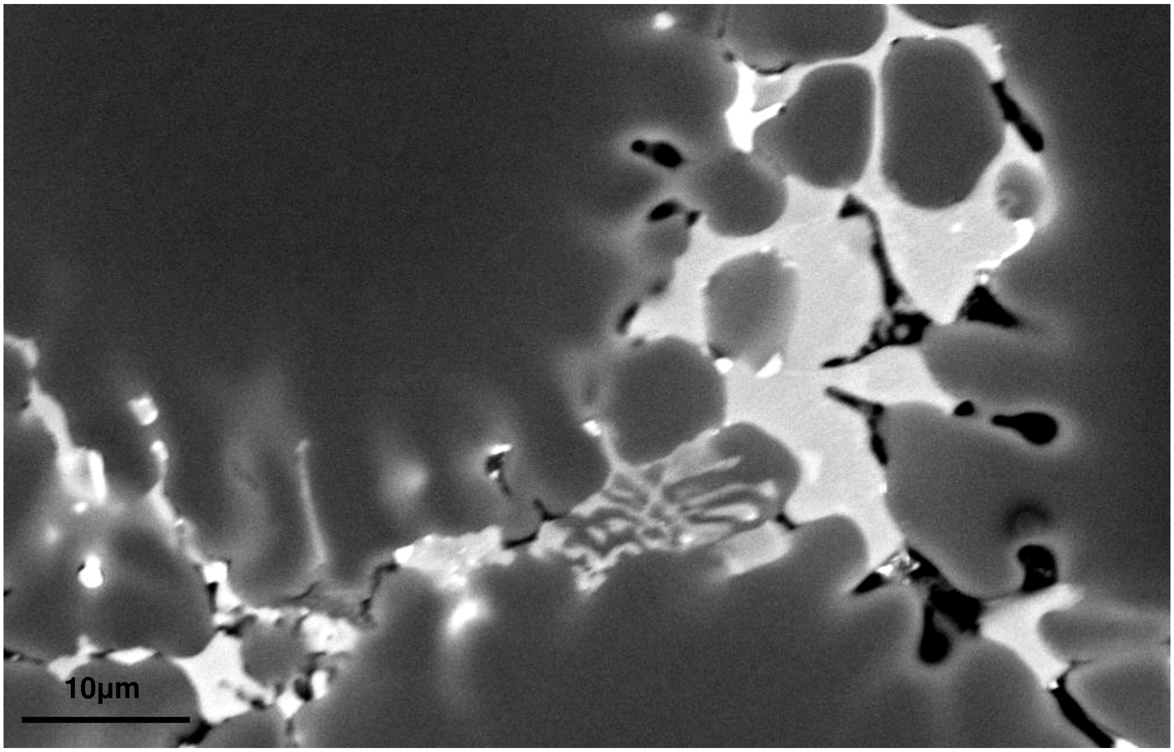

Figure 4.13: *SEM image of SSM cast A713 alloy interglobular region and cellular protrusions, showing the eutectic between the grains, porosity and iron inter-metallic in detail.*

The main difference could be identified in the eutectic. The AA7075 alloy exhibited a lamellar eutectic, whereas the A713 alloy had a eutectic with an irregular morphology at this magnification.

4.2.2. SEGREGATION AND COMPOSITIONAL INFORMATION

The segregation in the SSM as-cast microstructure was on both a macro- and micro-scale. The macrosegregation was due to the nature of the distribution of the grain structure, which was a result of the casting process. This is a phenomenon seen in all castings. The microsegregation was due to the solidification profile of the specific alloy, under the specific casting conditions. The microsegregation was a complex problem, where extreme compositional variations could be seen within a few microns of one another. This was especially noticeable in the interglobular regions, where the cellular protrusions and the small interglobular grains were surrounded by a solute-rich eutectic. However, another important degree of segregation to consider was the coring effect within all the grains – where a difference in composition could be seen between the first material to solidify (at the centre of the various grains) and the progression of the solidification front and its corresponding composition changes, through to the edge of the grains.

4.2.2.1. AA7075 ALLOY

The most obvious composition variation was between the globular grains themselves and the surrounding eutectic. The general composition of these two contrasting phases is shown in the table in **Figure 4.14**. Compositional analysis was completed using EDS. Each analysis point is marked with a "+" on the micrograph in **Figure 4.14**, and the corresponding values are indicated in the table below the micrograph. The values are shown in both weight percent (wt%) and atomic percent (at%). The elements considered in the analyses for the AA7075 alloy were Al, Zn, Mg, Cu, Cr, Fe and Si.

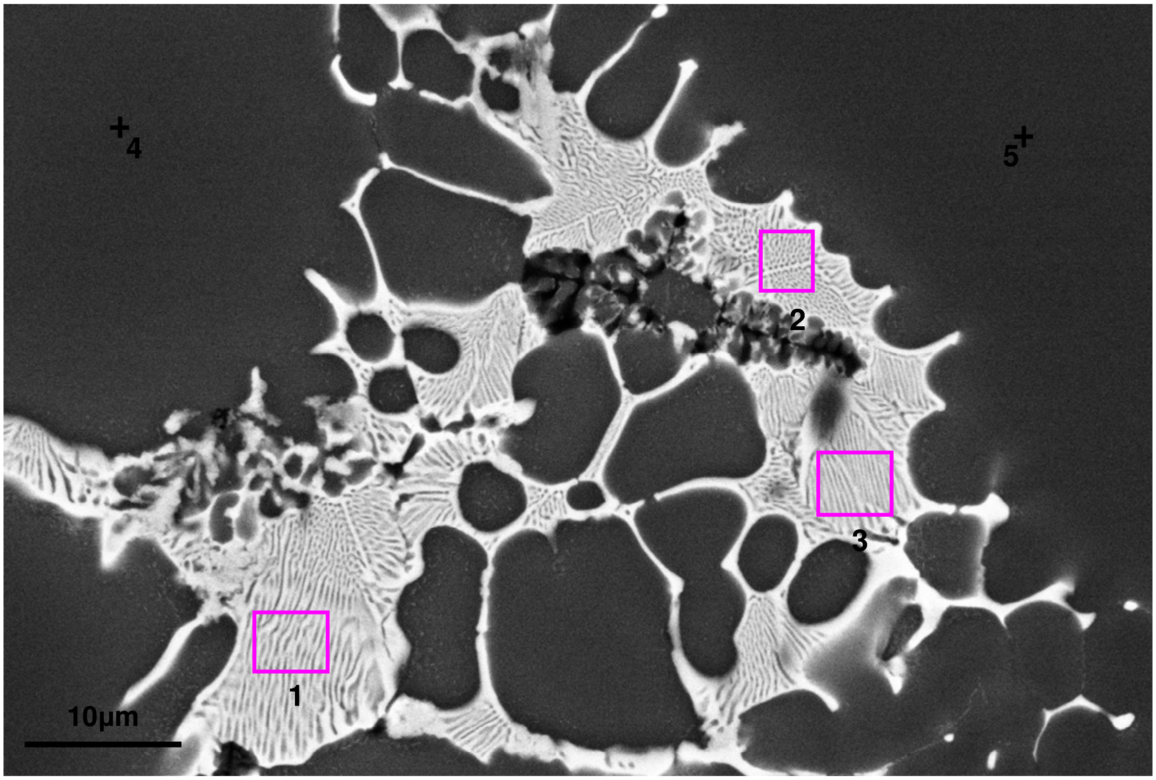

	Al		Zn		Mg		Cu		Cr		Fe		Si	
Point	Wt%	At%	Wt%	At%	Wt%	At%	Wt%	At%	Wt%	At%	Wt%	At%	Wt%	At%
1	41.5	54.4	30.2	16.3	14.8	21.6	13.1	7.3	0	0	0.3	0.2	0.2	0.2
2	43.0	56.3	30.2	16.3	13.9	20.3	12.6	6.9	---	---	0.3	0.1	---	---
3	44.0	57.1	29.4	15.7	13.9	20.0	12.3	6.7	0.05	0.03	0.1	0.07	0.2	0.2
4	93.9	96. 5	4.3	1.8	1.3	1.5	0.5	0.2	---	---	0.02	0.01	---	---
5	94. 6	96.9	3.8	1.6	0.9	1.1	0.3	0.1	0.4	0.2	---	---	---	---

Figure 4.14: *SSM cast AA7075 alloy, showing the interglobular region. The table shows the composition of the five points marked on the image, as determined by EDS.*

The globular grains (points 4 and 5 in **Figure 4.14**) have a typical composition of approximately 94wt% aluminium and 4wt% zinc. The composition of a homogenised sample of AA7075, prior to semi-solid casting, should have a zinc content of approximately 5,5wt%. This degree of difference is a result of the solidification path of semi-solid casting and the resulting segregation. The zinc-rich lamellar eutectic has a general composition ratio of 40:30wt% aluminium to zinc, with magnesium and copper contents of approximately 14 and 13wt% respectively.

The micrograph in **Figure 4.15** has contour lines superimposed over it that represent areas of similar concentration. Each contour band was roughly determined with at least three EDS analysis points, and should be viewed as a qualitative indication of coring bands that result from the casting process. The bands are numbered 1 to 5 and the composition values are averaged from the original points in the band. Points 6 to 10 are spot analyses and represent actual measurements.

From the compositional information shown in the table below the micrograph in **Figure 4.15**, it can be seen that, as well as coring within the globular grain, there is also a difference in composition along the cellular protrusions (indicated by the composition values at points 8, 9 and 10), causing further segregation.

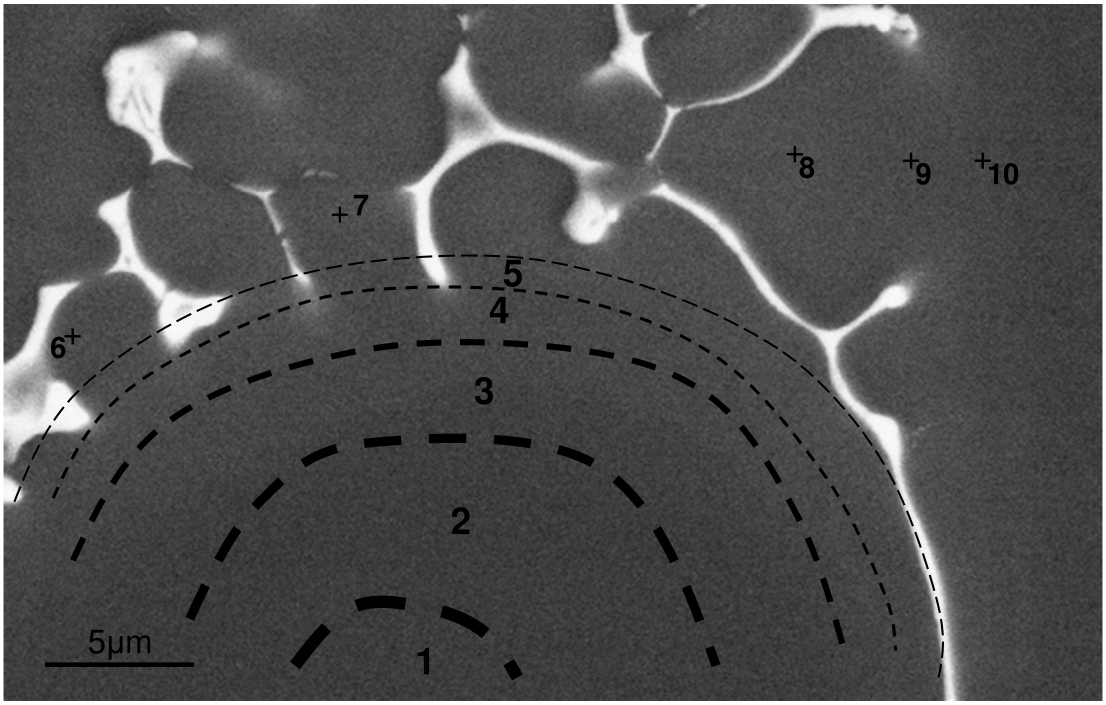

	Al		Zn		Mg		Cu		Cr	
Point no.	Wt%	At%	Wt%	At%	Wt%	At%	Wt%	At%	Wt%	At%
1	93.9	96.5	3.7	1.6	1.1	1.2	0.5	0.2	0.4	0.2
2	94.2	96.6	3.6	1.5	1.2	1.3	0.6	0.2	0.3	0.2
3	93.8	96.4	4.2	1.8	1.3	1.5	0.4	0.2	0.3	0.2
4	91.7	95.0	5.5	2.4	1.9	2.2	0.7	0.3	0.2	0.1
5	87.2	92.1	7.9	3.5	3.1	3.6	1.7	0.8	0.1	0.1
6	86.3	91.5	8.5	3.7	3.3	3.8	1.7	0.8	0.3	0.1
7	87.1	92.2	8.3	3.6	2.9	3.4	1.5	0.7	0.2	0.1
8	90.1	94.1	6.7	2.9	2.2	2.6	0.8	0.3	0.2	0.1
9	90.6	94.4	6.1	2.6	2.1	2.5	1.0	0.5	0.1	0.1
10	92.5	95.6	5.1	2.2	1.7	1.9	0.5	0.2	0.3	0.1

Figure 4.15: *SSM cast AA7075 alloy, with contour lines dividing areas of similar composition, indicating the coring bands, with corresponding EDS data in the table.*

Figure 4.16 shows a micrograph of the edge of a primary grain with cellular protrusions extending into a zinc-rich eutectic region. The image is in the BSD mode. The values of the main alloying elements for each point can be seen in the table below the micrograph.

In conjunction with the compositional values, there are elemental maps of the area that show the relative composition concentrations of the main alloying elements. The elements that are considered at this point are the main alloying elements: Al, Zn, Mg and Cu.

In the analysis of areas containing eutectic, such as in **Figure 4.14**, the elements that were considered were Al, Zn, Mg, Cu, Cr, Si and Fe. Si and Fe were added to the elements under analysis at this point because they formed the basis of the inter-metallics found within the interglobular regions. From the SEM image and the associated compositional information in **Figure 4.16**, it could be determined that the composition changed from the centre of the grain (at point 1) through to the tip of the dendritic finger at point 5. Across this line, progressing from points 1 to 5, there was a decrease in aluminium content and a marked increase in zinc content. There was also an increase in both the copper and magnesium contents. While the composition of point 6 at the centre of a smaller grain within the interglobular region was very similar to that of the dendritic finger, it still had a lower aluminium and a higher zinc content than at the centre of the larger primary or secondary type grains. This indicated that this small interglobular grain might either be a part of a dendritic finger from another grain within the bulk, or an isolated small grain that nucleated later in the SSM casting process.

The area maps showing composition distribution in **Figure 4.16** illustrate that the interglobular area is rich in zinc, magnesium and copper, owing to the solute rich phase $Mg(Zn,Cu,Al)_2$ which forms part of the lamellar structure of the eutectic. The elemental maps also show that copper and magnesium are relatively evenly distributed across the larger grains, while the zinc is located predominantly in the eutectic area. Thus, the zinc is more distinctly segregated than the other elements.

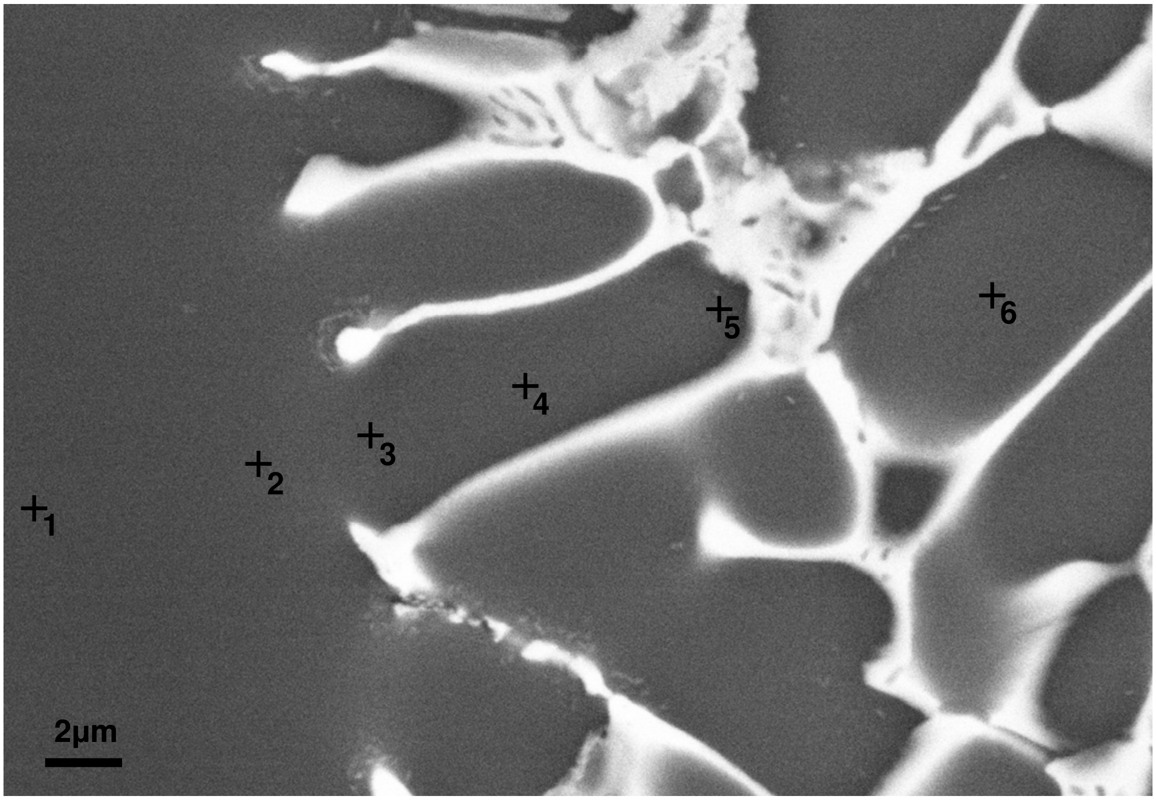

	Al		**Zn**		**Mg**		**Cu**		**Cr**	
Point no.	Wt%	At%	Wt%	At%	Wt%	At%	Wt%	At%	Wt%	At%
1	94.9	97.2	3.6	1.5	0.8	0.9	0.3	0.1	0.4	0.2
2	92.2	95.5	5.6	2.4	1.6	1.8	0.5	0.2	0.2	0.1
3	89.3	93.6	7.1	3.1	2.4	2.8	1.1	0.5	0.1	0.06
4	89.6	93.7	6.7	2.8	2.5	2.9	1.1	0.5	0.08	0.04
5	84.3	90.3	9.6	4.3	3.6	4.2	2.4	1.0	0.1	0.08
6	89.4	93. 6	6.5	2.8	2.5	2.9	1.5	0.6	0.1	0.08

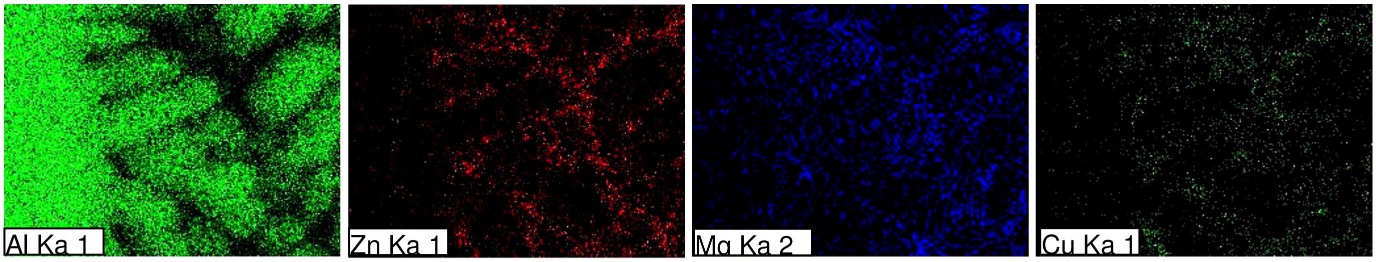

Figure 4.16: *SEM image of SSM cast AA7075 alloy, showing points where EDS point of interest scans have been completed. The composition information from the EDS spectra are shown in the table. EDS area maps of Al, Zn, Mg and Cu show the concentration of each element within the area shown in the SEM micrograph.*

4.2.2.2. A713 ALLOY

The contrast between the globular grains and the phases located between the grains in the interglobular region are shown in **Figure 4.17**. The composition was determined using EDS point analyses. Each analysis point is marked with a "+" on the micrograph, and the corresponding values are indicated in the table below the micrograph. The values are shown in both weight percent (wt%) and atomic percent (at%). The elements that were considered in the analyses for the A713 alloy were: Al, Zn, Mg, Cu, Fe and Si.

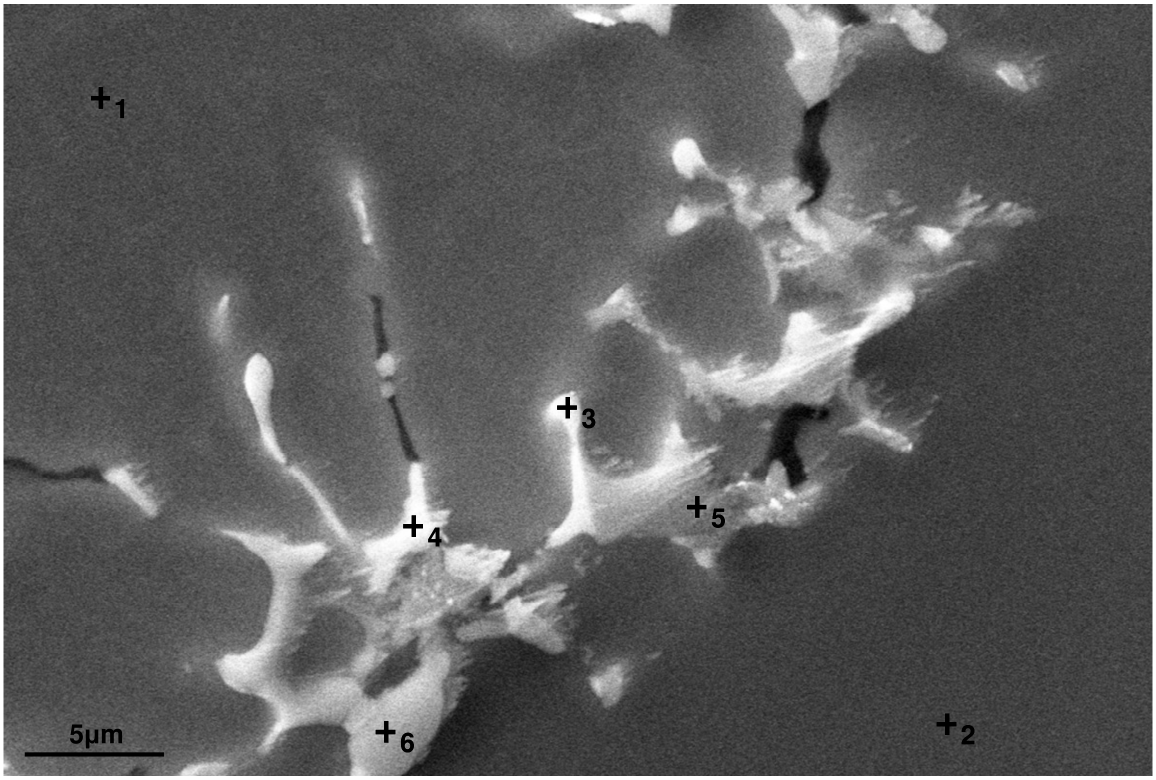

	Al		Zn		Mg		Cu		Fe		Si	
Point	Wt%	At%	Wt%	At%	Wt%	At%	Wt%	At%	Wt%	At%	Wt%	At%
1	92.7	96.6	6.2	2.6	0.3	0.4	0.8	0.4	---	---	---	---
2	90.7	95.6	7.5	3.3	0.5	0.5	1.2	0.5	---	---	---	---
3	45.6	63.8	42.8	24.7	4.7	7.2	6.9	4.1	0	0	0.08	0.1
4	49.7	69.5	7.9	4.6	0.5	0.7	40.7	24.2	0.9	0.6	0.3	0.4
5	48.8	68.9	8.2	4.7	0.2	0.3	41.4	24.8	0.9	0.6	0.5	0.6
6	37.7	58.4	10.7	6.8	0.6	1	50.3	33.1	0.7	0.5	0.08	0.1

Figure 4.17: *SSM cast A713 alloy, showing the phase contrast located between the grains. The table shows the composition of the six points marked on the image, as determined by EDS.*

The globular grains (points 1 and 2 in **Figure 4.17**) have a concentration range of approximately 90-92wt% aluminium and 6.2-7.5wt% zinc. In the fully homogeneous state, the A713 alloy should have in the order of 88.6wt% aluminium and 7.62wt% zinc. Points 3-6 are point analyses on the different contrast areas between the grains. As the areas themselves are small, and owing to the nature of the EDS technique and the consideration of an interaction volume, the compositional values are merely a qualitative guide to the elemental distribution at those points. It would be expected that areas of similar contrast in a backscattered image would represent areas of similar composition. Points 3 and 4 are viewed as white spots in the image, whereas their compositions are very different: point 3 has a 45:42wt% aluminium to zinc ratio, while point 4 has approximately a 50:40wt% aluminium to copper ratio. Owing to the similarities in atomic number of zinc and copper, similar contrasts for those elements could be expected. Points 5 and 6 have much lower contrast, but EDS results indicated that they too were very high in copper, having ratios of approximately 50:40wt% and 40:50wt% aluminium to copper respectively.

The solute distribution across the grains was evaluated in various ways. **Figure 4.18** shows an EDS linescan that crosses a full globular grain, and extends into the interglobular region on either side (indicated by the pink line across the micrograph). The linescan technique gives an indication of comparative concentrations of particular elements, in this case, Al, Zn and Cu. The relative concentrations are shown as graphs of intensity/count rate *vs* distance (μm).

The linescans indicate that there is coring at the edges of the grains with, for aluminium, a gradual decrease in intensity, from approximately 10-15μm from the outside edges of the grain. There are corresponding increases seen in zinc and copper. To verify this, more qualitative spot analyses were completed within those areas where coring was expected. The composition data in the table show that the aluminium content at the centre (point 3) is higher than those at the edges (points 1, 2, 4 and 5), and with the decrease in aluminium there is a corresponding increase in zinc and copper.

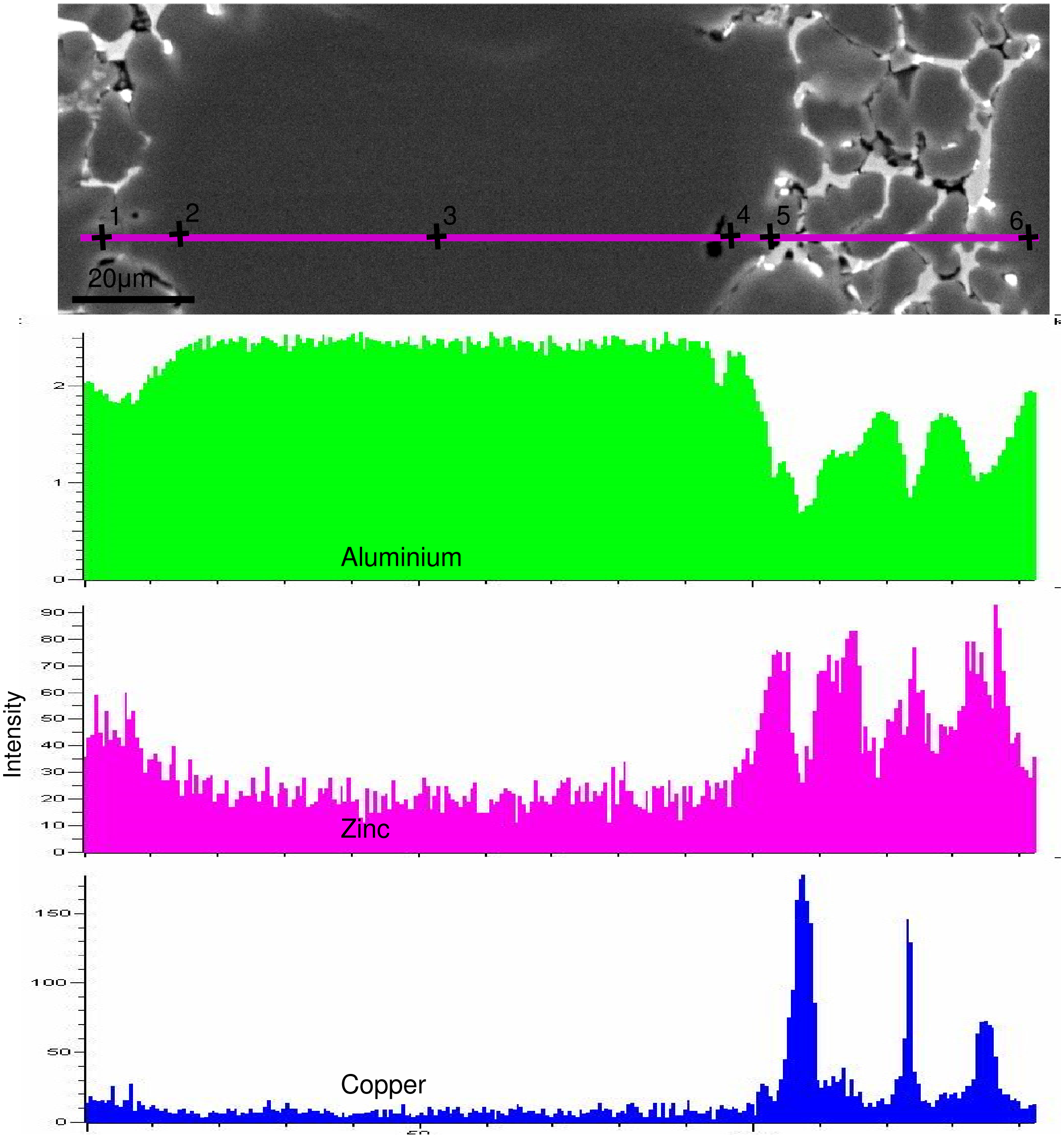

	Al		Zn		Mg		Cu		Fe		Si	
Point	Wt%	At%	Wt%	At%	Wt%	At%	Wt%	At%	Wt%	At%	Wt%	At%
1	75.6	87.7	19.3	9.3	0.6	0.8	3.4	1.7	0.1	0.1	0.3	0.3
2	92.3	96.3	6.4	2.7	0.3	0.4	0.9	0.4	---	---	0.1	0.1
3	93.7	97.1	5.4	2.3	0.3	0.3	0.7	0.3	---	---	0.1	0.1
4	91.8	96.1	6.8	2.9	0.4	0.4	0.9	0.4	0.03	0.02	0.1	0.1
5	82.9	91.4	13.1	5.9	0.5	0.6	2.8	1.3	0.01	0	0.6	0.6
6	87.7	94.1	9.8	4.3	0.5	0.6	1.2	0.8	---	---	0.2	0.2

Figure 4.18: *SSM cast A713 alloy, showing EDS linescan analysis of Al, Zn and Cu concentration (intensity vs distance), with corresponding EDS compositions in the table.*

In a more detailed analysis of the coring phenomenon, **Figure 4.19** shows a backscattered SEM image of a group of globular grains, all exhibiting contrast variation in the coring band area, where the band thickness varies from approximately 5 to 15μm. The width of the band appeared to be linked to the degree of impingement from other grains in adjacent areas. Where there was impingement, less solute-rich eutectic was available for diffusion, resulting in narrow coring rings. On the other hand, areas adjacent to interglobular regions that were solute-rich had increased coring band widths.

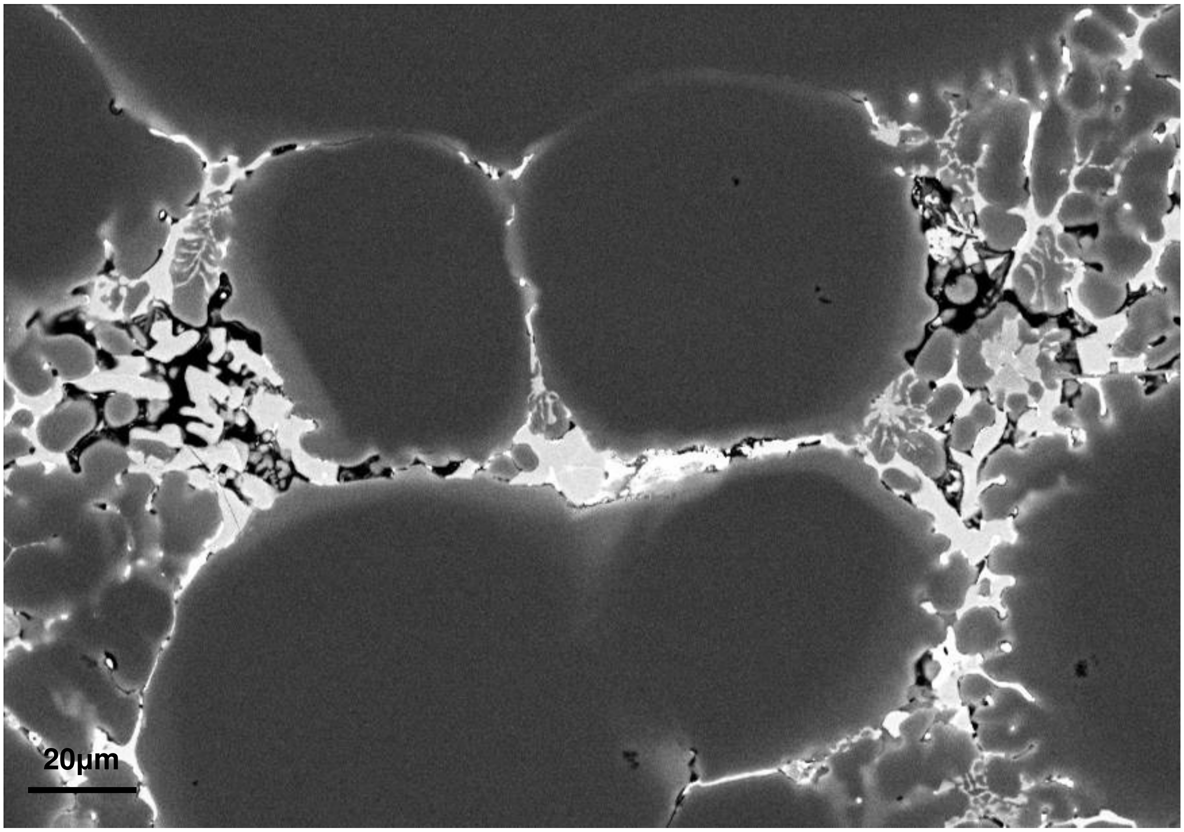

Figure 4.19: *SSM cast A713 alloy, showing coring bands around the edges of the globular grains.*

Figure 4.20 focuses more closely on the edge of one of the globular grains from the previous figure. **Figure 4.20** has contour lines superimposed over the micrograph that represent areas of similar concentration. Each contour band was roughly determined with EDS analysis points, and should be viewed as a qualitative indication of coring bands that result from the casting process. The elemental concentrations corresponding to the points marked on the figure are shown in the table below. The contours were positioned according to these values.

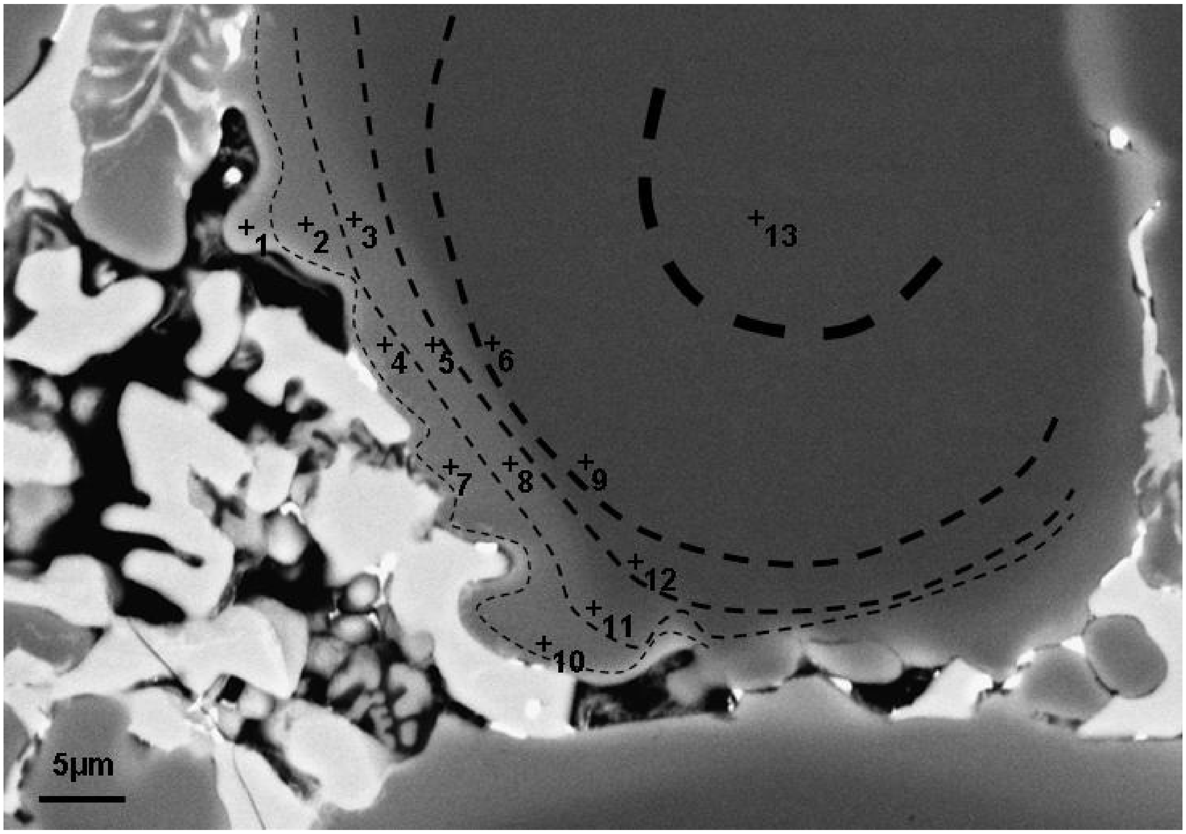

	Al		Zn		Mg		Cu		Fe		Si	
Point	Wt%	At%	Wt%	At%	Wt%	At%	Wt%	At%	Wt%	At%	Wt%	At%
13	93.6	96.9	5.3	2.3	0.3	0.39	5.2	2.6	0.1	0.1	0.8	0.9
6	92.5	96.4	6.0	2.6	0.4	0.4	4.7	2.3	0.0	0.0	0.3	0.3
9	92.8	96.6	5.7	2.5	0.4	0.5	3.6	1.7	0.0	0.0	0.2	0.2
12	92.6	96.4	6.0	2.6	0.5	0.6	5.0	2.5	0.0	0.0	0.3	0.3
3	82.1	91.2	13.6	6.2	0.6	0.7	3.6	1.7	0.1	0.0	0.2	0.3
5	82.1	91.1	13.3	6.1	0.7	0.8	1.0	0.4	0.0	0.0	0.1	0.1
8	84.7	92.6	11.8	5.3	0.6	0.7	5.0	2.4	0.2	0.1	0.4	0.4
11	86.5	93.5	10.8	4.8	0.5	0.6	2.7	1.2	0.1	0.1	0.1	0.1
2	78.3	89.1	16.1	7.6	0.6	0.8	0.9	0.4	0.0	0.0	0.1	0.1
4	76.0	87.8	18.0	8.6	0.7	0.9	4.5	2.2	0.0	0.0	0.2	0.2
7	77.1	88.2	16.6	7.8	0.8	1.0	2.2	1.0	0.0	0.0	0.0	0.0
10	78.6	89.4	16.2	7.6	0.6	0.7	0.9	0.4	0.0	0.0	0.1	0.1
1	71.6	85.1	21.9	10.7	0.5	0.6	0.6	0.2	0.0	0.0	0.1	0.1

Figure 4.20: *A higher magnification of the previous figure, with contour lines dividing areas of similar composition indicating the coring bands, with corresponding EDS data in the table.*

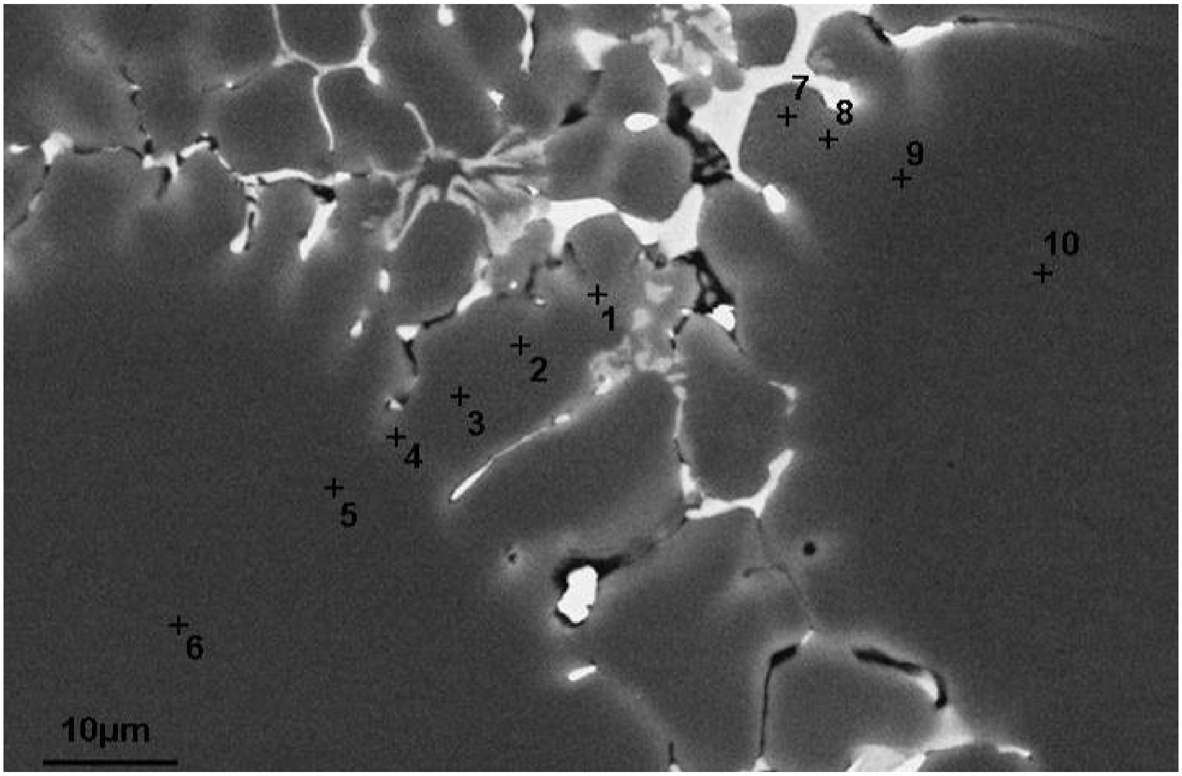

	Al		Zn		Mg		Cu		Fe		Si	
Point	Wt%	At%	Wt%	At%	Wt%	At%	Wt%	At%	Wt%	At%	Wt%	At%
1	79.3	89.8	17.2	8.0	0.4	0.6	2.8	1.4	0.1	0.1	0.2	0.2
2	88.4	94.4	9.1	4.0	0.6	0.7	1.7	0.8	0.1	0.0	0.1	0.1
3	90.4	95.3	7.4	3.2	0.5	0.6	1.3	0.6	0.1	0.1	0.2	0.2
4	90.1	95.2	8.1	3.5	0.5	0.6	1.2	0.5	0.0	0.0	0.2	0.2
5	93.2	96.8	5.6	2.4	0.4	0.5	0.8	0.4	0.0	0.0	0.0	0.0
6	93.6	96.9	5.3	2.3	0.3	0.4	0.6	0.3	0.0	0.0	0.1	0.1
7	83.5	91.9	13.1	5.9	0.6	0.7	2.6	1.2	0.1	0.1	0.2	0.2
8	85.6	93.0	11.2	5.0	0.6	0.7	2.3	1.1	0.2	0.1	0.2	0.2
9	91.8	96.1	6.2	2.7	0.4	0.5	0.9	0.4	0.1	0.1	0.1	0.1
10	93.2	96.8	5.5	2.4	0.5	0.5	0.5	0.2	0.0	0.0	0.0	0.0

Figure 4.21: *SSM cast A713 alloy, showing composition variation along the cellular protrusions.*

As with the AA7075 alloy, the A713 alloy also exhibited a composition variation that extended into the cellular protrusions. From **Figure 4.21** it can be seen that the composition near the centre of the grains (seen in points 6 and 10) is approximately 93wt% aluminium and 5.5wt% zinc. The composition is fairly constant until the edge of the grain, seen between point 5 and 4 and at point 9. This decrease in aluminium and increase in zinc and copper continues to the end of the cellular protrusions.

4.2.3. EBSD AND ORIENTATION ANALYSIS

Quantitative crystallographic information, such as orientation, regarding the as-cast structure was obtained using the electron backscattered diffraction (EBSD) technique. SEM micrographs were taken of the sample area prior to mapping. Once general area maps had been obtained, more detailed, higher magnification maps were generated. The step size ranged from 0.2μm to 1μm, depending on the magnification and quality requirements for individual maps.

4.2.3.1. AA7075 ALLOY

Figure 4.22 shows a band contrast image and a corresponding orientation map that gives the orientation at each point in the image in Euler colours. The green points in both images are non-indexed points, which are generally situated within the interglobular regions where the zinc-rich eutectic is located. Non-indexed points can also be found in areas with overlapping Kikuchi bands, such as at grain boundaries and areas with high dislocation densities. The EBSD maps show the globular grain morphology and the different orientations. The band contrast image in (a) shows clusters of small grains in the interglobular regions, and when the same areas are identified in the orientation map in (b), there is no clear definition between those individual small interglobular grains. They are seen as part of the larger grains of the same orientation. In addition, areas where cellular protrusions extend from the larger grains in the band contrast image are observed as an integral part of the globular grain, with no distinction between them and their parent grain. A closer look at the cellular protrusions is shown in **Figure 4.23**.

The band contrast images and EBSD maps in both **Figure 4.22** and **Figure 4.23** show that there are some grains in the structure that have, within them, a large amount of (a) contrast pattern and (b) misorientation angle variation. Some grains appear in a constant contrast colour and have no visible misorientation angle variations within them. The misorientations within the grains are shown as black or grey lines and represent HAGBs and LAGBs respectively. This effect will be discussed in more detail in **Chapter 4.2.4**.

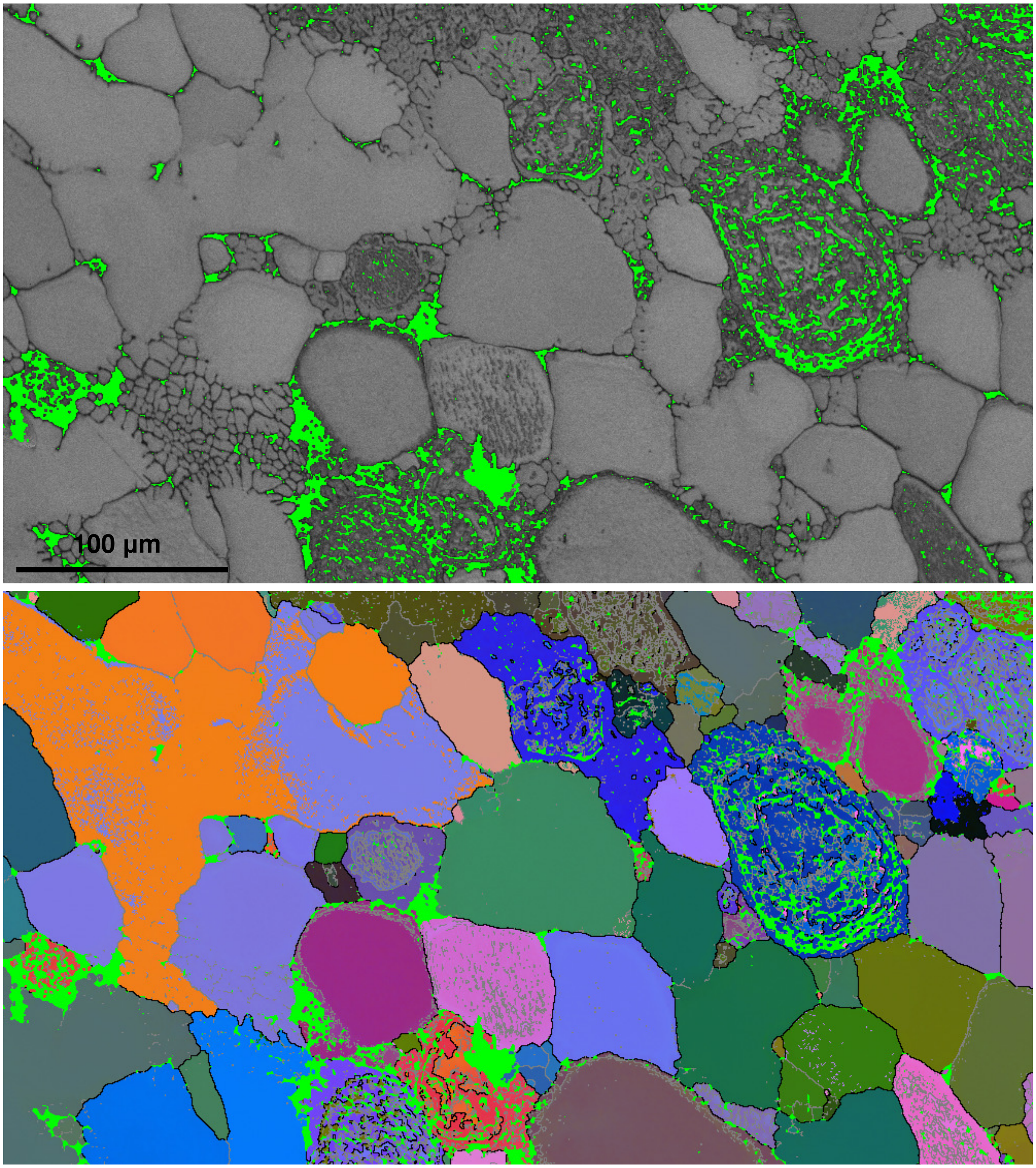

Figure 4.22: *SSM cast AA7075 alloy showing EBSD mapping. (a) Map viewed in band contrast, and (b) map viewed in Euler colour. LAGBs shown in grey and HAGBs shown in black. 0.3µm step size during mapping.*

The cellular protrusions that extend from the large globular grains have the same Euler colour in **Figure 4.23**. The non-indexed points between the cellular protrusions and between the small grains in the interglobular region are as a result of the zinc-rich eutectic in these areas. There are no visible misorientations in the cellular protrusions, and HAGBs are seen only where grains of different orientation impinge on one another. (These HAGBs can be seen between the purple and blue interglobular grains.) Other HAGBs are seen within the larger globular grain in the bottom right-hand corner of **Figure 4.23** (b). This effect will be discussed in **Chapter 4.2.4.**

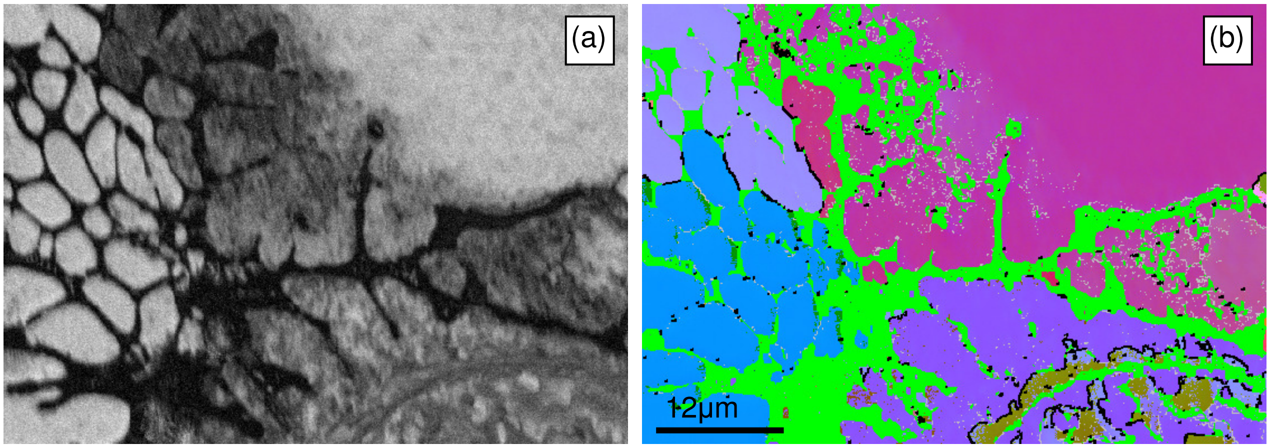

Figure 4.23: *SSM cast AA7075 alloy showing EBSD mapping. (a) shows the band contrast image of cellular protrusions and interglobular grains. (b) Shows an EBSD map of the area.*

4.2.3.2. A713 ALLOY

The previous chapters have shown that slight variations in the typical SSM as-cast structure of the AA7075 and A713 alloys can be identified. These variations are further evaluated by orientation analysis and EBSD.

Large area EBSD maps were completed for the A713 alloy. **Figure 4.24** shows a band contrast image and a corresponding EBSD orientation map. The map was completed using a 0.5µm step size between each point analysed. The green points are non-indexed points. The cellular protrusions are shorter and less easily identified in the band contrast image, but in the EBSD map they have the same orientation as an adjacent parent grain and, in a few cases, can be identified only by a cluster of non-indexed points that represent an entrapped eutectic or second phase between the protrusions.

This A713 alloy exhibits fewer contrast-free and misorientation variation-free grains than the AA7075 alloy, as seen in **Figure 4.22**. The contrast and misorientation that is located in the majority of the grains in the A713 alloy has a lamellar configuration, which is especially clear in the grain in the top right-hand corner of the band contrast image in **Figure 4.24** (a). The EBSD map in (b) does not have the misorientation boundary line superimposed on it, as the number of LAGBs is high, with the result that the clarity of the Euler colour variation is compromised.

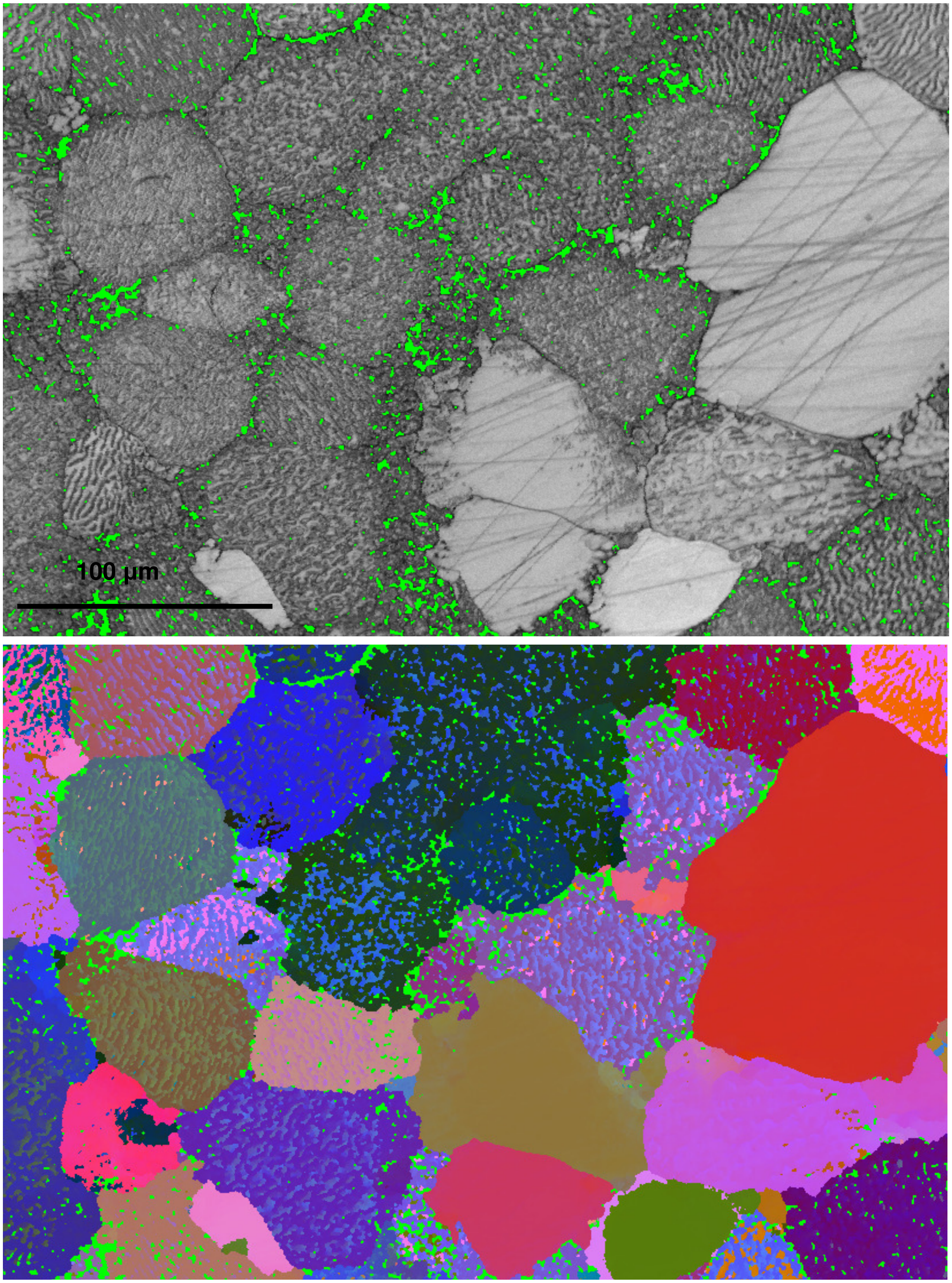

Figure 4.24: *SSM A713 alloy. (a) EBSD map viewed in band contrast, and (b) map viewed in Euler colours, 0.5µm step size during mapping.*

4.2.4. SUBSTRUCTURE WITHIN GRAINS

The EBSD mapping process revealed the presence of a substructure within some of the primary and secondary grains. This can also been seen in the SEM micrographs, in both the secondary electron and backscattered electron images.

The substructure can be divided into two types, one with a lamellar configuration and the other with a circular configuration. The lamellar configuration is shown in **Figure 4.25** (a) and (b) and the circular configuration is shown in **Figure 4.25** (c) and (d).

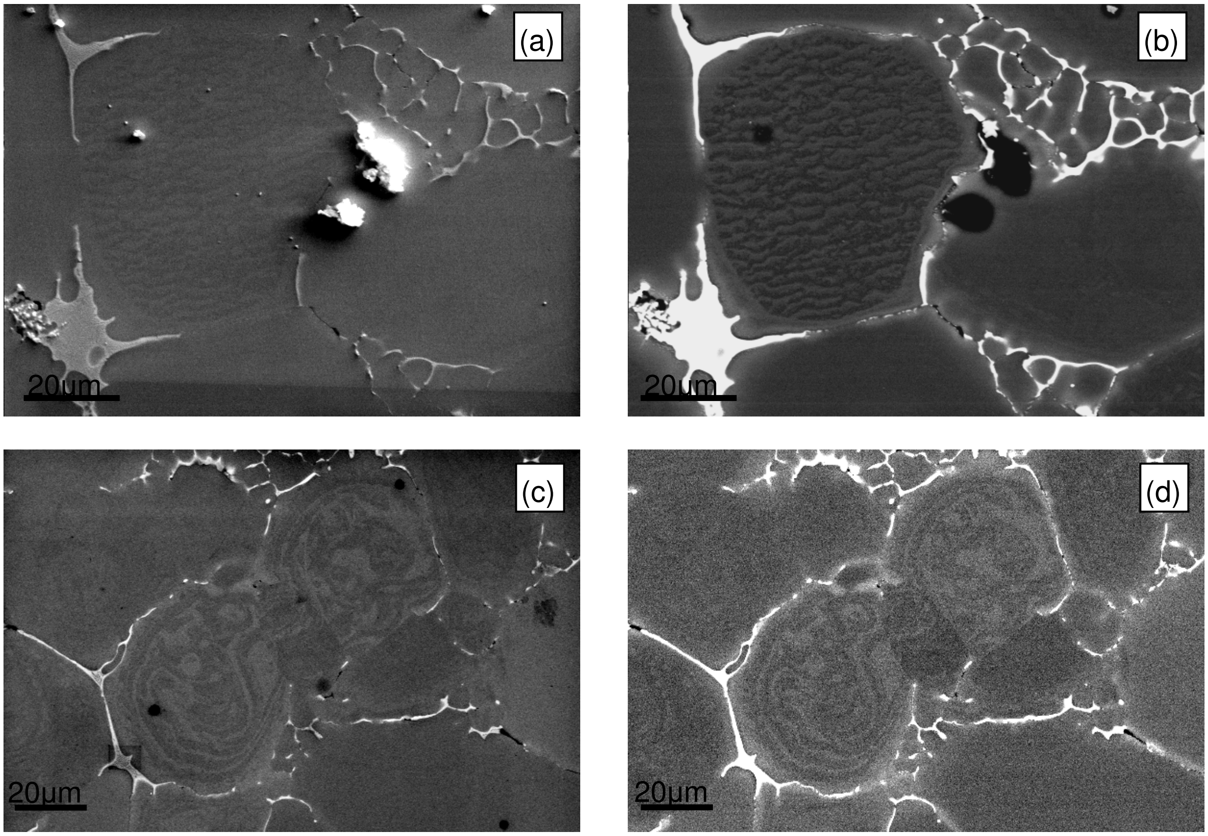

Figure 4.25: *SSM cast AA7075 alloy. SEM micrographs (a) and (b) show the lamellar substructure in secondary and backscattered mode respectively, and (c) and (d) show the circular substructure in secondary and backscattered mode.*

Because these substructure configurations are visible in the secondary electron images, it can be surmised that the effect is topographical in nature. However, they are also visible in the backscattered image, this suggesting a compositional variation as a source. Compositional effects can be evaluated through EDS.

4.2.4.1. AA7075 ALLOY

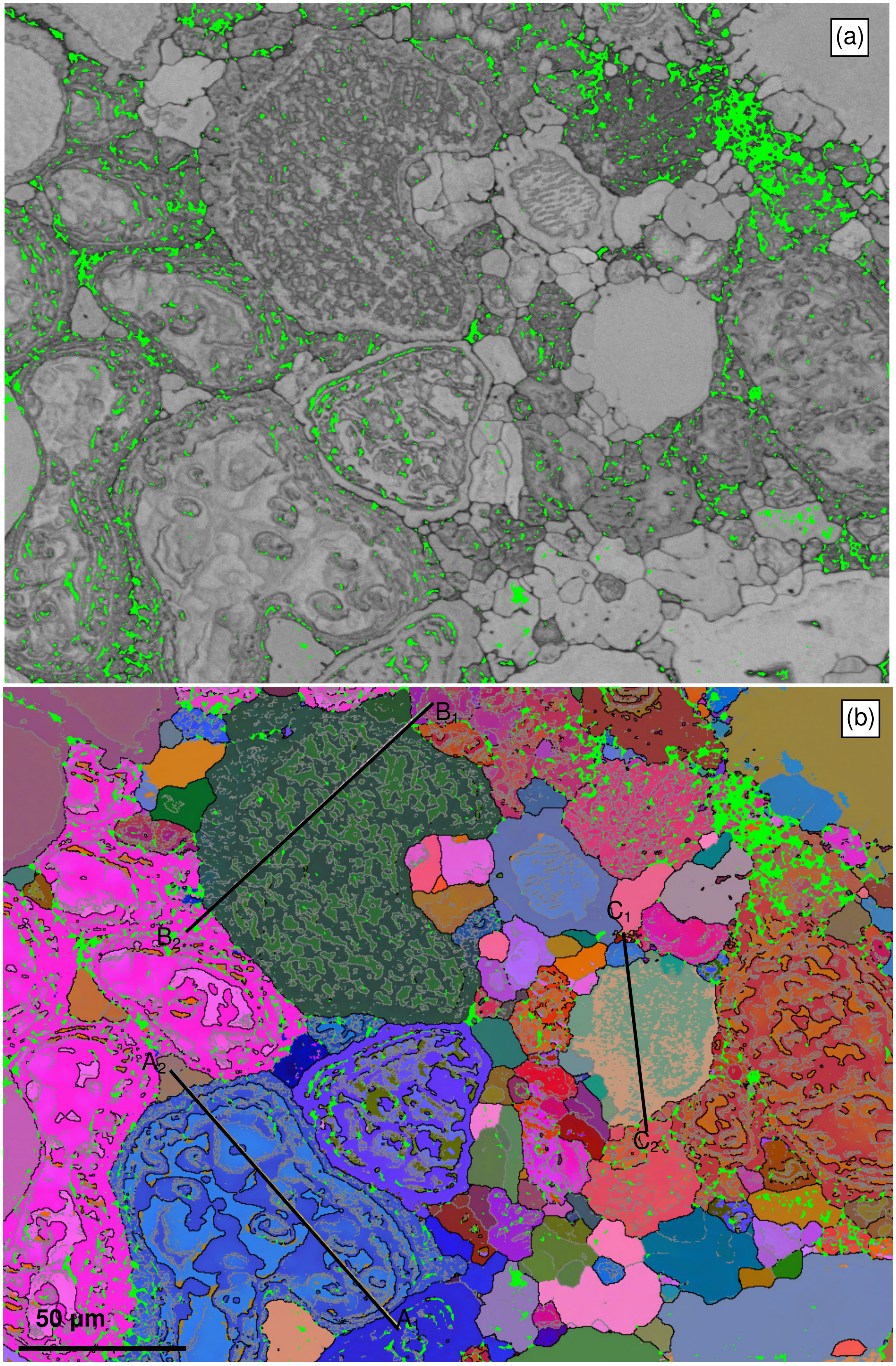

Figure 4.26: *SSM cast AA7075 alloy showing (a) band contrast and (b) EBSD map in Euler colours. Misorientation lines A_1-A_2 , B_1-B_2 and C_1-C_2 are indicated on the map.*

Figure 4.26 shows in (a), a band contrast image, and in (b) the corresponding EBSD map. These illustrate the misorientations that make up the internal substructure in the globular grains. Both the circular and lamellar substructure configurations can be identified in this EBSD map, as well as some strain-free grains.

Figure 4.26 shows the line A_1-A_2 crossing a grain with a circular substructure configuration. The corresponding misorientation profiles can be seen in **Figure 4.27**. The misorientation profiles are shown in two ways: first, with misorientations relative to the previous point on the profile line, and second, with cumulative misorientations relative to the starting point of the profile line. In general, misorientations of 15° or greater are considered to be high angle grain boundaries (HAGBs), and are associated with boundaries between neighbouring grains. Misorientations between 2° and 15° are considered to be low angle grain boundaries (LAGBs) and are regarded as sub-grain boundaries. The grains that exhibit the circular substructure have a high number of HAGBs within them, in addition to many LAGBs. The presence of these HAGBs suggests that there is a large amount of misfit within the lattice of these grains. The misorientation profile in **Figure 4.27** shows that the grain has approximately ten HAGBs within it, ranging from 15-21° in misorientation, with the same number with a range from 4-14°. The cumulative misorientation profile shows that each successive large increase in misorientation is followed by a large equivalent decrease in misorientation. In addition, the amount of cumulated strain within the individual grain can aid the interpretation of how the strain will affect the structure during heat treatment at a later stage.

The misorientation profiles corresponding to the line B_1-B_2 can be seen in **Figure 4.28**. The line B_1-B_2 cuts across a grain that exhibits the lamellar substructure configuration. There are a large number of grain boundaries associated with this structure, and they range between 2° and 13° misorientation. The misorientation profile shows that it is only where the line crosses into and out of the grain in question that HAGBs are to be found.

Line C_1-C_2 in **Figure 4.26** crosses a grain that does not exhibit any misorientations. The misorientation profiles corresponding to the line C_1-C_2 can be seen in **Figure 4.29**. It can be clearly seen in both graphs that the only misorientations that are present that are greater than 2° are the outside boundaries of the whole grain.

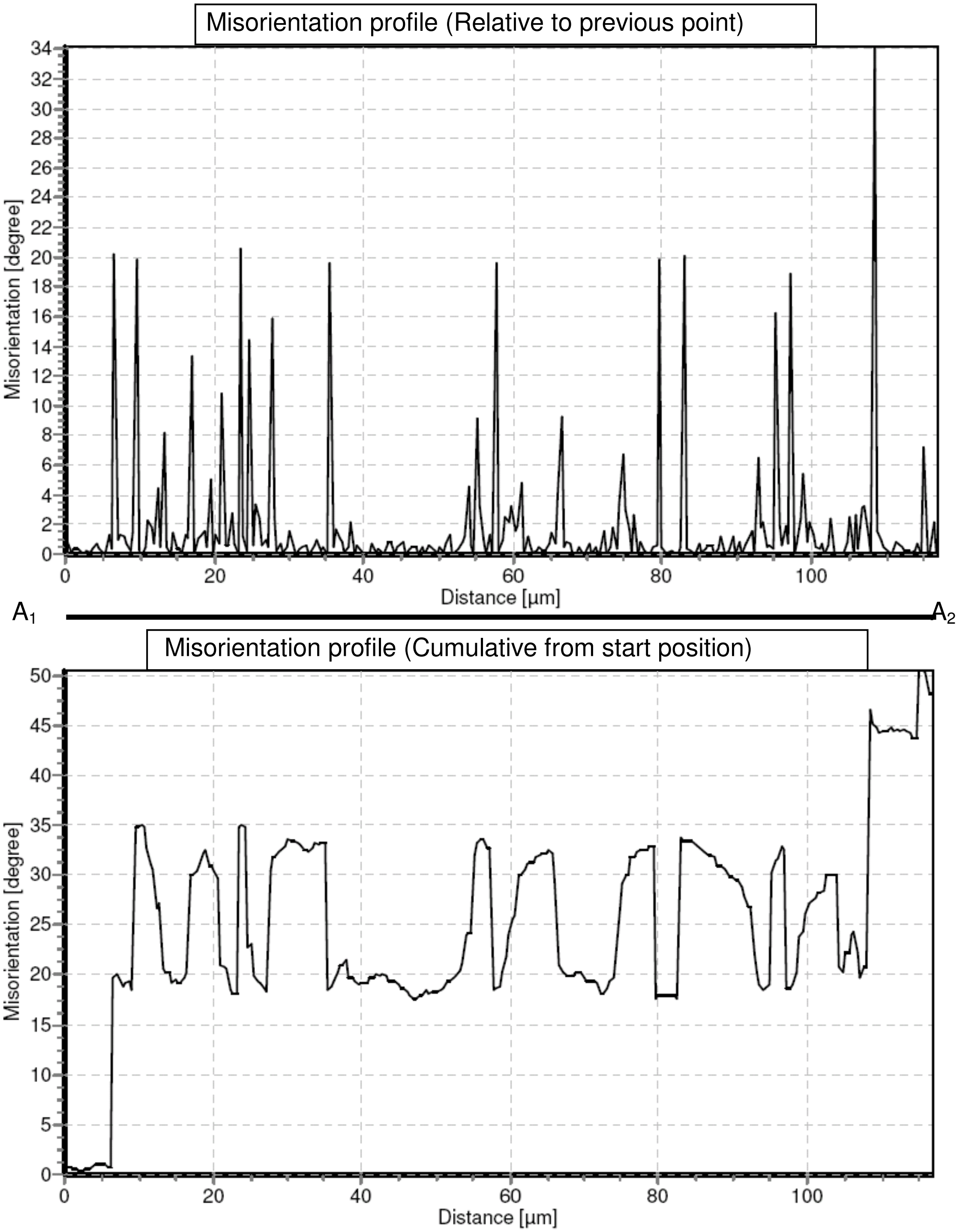

Figure 4.27: *Misorientation profile of line A_1-A_2 in* ***Figure 4.26****. The first graph shows the misorientation angles relative to the previous point along the A line and the second graph shows the cumulative misorientations from A_1 to A_2.*

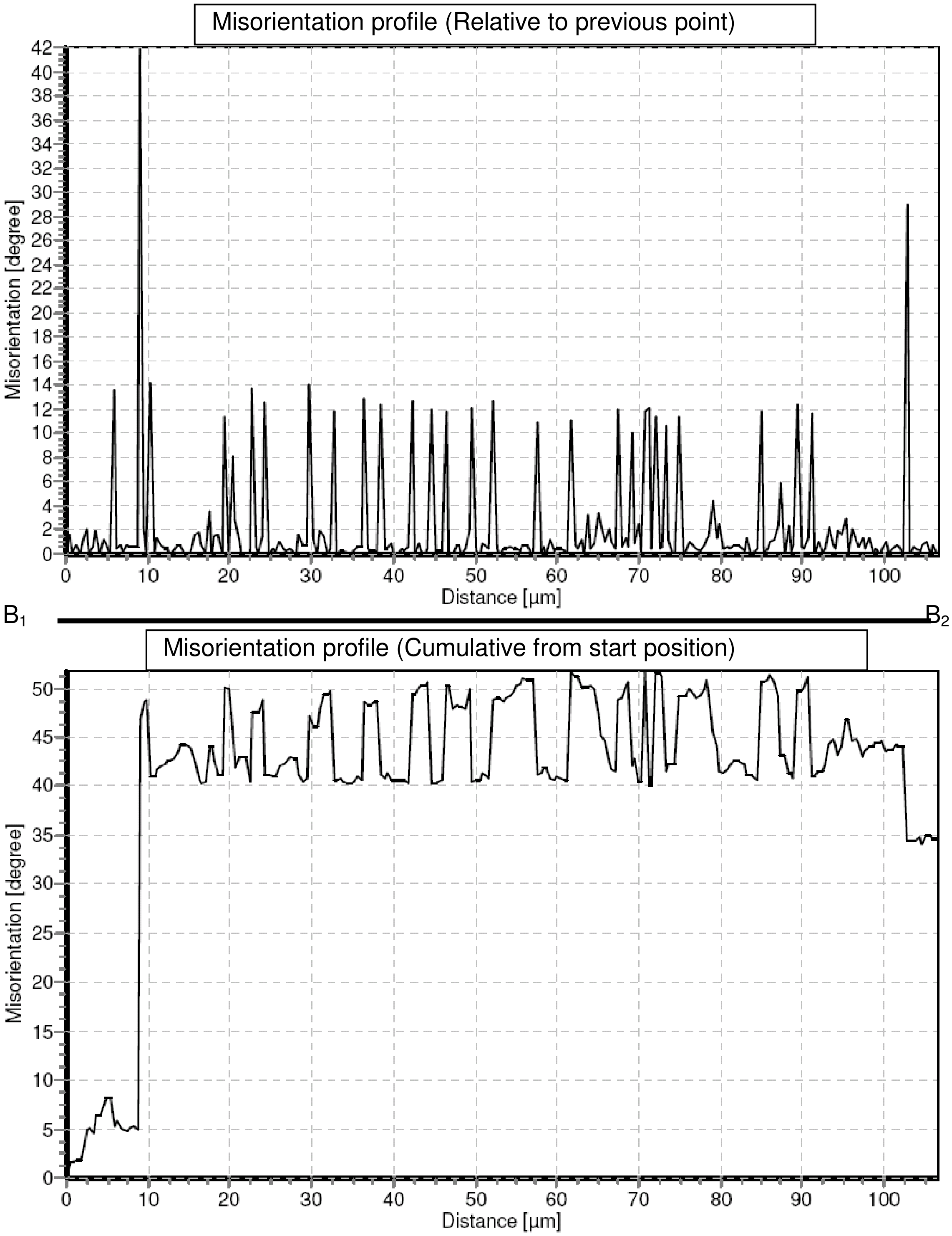

Figure 4.28: *:Misorientation profile of line B_1-B_2 in* ***Figure 4.26****. The first graph shows the misorientation angles relative to the previous point along the B line and the second graph shows the cumulative misorientations from B_1 to B_2.*

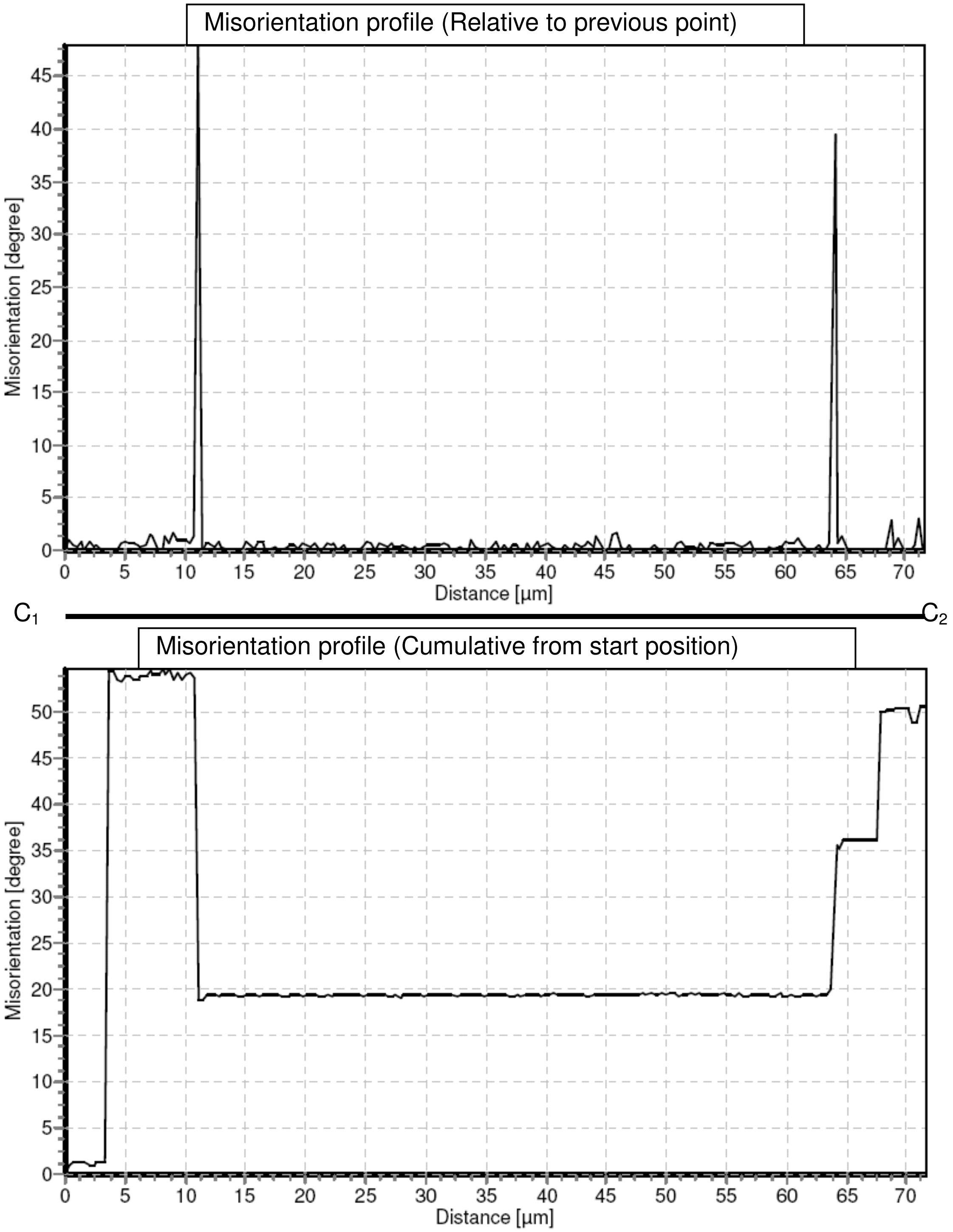

***Figure 4.29:** Misorientation profile of line C_1-C_2 in **Figure 4.26**. The first graph shows the misorientation angles relative to the previous point along the C line and the second graph shows the cumulative misorientations from C_1 to C_2.*

The presence of this substructure indicates that there could be residual strain from deformation that was incurred during the casting process. On closer inspection of the images in **Figure 4.25**, **Figure 4.26**, **Figure 4.30** and **Figure 4.31**, it can be seen that the substructure does not extend to the outer boundary of the grain, but is confined to the centre of the grain and surrounded by what appears to be a misorientation-free coring ring. From this, it can be surmised that this strain or substructure is formed during the induction stirring step of the semi-solid metal processing route. This will be discussed in greater detail in **CHAPTER 6**.

Because the substructure is visible in BSD mode, the indication is that there is a link between the substructure and compositional variations. To investigate this relationship, EDS was performed on a number of grains containing this substructure.

EDS linescans were completed across the grain in **Figure 4.30** and EDS values were plotted across the length of the line. **Figure 4.30** shows a SEM micrograph with a lamellar substructure and linescans of aluminium, magnesium and zinc, performed across the grain. The results show that, apart from the decrease in aluminium and the corresponding increase in the other alloying elements associated with the coring ring, there are no distinct fluctuations of composition that correspond to the changes in contrast that define the lamellar substructure. However, there are slight random fluctuations to be seen in the grain containing substructure, but the same random fluctuations can be seen when the line crosses the neighbouring substructure free grains. Therefore, although the curves do indicate slight fluctuations in the composition, there is no obvious evidence that links these compositional variations to the distinct substructure configuration.

For a more quantitative indication as to a link between the substructure and composition, EDS point analysis was performed at key positions on the grain seen in **Figure 4.30**. **Figure 4.31** shows the same substructure-containing grain of **Figure 4.30**. The positions of the EDS analysis and the resulting composition information can be found in the table below the figure. The substructure can be interpreted as a series of dark and light striations. Analysis point 2 shows the compositional values for a dark striation and point 5 shows the values for a light striation. The results show a negligible compositional variation between these two points within the substructure. Other values on this micrograph are for a dendritic finger, the eutectic and the coring ring, and these values agree with the results of the previous EDS for the AA7075 alloy after SSM casting. Owing to the nature of a substructure of this type, it is impossible to predict the extent of any variations below the surface seen in the micrograph. SEM techniques used thus far do not have this capability. The composition values cannot account for variation across very small distances, as the interaction volume of the analysed point will affect these composition values. Therefore, the substructure may indeed have a compositional variation associated with it, but the true values cannot be determined through EDS in the SEM.

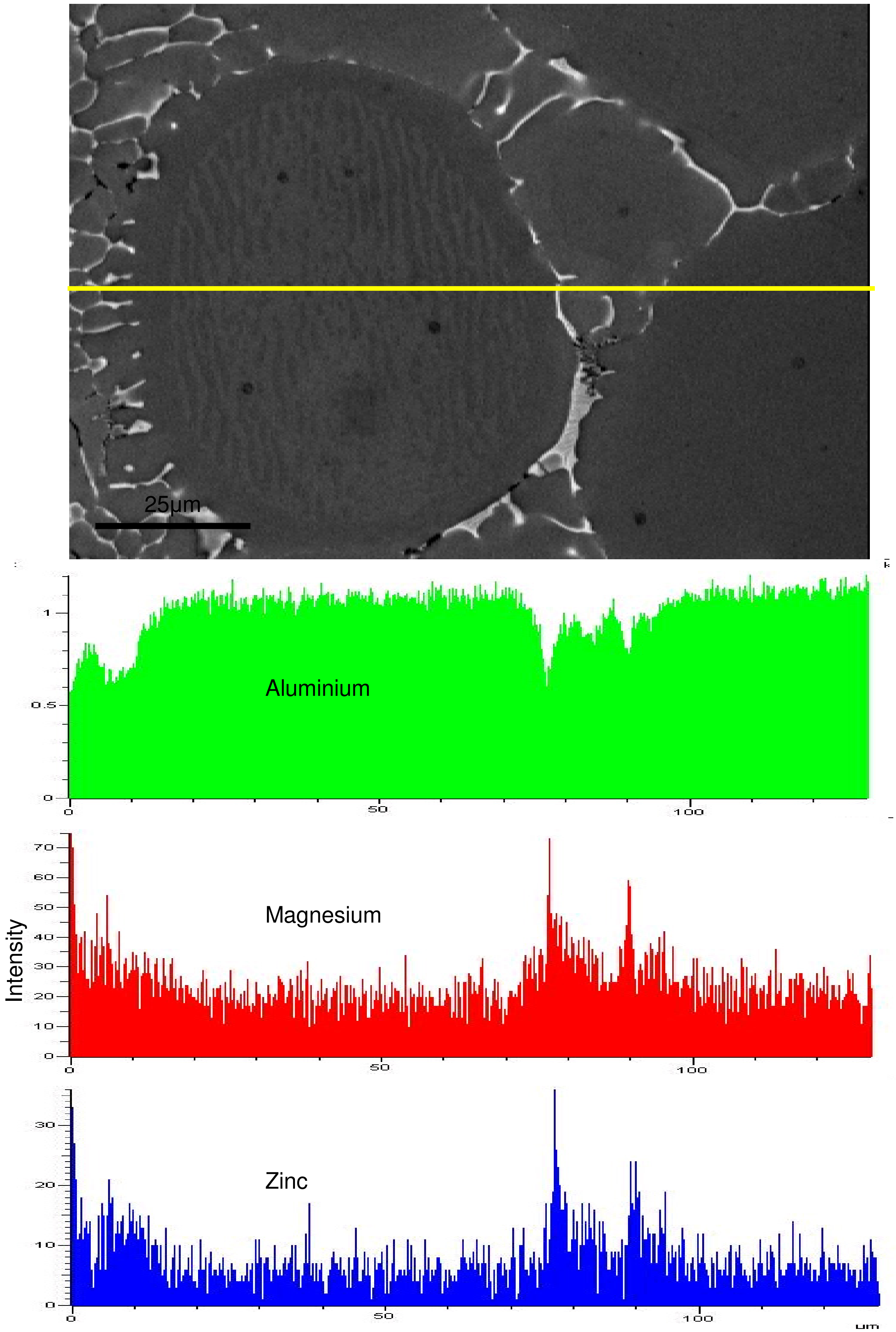

Figure 4.30: *SSM cast AA7075 alloys showing EDS linescans (intensity vs distance) of Al, Mg and Zn content across a grain with the lamellar substructure.*

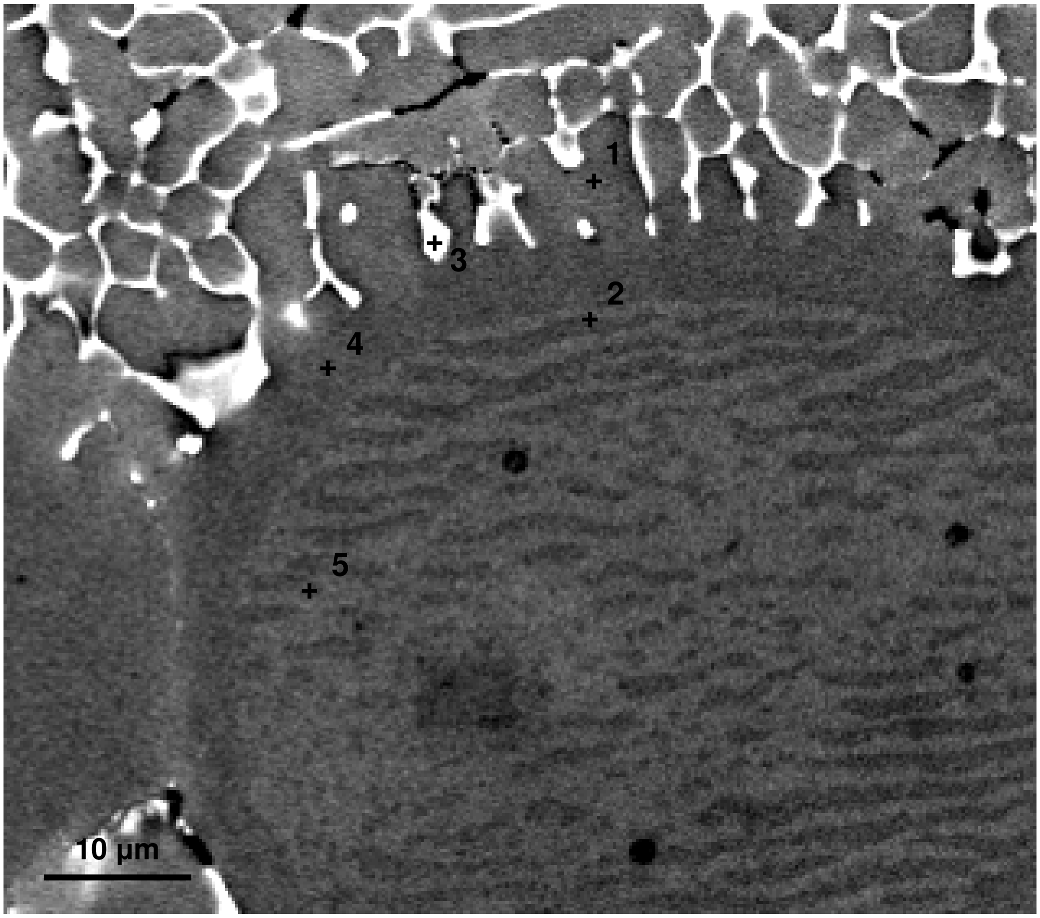

	Al		**Zn**		**Mg**		**Cu**		**Cr**	
Point .	Wt%	At%	Wt%	At%	Wt%	At%	Wt%	At%	Wt%	At%
1	90.7	93.7	6.0	2.6	1.8	2.0	0.8	0.3	---	---
2	93.9	95.6	3.8	1.6	0.9	1.0	0.3	0.1	0.2	0.1
3	50.8	60.5	24.2	11.9	11.7	15.5	10.2	5.2	---	---
4	92.0	94.6	5.0	2.1	1.3	1.5	0.7	0.3	0.2	0.1
5	93.9	95.8	3.5	1.5	0.8	0.9	0.4	0.2	0.4	0.2

***Figure 4.31**: SSM cast AA7075 alloy with compositional evaluation of a grain exhibiting lamellar substructure.*

4.2.4.2. A713 ALLOY

As discussed earlier in **Chapter** Error! Reference source not found., the A713 alloy exhibits a high number of grains with the lamellar substructure configuration. **Figure 4.32** is a higher magnification EBSD map of the map in **Figure 4.24**, focusing on a cluster of five grains, all of which exhibit the lamellar substructure configuration.

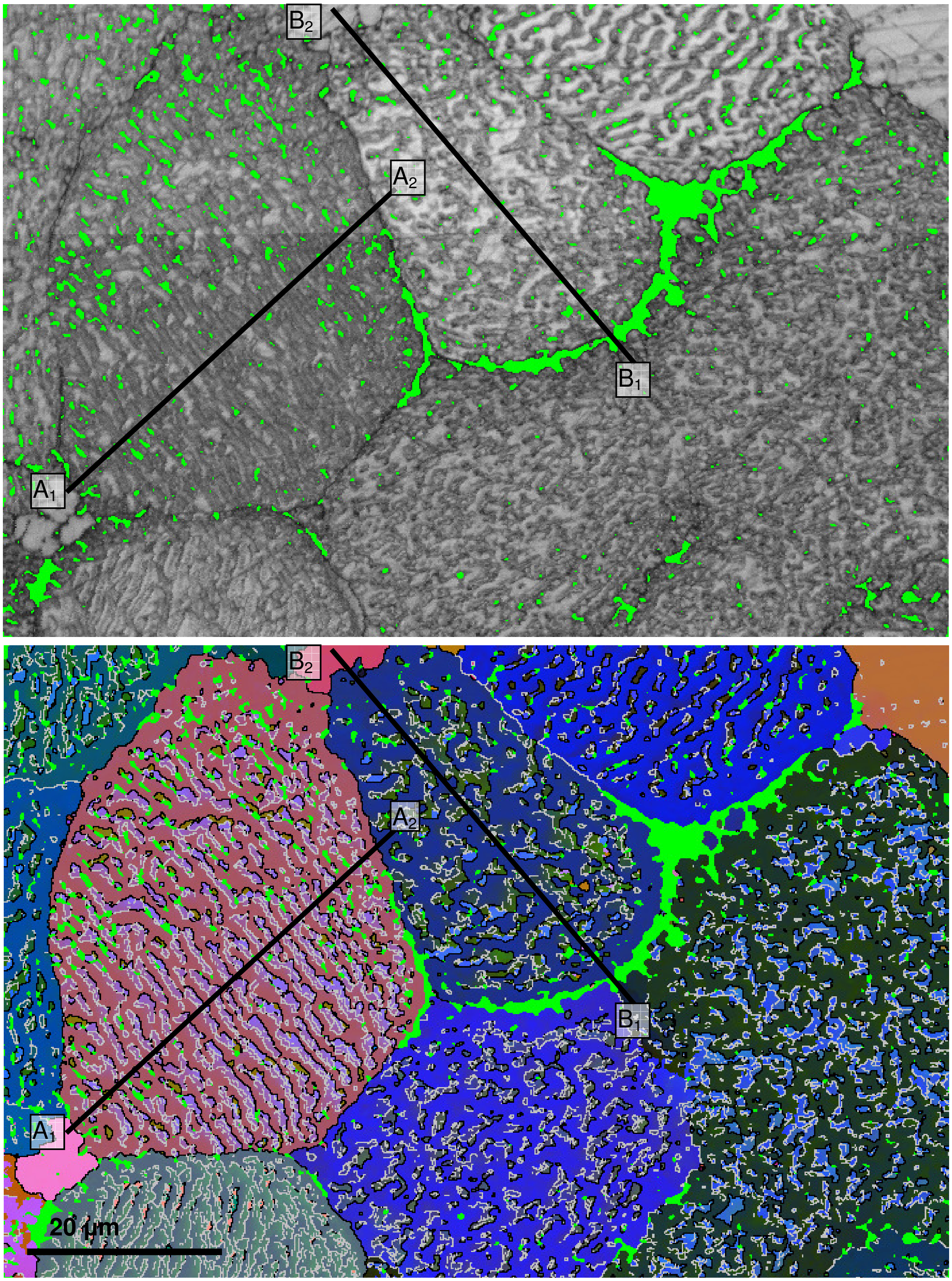

Figure 4.32: *SSM cast A713 alloy showing band contrast and EBSD mapping. Misorientation lines A_1-A_2 and B_1-B_2 are indicated on the map.*

In **Figure 4.32** the HAGBs are shown in black and represent angles greater than 15° of misorientation. The LAGBs are shown in grey and, in this case, represent angles between 5° and 15° of misorientation. The lower limit for the LAGBs was raised from the usual 2° to 5°, owing to the very high number of boundaries falling within that range, which hindered the visual interpretation of the map. The non-indexed points are largely due to porosity that is located between the grains, as well as to the presence of the zinc-rich second phase.

Figure 4.32 shows the line A_1-A_2 crossing a grain with a lamellar substructure configuration. On closer inspection of the Euler colours, the LAGBs and HAGBs and their location and arrangement, it can be seen that, progressing along the misorientation line from A_1 to A_2, the lamellar striations enclose an area of slightly-different Euler colour (in this case, light purple, as opposed to the general pink of the grain as a whole). This enclosed area is bound by a LAGB on the left and a HAGB on the right where the misorientation line crosses the lamellar substructure. When compared to the lamellar structure of the AA7075 alloy in **Figure 4.26** and the misorientation profile in **Figure 4.28**, the AA7075 alloy exhibits only LAGBs below 15° of misorientation, although these boundaries do also surround areas of different Euler colour. In both alloys, the areas of different Euler colour indicate a plateau bounded by an increase in misorientation on the one side and a decrease in misorientation on the other side. Beyond these boundaries, the orientation returns to that of the general parent grain. The misorientation profile of this line can be seen in **Figure 4.33**, and the plateau areas in question can be clearly seen in the cumulative misorientation profile.

The misorientation profiles corresponding to the line B_1-B_2 can be seen in **Figure 4.34**. The general configuration of the substructure here is lamellar, but the configuration is not as geometrical as that of the grain with the A_1-A_2 misorientation line. The ratio of HAGBs to LAGBs is approximately 1:1, and their arrangement is more random, but, as with the grain in **Figure 4.33**, the boundaries also surround areas of different Euler colour and thus crystal orientation.

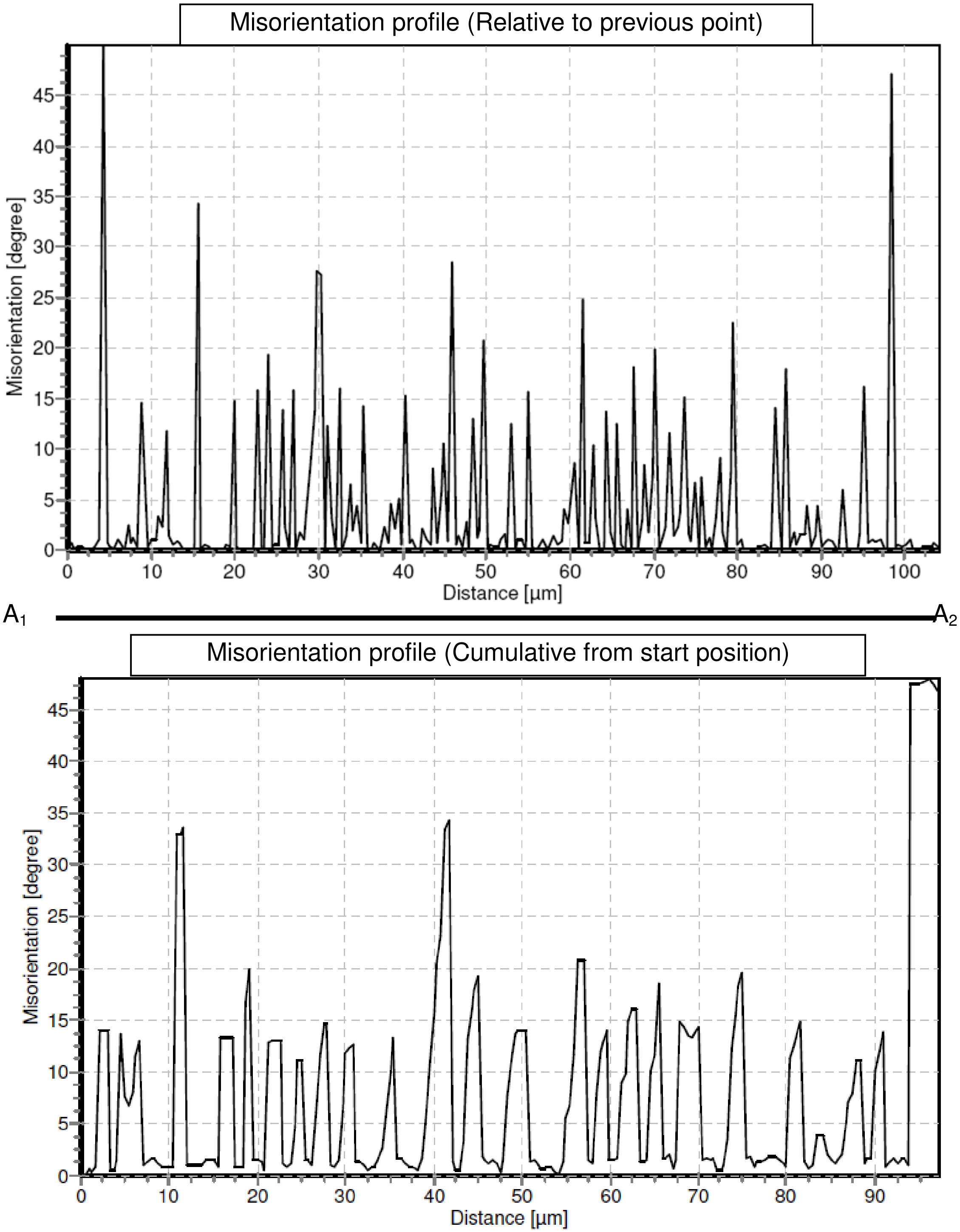

Figure 4.33: *Misorientation profile of line A_1-A_2 in Figure 1.27. The first graph shows the misorientation angles relative to the previous point along the A line and the second graph shows the cumulative misorientations from A_1 to A_2.*

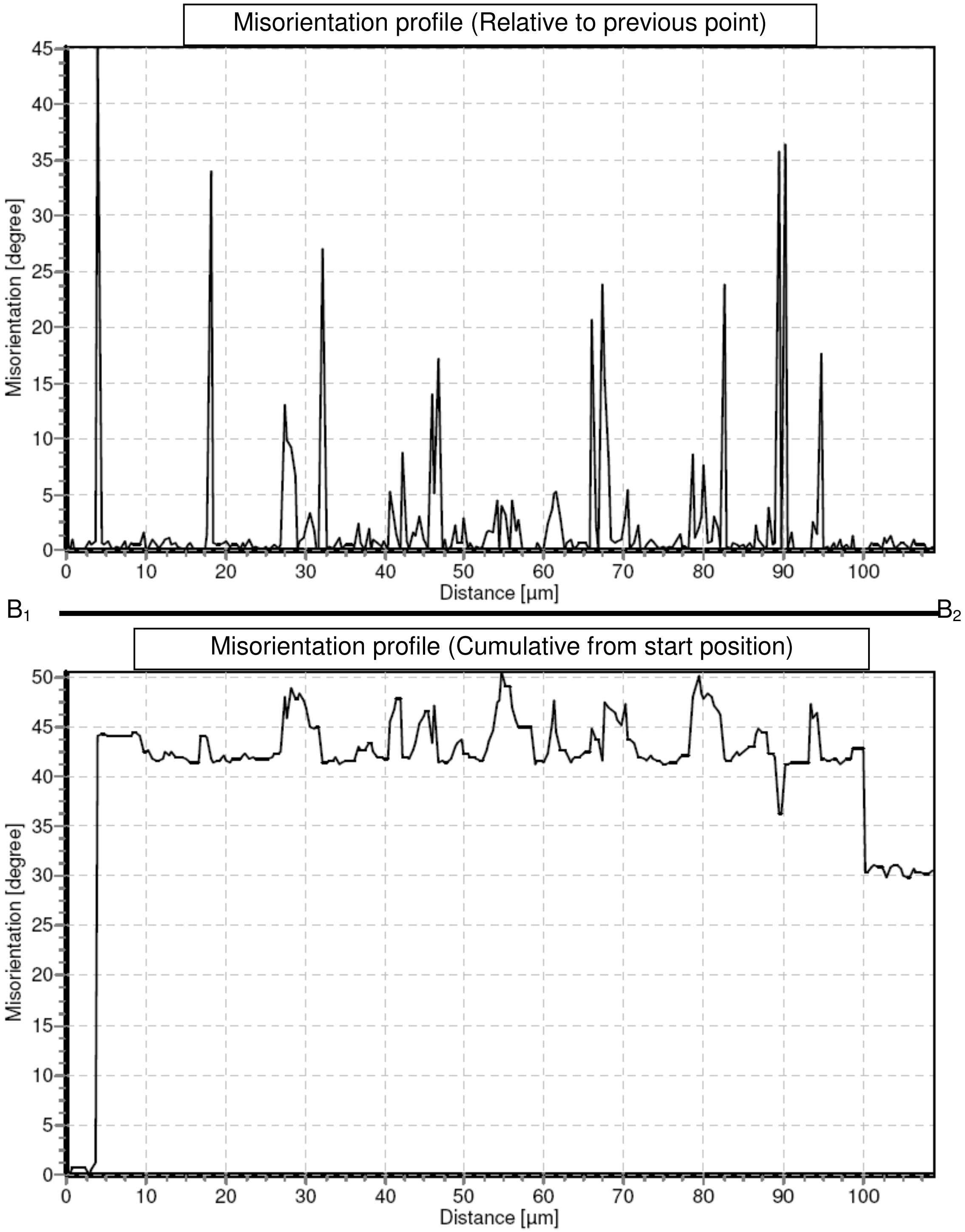

Figure 4.34: *Misorientation profile line B_1-B_2 in Figure 1.27. The first graph shows the misorientation angles relative to the previous point along the A line and the second graph shows the cumulative misorientations from B_1 to B_2.*

4.3. CONVENTIONAL CASTING

One of the primary aims of this investigation was to look into the possibility of using the semi-solid metal casting technique to create a near net-shaped part with properties comparable to a wrought or machined equivalent part, using an Al-Zn age-hardenable alloy. Therefore, it is necessary to evaluate the characteristics of the alloy when a conventional casting technique, such as high pressure die casting, is used. These data can then be compared to those generated with samples of the following: a SSM slug (stirred and quenched from slurry, with no HPDC); a SSM cast sample; and a wrought sample.

4.3.1. AA7075 ALLOY

Figure 4.35 shows the microstructure of a conventionally cast (HPDC) AA7075 alloy. The structure is dendritic in morphology. This is illustrated by the clusters of grains with similar orientations (shown as areas of the same colour in the PLOM image). Characteristic tree-like dendrites can be identified. There is a large amount of porosity, and second phase between the grains can be seen as dark grey areas between the grains in the image. This is as a result of the anodising process on the second phase. Therefore, this viewing technique alone is not sufficient to describe the dendritic structure.

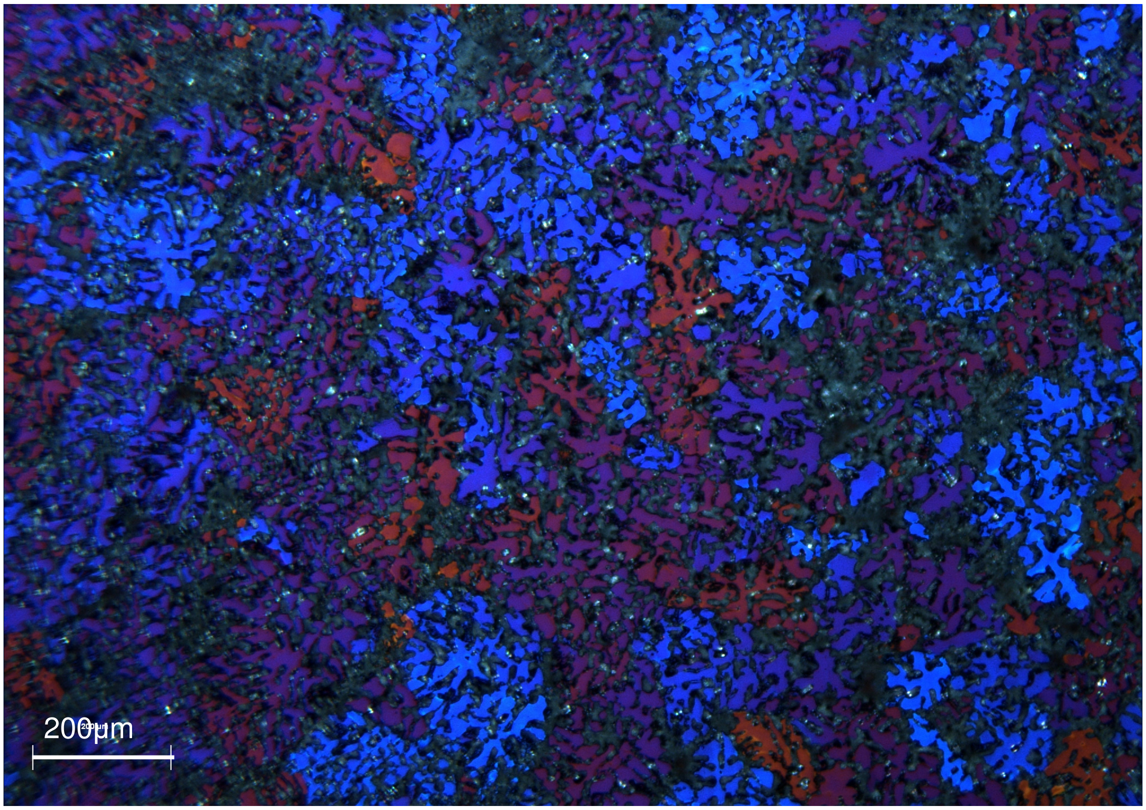

Figure 4.35: *PLOM of conventional HPDC AA7075 alloy, showing dendritic grains.*

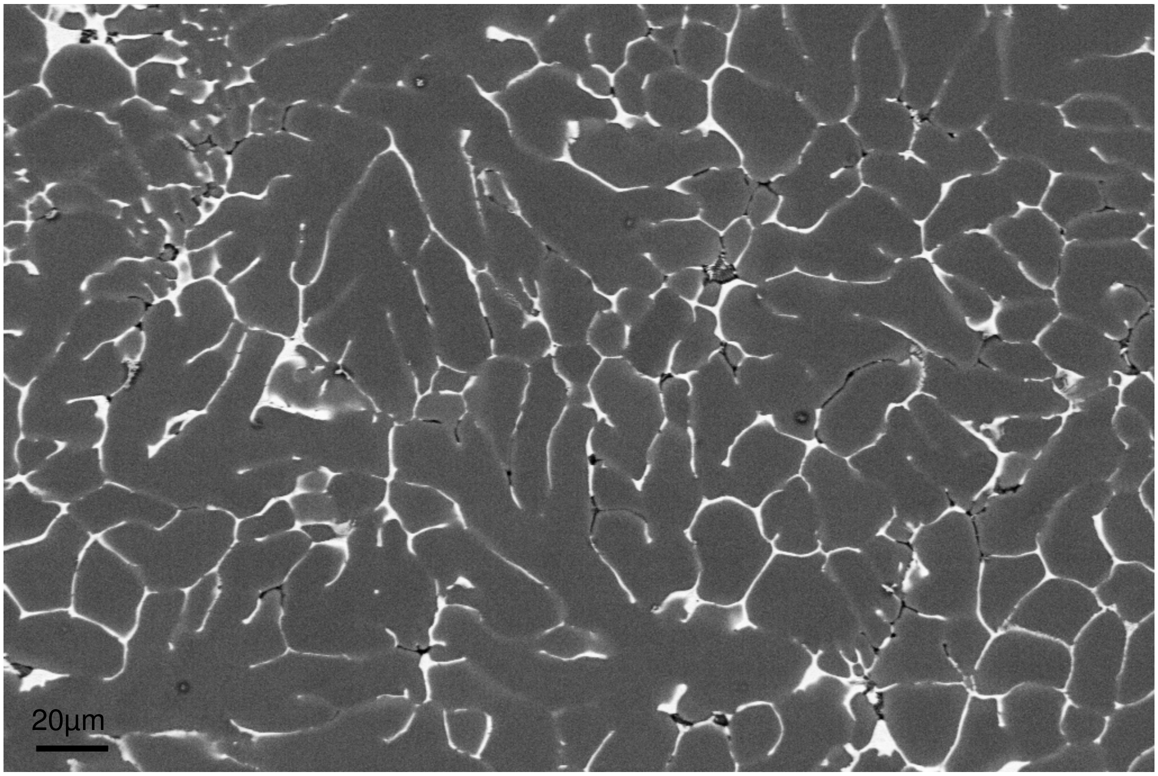

Figure 4.36: *SEM image of conventional HPDC AA7075 alloy. The porosity and second phase can be identified.*

The BSE SEM image in **Figure 4.36** shows the dendritic structure of the AA7075 alloy after conventional HPDC. Contrast between the grains and the eutectic can be seen clearly. The dendrite arm width varies between approximately 10-30 µm.

4.3.2. A713 ALLOY

Figure 4.37 shows a conventionally high pressure die cast A713 concentration sample. The grain structure is dendritic and exhibits none of the globular morphology associated with the semi-solid metal casting process. The second phase and fishbone-structured intermetallics cluster together and there is also second phase evident between the dendrite arms throughout the structure. The dendrite arms are approximately 30-40µm in width and their lengths are much greater than their thickness (giving them a high shape factor).

Composition variations along the length and width of an A713 composition dendrite are shown in **Figure 4.38**, where EDS analysis points are indicated on the image. The corresponding compositional information can be seen in the table below. In the same way as compositional variation was seen in the cellular protrusions of the SSM cast samples, there is evidence here of a decrease in zinc and copper content with a corresponding aluminium increase, progressing from point 1 to point 5 in the figure, as the analysis points move from the dendrite tip into the bulk of the dendrite.

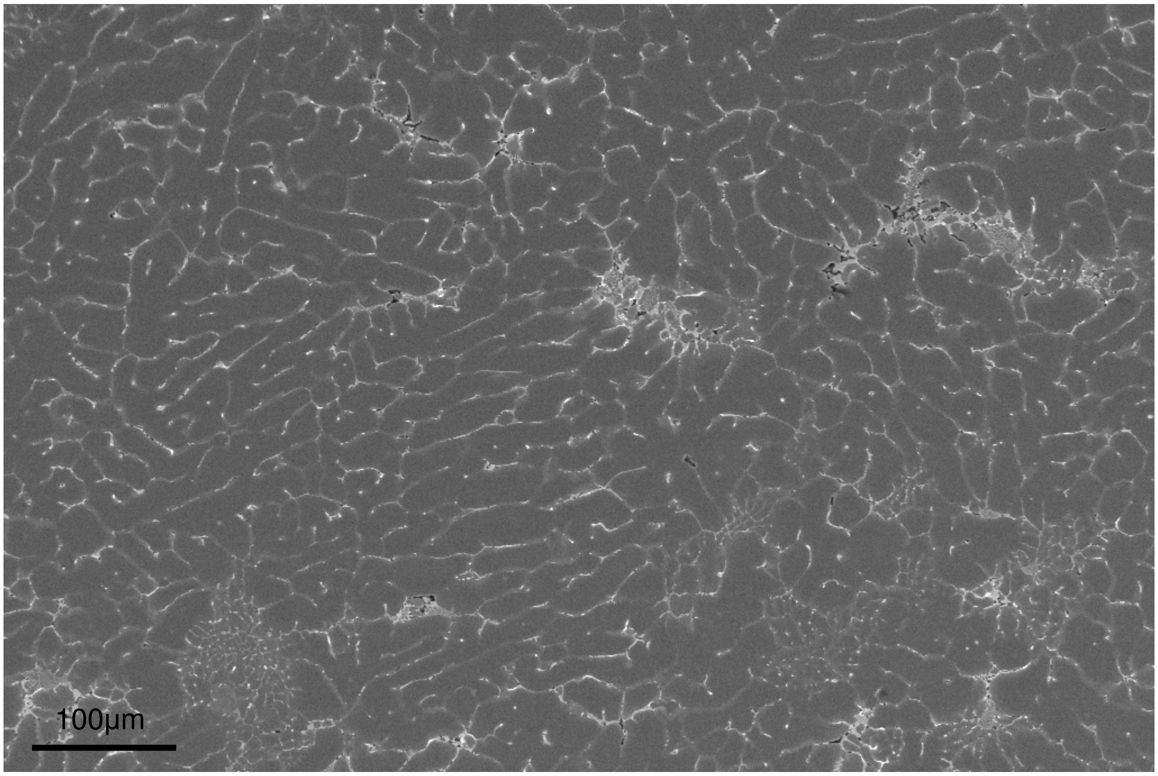

Figure 4.37: *Conventional HPDC A713 alloy, showing the general dendritic grain structure and presence of intermetallics and second phase.*

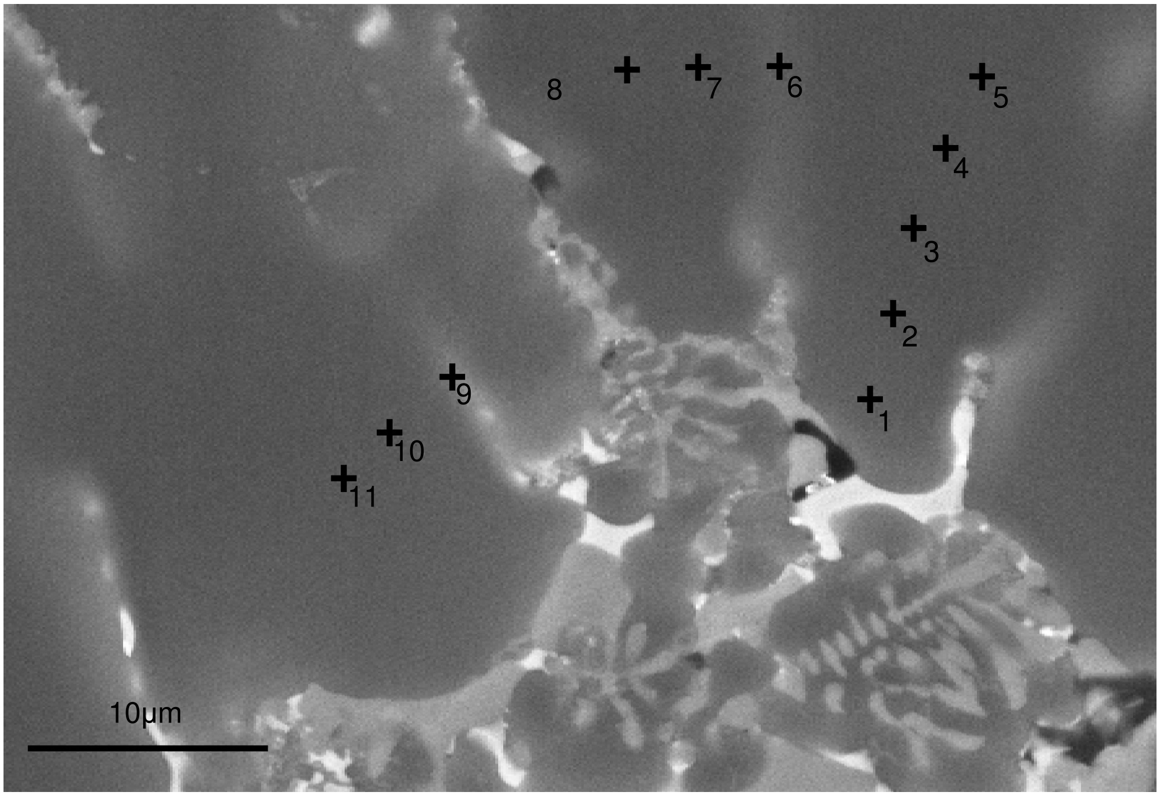

	Al		Zn		Mg		Cu		Fe		Si	
Point	Wt%	At%	Wt%	At%	Wt%	At%	Wt%	At%	Wt%	At%	Wt%	At%
1	82.9	91.7	13.3	6.1	0.5	0.6	3.0	1.4	0.1	0.1	0.1	0.2
2	88.9	94.7	9.1	4.0	0.5	0.6	1.6	0.7	---	---	0.0	0.0
3	91.4	96.0	6.9	3.0	0.3	0.4	1.3	0.6	0.1	0.0	0.0	0.0
4	91.3	95.9	7.2	3.1	0.4	0.5	1.0	0.4	0.1	0.0	0.1	0.1
5	91.7	96.2	7.2	3.1	0.3	0.4	1.0	0.4	---	---	---	---
6	89.7	95.2	8.4	3.7	0.4	0.5	1.5	0.7	0.0	0.0	0.0	0.0
7	89.9	95.3	8.2	3.6	0.3	0.4	1.4	0.7	0.0	0.0	0.1	0.1
8	90.9	95.7	7.2	3.1	0.6	0.6	1.3	0.6	0.1	0.1	---	---
9	85.3	92.8	11.4	5.1	0.6	0.8	2.6	1.2	---	0.0	0.1	0.1
10	89.5	94.9	8.4	3.7	0.5	0.6	1.4	0.7	0.0	0.0	0.2	0.2
11	86.3	93.4	10.7	4.8	0.5	0.6	2.2	1.0	0.2	0.1	0.1	0.1

Figure 4.38: *Conventional HPDC A713 alloy with EDS analysis points and compositional results.*

4.4. SEMI-SOLID METAL SLURRY SLUG

The semi-solid slugs were evaluated because the microstructure and segregation that existed at the end of the slurry production stage were the basis of the microstructure of the final cast part. Evaluation of these structures was also used to aid in the identification of the globularisation (spheroidisation) mechanisms upon which this process is based. Evidence of the mode of globularisation would be imprinted on the solid that was formed during that step, and the mechanism could be linked to this evidence. The SS slug samples were prepared by quenching after the stirring step that was used in the SSM rheocasting process.

4.4.1. AA7075 ALLOY

Figure 4.39 shows the general microstructure of AA7075 after the slurry production step of the semi-solid casting process. The structure is made up of clusters of globules, which are similar in size and morphology, with a grain size ranging from 50-100μm in diameter. These clusters are surrounded by areas of interglobular region, which appear dendritic in their arrangement.

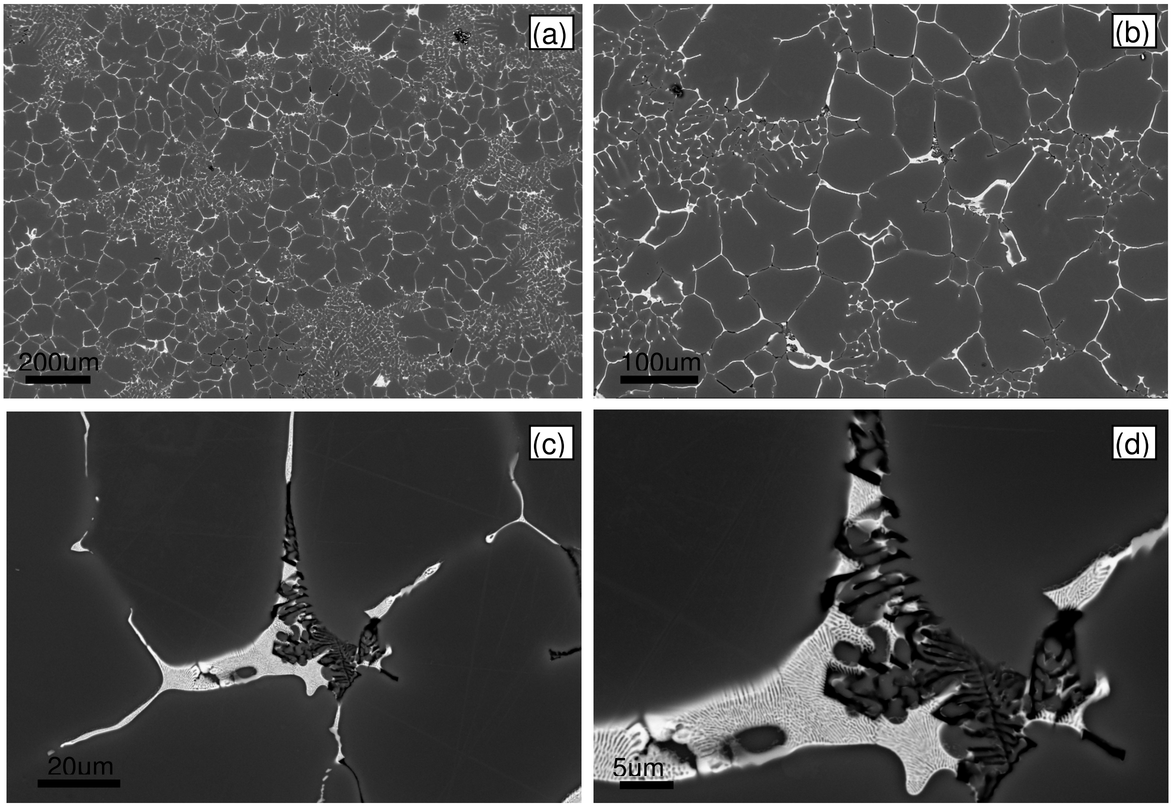

Figure 4.39: *AA7075 alloy semi-solid slurry sample at increasing magnification (shown in BS mode). (a) general microstructure, (b) globular grain morphology, (c) interglobular eutectic region, and (d) porosity and lamellar eutectic.*

The globular grains nucleated and grew during the slurry production step and their globular morphology could be attributed to the stirring during this step. When the sample was quenched, the fine interglobular grains would have solidified, with little time for growth and diffusion, resulting in a fine grain size and a high degree of segregation, owing to the lack of time for solidification of the solute-rich liquid within the slurry (as seen in the DSC results in **Figure 5.7**).

4.4.2. A713 ALLOY

Figure 4.40 (a) and (b) show that the A713 alloy has the same general microstructure in the SS slug state, comprising clusters of globular grains within a large area of much smaller dendritic type grains in the interglobular region. The typical globule diameter size within the clusters also ranges from 50-100μm. **Figure 4.40** (c) and (d) focus on the interglobular area and the eutectic, in which we see the typical eutectic that has previously been shown for this alloy (**Chapter 4.2.1**). The cellular protrusions can be seen in the interglobular region, with segregation highlighted by the variation in contrast in the BS image.

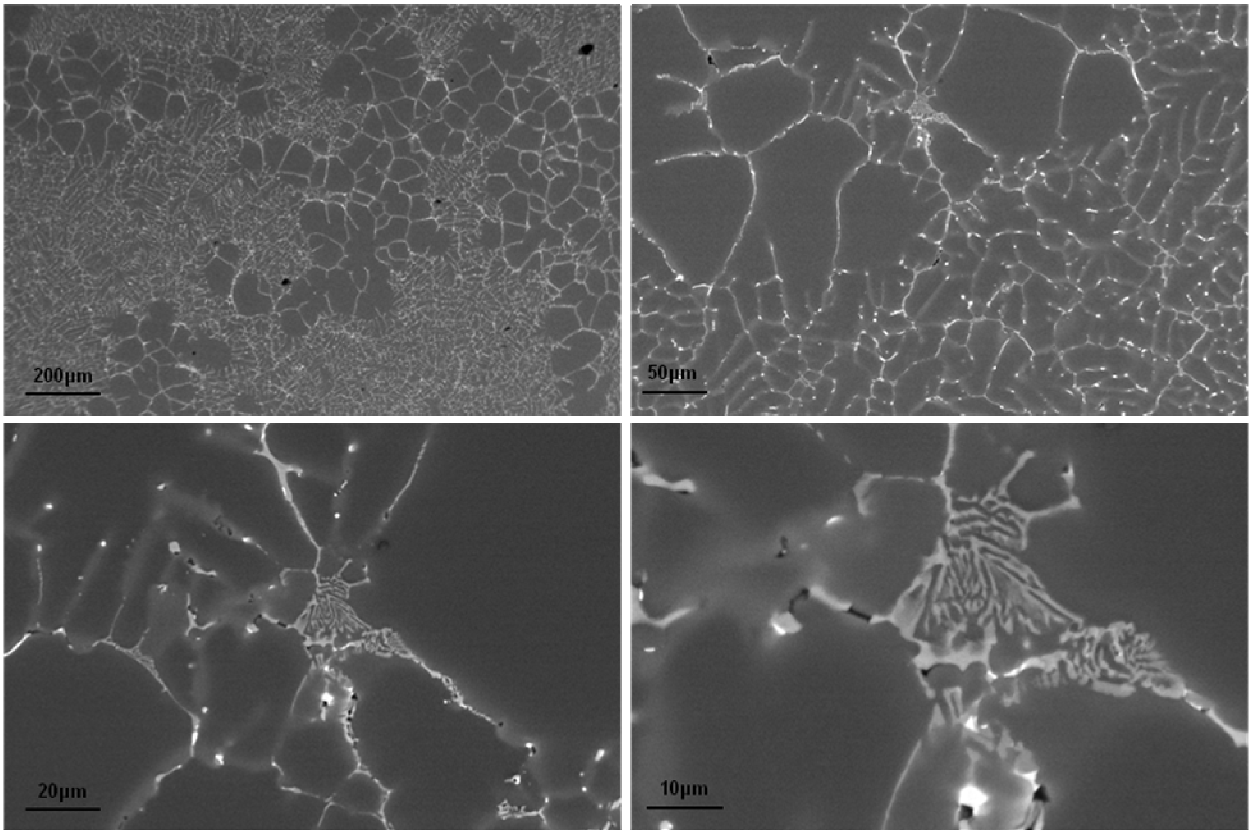

Figure 4.40: *A713 alloy semi-solid slurry sample at increasing magnification (shown in BS mode). (a) general microstructure, (b) globular grain and interglobular morphology, (c) interglobular region and (d) non- lamellar eutectic and intermetallics.*

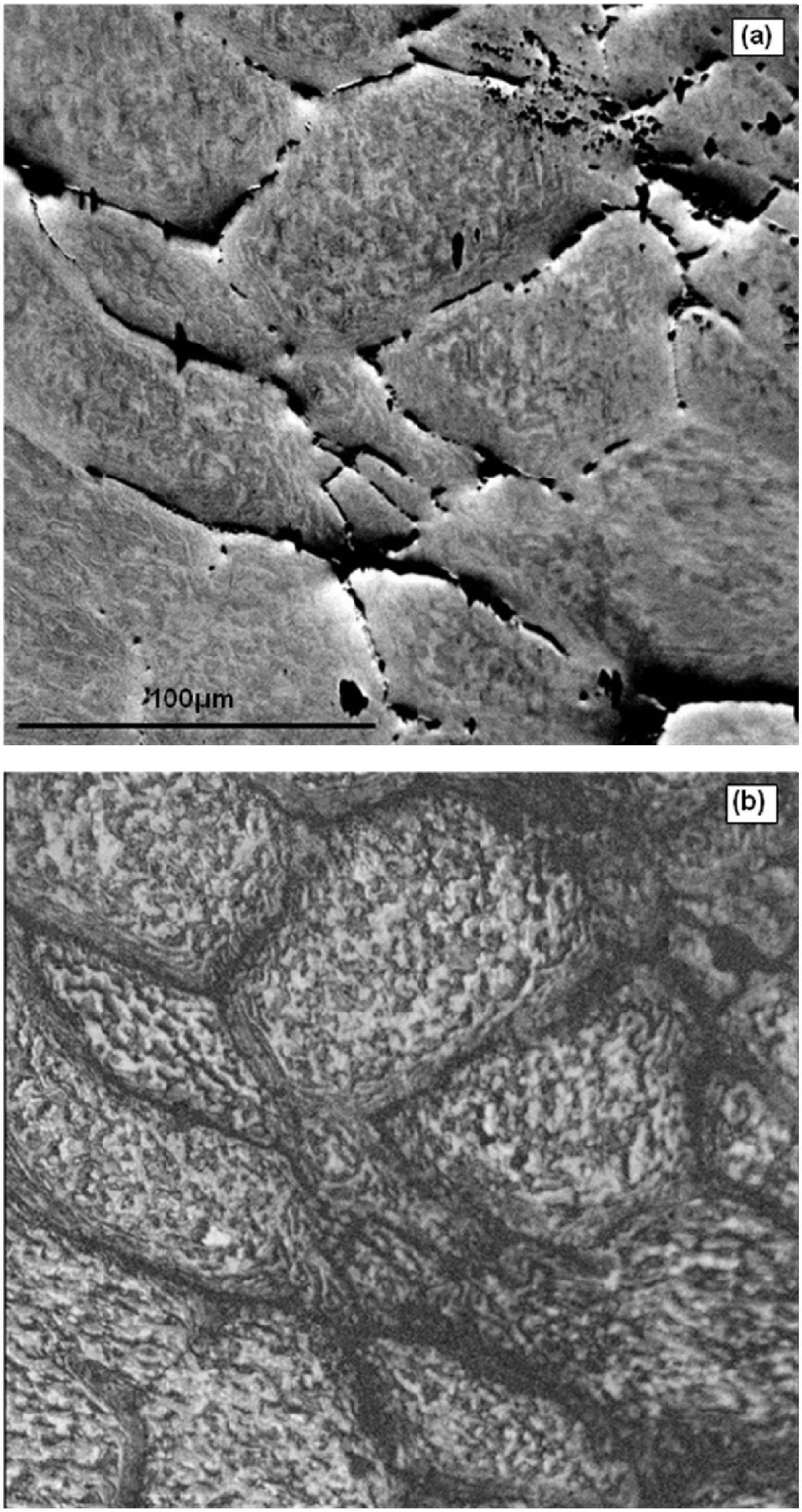

Figure 4.41: *A713 alloy SS slug sample (a) in SE SEM image, and (b) in EBSD band contrast image.*

Figure 4.41 (a) shows a secondary electron image of a cluster of globules within the SS slug microstructure. The image was taken in conjunction with the EBSD band contrast quality map in (b) of the same figure. Owing to the 70° tilt of a sample in the SEM for EBSD analysis, the topography in the image in (a) is exaggerated by shadow. The grains exhibit the typical lamellar substructure configuration that was observed in, and discussed with regard to the SSM cast microstructure for both AA7075 and A713 alloys. The band contrast image in **Figure 4.41** (b) is essentially a pattern quality image, where the light areas represent high pattern quality, which is associated with areas where there is no misorientation or overlap of patterns because of the presence of strain or dislocations, and the darker areas are associated with slightly worse pattern quality where there is pattern overlap and misorientations. This is in agreement with the pattern quality maps shown in **Figure 4.22** to **Figure 4.24**, **Figure 4.26** and **Figure 4.32**, where the dark areas of lower pattern quality coincide with the positions of LAGBs and HAGBs.

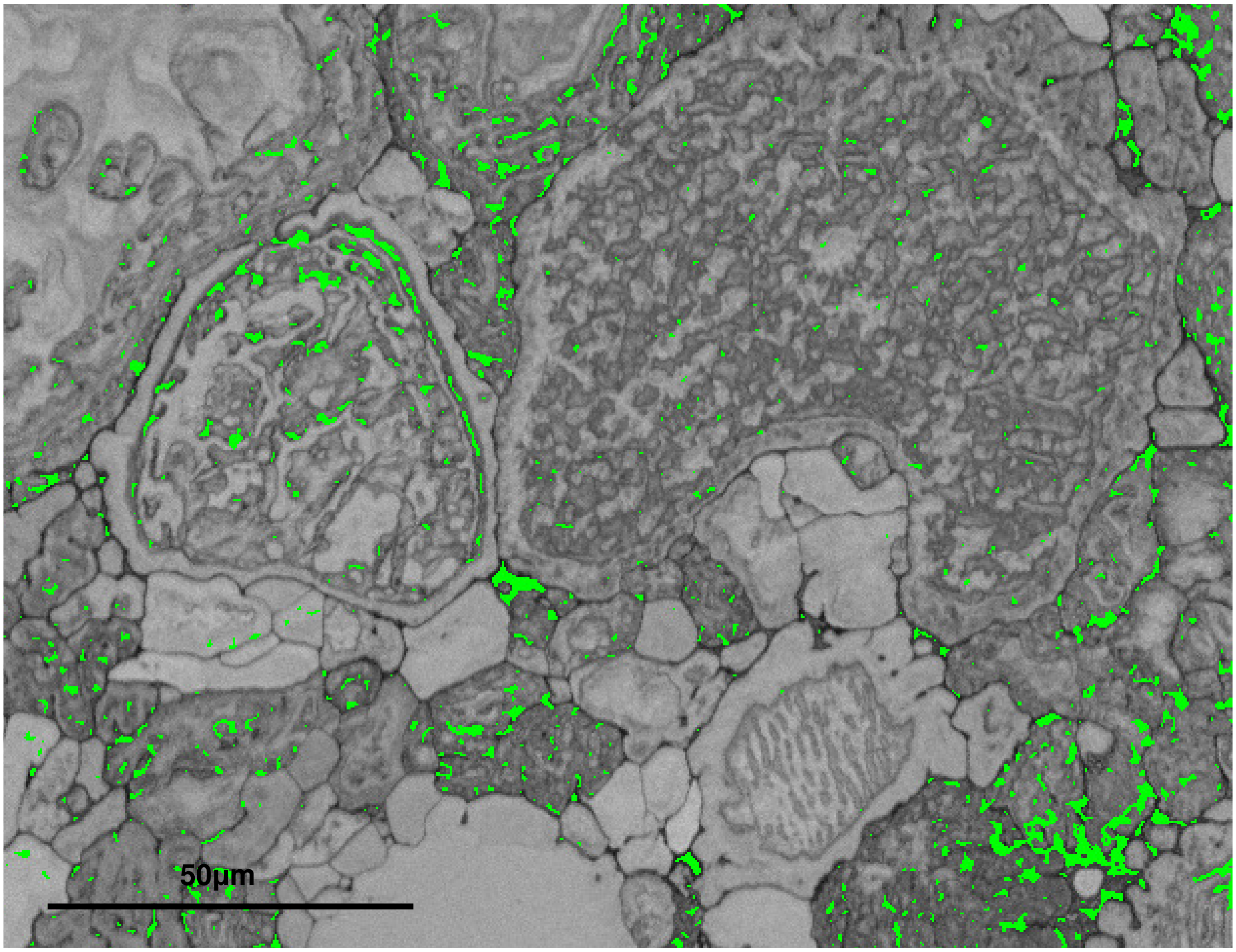

Figure 4.42: *A band contrast image of a SSM cast sample exhibiting coring rings surrounding the substructure within the globular grains*

When the configuration on this SS slug substructure is compared to that observed in a SSM cast microstructure (such as those seen in **Figure 4.26** and **Figure 4.32**) a difference in the location of the edge of the substructure is discernable: The substructure in the SS slug extends to the very edge of the globular grains; in the SSM microstructure, the substructure extends only to the start of the coring ring, which is approximately 5-15μm from the edge of the grain. Examples of these coring rings are illustrated in **Figure 4.42**.

4.5. SUMMARY OF OUTCOMES OF CHAPTER 4

The pertinent outcomes of the characterisation of the as-cast microstructure are:

- Macro-segregation is present in the as-cast plates, in the form of the grain morphology, size and distribution, both along the length of the plate and through the thickness

- SEM and EDS results showed the morphological features of the primary globular grains and the surrounding interglobular regions. The features that were highlighted were: the coring rings, the cellular protrusions and the eutectic and second phases present in the as cast condition.

- Characterisation using EDS showed the detailed analysis of the composition distribution within the primary globular grains, extending into the cellular protrusions and the second phase regions between the grains.

- EBSD orientation analysis revealed the presence of an internal misorientation substructure. Two misorientation configurations were evident: a lamellar configuration, made up of predominantly LAGBs, and a circular configuration, made up of a combination of HAGBs and LAGBs.

- Microscopy shows that the internal misorientations do not extend into the coring rings of the globular grains, indicating that they were formed during slurry production.

- The misorientations are arranged in a regular way relative to one another, showing a subsequent decrease in misorientation after every increase in misorientation.

CHAPTER 5: RESULTS AND DISCUSSION

POST-SOLIDIFICATION HEAT TREATMENT

Owing to the extremely large degree of segregation associated with the semi-solid metal cast microstructure in the as-cast condition, and to the amount of porosity that is an inherent casting defect, the effect of heat treatments is complex and needs extensive investigation. The investigation was carried out on samples from both the AA7075 alloy and the A713 alloy. The results generated were then compared to those from conventional liquid cast samples and slurry samples.

This investigation into how the microstructure changes when heat is introduced can form the basis on which homogenisation and solution treatment practices are designed, in order to maximise the strengths attained after ageing treatments.

5.1. THERMAL ANALYSIS USING DSC

Basic thermal analysis was performed using differential scanning calorimetry (DSC). This technique and the sample preparations needed were discussed in **Chapter 3**.

5.1.1. GENERAL THERMAL ANALYSIS OF AA7075 AND A713

An aim of this investigation was to realise a final SSM product whose properties were comparable to the wrought equivalent. The first step was to look at the differences between a SSM as-cast AA7075 composition sample, and a sample of wrought AA7075.

Figure 5.1 shows a DSC curve that compares a SSM cast AA7075 alloy sample to a wrought AA7075 sample. The curve for the wrought AA7075 shows only one endothermic melting peak, which represents the melting of the bulk. The SSM cast curve exhibits an extra, smaller peak at ~473℃. This is an incipient or early onset, melting peak, which is associated with the melting of the segregated phase. Therefore, the first peak is a measure of the degree of segregation of a particular sample and state.

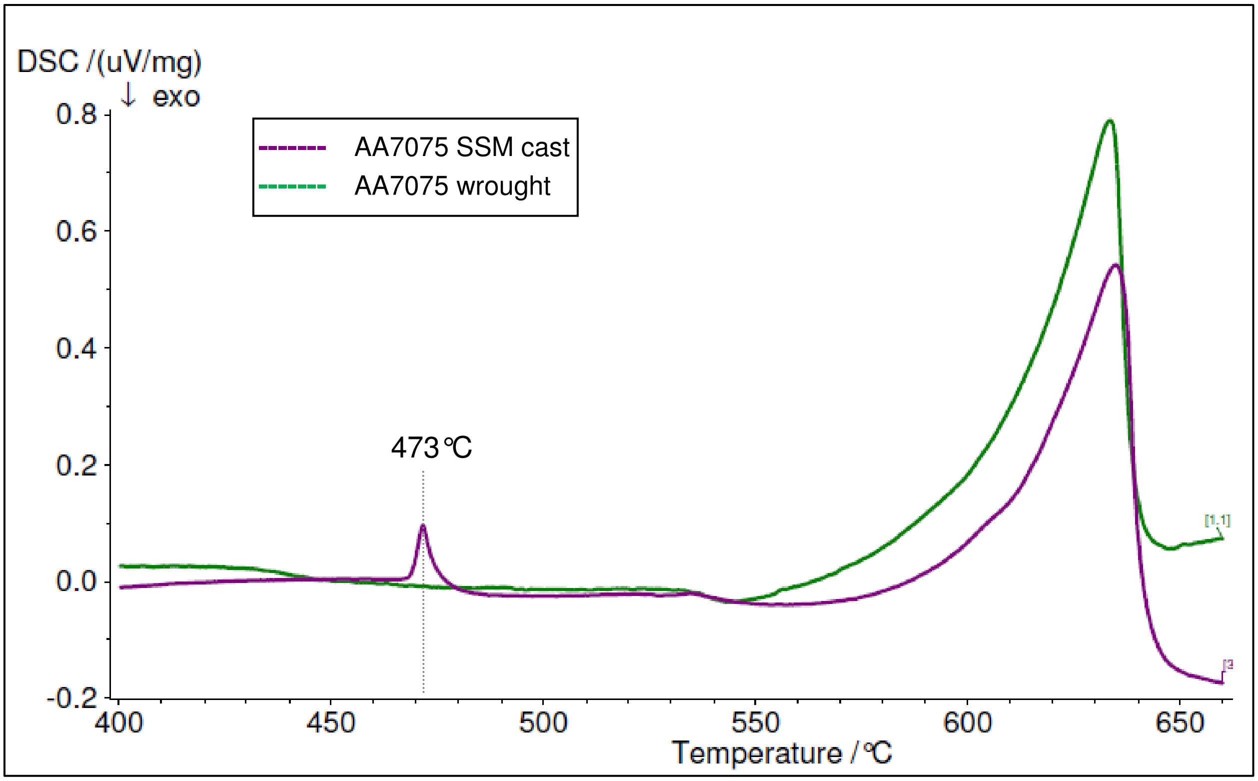

Figure 5.1: *DSC trace of a wrought AA7075 and SSM cast AA7075 alloy.*

The incipient melting peak is the result of the heterogeneity and elemental segregation that is seen in cast structures and also in this type of semi-solid metal cast structure. The main problem associated with the occurrence of this type of incipient melting peak is that it falls within the solution treatment temperature (480-500℃) range and would, therefore, have a strong effect on how the microstructure developed during any homogenisation or solution treatment procedures.

Figure 5.2 shows a comparison between the DSC traces for a SSM cast AA7075 alloy, in the as-cast condition (shown by the dotted line), and for a homogenised sample (shown by the solid line) that had undergone a 15-hour homogenisation treatment, prior to thermal analysis. The most noticeable difference is the presence of the first melting peak within the range of 470-480℃ in the as-cast sample, while, in the homogenised sample, the peak has been removed and a further instability is noticeable in the 520℃ range. An investigation into the length of time required for homogenisation at 460℃ was completed. Holding times of 5, 10 and 15 hours were used. After both 5 and 10 hours, there were still small incipient melting peaks below 500℃. While after 15 hours, as shown in **Figure 5.2**, the melting peak at approximately 470℃ was no longer evident. This indicated a homogenisation of the segregation associated with the SSM casting process. For this reason, 15 hours at 460℃ was selected for the homogenisation practices prior to ageing.

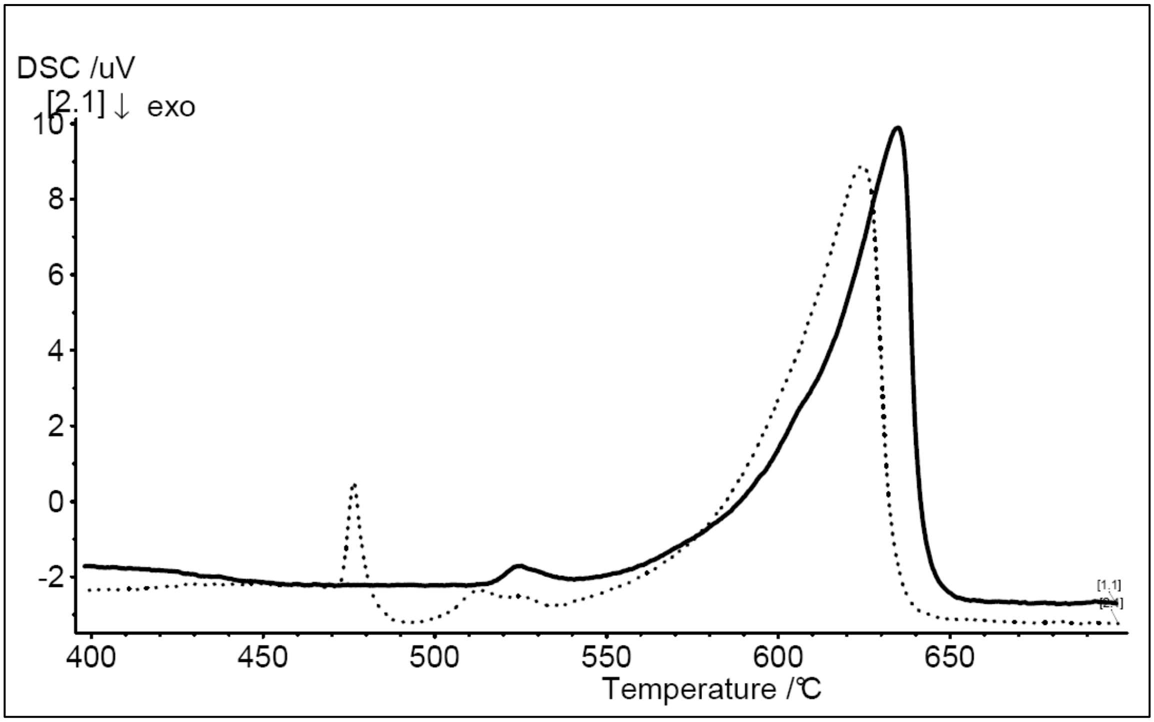

***Figure 5.2**: DSC trace for SSM as-cast AA7075 alloy (shown in the dotted line) and for AA7075 after homogenisation at 450 C for 15hours.*

AA7075 is a very complex quaternary alloy that achieves high strengths when it undergoes thermo-mechanical processing, followed by precipitation hardening heat treatments. The compositional complexities that allow for these high strengths also add to the high degree of segregation when material of this composition is cast. For this reason, an alloy based on the composition of A713 alloy was selected. A713 had been successfully used in casting operations in the past (known as Tenzaloy). This alloy is generally strengthened only through natural ageing, which takes place, after casting, over a number of days at room temperature.

The DSC curves in **Figure 5.3** show a comparison between SSM cast samples of AA7075 composition and A713 alloys. The AA7075 alloy has a much larger incipient melting peak, indicating a higher degree of segregation in the state. A closer look at the first peaks can be seen in **Figure 5.4**. The onset point for melting of the A713 composition is lower than that of the AA7075 composition, with values of 461℃ and 469℃ respectively. The areas of the peaks also vary considerably, with the area of the AA7075 sample being approximately three times greater than that of the A713 alloy.

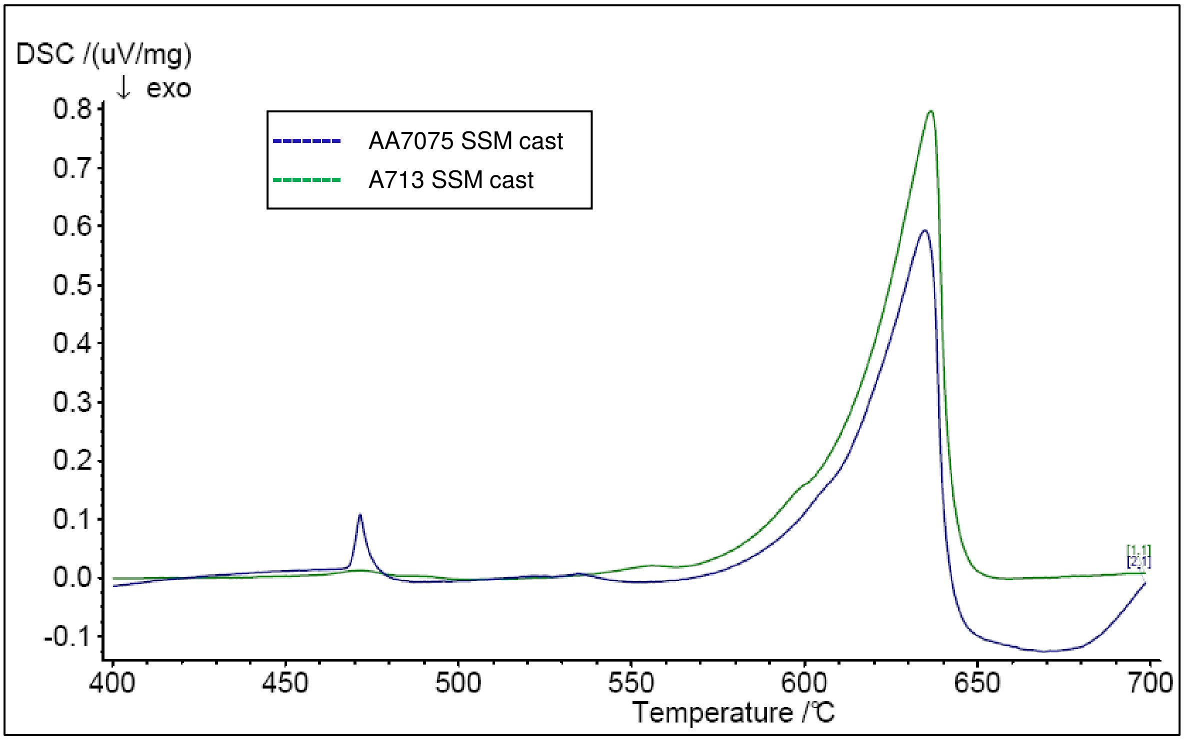

Figure 5.3: *DSC trace for SSM cast AA7075 and A713 alloys.*

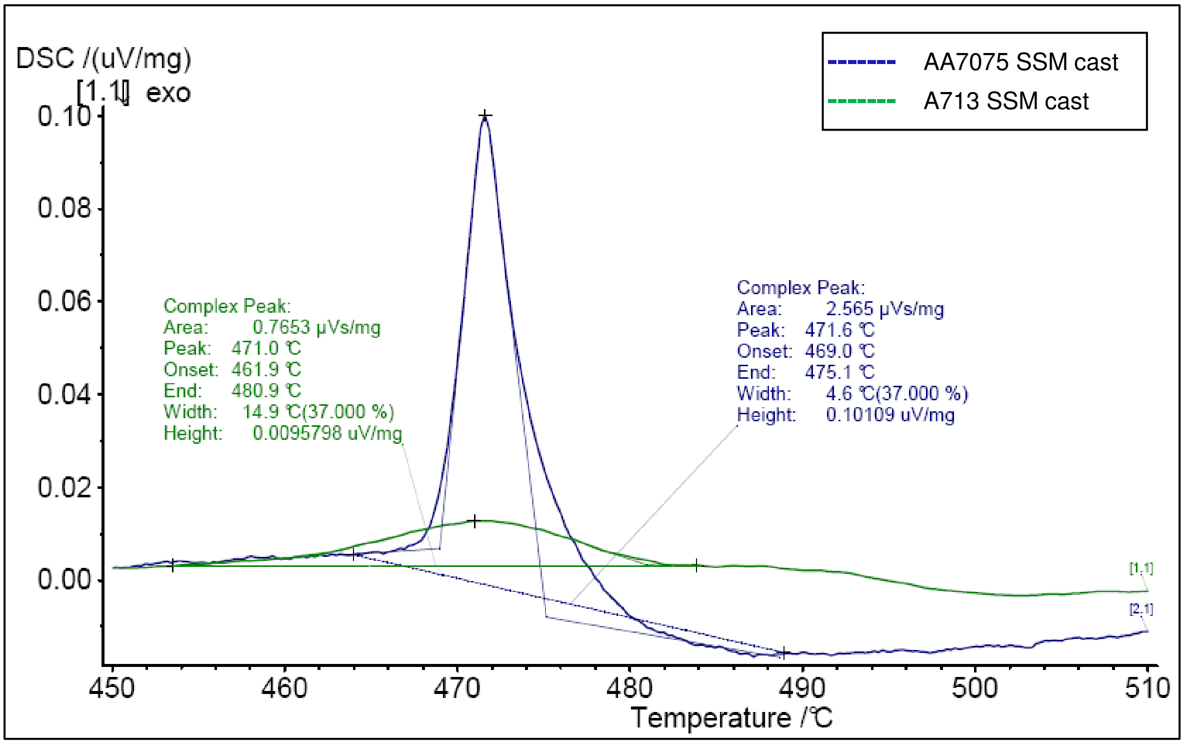

Figure 5.4: *First peak of DSC trace for SSM cast AA7075 and A713 alloys.*

The A713 alloy was mixed and ingot-cast locally. A thermal analysis DSC trace was performed on a sample taken from a cast ingot of the A713 alloy and another sample that was homogenised at 450℃ for 15 hours prior to thermal analysis. The thermal analysis traces were then compared to that of a SSM as-cast A713 sample. These results can be seen in **Figure 5.5**.

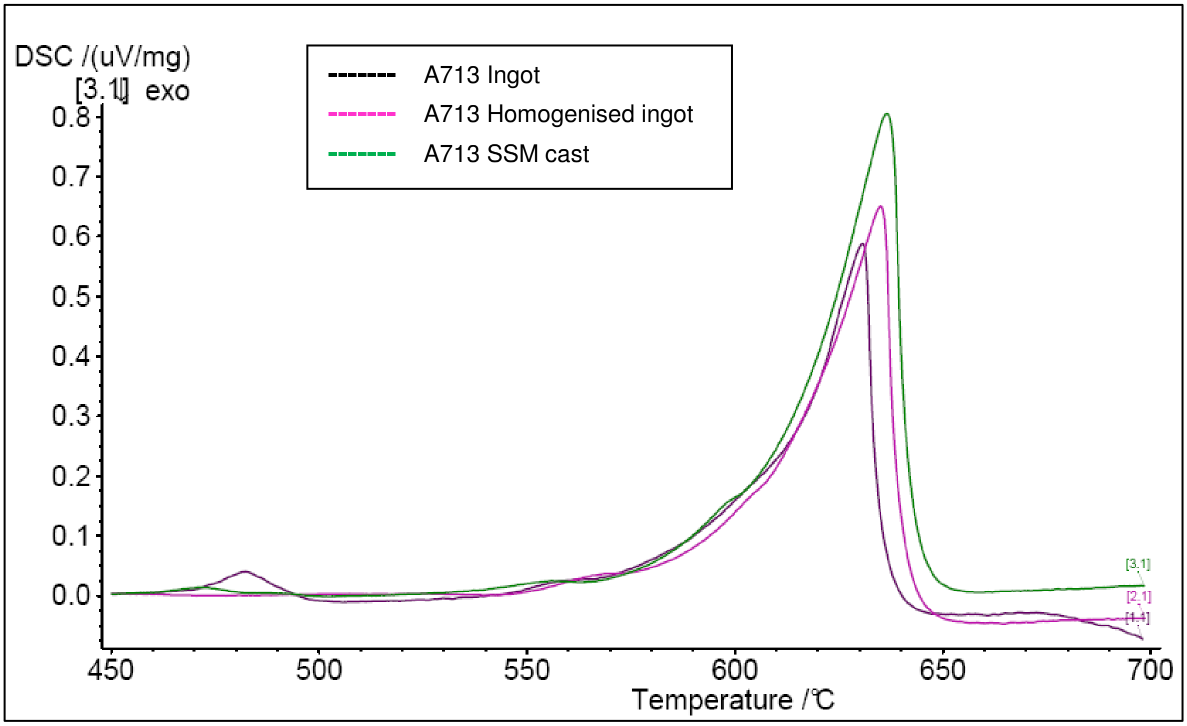

Figure 5.5: *DSC trace for A713 alloy ingot, homogenized ingot and SSM as-cast samples.*

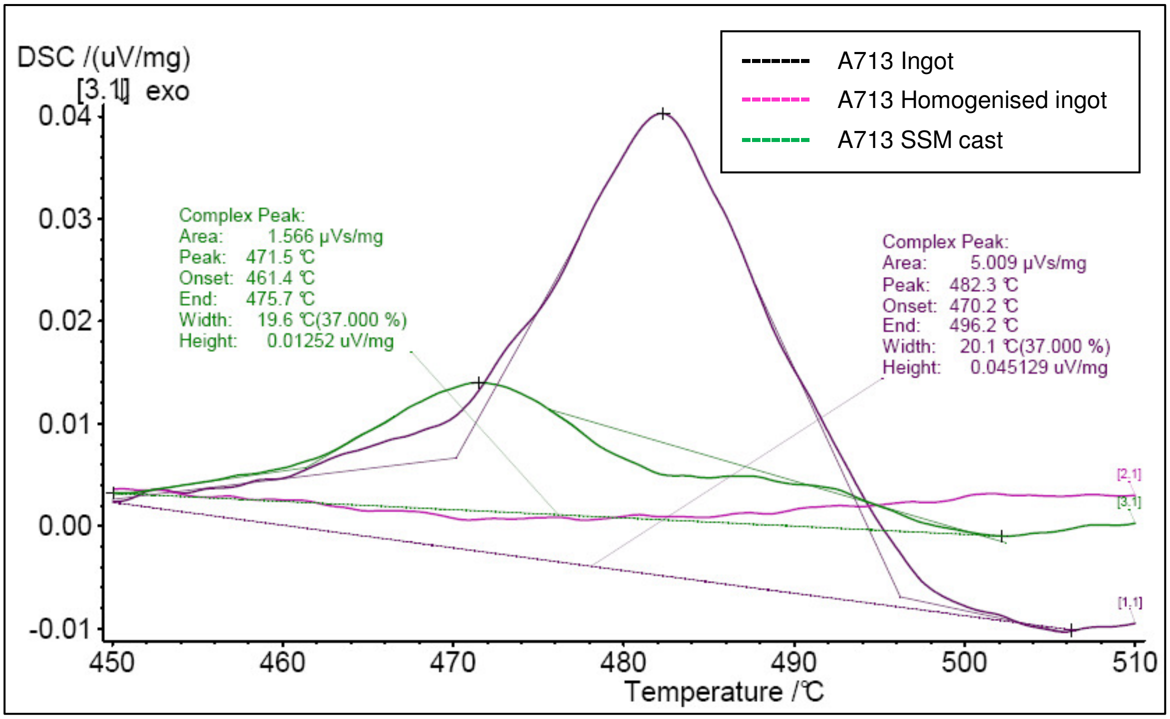

Figure 5.6: *First peak in DSC trace for A713 alloy ingot, homogenized ingot and SSM as-cast samples.*

Figure 5.5 shows a general DSC trace curve for A713 ingot, homogenized ingot and SSM cast samples. The location of the large melting peak is very similar for each of them. The area of interest is within the incipient melting range of 450-510℃. In this figure it can be seen that there is a marked difference in 1st peak size between the three states. **Figure 5.6** shows a closer look at the 450-510℃ temperature range of the trace seen in **Figure 5.5**.

Figure 5.6 shows the 1st peak of the DSC traces with the complex peak data indicating, among other data, the onset temperature of melting, the temperature at the peak and the area of the peak. The curve of the homogenized ingot sample (shown in pink) has no peak within the incipient melting temperature range, while the as-cast ingot (shown in purple) has a large peak within that region, indicating a large degree of segregation, resulting from the solidification process. The onset temperature of the incipient melting is at approximately 470℃. The SSM cast sample (shown in green) has a much smaller incipient melting peak (with an area approximately 60% smaller than that of the cast ingot), and the onset temperature is 10 degrees lower than that of the cast ingot. This earlier onset and reduction in area indicate that the segregation seen in the SSM cast sample is much less than that of a cast ingot.

5.1.2. COMPARISON BETWEEN SSM CAST, CONVENTIONALLY CAST AND SEMI-SOLID SLUG SAMPLES

5.1.2.1. AA7075 ALLOY

The extent of segregation attributed to different methods of casting the AA7075 alloy can be determined by comparing the incipient melting peak in a DSC trace for samples of each casting technique. As shown in **Figure 5.1**, a wrought sample exhibits no incipient melting peak, as is the case with a successfully homogenised sample, shown in **Figure 5.2**.

Figure 5.7 shows the DSC traces for a conventionally cast, a SSM cast and a SS slug of AA7075 alloy. The bulk melting peaks are very similar in size and location. All three samples exhibit the incipient melting peak associated with segregation at the 470℃ range.

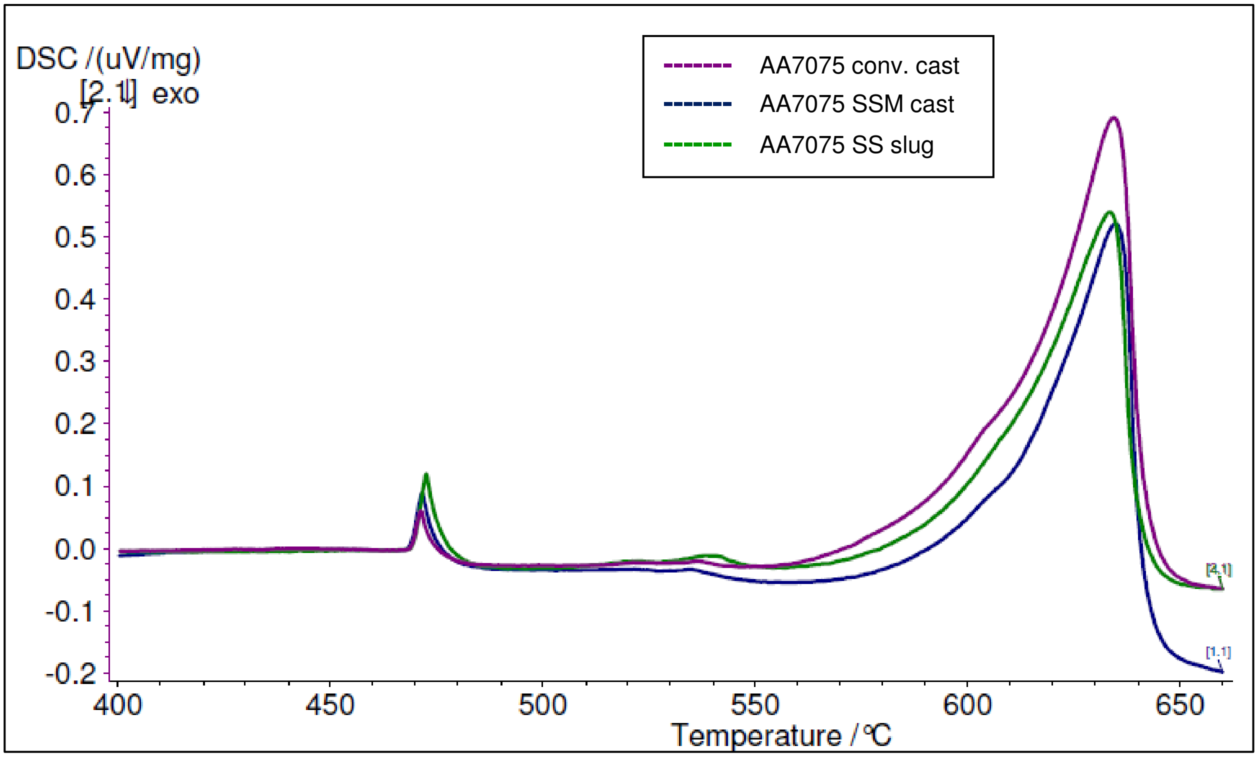

Figure 5.7: *DSC traces for AA7075 alloy, showing differences between SSM cast, conventional cast and SSM slug samples.*

5.1.2.2. A713 ALLOY

As shown previously in **Figure 5.3** and **Figure 5.4**, the A713 alloy exhibits a much smaller incipient melting peak than the AA7075 alloy. To investigate the extent of segregation associated with this alloy in more detail, DSC traces were performed on conventionally cast, SSM cast and SS slug samples. **Figure 5.8** shows the DSC trace curves generated by these tests. As with the AA7075 alloy test discussed in the previous chapter, the bulk melting curves for these three samples were very similar in size and location. All three samples exhibited incipient melting peaks at the 460°C range. The size of these incipient melting peaks for the A713 alloy are smaller than those seen in **Figure 5.7** for the AA7075 alloy samples.

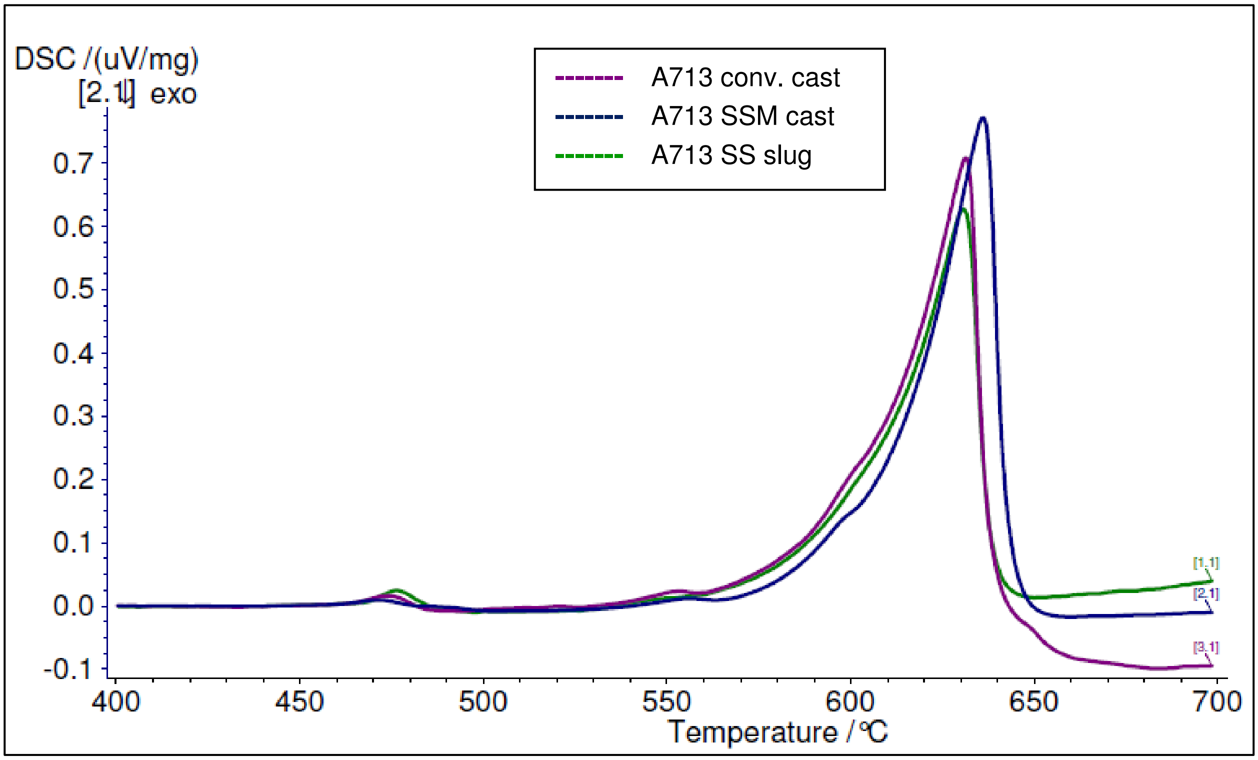

***Figure 5.8:** DSC traces for A713 alloy, showing differences between SSM cast, conventional cast and SSM slug samples.*

5.2. THERMODYNAMICS USING JMatPro

The solidification curves for both the AA7075 and the A713 alloys were generated. **Figure 5.9** shows the fractions of solid of the different phases as solidification proceeds for the AA7075 composition, and **Figure 5.10** shows a closer look at the minor phases that solidify in the low weight percent range. The last phase that solidifies is the $MgZn_2$. The eutectic of this alloy is thought to be made up of α-Al and $MgZn_2$[75], although, in some instances, the Zn can be substituted by Cu atoms in the lattice, resulting in a higher Cu content value, as seen in the EDS results in the previous chapter. This type of substitution can be made with extended composition ranges, namely $Mg(Al, Cu, Zn)_2$[76]. This is the phase combination that results in the incipient melting peak seen in the DSC results. The other phase of interest is the iron-rich intermetallic phase, Al_7Cu_2Fe, which is a phase that will not dissolve during homogenisation treatments.

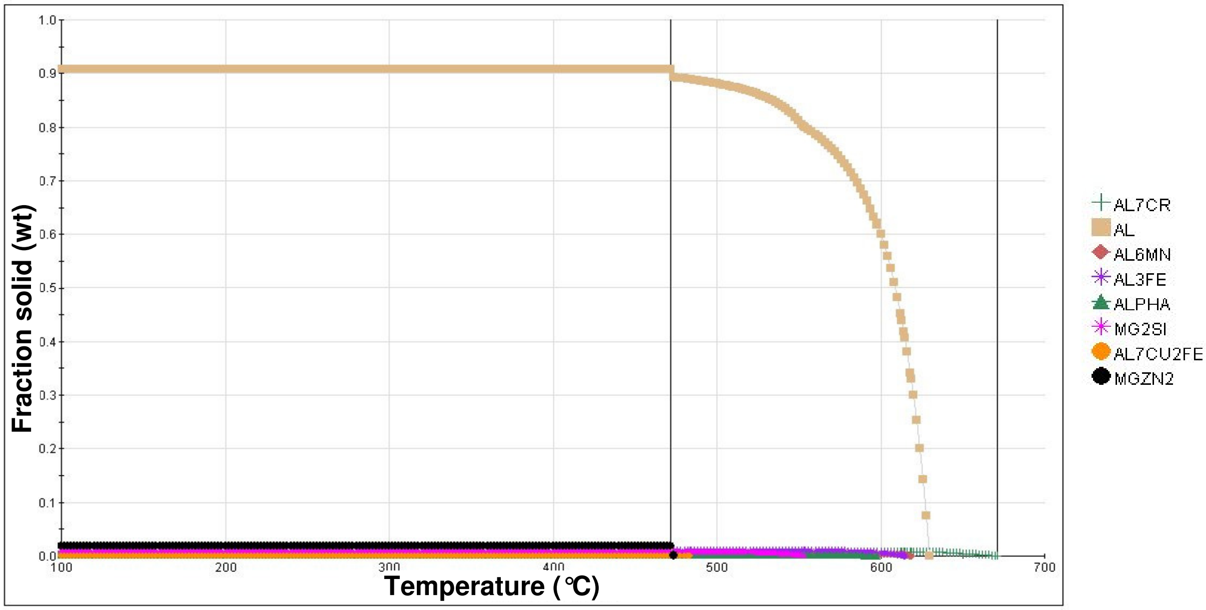

Figure 5.9: *Solidification profile of AA7075*

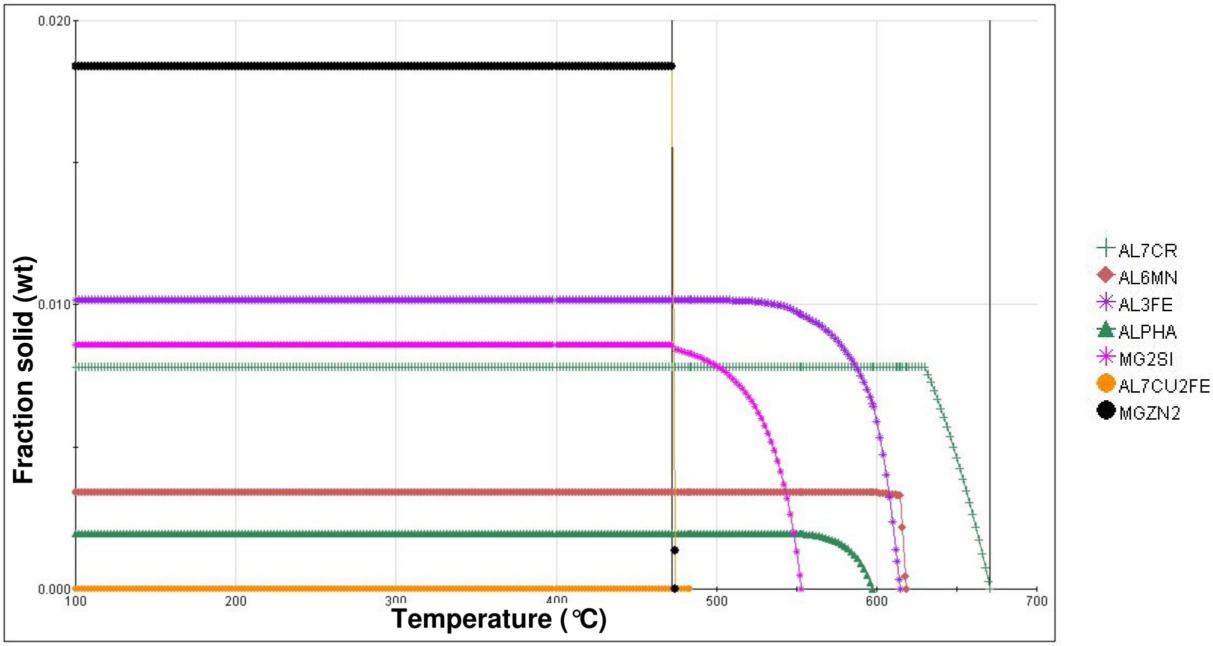

Figure 5.10: *Closer look at the minor phases that form during the solidification of AA7075.*

Figure 5.11 shows the fractions of solid of the different phases as solidification proceeds for the A713 composition, and **Figure 5.12** shows a closer look at the minor phases that solidify in the low weight percent range.

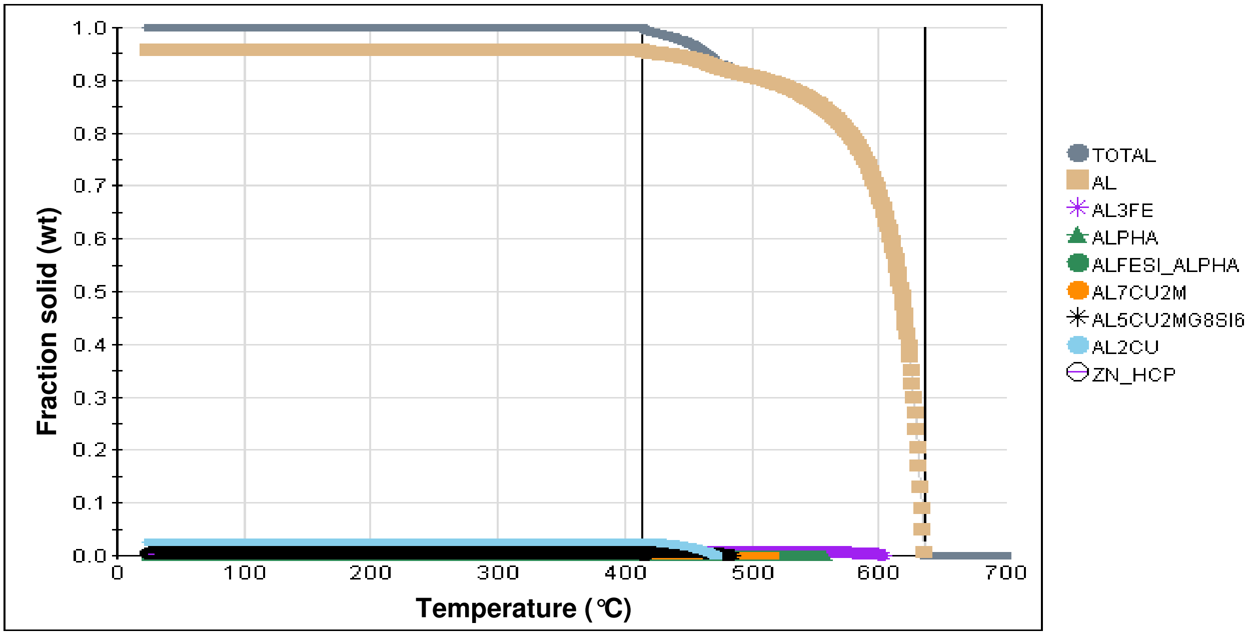

Figure 5.11: *Solidification profile of A713.*

Figure 5.12 shows that the last phase to solidify in this alloy is hexagonal close-packed (HCP) zinc. Al_2Cu is another phase that is predominant in this alloy. These phases indicate that the eutectic in the A713 composition area are the Cu-rich phase and HCP zinc.

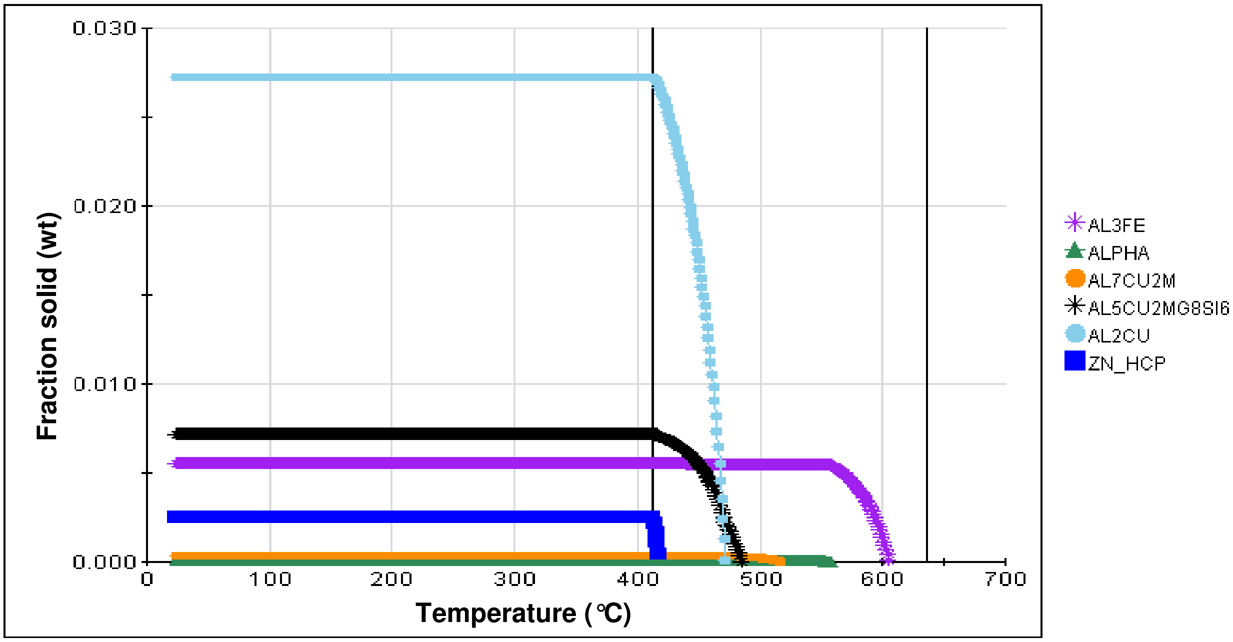

Figure 5.12: *Closer look at the minor phases that form during the solidification of A713.*

The EDS analyses of the as-cast A713 composition structure shows that the two phase eutectic is generally of the order of 58-64at% Al, with either Cu at approximately 24-33at% or Zn at approximately 25at%. The interaction volume of the areas analysed for these EDS values would have added some degree of error. These ratios agree with the presence of Al_2Cu, Zn (HCP) and α-Al.

5.3. HEATING AND SEGREGATION

Heating experiments were carried out to evaluate the effect of different temperatures and times on the distribution of the alloying elements within the structure. Samples were heated to 300℃, 460℃ and 500℃, and held for one minute for the lower temperatures, and nine minutes for the higher temperatures. The samples were then prepared for SEM, according to the polishing procedure in **Chapter 3**. EDS area map analyses were performed on each sample.

5.3.1. AA7075 ALLOY

Previous EDS analysis of the as-cast condition, focusing on the segregation and compositional distribution within the globular grains, had shown that Mg and Cu were relatively evenly distributed throughout the grains, with increased concentrations of both elements noticeable within the eutectic regions, 20at% and 7at% respectively. These compositions can be seen in **Figure 4.14**, **Figure 4.15** and **Figure 4.16**. Zn, on the other hand, is only seen in very low concentrations within the centre of the grains, and the concentration increases dramatically in the coring rings. In addition, small increases are seen in the cellular protrusions. The Zn concentration within the eutectic regions is of the order of 16at%, compared to the 2at% at the centre of the grains.

Figure 5.13, **Figure 5.14** and **Figure 5.15** show BS SEM images of samples that have been heated in a salt bath at 300℃ for one minute, at 460℃ for nine minutes and at 500℃ for nine minutes respectively. Each image has corresponding EDS elemental area maps. These area maps show concentration distributions of the main alloying elements, namely, Al, Zn, Cu, Mg and Fe.

The SEM image in **Figure 5.13** shows the lamellar eutectic and little contrast in the coring rings. The EDS area maps confirm that Mg is evenly distributed throughout the structure. The globular grains are Al-rich and there is a much lower concentration of Mg in the interglobular region. The Zn and Cu concentrations in the interglobular areas are high.

Figure 5.14 shows the structure after nine minutes at 460℃. This temperature is below the incipient melting temperature, and diffusion of the solute elements in the eutectic area is expected. The SEM image shows the breakdown of the lamellar eutectic structure, although the eutectic in the bottom right-hand corner still exhibits part of the lamellar structure. Large pores have been exposed at this point. The Zn concentration is more evenly distributed, although there are still areas within the centres of the large globular grains that have only small concentrations of Zn. This distribution indicates that there is diffusion from the eutectic region into the globular grains. Cu continues to be locked in the eutectic regions.

The EDS area maps in **Figure 5.15** are of a sample after heating in a salt bath at 500℃ for nine minutes. This temperature is above the incipient melting temperature. After this heat treatment, there is no evidence of the lamellar structure of the eutectic, although there is a second phase in evidence. The porosity is exaggerated. The SEM image shows that there are coring rings in the larger globular grains. The EDS area maps show that the Mg and Zn distribution is even within the globular grains, but that there are comparatively high Zn and Cu concentrations in the upper portion of the area. There is a high concentration of Fe in this same area.

The most noticeable difference between composition distributions after heat treatments at the three temperatures shown in the following figures are as follows:

- The 460℃ sample indicates that diffusion is occurring and the delineation of the Zn and Cu containing areas is soft.
- In the 500℃ sample, there is diffusion in the structure but the area that still contains the Zn, Cu and Fe is distinctly outlined, indicating that the elements are locked into these areas in an intermetallic phase and that there is no diffusion from this area.

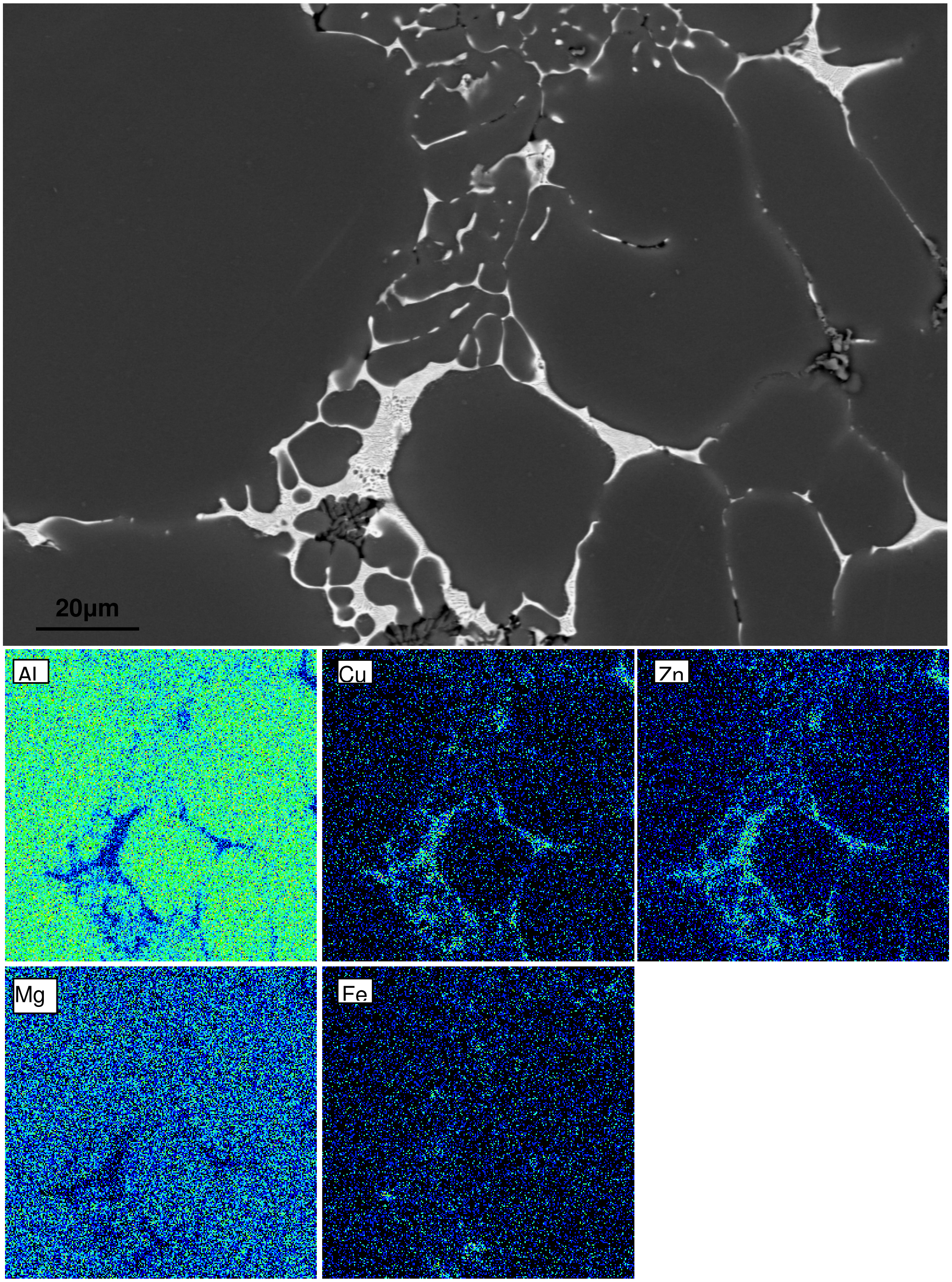

Figure 5.13: *AA7075 alloy after heat treatment at 300℃ for 1 minute, showing BS SEM image and elemental maps.*

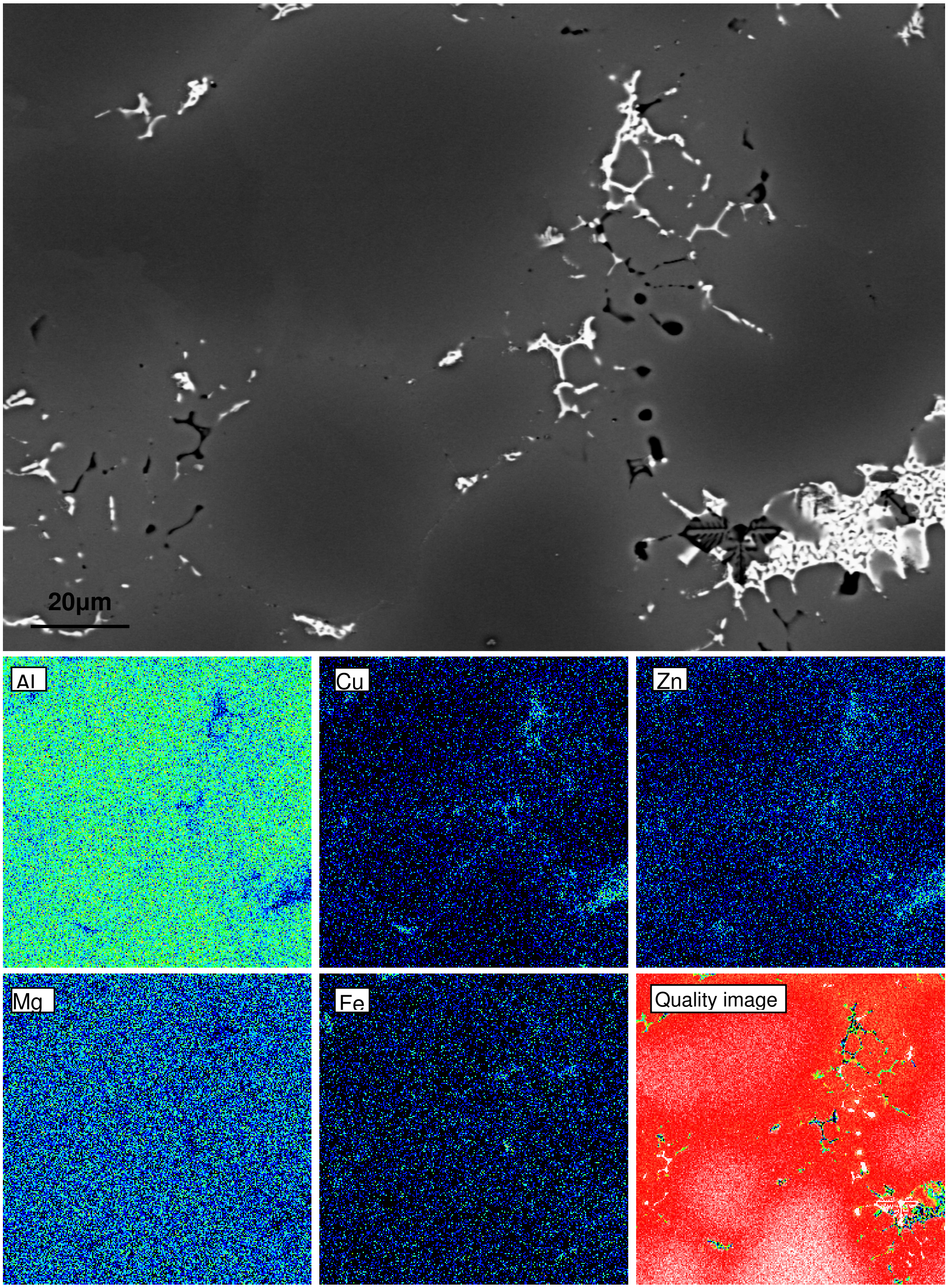

Figure 5.14: *AA7075 alloy after heat treatment at 460℃ for 9 minutes, showing BS SEM image and elemental maps.*

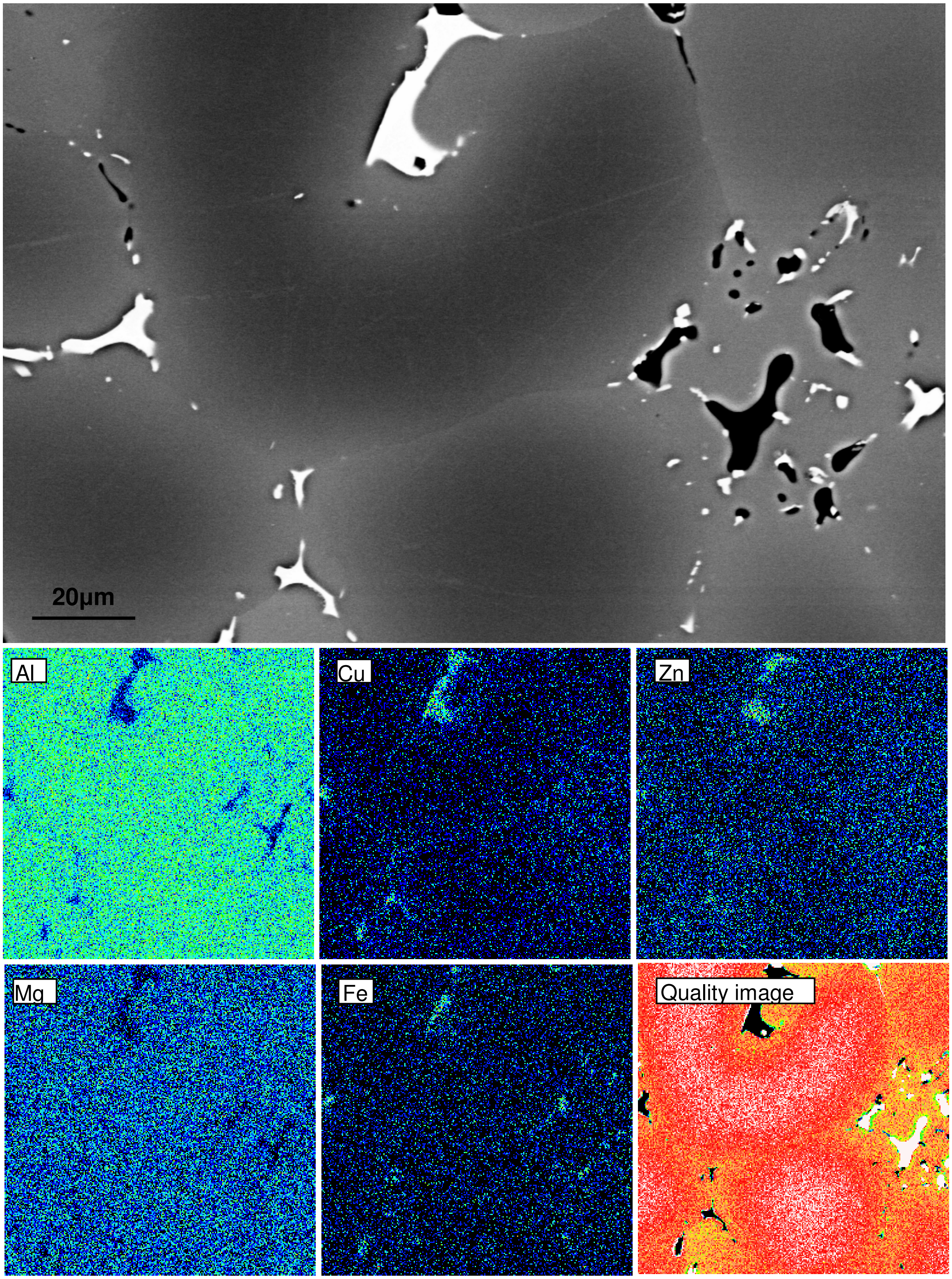

Figure 5.15: *AA7075 alloy after heat treatment at 500℃ for 9 minutes, showing BS SEM image and elemental maps.*

5.3.2. A713 ALLOY

The A713 alloy has a lower Mg content and higher Zn and Cu contents than the AA7075 alloy. Previous EDS analysis of the as-cast condition, focusing on the segregation and compositional distribution within the globular grains, had shown that, as with the AA7075 alloy, Mg was relatively evenly distributed throughout the grains, with values of approximately 0.4-0.5at% across the structure. These compositions can be seen in **Figure 4.17**, **Figure 4.18**, **Figure 4.20** and **Figure 4.21**. Zn is seen in low concentrations only within the centres of the grains, and the concentration increases dramatically in the coring rings. Further small increases are seen in the cellular protrusions. The Cu concentration is of the order of 25-30at% within the eutectic regions when compared to the 1-2at% at the centres. The concentration of Zn within the eutectic regions is of the order of 25at%, compared to the 3at% at the centre of the grains, although this is still higher when compared to the Zn concentration at the centre of the grains in the AA7075 alloy.

Figure 5.16, **Figure 5.17** and **Figure 5.18** show BS SEM images of samples after heating in a salt bath at 300℃ for one minute, at 460℃ for nine minutes and at 500℃ for nine minutes respectively. Each image has corresponding EDS elemental area maps. These area maps show concentration distributions of the main alloying elements, namely, Al, Zn, Cu, Mg and Fe.

The SEM image in **Figure 5.16** shows that, after one minute at 300℃, there is still stark contrast between the globular grains and the second phase. There is minimal exposed porosity within this second phase. There is also a contrast pattern within the globular grains similar to that explained in **Chapter 4.1.4**. The EDS elemental maps show that the Zn concentration is higher in the areas where eutectic is located, but the delineation of these areas is less distinct, indicating diffusion of the Zn into the surrounding areas. The interglobular regions contain a high concentration of both Cu and Fe.

Figure 5.17 shows that there is still some second phase present in the structure and contrast in the coring rings. There is also exposed porosity, which has a rounded shape. The EDS area maps show that Zn is evenly distributed across this area of view. There are still points where there are relatively high concentrations of Cu and Fe.

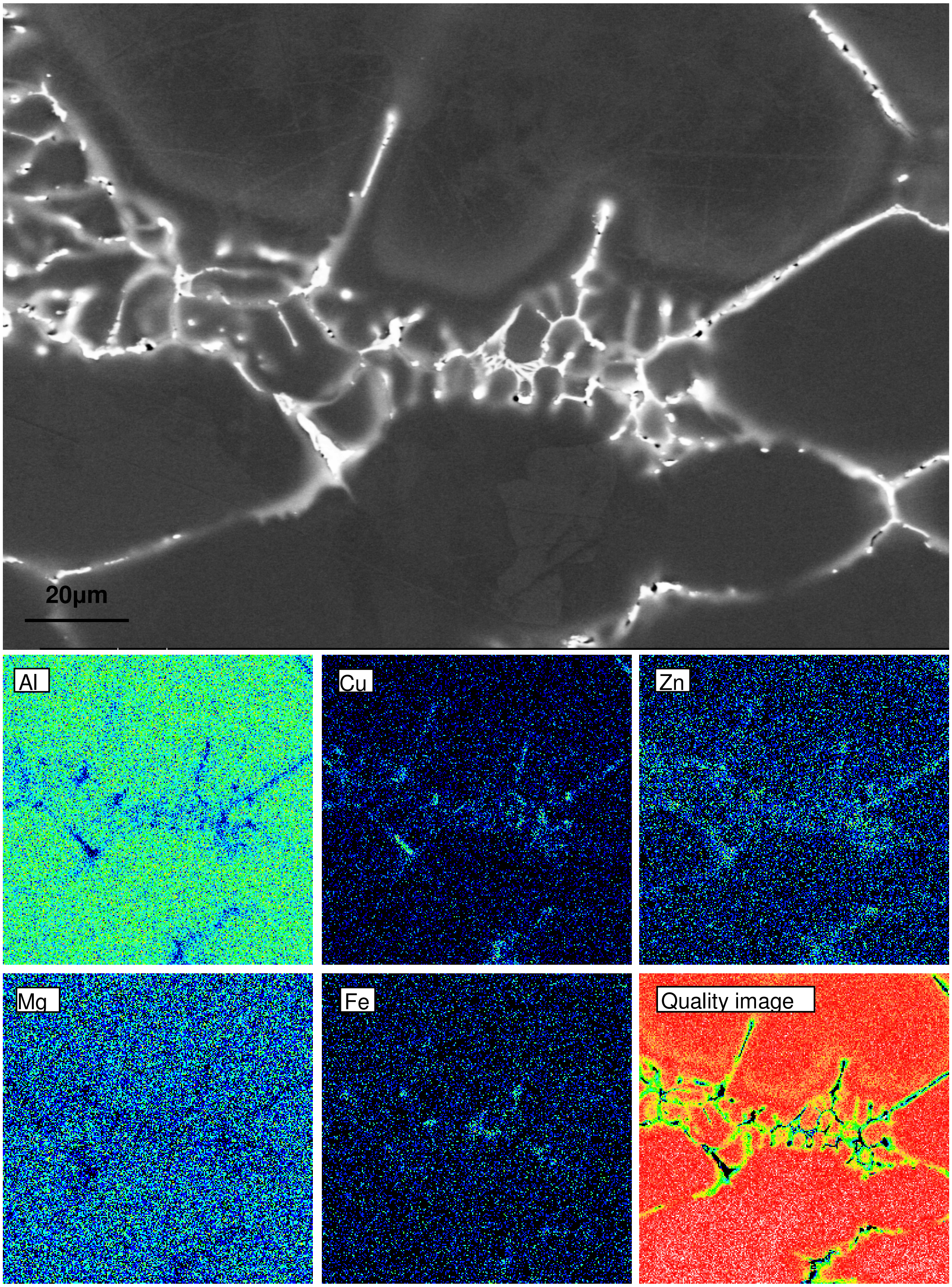

Figure 5.16: *A713 alloy after heat treatment at 300℃ for 1 minute, showing BS SEM image and elemental maps.*

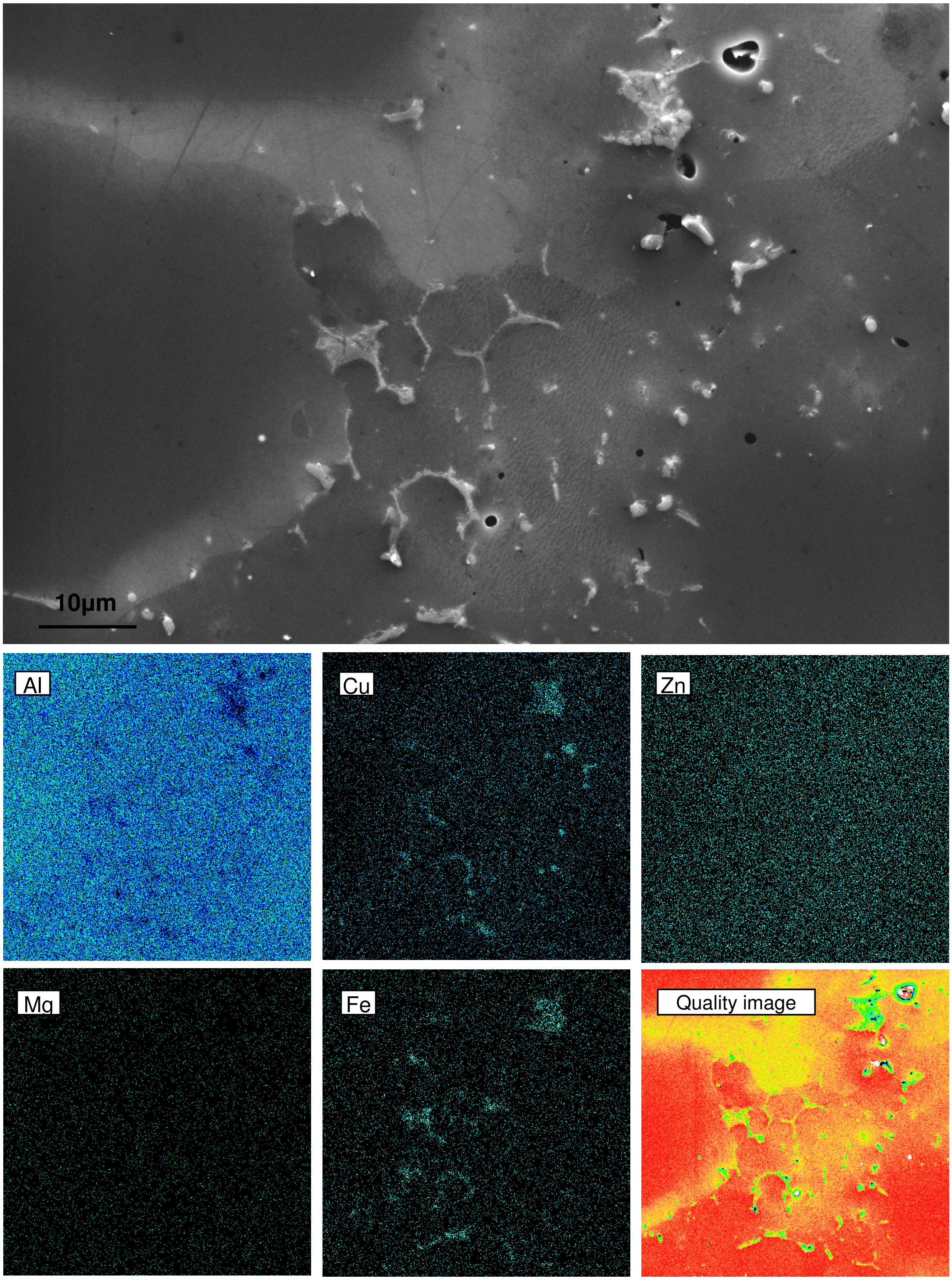

Figure 5.17: *A713 alloy after heat treatment at 460℃ for 9 minutes, showing BS SEM image and elemental maps.*

The SEM image and the Zn EDS area map in **Figure 5.18** show that there is a slight Zn depletion at the centre of the large globular grains, indicating the continued presence of the coring rings. Notwithstanding this minimal concentration difference, the Zn concentration distribution is very even, with no high concentrations in the areas that exhibit second phase contrast in the SEM image. The second phase in this field of view is made up of Cu and Fe, as can be seen in the Cu and Fe EDS area maps. The SEM image shows a large amount of exposed porosity.

The Zn distribution in the A713 alloy after the 500℃ heat treatment, when compared to that of the AA7075 after the same temperature treatment, is more evenly distributed across the structure. In addition, there are no clusters of high concentrations of Zn, as is seen with the AA7075 alloy. This indicates that, if incipient melting has occurred, as the DSC information suggests, then the homogenisation process in the AA7075 is negatively affected to a higher degree than the A713 alloy.

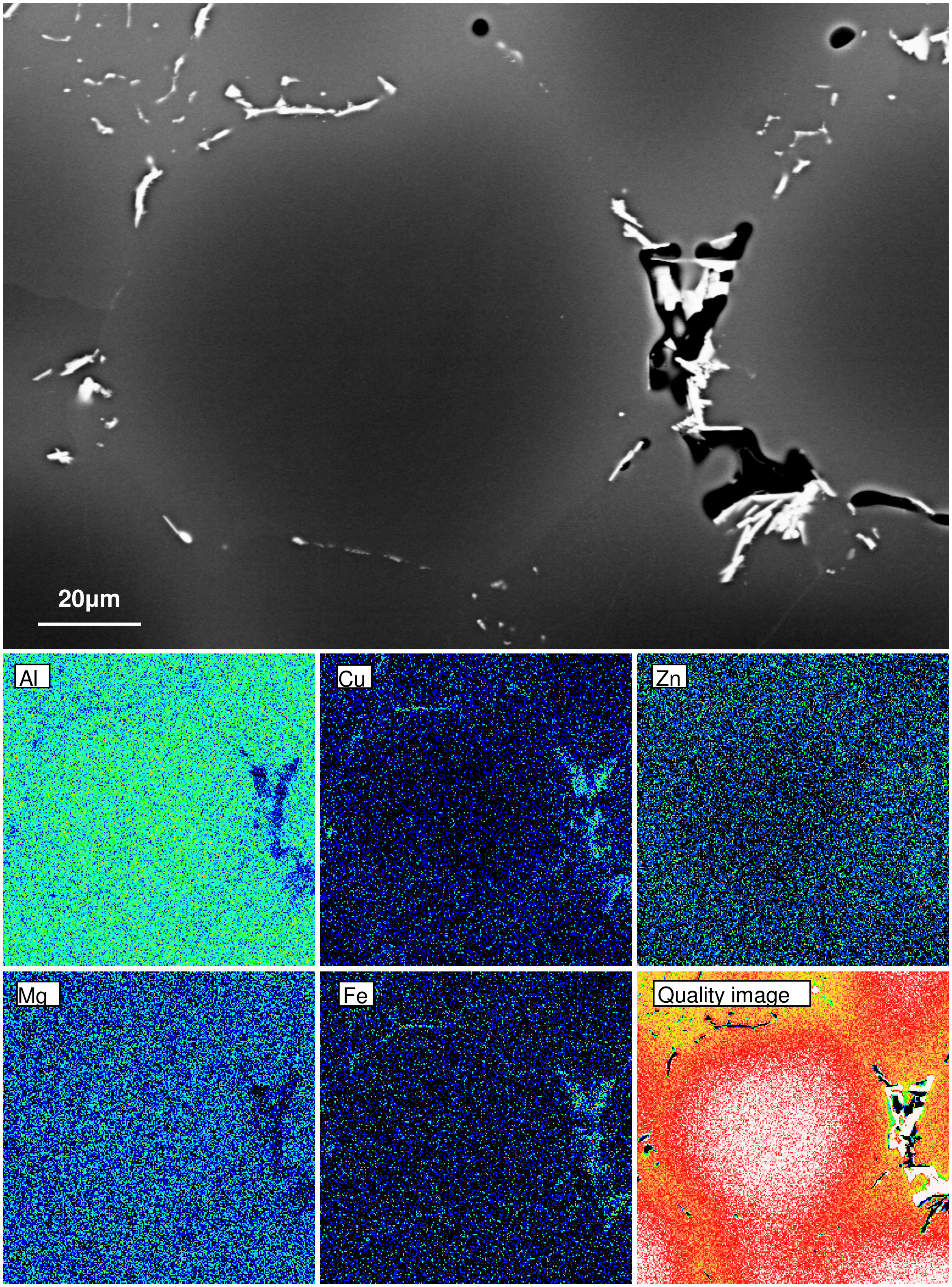

Figure 5.18: *A713 alloy after heat treatment at 500°C for 9 minutes, showing BS SEM image and elemental maps.*

5.4. *IN SITU* HEATING

In situ heating experiments were performed in a CamScan MX2500 SEM, which had been fitted with a custom designed and built heating stage. Samples were viewed with both secondary and backscattered electron detectors. Micrographs were taken at regular temperature intervals and a progression of microstructural changes associated with temperature changes was viewed.

5.4.1. AA7075 ALLOY

The *in situ* progression on an AA7075 SSM sample can be seen in **Figure 5.19**. The micrographs are in BSE mode, in order to give more information about how the composition is changing as a result of the temperature. (It must be noted that the information in these BSE images may show evidence of topographical shifting, as a result of the free surface of the sample.)

The main observations reflected in **Figure 5.19** are described with respect to dissolution of the eutectic, or any second phase, change in the morphology of the porosity and the generation or alteration of grain boundaries (which may be emphasised as a result of the surface effects). In the RT micrograph, the lamellar morphology of the eutectic is clear in the centre of the micrograph, as well as in the smaller areas located between the various grains. In the 400℃ micrograph, it is clear that there is already significant dissolution of the eutectic in all the areas, and the clear lamellar structure of the central eutectic area is now less defined. As the micrographs progress through the temperature range, this dissolution continues, until the main area of eutectic has nearly completely dissolved. However, there are areas where there are light-coloured phases that have not dissolved. These may be intermetallics, which will not be affected by these temperatures. (This will be verified later using EDS.) This particular location (seen in **Figure 5.19**) does not have a large amount of porosity, so the morphology of the porosity cannot be evaluated in these micrographs. There is clear grain boundary shifting, most of which appears to create topographical effects. The sinking of some of the edges or smaller grains may be as a result of incipient melting or extensive dissolution of second phase in what would be an interglobular area below the visible surface, which would cause a volume change below the surface.

The above discussion illustrates one limitation of the *in situ* heating technique, where the sample can only be seen as a 2-D surface, with no indication of the structure below the area on which the set-up is focused. However, after the completion of the *in situ* experiment, the sample was sectioned and viewed on edge, in order to verify the information.

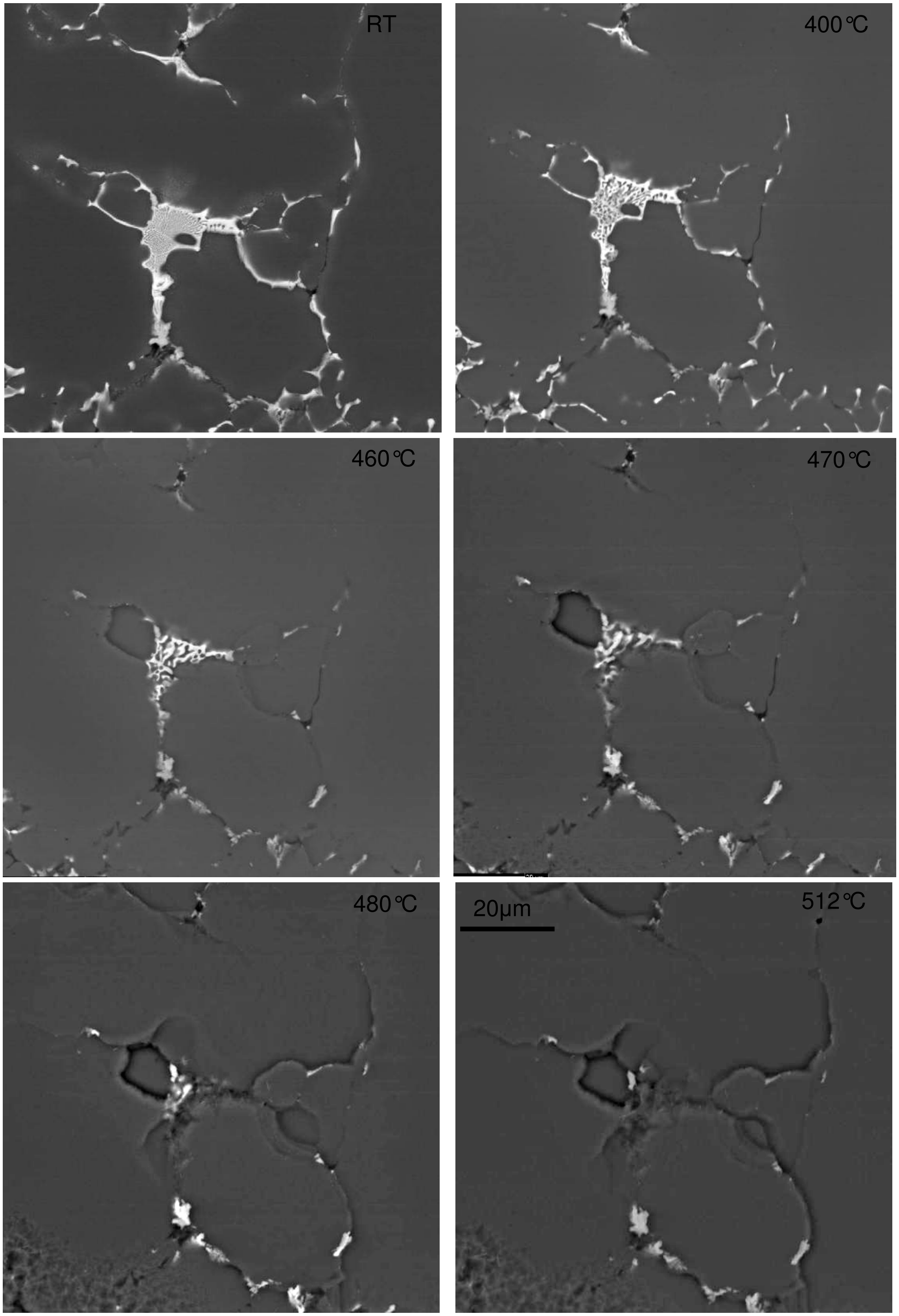

Figure 5.19: *AA7075 SSM – Microstructural changes seen during in situ heating from room temperature through to 512℃. Temperature of each micrograph as indicated. Scale of all micrographs the same.*

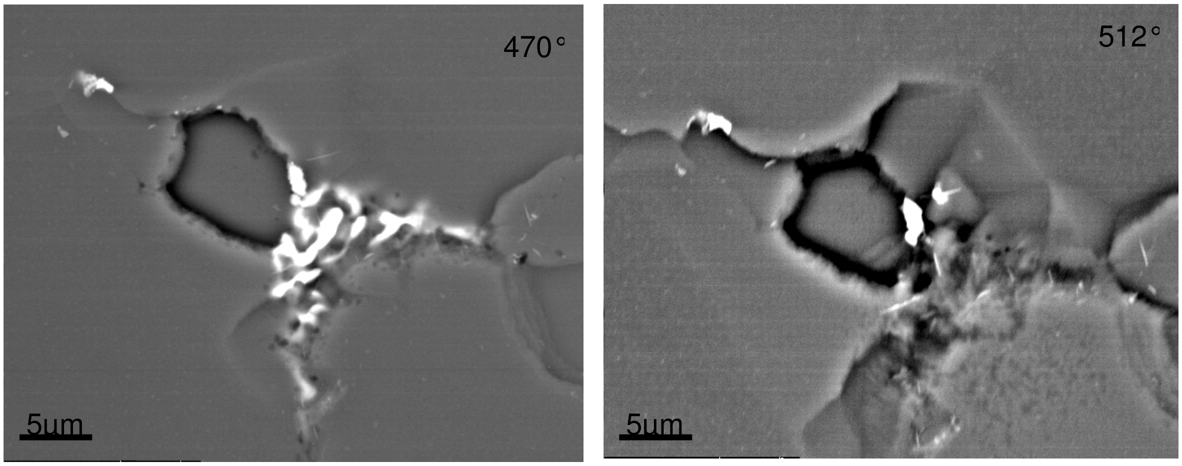

Figure 5.20: *AA7075 SSM, showing the eutectic area during in situ heating at 470°C & 512 °C.*

Figure 5.20 shows a closer look at the main eutectic area discussed in the previous figure. From these micrographs the dissolution of the eutectic can be clearly seen. The other feature of significance is the formation of needle precipitates at the boundaries of the grains, evident at this higher magnification, especially in areas that were previously rich in eutectic. In addition, at 512°C there is a fine spherical precipitate that has appeared in the main portion of the grains.

The sample was cooled back to 400°C and then left to cool to room temperature. Micrographs were taken at these temperatures and are shown in **Figure 5.21**. The most noticeable feature is that the contrast in the interglobular regions is still visible, indicating that some phases had not dissolved completely during heating to 512°C, and on cooling, the elements that had not gone into stable solution, had precipitated out. The location of this precipitated phase is in the same vicinity as the original interglobular regions. This indicates that very little diffusion from the solute-rich interglobular areas towards the centres of the larger grains has taken place.

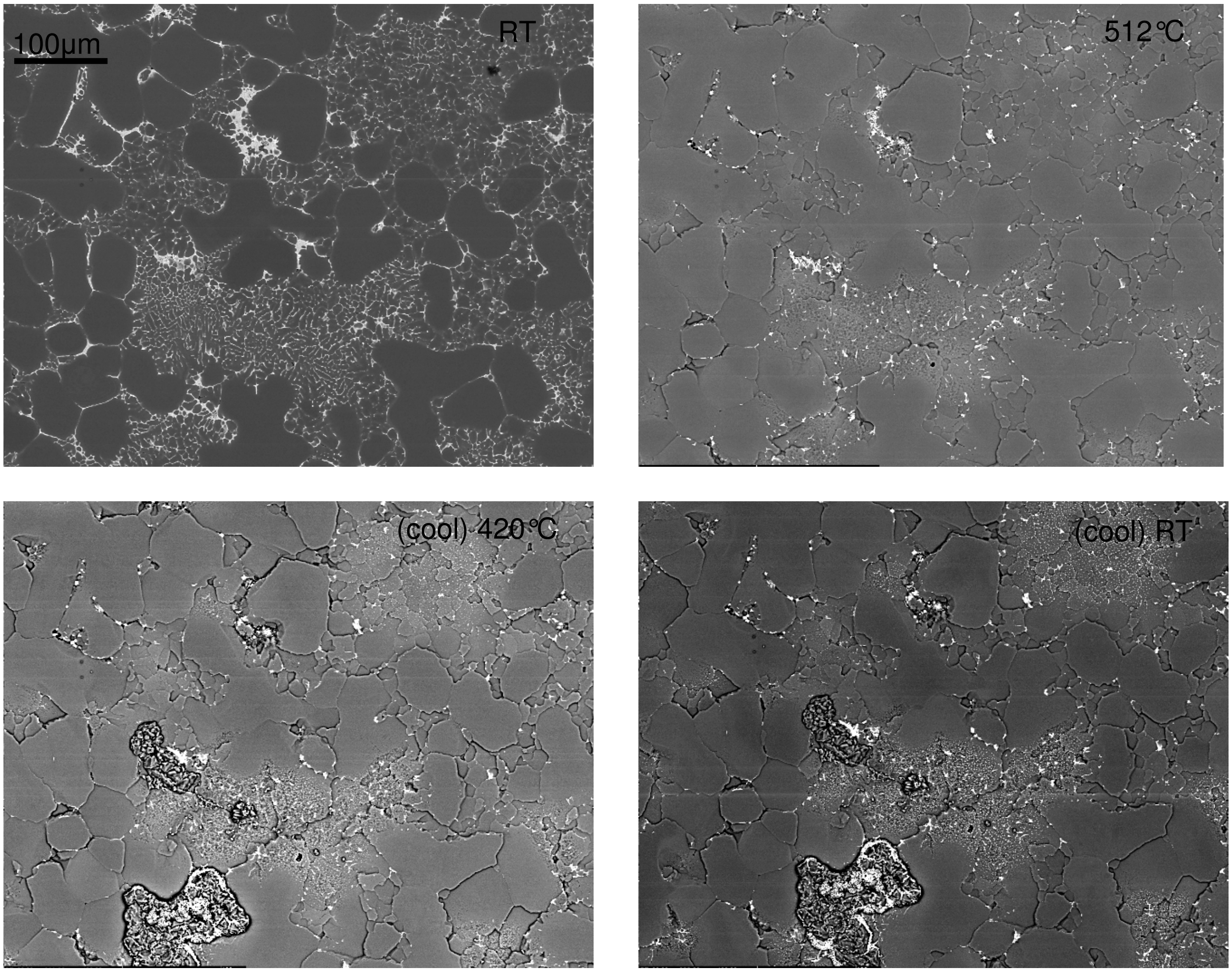

Figure 5.21: *AA7075 SSM – Microstructural changes seen on cooling from 512°C during the in-situ heating experiment. Temperature of each micrograph as indicated.*

5.4.1.1. MICROSTRUCTURE AND COMPOSITION DISTRIBUTION AFTER IN SITU HEATING

Owing to the nature of the *in situ* experiment and the presence of a free surface, the location of the precipitated phases needed verification. After the *in situ* experiment, the sample was sectioned and re-polished. The sample was then viewed in the SEM, and the location of the different phases was evaluated and their compositional information analysed, using EDS.

Figure 5.22 (a) shows the general microstructure of the AA7075 alloy after *in situ* heating. The micrograph is in backscattered mode to show contrast between areas of different composition. The micrograph in (a) shows that the composition distribution appears even within the large globular grains, while in the previously interglobular regions, there are a lot of second phase precipitates and intermetallics.

On inspection of this microstructure at higher magnification, as seen in **Figure 5.22** (b), the previously smaller interglobular grains now have a dense distribution of needle-shaped second phase precipitates. This can be seen throughout the previously interglobular regions. There is a ring of finer precipitates in a band at a depth of approximately 20-50µm from the globular grain edge [located between the dashed lines indicated on the micrograph in **Figure 5.22** (b)]. This ring of precipitates indicates that the diffusion distance from the zinc-rich eutectic areas to within the larger globular grains during heating in the *in situ* experiment is limited to a maximum distance of 50µm. This in turn indicates that the homogenisation process for the AA7075 alloy needs more than the three hours of the *in situ* experiment Homogenisation also requires strict temperature controls, because of the incipient melting that occurs in the 465°C temperature range, as shown in the previous DSC results and by the dramatic topographical changes seen in the *in situ* progression images in **Figure 5.19** and **Figure 5.21**.

Figure 5.23 shows a micrograph of the interglobular region after *in situ* heating, indicating the location of EDS analysis points, and a table of the resulting compositional information. The compositional analysis indicates that the phases that did not go into solution during the *in situ* heating experiment are Fe-based intermetallics. Any values attained using EDS on such small areas are influenced by the interaction volume, and the actual compositions can only be alluded to. The phases that would have been present during heating and subsequent cooling within the 510°C temperature range would be Al_2Cu_2Fe, $MgZn_2$, S-Al_2CuMg and (alpha)Al[77]. The values in the table agree with the ratios of these phases.

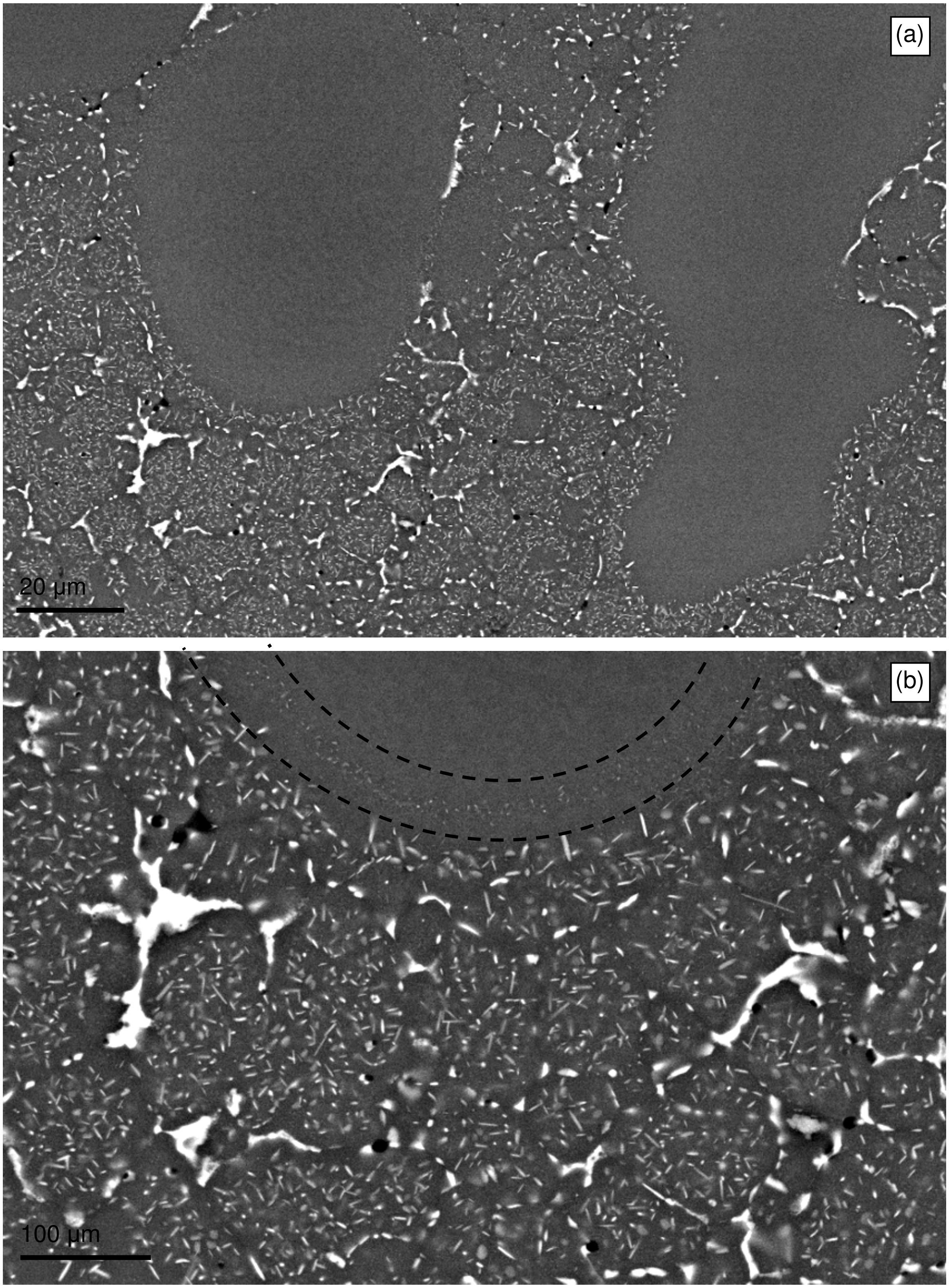

Figure 5.22: *AA7075 SSM – SEM micrographs of sample after in situ heating, at different magnifications, (a) showing the centre of two large globular grains with no precipitates, and (b) showing the precipitates in the interglobular region and a fine ring of precipitates at the edge of the globular grains.*

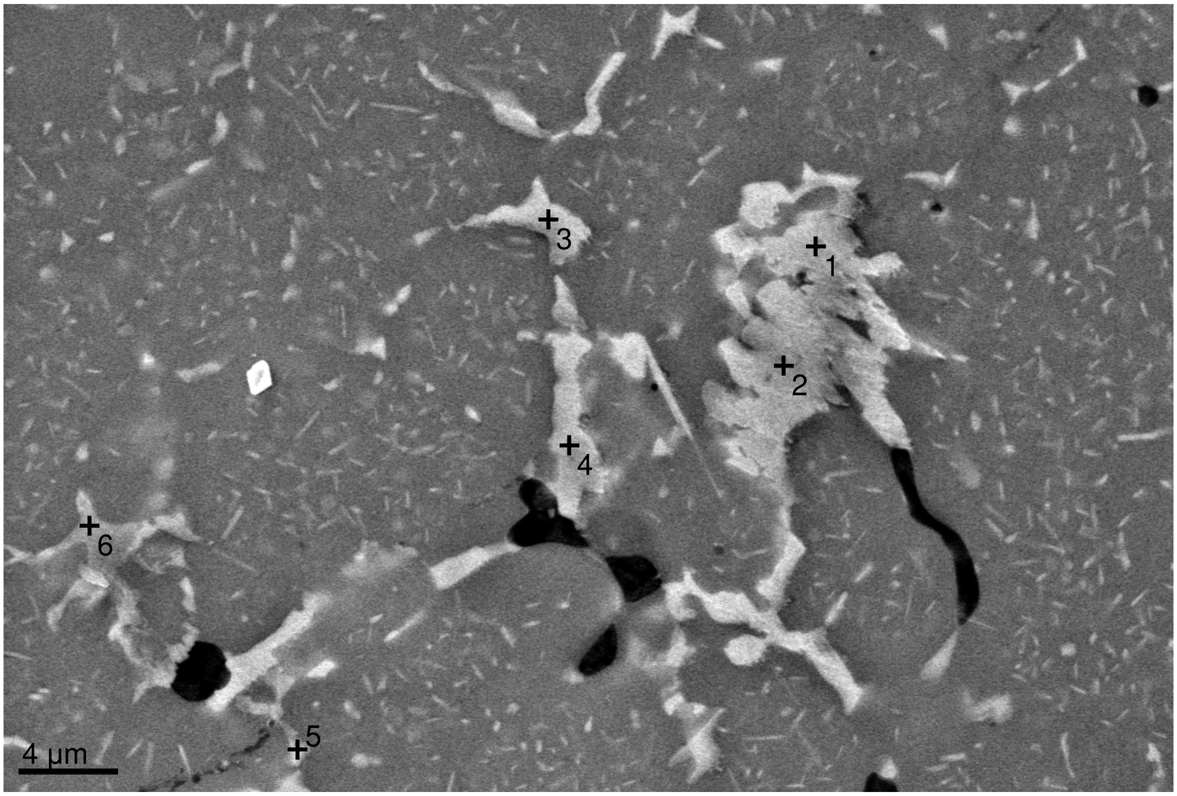

	Al		Zn		Mg		Cu		Cr		Fe	
Spectrum	Wt%	At%	Wt%	At%	Wt%	At%	Wt%	At%	Wt%	At%	Wt%	At%
1	54.8	72.8	4.1	2.2	0.8	1.2	27.4	15.4	0.1	0.1	12.7	8.1
2	61.7	77.6	2.4	1.2	1.3	1.8	23.5	12.5	---	---	11.2	6.8
3	65.8	80.0	2.1	1.0	2.0	2.7	21.2	10.9	0.3	0.2	8.5	5.0
4	61.2	77.1	3.2	1.7	1.1	1.5	17.6	9.5	0.8	0.5	16.1	9.8
5	60.5	76.1	5.9	3.1	2.4	3.4	20.9	11.2	1.5	0.9	8.7	5.3
6	74.3	85.3	5.6	2.7	1.6	2.1	4.9	2.4	0.3	0.2	13.1	7.3

Figure 5.23: *AA7075 SSM – EDS results on precipitates formed after the in-situ heating experiment.*

5.4.2. A713 ALLOY

As discussed in **Chapter** Error! Reference source not found., the A713 composition SSM cast samples exhibit a large amount of the lamellar substructure in the primary globular grains throughout the microstructure. The presence of the LAGBs associated with this substructural configuration indicates that there is stored energy within the microstructure that may influence the microstructural changes that occur with the addition of heat.

The microstructural changes that can be observed during *in situ* heating are numerous; therefore the images from a second *in situ* experiment are shown. The progression in **Figure 5.24** focuses on the changes in features, such as any obvious compositional variations (seen as contrast and brightness changes when backscattered images are viewed), grain boundary migration within the interglobular region, dissolution of the eutectic, formation of any second phases, and the change in the morphology of the porosity. The other evident features seen in this progression are the dissolution of the eutectic and the exacerbation of the porosity as the dissolution progresses from 380℃ through to 512℃, where there are only intermetallic phases left in what was previously the solute-rich eutectic region. Here the morphology of the porosity has changed from the characteristic irregular shape with rough edges, associated with shrinkage porosity, to smooth-edged spherical holes.

The RT micrograph in **Figure 5.24** shows the presence of a lamellar type of sub-structure configuration in the left-hand grain, and a circular type of substructure in the right-hand grain. There is a large amount of second phase between the two grains and within the interglobular region. In addition, the brightness and contrast show that there is compositional variation within these small interglobular grains, as well as a slight difference in the coring band.

The 360℃ micrograph shows that a large amount of the eutectic phase has already dissolved. There is also now a much more emphasised coring ring, which is due to the diffusion of the solute from the eutectic area into the surrounding grains. The morphology of the porosity has also changed, with the removal of the surrounding eutectic. Some of the smaller interglobular grains have what appear to be needle-shaped precipitates within them. Where the eutectic has been dissolved, the presence of intermetallic formations is revealed.

The 410℃ micrographs shows that the diffusion ring is no longer as pronounced, that there is a further reduction in the eutectic phase, and that there is an increase in the visibility of the porosity. In addition, the precipitates in the interglobular grains have now disappeared.

The micrograph at 470℃ in **Figure 5.25** shows that the coring ring is no longer identifiable, indicating that extensive diffusion has already taken place and that homogenisation of the individual grains is underway. Fine precipitates can now be identified within the larger grains and these have a spherical morphology. In addition, needle-shaped precipitates can be identified in some of the interglobular grains and at the boundary of the larger, left-hand grain. In both the 470℃ and 490℃ micrographs, boundaries within the larger grains are becoming more visible and the porosity has increased considerably in size.

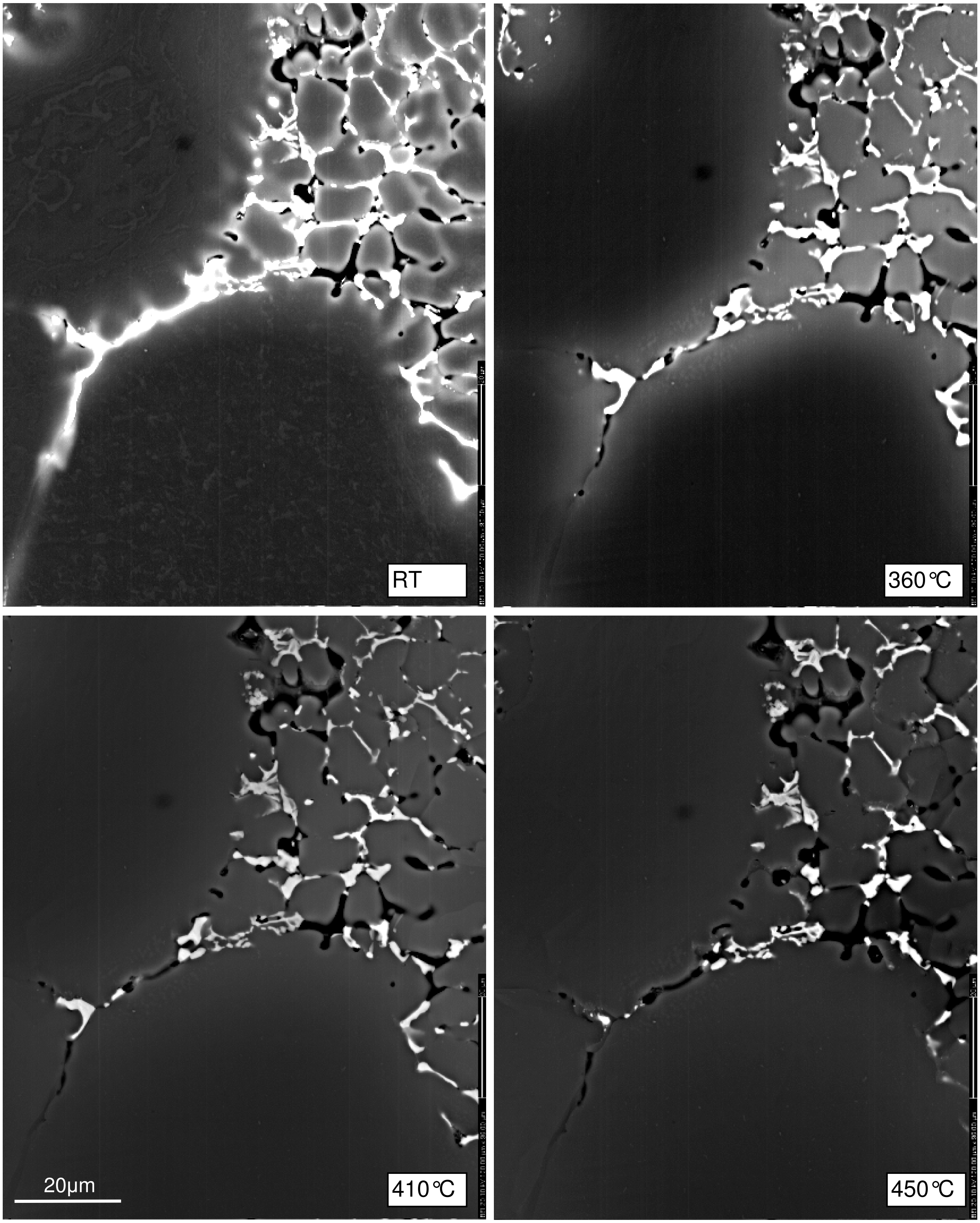

Figure 5.24: *A713 SSM – in situ progression, showing the microstructural evolution during heating from room temperature to 360℃, 410℃ and 450℃. The temperatures of each micrograph are indicated.*

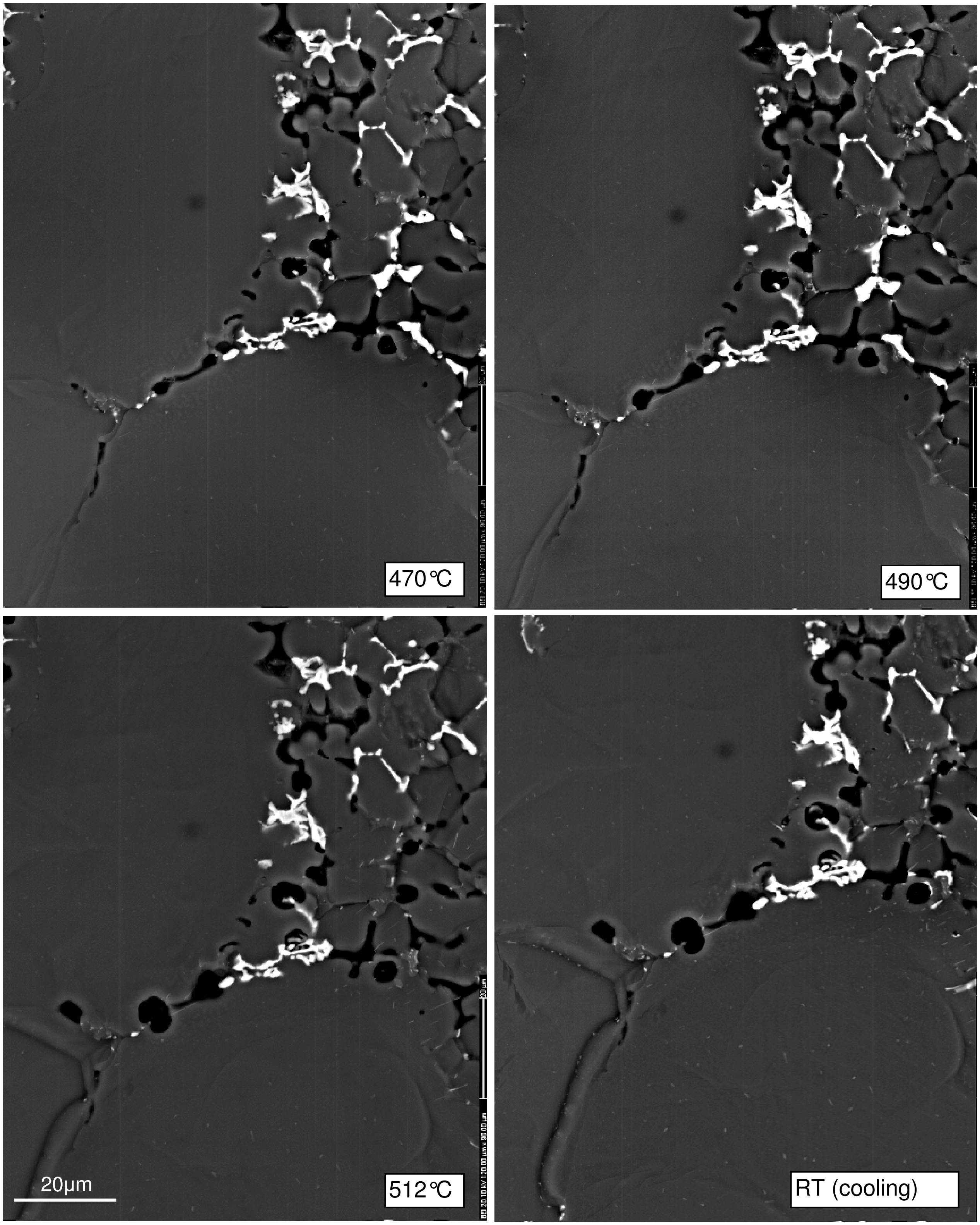

Figure 5.25: *A713 SSM – in situ progression, showing the microstructural evolution during heating continuing from* ***Figure 5.24*** *to 470℃, 480℃ and 512℃, and cooling back to room temperature. The temperatures of each micrograph are indicated.*

In the 512°C micrograph, the size of the needle precipitates has increased significantly and the spherical precipitates within the centre of the larger grains can still be detected. In addition, the boundaries detected in the previous two micrographs now exhibit a slight topographical effect and are more obvious. The porosity has increased further in size, probably owing to sub-surface melting of some second phase material.

The final micrograph shows the microstructure after cooling back to room temperature. The internal boundaries are clearer, the size of the spherical precipitates has increased and the number of needle precipitates has also increased.

5.4.2.1. *IN SITU* EBSD MAPPING

The results so far for both alloys have alluded to the importance of the substructure that is present prior to heating, and the effect that the presence of the boundaries of this structure have on the diffusion and mobility of the solute during heating. Previously, in the characterisation investigation, EBSD had been performed before heating, and the sample viewed, using SEM imaging, only during the heating cycle. This was due to the fact that the SSM cast microstructure itself is very complicated and exhibits a large percentage of second phase that would not be indexable. The use of EBSD for investigation into this kind of microstructure during heating would be used mainly to gain information about structure and changes to the larger grains. It would not be appropriate for investigation into areas with a high percentage of second phase, such as within the interglobular regions.

The EBSD maps were typically 400 x 300μm in size. This allowed for the analysis of an area containing a few larger primary grains, as well as secondary grains and interglobular regions. Therefore, the results from these EBSD maps would give information about the effect of heat on the general microstructure, but no information about the small grains within the interglobular regions. A step size of 2μm was used for these *in situ* EBSD maps. This large step size allowed for fast mapping times while maintaining some degree of detail. Typically, each EBSD map at the designated temperatures was completed in less than seven minutes. At each temperature, both a secondary electron and backscattered electron image were captured for further complementary analysis. **Figure 5.26** to **Figure 5.29** show the progression of the as-cast microstructure during *in situ* heating, from room temperature through to 500°C, and then after subsequent cooling down to 400°C. The backscattered electron images, as well as the EBSD maps for each temperature, are shown.

In **Figure 5.26**, the initial as-cast microstructures exhibit a large number of boundaries, both HAGBs and LAGBs. The indexing rate was relatively low at room temperature. The larger step size and the presence of the internal substructure, resulting in unsolved Kikuchi patterns from pattern crossover, may account for this. There are LAGBs visible inside the larger grains, as well as within the interglobular regions. The other noticeable feature is that the cellular protrusions, seen in the SEM BSE images at room temperature extending from the larger grains, and some of the small grains within the interglobular areas, cannot be distinguished from the orientations of the larger grains shown in the EBSD maps. This indicates a loss of detail in the *in situ* maps, owing to step size and time constraints. In **Figure 5.26**, it is evident from the BSE image that at 200℃ the contrast has not changed significantly, although the number of HAGBs has decreased. When the temperature reaches 300℃, the contrast in the BS image suggests that the coring rings are changing in width because of diffusion from the solute-rich interglobular regions towards the centre of the large globular grains. The corresponding EBSD map shows a further decrease in HAGBs and an organisation of the LAGBs into a subgrain structure. This change in coring ring contrast and LAGB reorganisation continues through to 375℃, as seen in **Figure 5.27**.

Figure 5.27 shows a dramatic decrease in the number of LAGBs within the centre of the globular grains, but there are still a large number of these LAGBs in the areas that represent the cellular protrusions with the same orientation that extend into the interglobular regions. In addition, at these temperatures we begin to see topographical changes associated with the free surface of the sample during the experiment.

Between 450℃ and 500℃, as seen in **Figure 5.28** and **Figure 5.29**, the coring contrast is no longer discernable, and the amount of visible second phase has decreased considerably. Also, the topographical shifting in the BSE images has become more pronounced. The EBSD maps at this point show very few remaining LAGBs, indicating strain-free grains. There are also a number of non-indexed points within the previously eutectic areas, where the undissolved intermetallics are located.

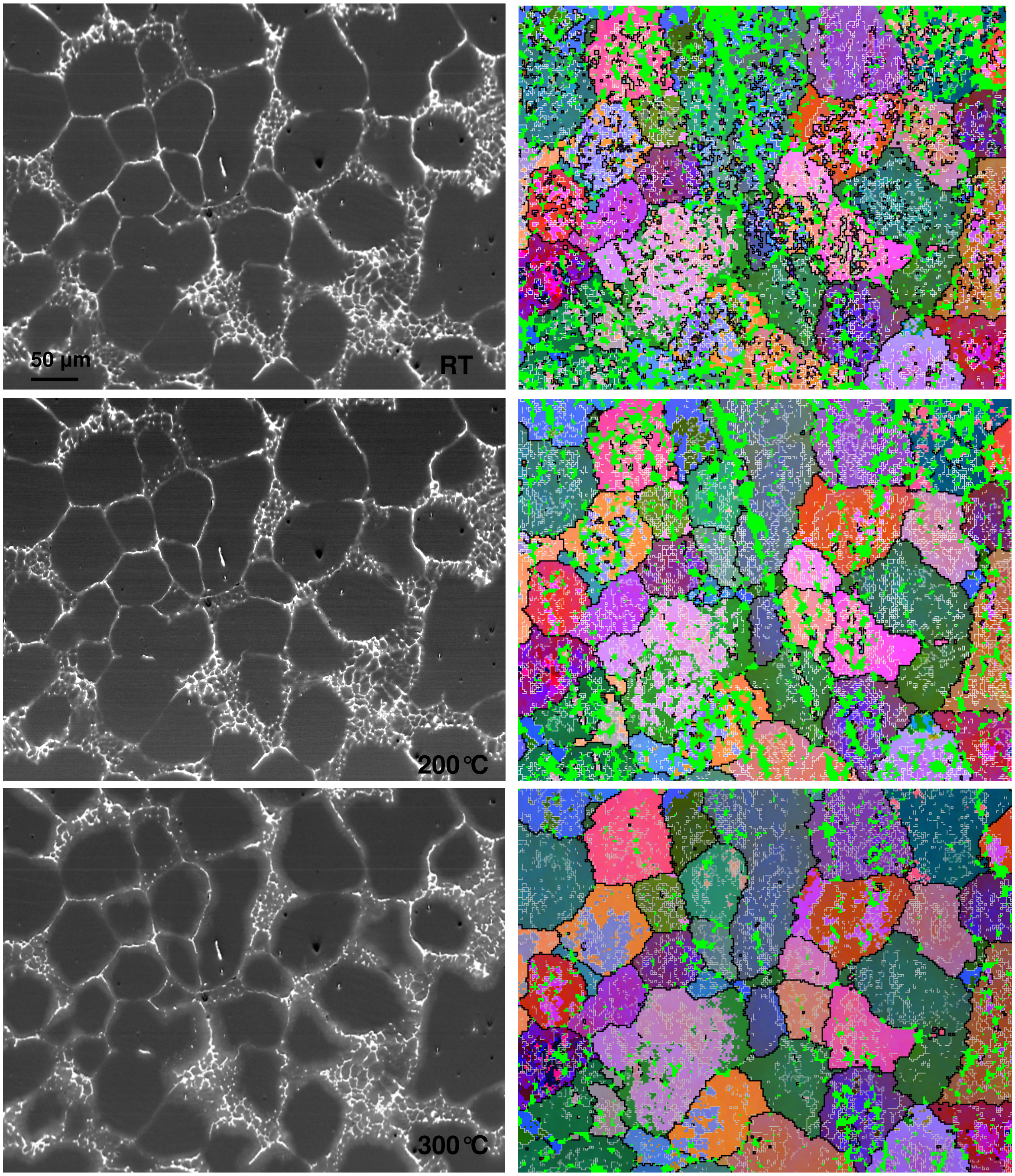

Figure 5.26: *A713 SSM – in situ progression at RT, 200℃ and 300℃, showing SEM BSE images and corresponding EBSD maps at the temperatures indicated.*

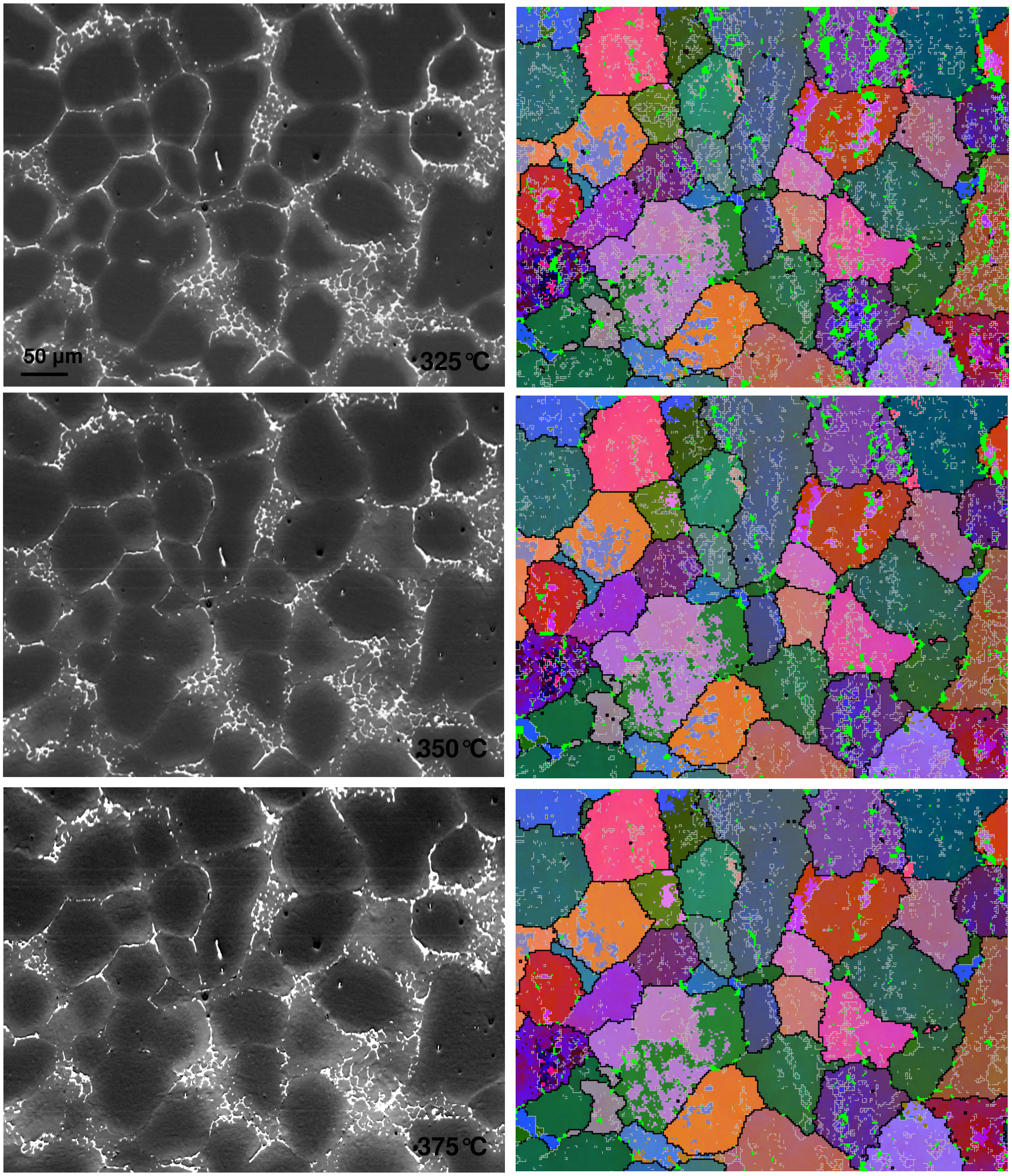

Figure 5.27: *A713 SSM – in situ progression at 325℃, 350℃ and 375℃, showing SEM BSE images and corresponding EBSD maps at the temperatures indicated.*

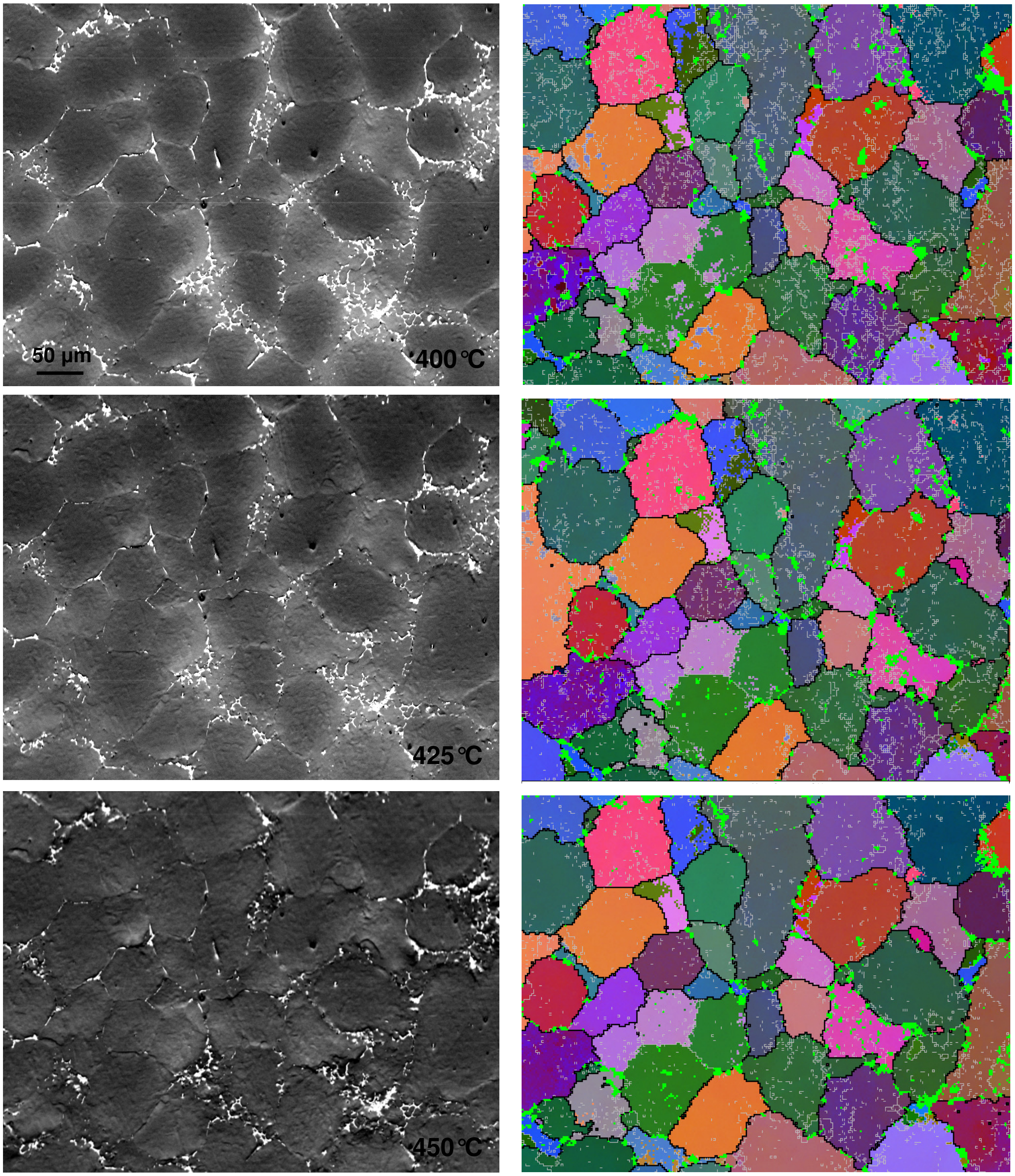

Figure 5.28: *A713 SSM – in situ progression at 400 °C, 425 °C and 450 °C, showing SEM BSE images and corresponding EBSD maps at the temperatures indicated.*

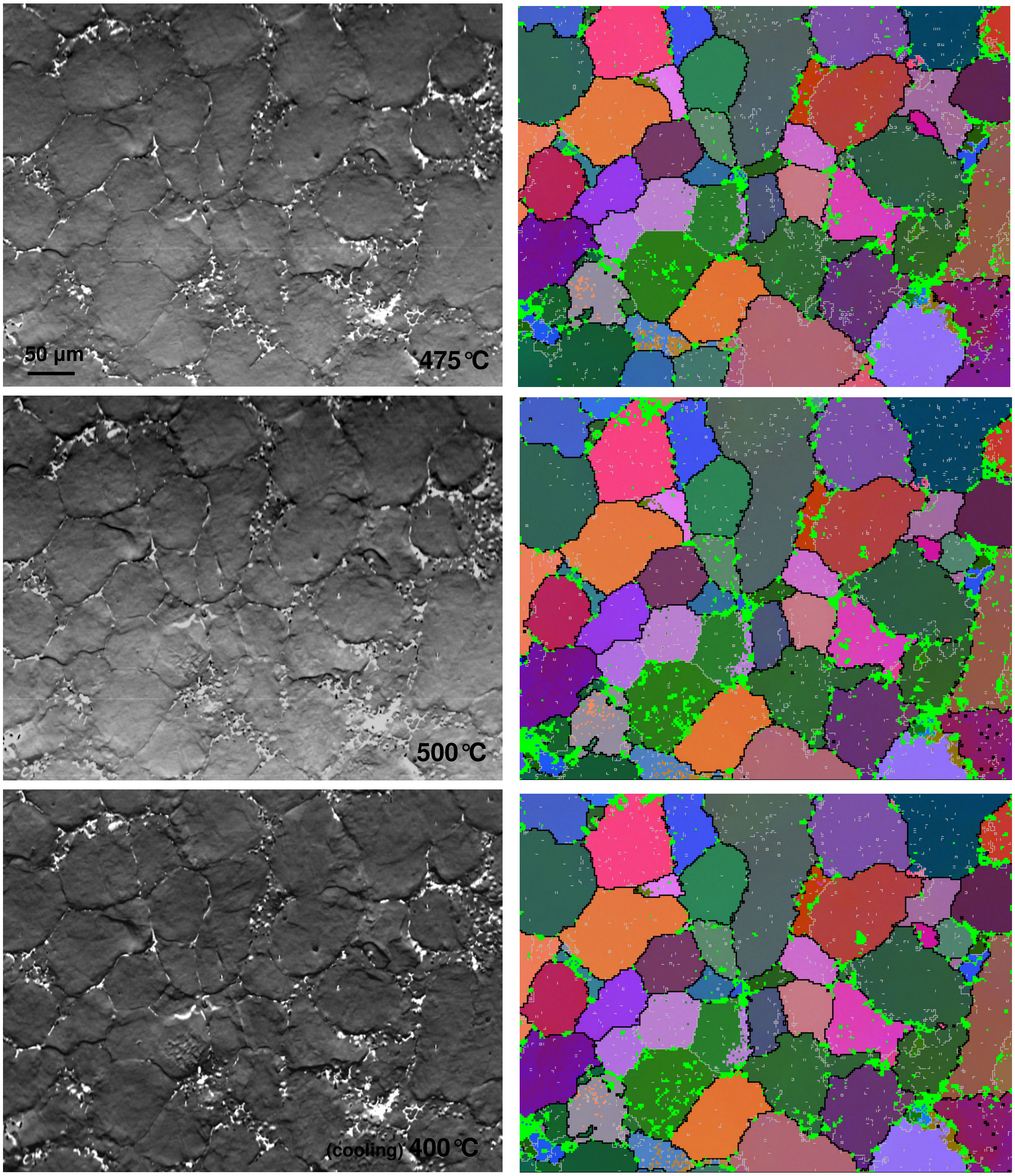

Figure 5.29: *A713 SSM – in situ progression at 475℃, 500℃ and after cooling back to 415℃, showing SEM BSE images and corresponding EBSD maps at the temperatures indicated.*

Figure 5.30 shows BSE SEM images, and corresponding EBSD maps, of another SSM cast A713 alloy during the initial stages of an *in situ* experiment. The room temperature map shows evidence of the circular substructure configuration, which has been discussed previously. The misorientation profiles for A_1-A_2 and B_1-B_2, showing both the profile relative to the previous point along the line and the accumulative profile relative to the start point, are shown in **Figure 5.31**. Both misorientation profiles A_1-A_2 and B_1-B_2 show HAGBs with misorientations of up to 25° within the centre of the grains.

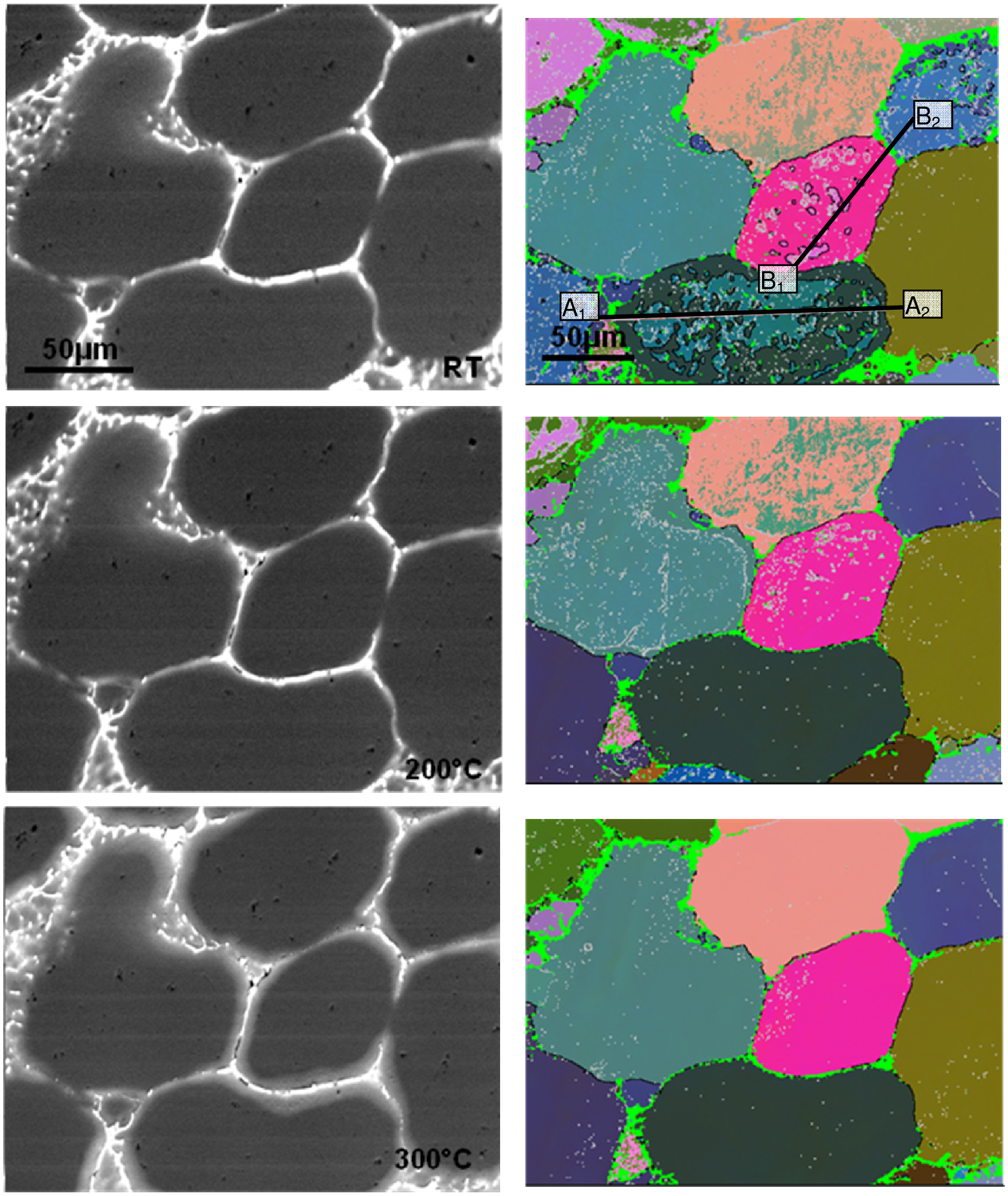

Figure 5.30: *SSM A713 alloy during initial stages of in situ heating, with misorientation profile lines A_1-A_2 and B_1-B_2 on the RT EBSD map.*

Figure 5.30 shows the structure after heating to 200℃ and holding for 15 minutes. It can be seen that the HAGBs are no longer visible, and that there are only LAGBs, which are distributed within some of the grains, some of which not being evident in the RT map. It is speculated that the HAGBs form to accommodate growth faults that occur as the planar solidification front becomes unstable as solidification advances (see later discussion in **Chapter 6.2.1.3**). It is likely that defects, in the form of dislocations, arise from the growth faults. The disappearance of the HAGBs, at temperatures as low as 200℃, suggests that the dislocations can be annihilated during reheating to this low temperature. The change in the misorientations is especially noticeable in the blue-grey grain on the left which now exhibits a ring of LAGBs that coincide with the coring ring that can be seen in the BSE SEM image. As with the previous *in situ* example, the coring rings in the BS image become very distinct in the 300℃ image, indicating a large amount of diffusion from the solute-rich eutectic region over a short distance into the globular grains.

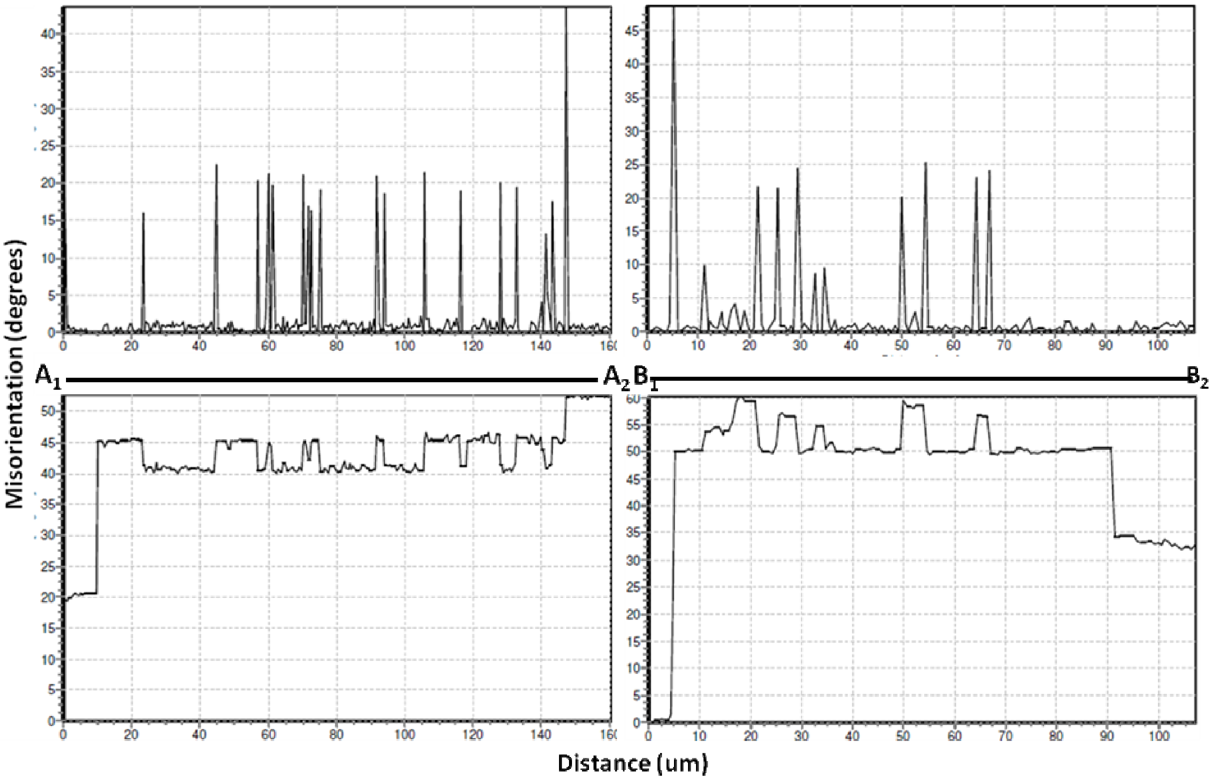

Figure 5.31: *Misorientation profiles A_1-A_2 and B_1-B_2 for Figure 5.30.*

5.4.2.2. MICROSTRUCTURE AND COMPOSITION DISTRIBUTION AFTER IN SITU HEATING

Figure 5.32 shows the A713 composition after in situ heating, during which time there is visual evidence of the dissolution of the eutectic and the diffusion of the solute into the centre of the globular grains. There is also evidence of the melting of the remaining eutectic at around 475℃, which would hinder the homogenisation process taking place during this heating experiment. In contrast to the AA7075 alloy, very little second phase precipitated out of the A713 composition samples during the cooling step of the in situ experiment. **Figure 5.32** (a) shows that there is mainly contrast at the grain boundaries, many of which have the extreme contrast that would be expected of an Fe-based intermetallic.

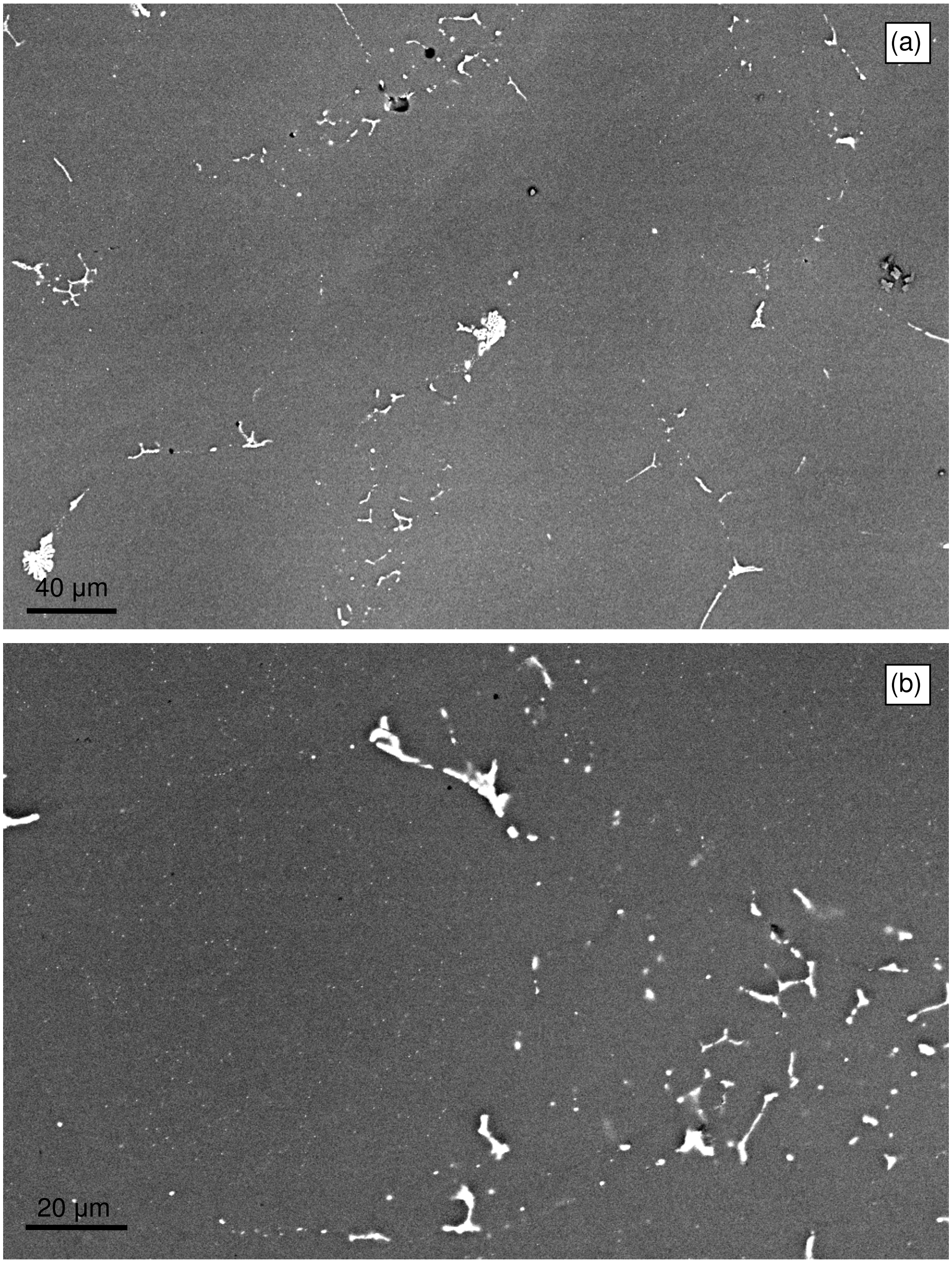

***Figure 5.32**: A713 alloy after in situ heating, with (a) showing the general structure, and (b) at a higher magnification, showing the fine precipitates distributed throughout the microstructure.*

Figure 5.32 (b) shows that there are fine, evenly-distributed precipitates throughout the structure of the A713 alloy after *in situ* heating. Owing to the location and size of these precipitates, it can be inferred that the type of homogenisation that occurs during the *in situ* experiment is far more effective in the A713 alloy than the AA7075 alloy. From this it can be deduced that the A713 composition is far more suitable for SSM casting when post-production strengthening is to follow, in the form of the traditional T6 type heat treatment, which includes solution treatment and ageing. Further investigation into the homogenisation and subsequent ageing processes would be required to reach a definitive result.

Figure 5.33 shows the different contrasts of phases present in the sample after *in situ* heating, followed by the composition of these phases, as determined by EDS analysis.

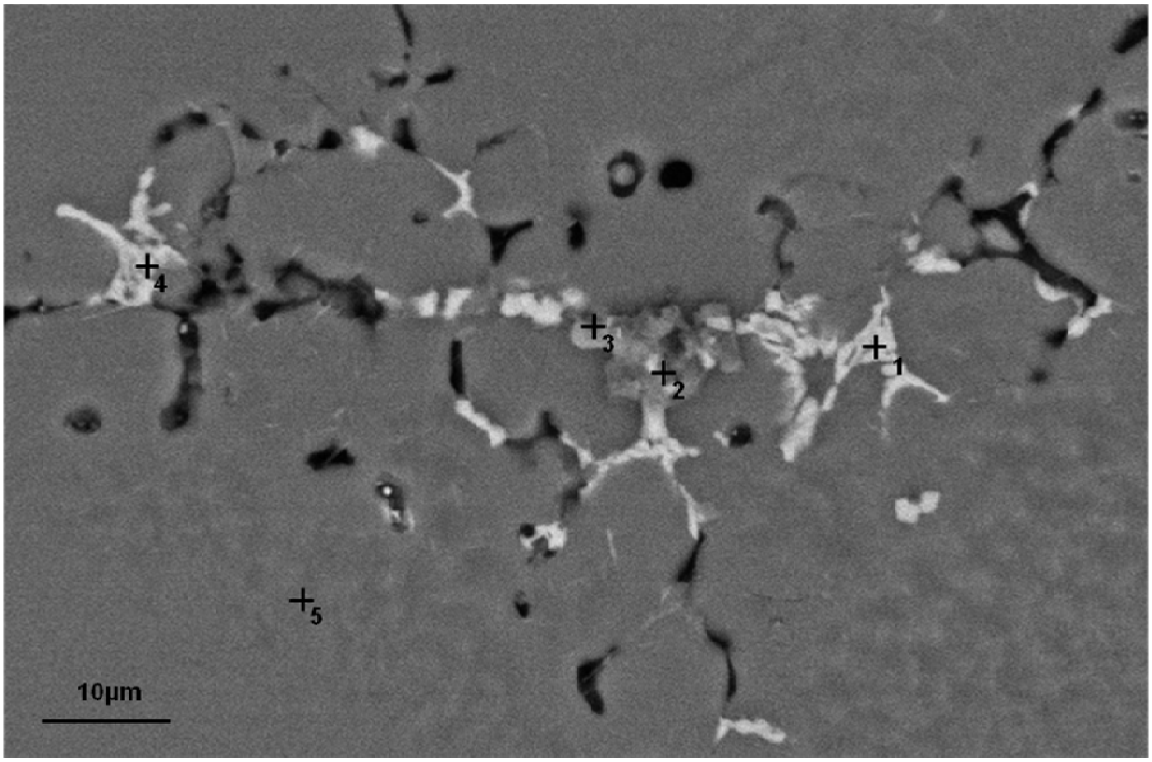

	Al		Zn		Mg		Cu		Fe		Si	
Point	Wt%	At%	Wt%	At%	Wt%	At%	Wt%	At%	Wt%	At%	Wt%	At%
1	52.4	71.4	1.4	0.8	0.6	0.9	39.3	22.7	6.1	4.0	0.1	0.2
2	82.0	89.6	3.2	1.5	2.1	2.6	11.2	5.2	0.7	0.4	0.8	0.8
3	81.5	89.1	1.7	0.8	2.4	2.9	10.2	4.7	3.8	2.0	0.5	0.6
4	58.0	74.8	1.6	0.9	1.2	1.7	27.5	15.0	11.2	7.0	0.6	0.7
5	91.5	95.8	5.3	2.3	0.5	0.6	2.4	1.1	0.0	0.0	0.2	0.2

Figure 5.33 *A713 SSM - EDS results on precipitates formed after in situ heating experiment.*

The high contrast phases seen in points 1 and 4 are copper- and iron-rich, with ratios approximately 70:20:6 (Al:Cu:Fe) of aluminium, copper and iron respectively, closely resembling the Al_7Cu_2Fe phase that forms during overheating of the low melting temperature solute rich phases that occur in the Al-Zn-Mg-Cu alloy series.

5.4.3. INCIPIENT MELTING DURING *IN SITU* HEATING

Figure 5.34 shows the progression of the microstructure of an A713 composition sample during an *in situ* heating experiment. The focus of this progression is on the occurrence of incipient melting. Incipient melting of the eutectic phases would occur at approximately 470℃, according to the DSC information at the start of the chapter. The extent of incipient melting can be monitored by tracking the evolution of the porosity within the structure[78]. The porosity is generally located within the interglobular regions and is surrounded by eutectic. As the eutectic dissolves, diffuses and melts, the surface area of the porosity will change. A basic surface area analysis of the visible porosity was performed on the micrographs in the progression in **Figure 5.34**. Porosity is located in the top left-hand corner of the RT micrograph. It is surrounded by small interglobular grains and eutectic. Another feature that is visible in this RT image is the lamellar substructure. As the experiment progresses and the temperature is raised, grain boundaries within the large globular are revealed, this may be as a result of the bulging out of existing grains during heating. These boundaries are visible from approximately 380℃. These images are BSE images and the boundaries are clearly defined. This type of boundary is often seen during recrystallisation.

The surface area and morphology of the porosity changes as the temperature increases. The percentage of surface area covered by porosity is measured and graphed at increasing temperatures. This is shown in **Figure 5.35**. The graph shows a sudden increase in the coverage of porosity at 470℃, which coincides with the incipient melting temperature of the zinc-rich phase. The more gradual increase in surface area coverage before this point can be attributed to the diffusion of the alloying elements from the solute-rich eutectic region into the surrounding grains.

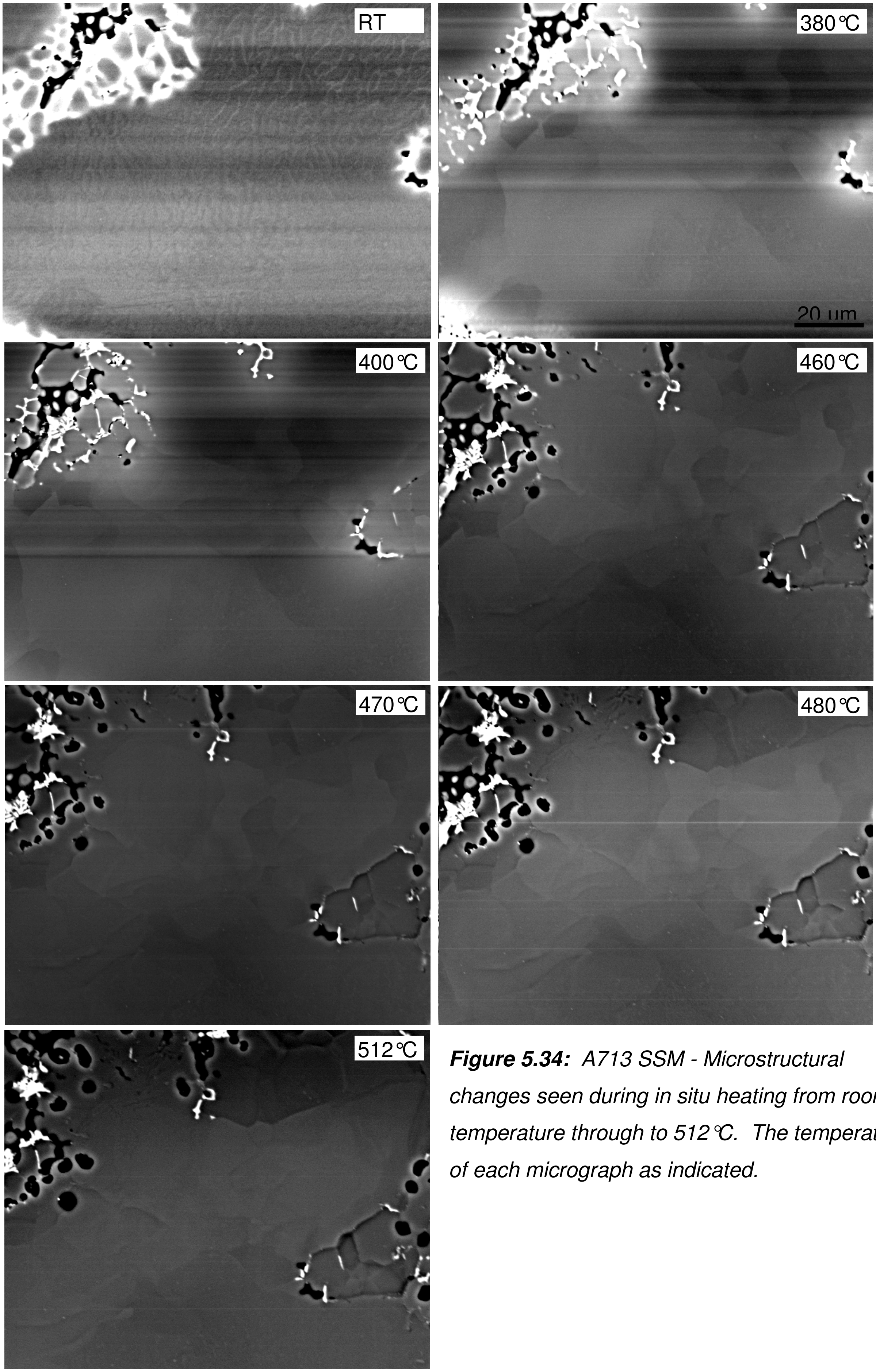

Figure 5.34: *A713 SSM - Microstructural changes seen during in situ heating from room temperature through to 512℃. The temperature of each micrograph as indicated.*

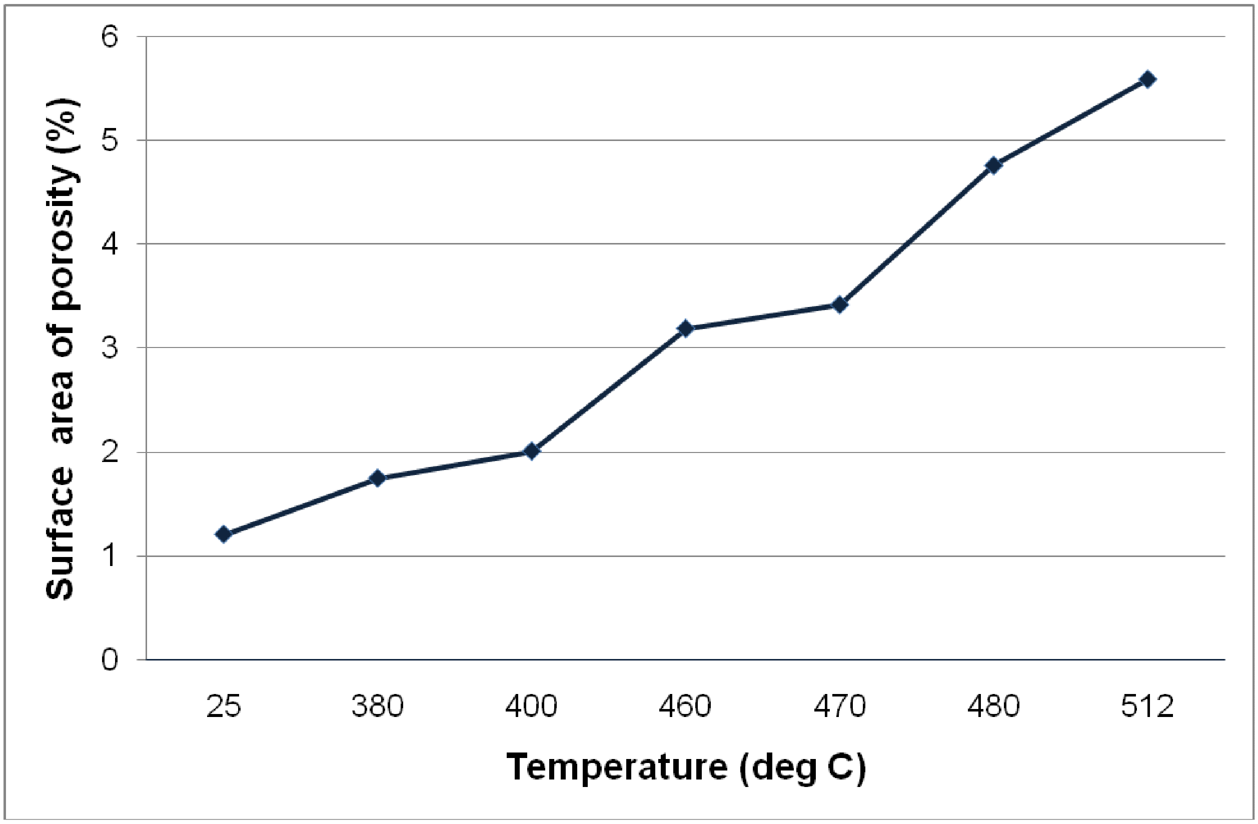

Figure 5.35: *Measure of the increase in porosity with increasing temperature, relating to the* in situ *microstructural progression for A713 in* ***Figure 5.34****.*

From the principles of quantitative metallography, a planar surface section with a planar fraction of porosity, A_A, is the same as the volume fraction, V_V, of the porosity. This may not necessarily hold true in the case of *in situ* heating, where the presence of a free surface and the effects of gravity on the melting of the low melting point phases may affect the relationship. Also, the presence of entrapped gases, which is lower in SSM casting when compared to traditional casting methods, may also affect the relationship on heating. Therefore, the results of increased porosity on the planar surface during heating is a guide to the fact that once the incipient melting temperature is reached, there is a large change to the microstructure which will have an adverse effect on both the homogeneity within the structure and the integrity of the final part.

5.5. SUMMARY OF OUTCOMES OF CHAPTER 5

The pertinent outcomes of the investigation into post solidification heat treatments are:

- Thermal analysis and DSC show the presence of an incipient melting peak that falls within the solution treatment temperature range for both the AA7075 and A713 alloys. It also shows the size of the peak associated with the A713 alloy is smaller than that of the AA7075 alloy.

- The incipient melting peak can be removed by careful and lengthy homogenisation treatments.
- Zn diffuses more easily in the less complex A713 alloy.
- Heating near or above the incipient melting temperature has an effect on the morphology of the porosity.
- *In situ* EBSD orientation analysis shows the removal of the internal misorientation substructure during heating.

CHAPTER 6: SOLIDIFICATION MODEL

The solidification path that is followed during semi-solid metal rheocasting is that of a multistage solidification process that deviates considerably from the conventional solidification of alloys, both in net-shaped casting and ingot casting. The following Chapter discusses the solidification path for this SSM casting operation, based on the microstructural evidence presented in the experimental results from previous chapters and on the theory presented in the literature review.

6.1. TEMPERATURE AND TIME PROFILE DURING SOLIDIFICATION

The schematic diagram in **Figure 6.1** is based on a similar figure by Fan and Liu[79] for the rheo-die casting (RDC) process. The RDC process is a one-step processing technique for manufacturing near net-shaped components. The SSM Rheocasting process for this investigation is similar in concept, although the stirring process utilised an induction stirring technique, rather than a twin-screw melt shearing device. The schematic in **Figure 6.1** is constructed using the time-scale and approximate cooling rates from the CSIR rheocasting process, as described in **Chapter 3**.

Figure 6.1 shows a temperature *vs* time curve that breaks the process down into the different stages experienced during the SSM casting process. There are two distinct stages to the solidification path, namely, primary solidification, which occurs between the maximum temperature of 700℃ until the end of the slurry production stage, and secondary solidification, which occurs from the transfer of the slurry to the HPDC through to the solidification in the die itself.

Figure 6.2 illustrates, with the aid of schematic diagrams along a portion of the temperature *vs* time curve, the progression of the solidification process from nucleation through to the HPDC step as interpreted in the present study.

The first image in the progression in **Figure 6.2** shows the onset of nucleation, which occurs at the start of the semi-solid slurry production stage. The second image shows that the initial growth of the nuclei during slurry production is cellular. At this point, the turbulence is not high enough to affect the growth mode and the collisions between solid nuclei are minimal. In addition, the diffusion boundary layer is still thick and the convective mixing zone (see **Figure 2.20**) does not penetrate between the dendrite arms, thus allowing for a dendritic growth mode. In the third image there is a thickening of the dendrite arms and a morphology change from dendritic to rosette, as the solidification process progresses. This is a result of the turbulence during stirring and the reduction in the boundary layer thickness.

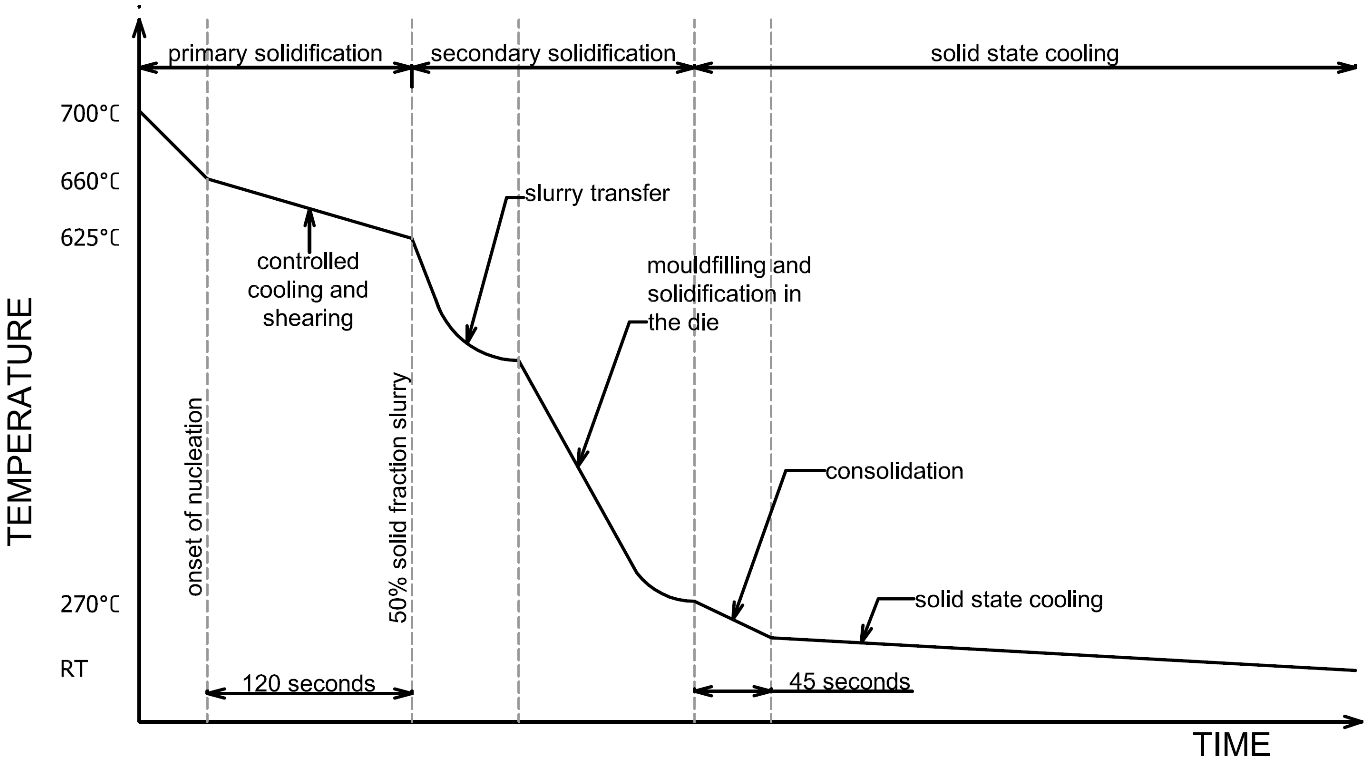

Figure 6.1: *Schematic illustration of solidification profile for the SSM Rheocasting process.*

Again referring to **Figure 6.2**, at the end of the semi-solid slurry production stage, the grains have a globular morphology, which gives the semi-solid cast structures their characteristic morphology. During slurry transfer, the slurry no longer experiences any turbulence or shearing and there is a more rapid decrease in temperature. During this stage, the solid-liquid interface is stable and the growth front progresses with a planar morphology. The degree of mixing in the melt changes and so does the composition gradient in the liquid, resulting in coring rings around the globular grains during further growth. Finally, the solid-liquid interface again becomes unstable, as the thermal and solutal concentrations change dramatically from a stirred melt with complete mixing to one with no stirring and diffusional mixing. The growth morphology of the solid becomes cellular and protrusions grow from the interface to form cellular protrusions that extend from the globular grains into the solute-rich melt.

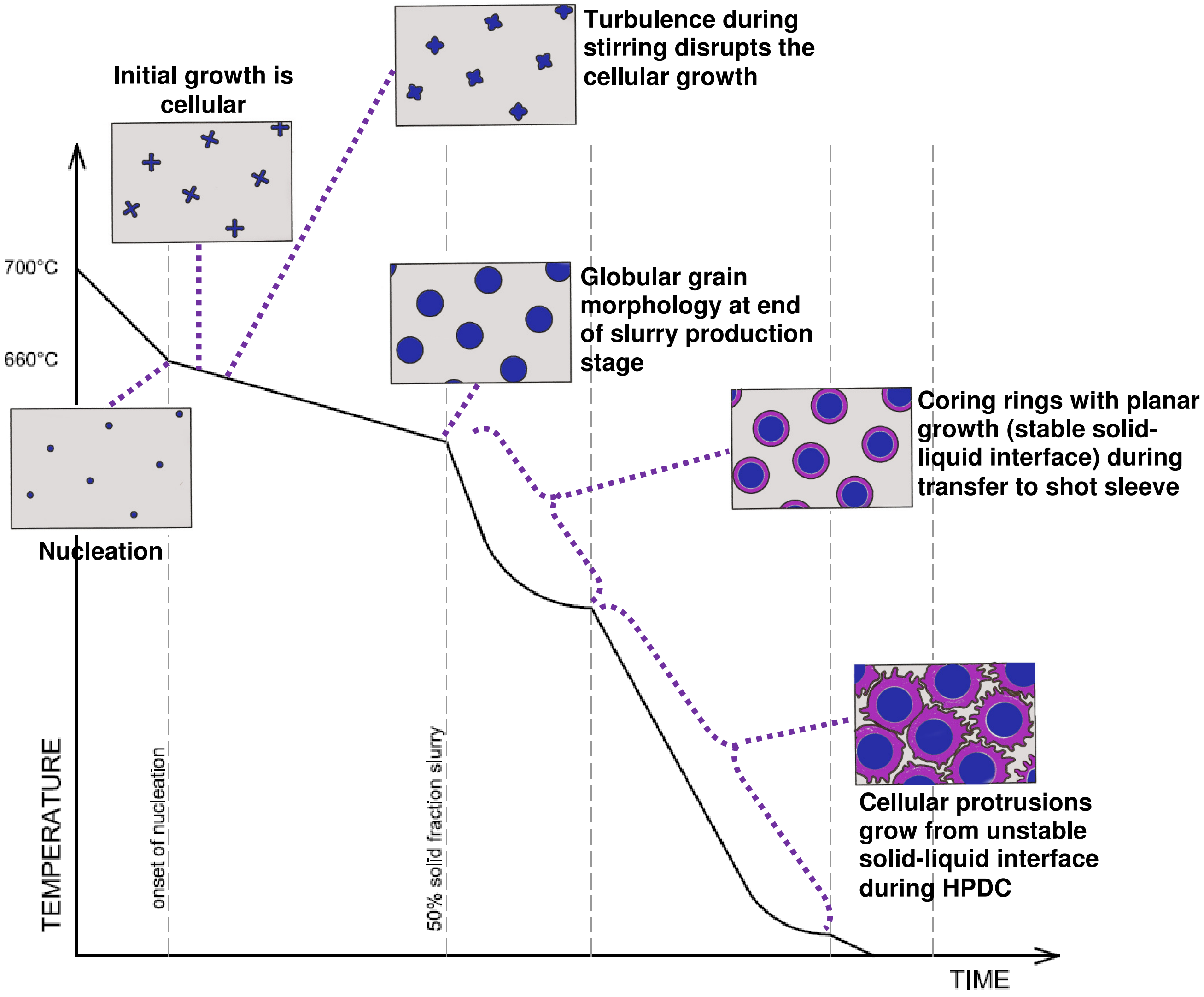

Figure 6.2: *Solidification progression with schematic diagrams that indicate the microstructural evolution.*

6.2. SOLIDIFICATION PATH

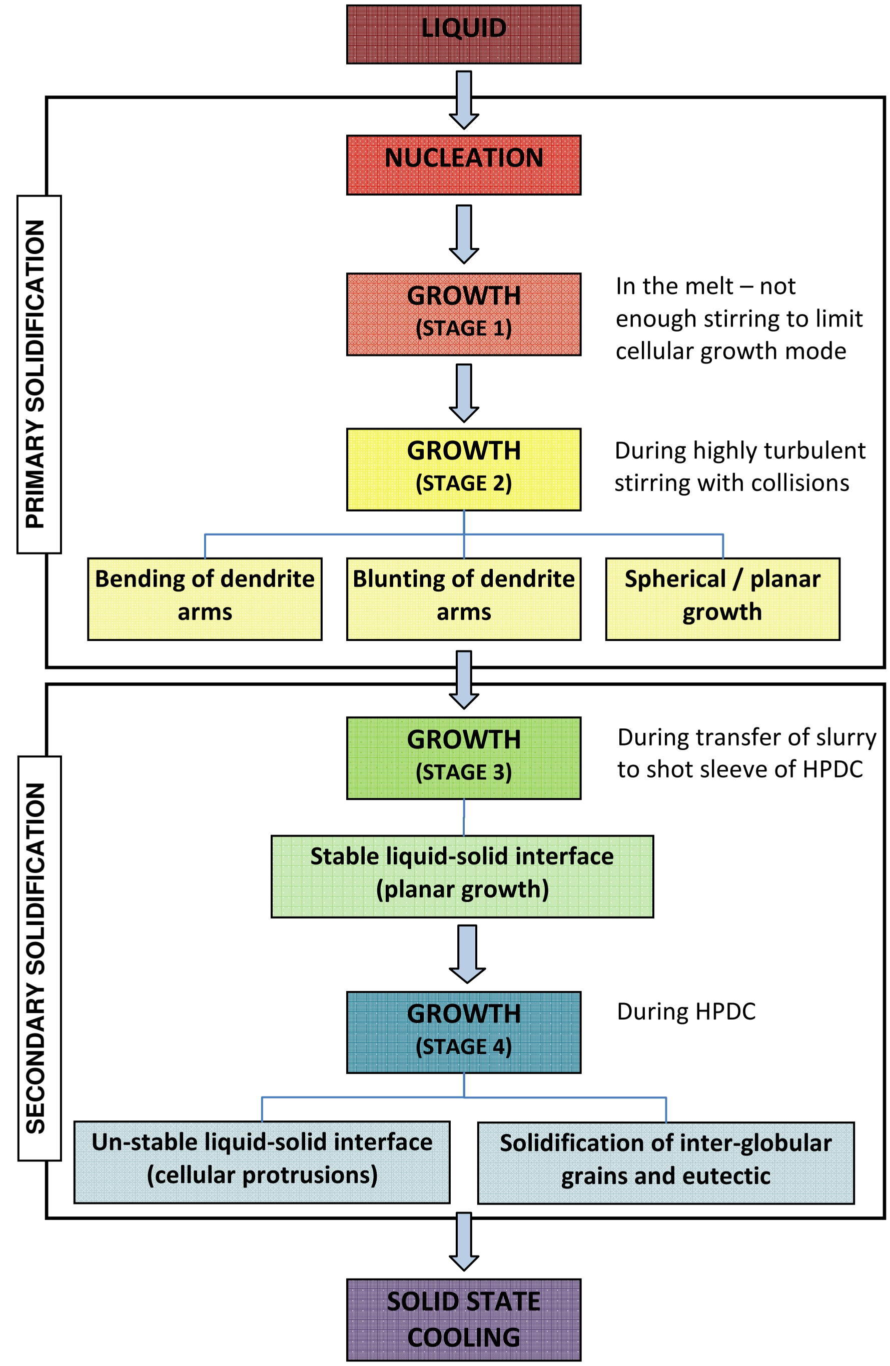

Figure 6.3: *Flow chart indicating the steps of the semi-solid casting process*

The morphology of the grains formed during primary solidification is a result of the controlled cooling and induction stirring of the slurry production step. As solidification progresses, the solid will experience high shear and a very high collision rate, until a 50% solid fraction is reached. The shear rate, solutal distribution and thermal distribution will affect the morphology and the interface stability as the nuclei grow into the globular grains that are associated with the semi-solid cast microstructure.

There are several conflicting theories about the mechanisms for the globularisation of the grains during stirring, which were discussed in greater detail in **Chapter 2.3.3**. These can generally be divided into two main themes: dendrite fragmentation and spherical growth.

6.2.1. GROWTH STAGES

During primary and secondary solidification, there are four distinct stages of growth that can be pinpointed by analysing the globular grains within the microstructure, as presented in **Figure 6.3.** The image in **Figure 6.4** shows a globular grain from a semi-solid cast AA7075 composition alloy. The dotted lines superimposed on the image represent the different growth stages experienced by a grain during the solidification process. The colours of each dotted line correspond to the stage of growth shown in **Figure 6.3**, namely growth stage 2 in yellow, growth stage 3 in green and growth stage 4 in blue.

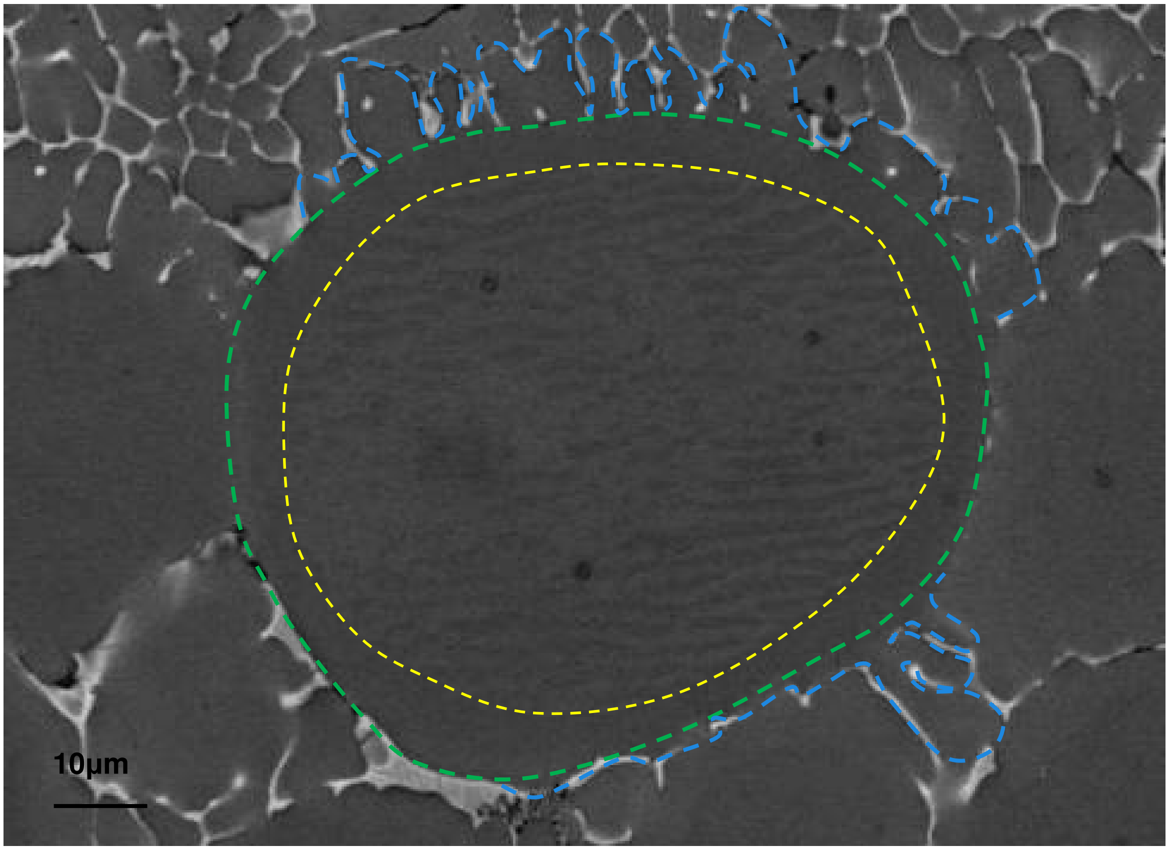

Figure 6.4: *SSM cast grain, with dotted lines indicating the different stages of solidification.*

The central area of the grain, surrounded by the yellow dotted line, exhibits the lamellar type substructure configuration, which was observed in **Chapter 4.2.4**. This stage of growth, referred to as growth stage 2 in **Figure 6.3**, occurred during the turbulent stirring of the slurry production stage.

The area of the grain between the yellow and green dotted line in **Figure 6.4** has been referred to as the coring ring in the previous chapters. This ring is different to the centre of the grain, in that it does not exhibit any of the sub-structure seen at the centre of the grain. The contrast seen in this BSE image indicates that there is also a change in composition distribution in this area when compared to the centre of the grain. Furthermore, the morphology of this band of growth indicates that the solid-liquid interface during this growth stage was stable and the growth front was planar. This is growth stage 3 and during this stage growth occurred during the transfer of the slurry to the shot sleeve of the HPDC.

The next stage of growth, stage 4, is outlined by a blue dotted line, which traces the cellular protrusions that extend from the globular grain into the interglobular region. During this stage, the solid-liquid interface has become unstable, and the growth front is cellular. This growth stage was the last to occur before full solidification and the formation of the solidified second phase. Based on the predicted timeline, this would have occurred during the filling of the die at high pressure and the consolidation period prior to removal of the final cast part from the die itself.

6.2.1.1. GROWTH STAGE 2: EVOLUTION BY DEFORMATION

The growth that occurs during stage 2 causes the globularisation of the semi-solid microstructure. Evidence taken from this stage is used to explain the globularisation mechanisms.

The EBSD map in **Figure 6.5**, shows that, within the general microstructure of the SSM cast samples, some grains exhibit a circular substructure configuration and others a lamellar configuration, while there are also some grains that exhibit no substructure at all. The presence of these different substructures can infer that, within the growth stage during slurry production, there are different types of growth occurring, each of which is affected by the surrounding slurry in different ways.

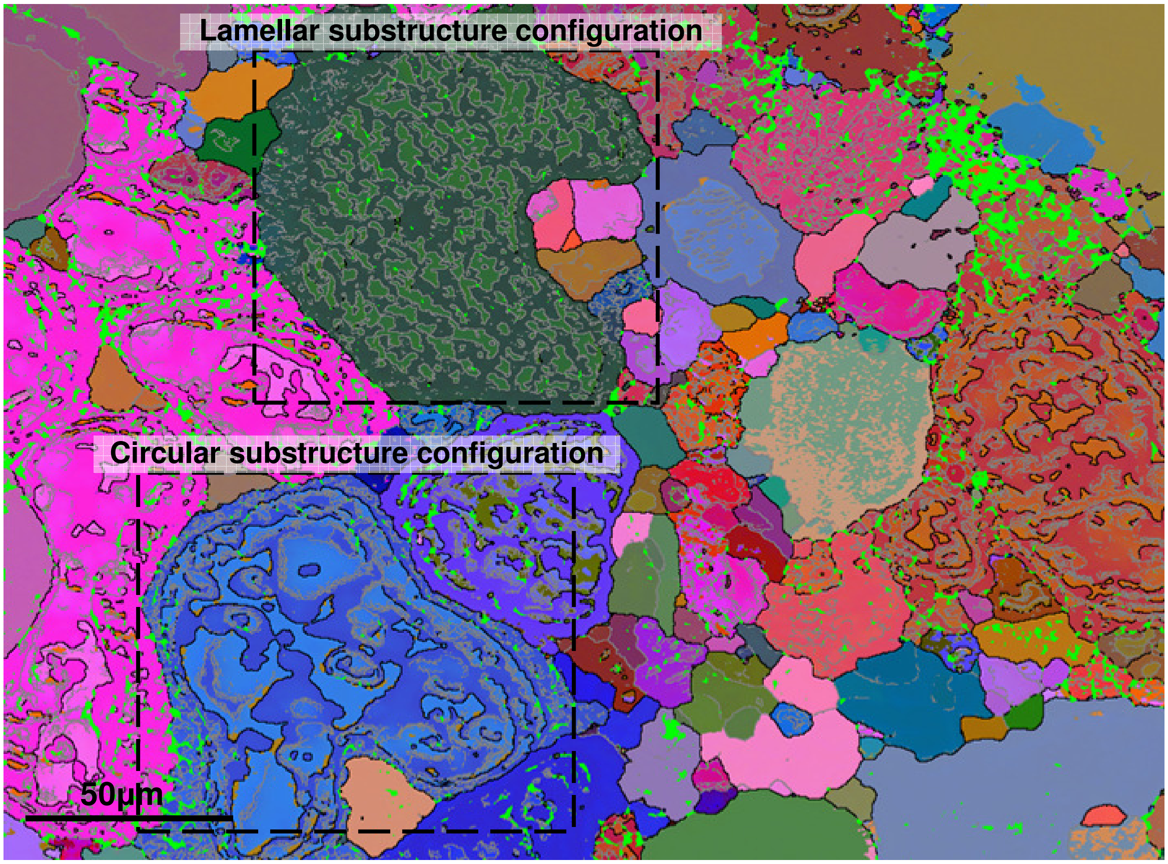

Figure 6.5: *EBSD map showing the areas with the different substructure configurations.*

The literature shows conflicting theories as to the true mechanisms involved in the production of the globular grains.

According to one school of thought, the mechanisms are deformation-based, and include fragmentation, melting, bending and twisting, as a result of the turbulent fluid flow. Evaluating the microstructure and the substructure from a deformation point of view leads to the interpretation of growth stage 2 as being defined as having three possible mechanisms that occur within the same range. Firstly, that the mechanism resulting in the circular substructure is a dendrite arm bending deformation process. Secondly, that the mechanism resulting in the lamellar substructure is a blunting of the dendrite arms as solidification proceeds. And lastly, that there are grains that exhibit no substructure, this indicating that their growth modes are spherical. From this it can be determined that there are elements of each of the different mechanisms that are occurring simultaneously. (These mechanisms are presented in the Literature Review.)

Simple 2D schematic representations of the different mechanisms that occur during the induction stirring step of the rheocasting process are illustrated in **Figure 6.6**. The basic shape of the solid represented in the images is that of a six-armed symmetrical equiaxed dendrite, growing in a free

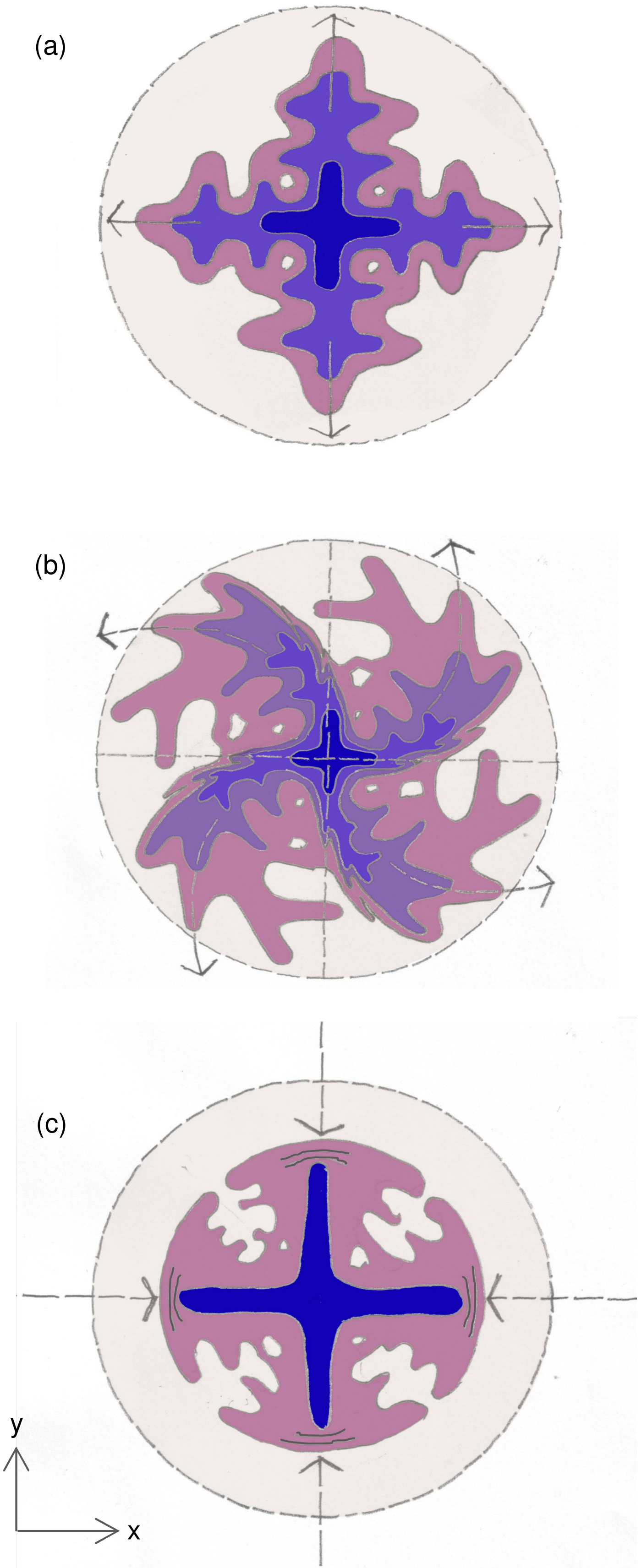

Figure 6.6: *Schematic diagrams of (a) dendritic growth, (b) dendrite arm bending, and (c) dendrite arm blunting.*

liquid, similar to the example discussed in **Chapter 2.3.1.4.** (The dendrite arms in the z-direction have been ignored in the interest of clarity.) The dotted circular line in each image represents a common maximum volume/area for the final grain to occupy. In each schematic, the arrows indicate the direction of the growth of the primary dendrite arms. Generally, the make-up of a grain represents evidence of its processing history. Therefore, analysis of the grain's features, such as grain boundaries, morphological changes and elemental concentration variations can aid in the interpretation of the mechanisms that have shaped its growth process.

The initial growth morphology is dendritic and this is represented by the four primary arms, in blue, at the centre of the diagrams in **Figure 6.6** (a), (b) and (c). The variation in colour as the solid grows represents the time progression of the continuous growth of solid during solidification. The schematic diagrams are colourised in order to aid interpretation, and each colour captures the growth at a moment in time during the solidification process.

Figure 6.6 (a) shows, schematically, a situation where there is no stirring in the liquid. Therefore, there is equiaxed dendritic growth in every direction. The primary arms grow in the x- and y-directions. As the secondary arms form and grow, their growth will terminate once their growth path impinges on that of another dendrite arm or surrounding solid. This termination of growth will result in areas of entrapped liquid, as illustrated by the four white circles in the final layer of growth seen in the image.

Figure 6.6 (b) shows the growth of an equiaxed dendrite. It is growing in the presence of laminar and mild turbulent flow in the melt. This flow causes a rotation of the equiaxed grain during the growth process, within a free liquid. The grain also experiences compressive forces from the pressure of the fluid. (The effect of collisions has not been considered at this point.) This type of flow causes deformation of the dendritic growth by dendrite arm bending, during the simultaneous growth of the dendrite arms, both in length and with lateral fattening of the arms. The bending and applied strain on the grain during growth results in changes in misorientation.

In the schematic in **Figure 6.6** (b), the progression of the growth of the solid with time is represented by a slightly different colour. Each colour stage has variations in orientation, as a result of changes in the growth direction during solidification. The rotation caused by the fluid flow incurs a greater amount of strain on one side of the main dendritic growth axes and growth is impeded in this direction. The opposite side of these primary dendrite arms are sheltered from the full force of the strain, resulting in unconstrained dendritic arm growth in these areas. Growth flaws, or faults, do occur during the growth of the solid and introduce slight misorientation variations within the crystal structure. One would expect the dislocations that arise as a result of the deformation of dendrite arms to be annihilated as a result of recovery at the sustained high temperature. The fact that they are maintained, suggests that the dislocations do not result from deformation, and that the misorientation is the result of faults in the crystal orientation. The occurrence of these faults is increased with the conditions experienced during turbulent flow. Therefore, localised misorientations are to be expected within the grains, as a result of these growth flaws or faults.

The mechanics of the deformation schematic set out it **Figure 6.6** (b) would only occur in extreme cases where the shearing conditions in the liquid result in a pure rotation of the solid globules. Even though this particular situation of pure rotation is unlikely, the turbulence condition experienced during the slurry production stage of SSM casting would cause some form of rotation of the globules in the liquid. The true forces and conditions experienced during the slurry production stage are likely to be a combination of uni-directional shearing, rotation and impingement from neighbouring globules.

By referring to **Figure 6.5** and the corresponding misorientation profiles in **Figure 4.27**, the presence and location of LAGBs and HAGBs, and their associated misorientation degrees, do allude to their origination being from some form of strain or deformation. **Figure 6.7** shows simplified schematics of the typical cumulated misorientation profiles that are associated with the lamellar configuration and circular configuration substructures. These schematics illustrate the most noticeable trends attributed to the substructures: the paired increase and decrease in misorientation that repeats across a grain, the plateau areas within and between the misorientation pairs, and the regularity of the occurrence of these pairs (non-randomness). According to the deformation model described in **Figure 6.6** (b), the predicted positions of deformation-induced boundaries from strain experienced during solidification can be seen to coincide with changes in misorientation on the misorientation profile from a circular substructure configuration, seen in **Figure 4.27**. The circular substructure seen in **Figure 6.5** is made up of swirls of both HAGBs and LAGBs, and their arrangement within the grains corresponds with the projected positions indicated in the schematic image of **Figure 6.6** (b). This model illustrates the HAGBs being the result of dendrite arm twisting about the z-axis, as well as of bending in the x-y plane. In addition, in areas with narrow spacing between the successive growth layers, the strain gradient is high, resulting in dislocation pile-ups and HAGBs. The cumulative misorientation profile for the circular substructure configuration, as seen in **Figure 4.27** and illustrated schematically in **Figure 6.7**, shows that the majority of the misorientations are between 15-18°, and, as such, are considered to be HAGB misorientations. These HAGBs are paired and there are plateau areas within and between the misorientation pairs. When referring to the cumulative misorientation profile for the circular substructure in **Figure 4.27**, there are 15 boundaries over the grain diameter of approximately 90μm, with the plateau areas ranging between 3 and 15μm in width.

Figure 6.6 (c) illustrates the effect of the compressive force on the growth of an equiaxed grain. This force stems from the turbulent flow during the stirring process. The dendritic growth is deformed by dendrite arm blunting. Growth in the direction of the x- and y- axes is slowed by the pressure that these primary arms experience. The secondary arms grow laterally and thicken with little disruption, until their growth is stopped by impingement. Strain is introduced into the lattice by the compression at the growth front. This results in slight rotations in the growing crystal to accommodate the strain. Evidence of this strain can be seen as bands of slight misorientation changes, such as those evident in the lamellar substructure configuration in the EBSD map in **Figure 6.5** and **Figure 4.26**, and the corresponding misorientation profile in **Figure 4.28**. The cumulative misorientation profile for the lamellar configuration substructure is illustrated schematically in **Figure 6.7**, and shows that the majority of the misorientations are between 8-10°, and, as such, are considered to be LAGB misorientations. These LAGBs are paired and there are plateau areas within and between the misorientation pairs. When referring to the cumulative misorientation profile for the lamellar substructure in **Figure 4.26**, over the grain diameter of approximately 80µm, there are 42 boundaries, with the plateau areas ranging between 2 and 5µm in width. Therefore, the frequency of the boundaries is higher in the lamellar substructure.

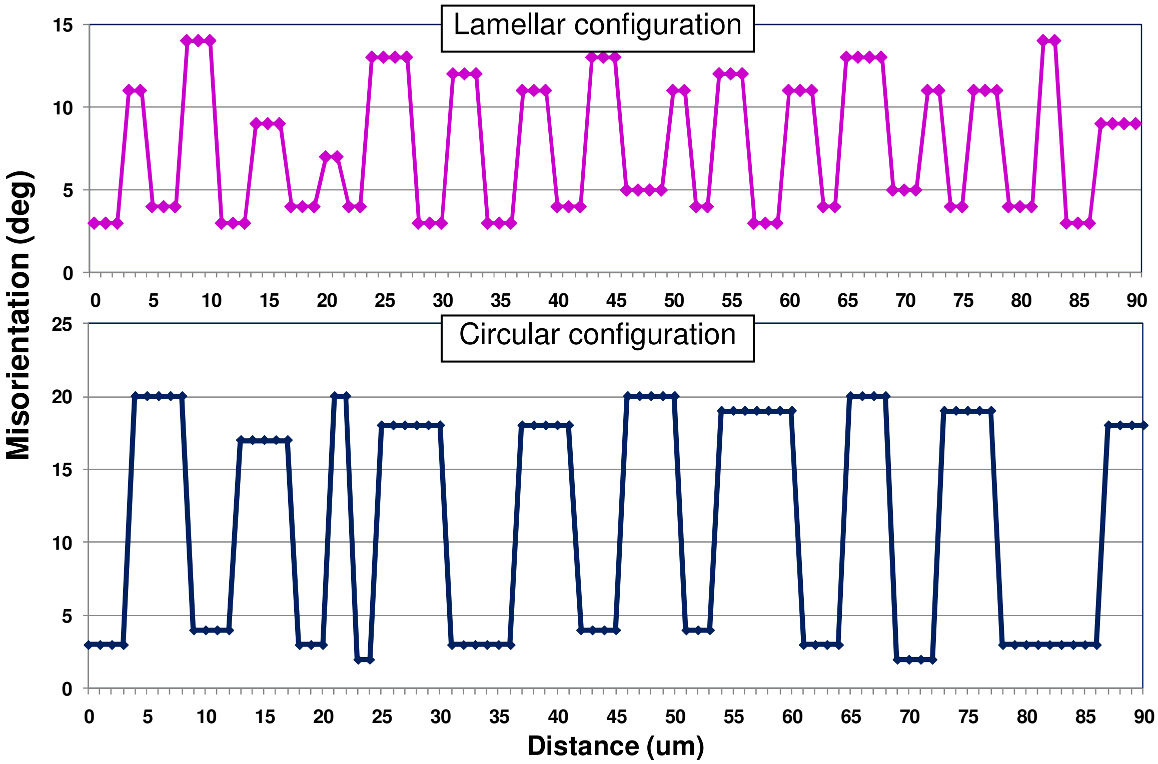

Figure 6.7: *Schematic graph illustrating misorientation trends associated with the circular and the lamellar configuration substructures.*

While the deformation pattern that is illustrated in the schematic diagrams agrees in many ways with the location of the internal grain boundaries of the substructure, there are, owing to the nature of the described mechanism, some features that should be present, but that are conspicuous in their absence. The primary missing feature is entrapped liquid. Entrapped liquid is associated with the growing together of dendrite arms and it would produce solute enriched regions within the primary globular grains. This feature has not been detected within the globular grains in the present study.

6.2.1.2. GROWTH STAGE 2: SPECIAL GROWTH ORIENTATION RELATIONSHIPS

The misorientation profiles for both the lamellar and circular configuration substructures, for both alloys, exhibit grain boundary misorientation increases, paired with subsequent decreases. The occurrence of these pairs, as well as the actual misorientation angle range, is regular. This regularity indicates that the boundaries themselves (their particular misorientation angles and their locations within the grain) are not produced by a random process, such as deformation of dendrites in a turbulent fluid flow. A high incidence of boundaries with the same misorientation angle and the regular intervals at which they occur indicate the presence of some type of special grain boundary. An example of this is twinned boundaries. Twinned boundaries in dendritic solidification are a result of "feathery grains", which are made up of twinned dendritic grains[80]. Generally, once a feather grain has nucleated, the grain grows and forms a series of twinned and un-twinned lamellae[81]. Twinned boundaries have ideal misorientation relationships with the crystal orientation and form sigma3 boundaries. The boundaries associated with the substructures in the SSM cast microstructure do not exhibit the sigma3 type that indicates the presence of twinning. Therefore, although there may be some particular special boundary relationship associated with the substructure configuration seen in the SSM as-cast microstructure, it is not the result of twinning. This is in agreement with Li *et al*[82]*,* who stated that one never observes any twins in rounded grains during the use of forced convection techniques, where shear stresses are involved. Such are the conditions associated with SSM rheocasting.

Figure 6.8 shows a portion of the EBSD map of SSM cast AA7075 composition alloy, seen previously in **Figure 6.5**, with an area selection highlighted by the dotted line. The {002} and {111} pole figures have been generated for that area, showing the density contours. If the globular crystal were perfect, then the pole figure plot would indicate only one position for each pole direction. However, in this case there is a distinct shift in the pole directions, as indicated by the density contours. The {111} pole figure shows an equivalent shift of all the poles, whereas the {002} pole figure demonstrates that the crystal is rotated about one of the {002} poles, as indicated by the dashed line on the {002} pole figure.

The growth direction during solidification is expected to be in the <100> direction[83]. The rotation about the main growth direction can be attributed to minor growth faults that occur as atoms add to the solid-liquid interface during solidification by cellular growth.

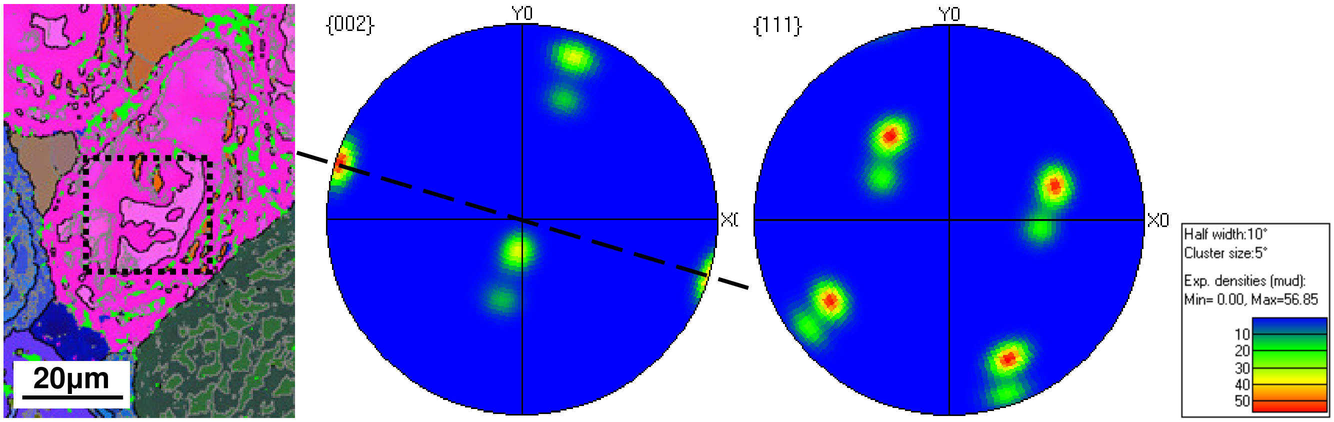

Figure 6.8: *Contour pole figures for the selected area, exhibiting a circular substructure configuration, in the EBSD map (SSM cast AA7075composition alloy).*

6.2.1.3. GROWTH STAGE 2: EVOLUTION BY CELLULAR GROWTH

Based on the literature, the second school of thought regarding the mechanisms of globularisation during turbulent mixing is one of cellular or spherical growth. Molenaar *et al*[45] [84] state that cellular growth morphology is present from the onset of solidification. Growth of solid occurs by constant fluctuations, on a micro level, between stabilisation and destabilisation of the interface (planar and non-planar), where the average growth will still appear to be planar on the scale of an entire grain. During dendritic and rosette type growth, evidence of entrapped liquid would be visible within the globular grains of the fully solidified structure. However, there is no direct evidence of this in the microstructural evaluation of the semi-solid rheocast microstructures for these particular alloys, this substantiating the theory of cellular growth as the globularisation mechanism associated with SSM casting.

The compositional analyses of both alloys in the as-cast condition shows an almost uniform solute distribution across the bulk of the individual grains, with no distinct coring rings and only slight fluctuations in solute distribution. This can be seen in **Figure 4.30** and **Figure 4.18**. and is indicative of segregation variations that occur over distances equivalent to small cell spacings, rather than over a full grain.

Owing to the solute content in the liquid, there are instances of constitutional supercooling within the slurry melt, as well as the presence of negative thermal gradients. These conditions result in the destabilisation of a planar interface, initially seen as undulations on the surface that may later develop into protrusions. Protrusions that have a cellular growth morphology form and grow perpendicular to the liquid-solid interface, regardless of crystal orientation[22]. Solid forms at the solid-liquid interface as individual atoms are added to this interface during a continuous growth process. Therefore, the atoms have a crystallographic orientation that aligns with the growth direction of the bulk. When cellular protrusions first form on the interface, they grow radially, and the orientation may vary locally over a distance relative to the cell spacings, while still complying with the overall crystallographic orientation of the bulk solid. Cellular protrusions, or nodules, have a circular geometry and a large radius of curvature, proportionate to their lengths. Many protrusions may cover the entire surface of the 3D globular grain. This can be seen in **Figure 6.9**. During the continuous growth, faults occur as the atoms add to the interface to form the radially growing cellular protrusions. This results in misorientations relative to the main growth direction.

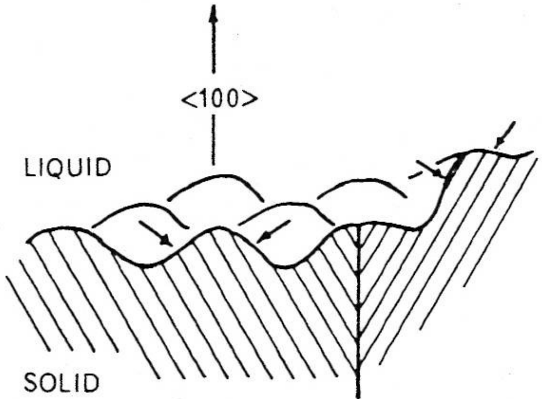

Figure 6.9: *schematic representation of nodes developing on the surface of a solid in an arrayed arrangement, with growth in the <100> direction*[22].

Figure 6.10 shows schematic illustrations of cellular growth scenarios. The variation in colour as the solid grows represents the time progression of the continuous growth of solid during solidification. The schematic diagrams are colourised in order to aid interpretation, and each colour captures the growth at a moment in time during the solidification process. The growth mode fluctuates between near-planar growth and cellular growth.

Figure 6.10 (a) shows a schematic diagram of the consecutive growth layers of an idealised grain during solidification in the presence of turbulent fluid flow. The globularisation mechanism is one of cellular growth. The nucleus at the centre has undulations that are indicative of cellular growth. As the solid grows into the liquid, the growth shows an overall distribution that appears as planar growth. At some point, the interface is destabilised to a point where the nodules grow and the cellular protrusions are distinct. The geometry is such that the radius of curvature is still large and the lengths of the protrusions are not great enough for the growth mode to transition to that of dendritic growth. The curvature of the valley between the protrusions is large and there is no liquid entrapment, which is characteristic of dendritic growth. The growth of these cellular

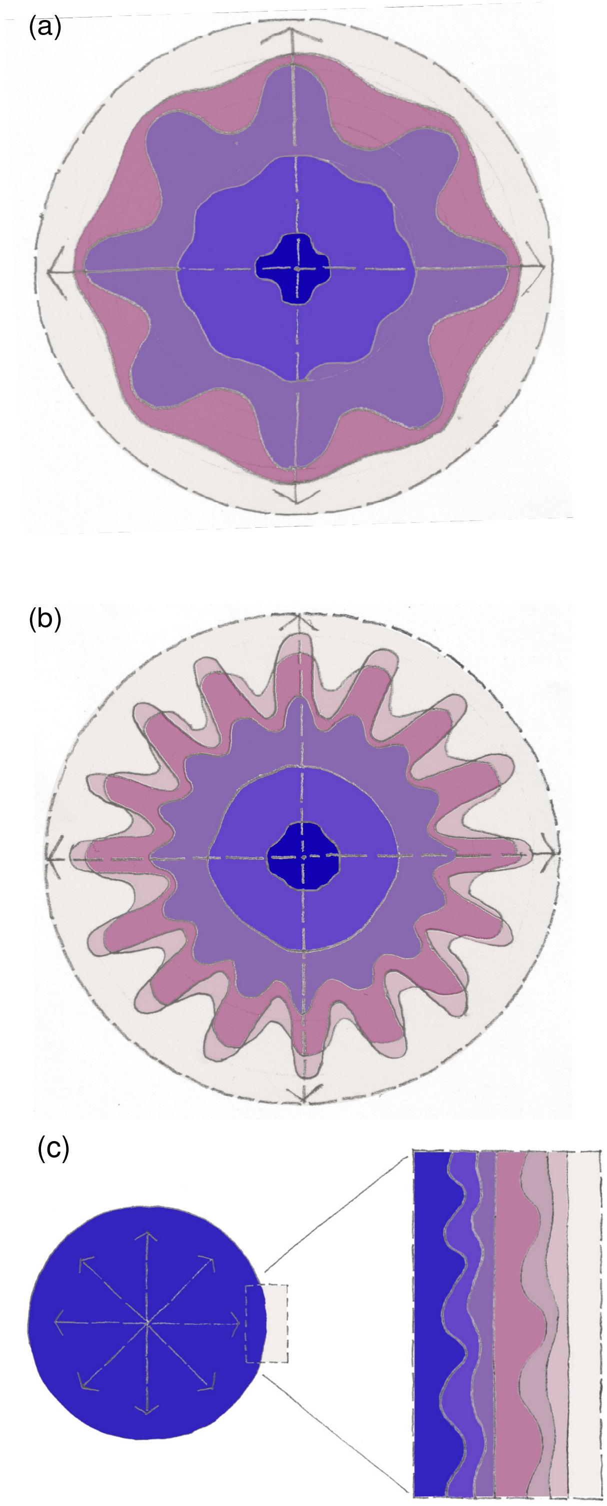

Figure 6.10: *Schematic diagrams of (a) cellular growth with alternating dominance of cellular and planar growth, (b) cellular growth with effects of constitutional supercooling and thermal gradient in the melt, and (c) area magnification of cellular growth at the interface of the solid and liquid.*

protrusions changes over time. The conditions favour the growth of the interface in the valleys and hinder the growth of the tips of the protrusions. The liquid-solid interface growth morphology approaches that of near-planar growth.

Figure 6.10 (b) shows a schematic representation of cellular growth where the radius of curvature and length of the cellular protrusions are affected by variations experienced in the turbulent melt. The growth pattern for the first three colours (where each colour change represents time progression during solidification) mimics that illustrated in **Figure 6.10** (a). Beyond the first three colours, the subsequent colour, pink, indicates a more dramatic growth of the cellular protrusions. The radius of curvature begins to decrease and the length increases. The growth mode approaches a dendritic morphology, where the shape is that of rosette cellular growth. The final layer of growth shows that the conditions favour the growth of the interface in the valleys between the protrusions, while the tips have extended into a superheated area of the liquid and the tips of the protrusions are melted back. The net effect of these combined growth segments is an increase in the radius of curvature of the protrusions. This eliminates the possibility of entrapped liquid, and the overall diameter of the grain continues to increase with a global growth morphology that appears planar.

Figure 6.10 (c) shows a schematic globular grain, with radial growth directions indicated by the arrows. An area at the solid-liquid interface has been highlighted and the growth at the interface of that area has been magnified. The variation in colour, as the solid grows, represents the time progression of the continuous growth of solid during solidification. The cellular protrusions form when there is a destabilisation of the interface and, as time progresses, the morphology of the protrusions changes when the growth at the valley of the protrusion increases and begins to level out with the tip. When this occurs, the interface approaches a planar growth mode. This fluctuation in growth morphology happens continuously throughout the solidification process. When nodules form on the interface, the direction of the growth of the tip is not dominant and the direction does not necessarily align with the crystallographic orientation of the whole. The nodule grows radially in all the free directions with equal speed. This gives the protrusion the typical large radius of curvature of growth that is associated with cellular growth. Considering that the diameter of the protrusion (which is similar in size to the length of the protrusion) is much smaller than the diameter of the whole grain, it is unlikely that liquid will become trapped between the cells. Hence, an 'inter-cellular solute enrichment' is not visible in the solidified globule. Consequently, the composition profile appears as if planar growth has occurred and distinct coring rings are not seen. The radial growth of the protrusion has slight misorientations to the alignment of the bulk; therefore, each cell does not grow at the perfect orientation relative to the whole grain. Misorientations also result from growth faults that occur during continuous growth. For a particular grain, the level of misorientation across the grain is more or less regular and is related to the cellular spacing and the rate of progression of the growth front.

6.3. SUMMARY OF OUTCOMES OF CHAPTER 6

The pertinent outcomes of the investigation into solidification path followed during SSM casting are:

- A temperature-time profile was mapped for the CSIR SSM rheocasting process and the morphological and compositional information from the previous chapters was used to relate the evolution of the SSM microstructure to this profile.

- An interrogation of two different theories thought to describe the mechanisms involved in the formation of the globular grains that are characteristic of the SSM casting process was performed. The theories are: a deformation theory and a cellular growth theory. The results from the previous chapters offer support for the cellular growth theory.

CHAPTER 7: DISCUSSION

The main areas of interest identified from the results in the preceding chapters will be discussed in this section. The discussion will refer back to the figures in **CHAPTER 4** and **CHAPTER 5**.

The main objective of this investigation was to determine whether SSM casting, and, more specifically, the CSIR Rheocasting process, was a viable alternative for the production of high strength parts for the automotive and aerospace industries. In order to achieve this goal, the SSM cast samples needed to fulfil certain basic requirements with regard to structural integrity, grain morphology, size and distribution, and age hardenability. All cast structures exhibited segregation, on both a macro- and a micro-scale. For this reason, the main areas of interest were: the segregation associated with the as-cast microstructure; and the effect of heat treatment conditions on the homogenisation processes that were needed prior to effective precipitation hardening.

7.1. STRENGTH POSSIBILITIES IN SEMI-SOLID CAST SAMPLES

The results from the T6 heat treatments showed that the maximum strengths achievable with the SSM cast structure were dependent on the extent of homogenisation achieved prior to ageing. For both the AA7075 and A713 alloys, the samples that were solution treated at 460°C (below the incipient melting temperature), exhibited hardness values higher than those from samples solution treated at 500°C (above the incipient melting temperature). The time at temperature necessary for full homogenisation was greatly increased for treatments at 460°C (this is seen in the DSC curves in **Figure 5.2**, where the soak time for homogenisation and removal of the incipient melting peak was investigated) when compared to the standard solution treatment on a wrought sample of 500°C for six hours in the T6 regime. The T6 regime is an age hardening heat treatment practice that is used on wrought parts to maximise their strengths. In wrought parts, segregation is effectively removed through extensive thermo-mechanical treatments; therefore, the structure after solution treatment would be homogenous. The composition distribution, which was analysed in great detail in this investigation, showed that the SSM rheocast structure had a very high degree of segregation. Therefore, increased times were required for homogenisation practices, in order to minimise the segregation associated with the SSM cast structure. Chena *et al*[85] showed an improvement in the dissolution of the soluble constituents in an AA7055 alloy, with the use of two-step heat treatments, where the first step was a homogenisation step at lower temperatures for extended lengths of time, up to 50 hours. This then allowed for a second higher temperature solution treatment step, for the complete dissolution of the constituent particles. The maximum homogenisation time for this investigation was 15 hours, a relatively short length of time in comparison to those used by Chena *et al*.

In both alloys, the maximum hardness achieved from the SSM cast samples was below that achieved from the wrought AA7075 sample (172HV) and the fully homogenised ingot sample (118HV), where the differences in hardness between the maximum achieved and the SSM cast were approximately 15HV and 20HV respectively.

The hardness values achievable with the A713 alloy were markedly lower than those for the AA7075 in all cases considered. Although, owing to the difference in composition when compared to the AA7075 alloy, the A713 alloy might need temperature and time profiles for age hardening different from those used in this investigation, in order to maximise the alloy's property potential. The A713 alloy, Tenzaloy©, is considered a self-ageing or naturally ageing alloy. After casting, it is left to age naturally at room temperature and a maximum hardness of approximately 85HV is achieved after 10-14 days. Owing to the natural precipitation kinetics, the critical stable cluster sizes and the temperatures needed to achieve them require further evaluation if this A713 alloy is to be used as a comparable alloy to the AA7075 composition.

If the deficit in these hardness values for the SSM cast samples of both alloys were to be overcome, the SSM cast samples would require tailor-designed homogenisation processes, in order to fully homogenise the structure. Appropriate temperatures would have to be selected, in order to avoid the occurrence of incipient melting, as melting exacerbates the porosity morphology to a very significant extent, resulting in a negative impact on the strength and integrity capabilities of the SSM cast part. The homogenisation process should be a two-step heat treatment that includes a homogenisation step and a solution treatment step at a slightly higher temperature. The solution treatment step is important for the production of a super saturated solid solution upon quenching. This will be the driving force for the subsequent natural and artificial ageing steps.

7.2. SEGREGATION AND ALLOY COMPOSITION

The extent of the segregation in the as-cast conditions for both the AA7075 and the A713 alloys has been investigated thoroughly.

DSC thermal analysis curves give an indication of the presence of segregation in a tested sample. This is seen by the incipient melting peak in the DSC curves. The DSC results show that the segregation in the SSM as-cast AA7075 alloy is much greater than that of the A713 alloy.

This comparison is based on the sizes of the incipient melting peaks seen in **Figure 5.4**. This difference in the level of segregation is verified by the composition analyses seen in the EDS results in the previous chapters.

The EDS linescans and sequential spot analyses that evaluate the segregation through the grains into the coring rings and extending into the cellular protrusions show that the centre of each grain has an even solute distribution and that noticeable composition changes correspond to the start of the coring rings, which are visible in the SEM BSE images for both alloys. The location of the coring rings, with respect to the solidification path followed during SSM casting was discussed in **Chapter 6**, and can be seen in **Figure 6.4**. The coring rings originate after stirring has ceased, corresponding to Stage 3 in the growth path seen in **Figure 6.3**. The compositional distribution is process specific, rather than alloy specific.

The EDS results do show that the Zn in the A713 alloys is less segregated than the Zn in the AA7075 alloy in the SSM cast samples. This is highlighted by the distribution of Zn throughout the structure for both alloys, seen in all the EDS analyses of the as-cast condition. The distribution difference is determined by the balance between the overall Zn content and the ratios between the Zn composition at the centre of the grains (the first solid to form), the Zn composition at the edges of the grains and the remaining Zn in the eutectic. Results show that the Zn in the A713 alloy is more evenly distributed. This may be the result of the decreased Mg content in the A713 alloy (0.5wt% as opposed to the 2,5wt% in the AA7075 alloy). The AA7075 composition contains a greater variety of alloying elements, which would certainly affect the mobility of the individual alloying elements during solidification.

The fact that the SSM cast structure from the A713 alloy, when compared to that of the AA7075 alloy, has been shown to have the lowest degree of segregation indicates that it is well suited to this particular casting operation.

The extent of and the comparison between the segregation for the two casting operations, namely the high pressure die casting operation (HPDC) and the SSM rheocasting operation, cannot be used as mitigating factors when determining whether the alloy is actually suitable for this casting operation. As mentioned in **Chapter 1**, the main benefit of the SSM casting operation is the non-turbulent filling of the die during casting, thus effectively reducing the gas porosity within the cast structure and increasing the structural integrity of the casting itself. The selection of any production process for a particular application hinges on a compromise between various features. The use of SSM casting for high strength parts is beneficial for both structural integrity, when comparing it to other casting operations, and for cost, when comparing casting to machining.

Therefore, if AA7075 can be successfully age hardened to a comparable maximum within a competitive range to the wrought equivalent, without affecting the structural integrity of the SSM cast part, then it cannot be excluded from selection, owing to an increased level of segregation.

7.3. SEGREGATION AND PROCESSING ROUTE

The SSM casting process results in a globular grain structure that has an equiaxed primary grain size of the order of 80-100µm. The interglobular regions are solute rich, while the central part of the globular grains have an even composition distribution, with relatively high aluminium contents. This distribution changes with the occurrence of the coring rings.

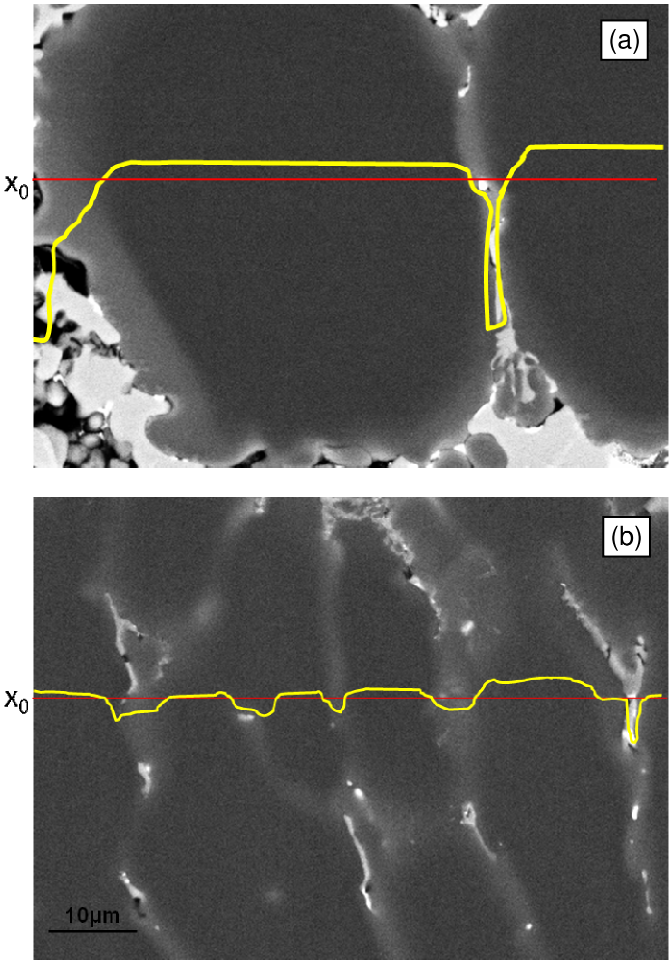

Figure 7.1: *Schematic representation of the variation in average bulk composition with respect to an average composition X_o, for (a) SSM cast A713 alloy, and (b) conventionally cast A713 alloy.*

EDS results can be seen in **Figure 4.17** to **Figure 4.21**. The results show that the composition distribution between the globular grains and the interglobular regions indicates that the micro-segregation is high.

Conventional casting results in a higher degree of macro-segregation than SSM casting. This can be seen in the micrographs in **Figure 4.37** and the EDS analyses in **Figure 4.38**.

The distribution of the segregation and the grain sizes associated with the different processing routes influence the homogenisation of the respective structures. The homogenisation is dependent on the diffusion distances between the solute rich interglobular and eutectic regions and the centre of the primary grains.

Figure 7.1 shows micrographs of (a) a SSM cast A713 alloy, and (b) a conventionally cast A713 alloy. The red line on both micrographs represents the average overall composition of a fully homogenised sample, X_o. The yellow line represents an estimated deviation from the average bulk composition. The position of the line was based on the EDS analyses from **Figure 4.17** to **Figure 4.21** for the SSM sample and **Figure 4.38** for the conventionally cast sample.

The position of the yellow line with respect to the average bulk composition (red line) in **Figure 7.1** shows that, during homogenisation, not only does the conventionally cast sample offer a shorter diffusion distance when compared with the SSM cast samples, but the composition deficit in the solute rich areas is much lower. From this it can be inferred that the homogenisation of a conventionally cast (HPDC) sample would occur more easily. For this reason, the benefits of the globular microstructure and the reduced porosity associated with the SSM casting process must outweigh the negative implications of segregation, in order for SSM to be considered as a preferable processing route to conventional casting.

7.4. POROSITY AND INCIPIENT MELTING

Porosity is a common feature in cast parts. The two sources of porosity are entrapped gas and shrinkage. During conventional casting, there is a turbulent filling of the die. This turbulence causes the entrapment of air, which results in gas porosity within the structure. Shrinkage porosity arises from the change in volume of the liquid as it solidifies. Porosity is located between the grains and is surrounded by eutectic. Porosity is detrimental to a casting as it lowers the structural integrity of the part. In the slurry production step of SSM casting, the actual casting of the slurry occurs with a 50% solid fraction and at lower temperatures. The benefits of this are two-fold. Firstly, the flow characteristics of the slurry eliminate turbulence during die filling, and, secondly, the already lowered casting temperature reduces the amount of shrinkage porosity during the final solidification.

Microstructural evidence shows that there is still porosity within the structure. For both the AA7075 and A713 alloys, it is located within the interglobular regions, surrounded by solute-rich eutectic. In the as-cast condition, the shrinkage pores are small, of the order of a few microns in length, and within one area of eutectic there may be multiple individual pores.

If the structure is overheated to above the incipient melting temperature of the eutectic, the volume occupied by the solid eutectic changes as it melts. When this happens, the morphology of the porosity changes from small isolated pores, to that of larger agglomerated pores of increased length. This coalescing of porosity will lead to large pores, and this will inevitably reduce the structural integrity of the part. This coalescing of porosity can be seen in the *in situ* heating progressions in **Figure 5.24** and **Figure 5.34**.

Incipient melting is not the only mechanism to change the morphology of the porosity. During heating below the critical temperature, diffusion of the solute from the solute-rich eutectic into the surrounding structure occurs. The change in morphology of the porosity at temperatures below the incipient melting temperature can be seen in the *in situ* heating progressions in **Figure 5.34**.

Analysis of the change in porosity during heating to above the incipient melting temperature revealed a large and sudden increase in the volume fraction of porosity on micrographs taken during *in situ* heating experiments. The increased surface area percentage can be seen in **Figure 5.35**.

Homogenisation and solution treatment are key steps in the heat treatments that are needed to maximise the strength of the precipitation hardenable, high strength aluminium alloys under investigation. If these steps could not be achieved, the primary aim of this investigation would not be realised.

If the integrity of the casting were risked during heat treatment because of the morphological changes in porosity, the objective of using SSM casting as an alternative processing route for the production of high strength parts would be negated. In addition, the extent of the porosity and eutectic interaction would be a mitigating factor. If very slow heating rates could be used to create a sintering effect, whereby the volume occupied by the two-phase solid would be maintained during the diffusion of the solute into the bulk, the sudden increase in porosity volume fraction could be avoided, thus maintaining the integrity of the part.

7.5. HOMOGENISATION TO AVOID INCIPIENT MELTING

The solidification process of SSM casting results in the presence of low melting temperature phases within the structure. The presence of the low-melting temperature, non-equilibrium eutectic phases is confirmed by the incipient melting peaks in the DSC evaluations of the two alloys. In order to avoid the occurrence of incipient melting during homogenisation, heat treatment temperatures must be selected below this point. Unfortunately, non-equilibrium eutectic that contains many alloying elements, such as those seen in the SSM cast AA7075 and A713 alloys, cannot dissolve completely during homogenization at these low temperatures[86]. For this reason multi-stage homogenisation practices can be employed. The initial stage should have a temperature below the incipient melting temperature of 470°C. Here the eutectic will dissolve, but other phases will form with slightly higher dissolution temperatures, such as the Al_2CuMg and Al_7Cu_2Fe phases that form in the Al-Zn-Mg-Cu alloys[75]. Xigang Fan *et al*[87] have shown that the evolution of the eutectic structures in these alloys involves three processes: the dissolving of $Mg(Zn,Cu,Al)_2$ phase; the formation of Al_2CuMg phase and the increasing of its volume; and, the coarsening of Al_2CuMg phase and the decreasing of its volume. The melting temperature of this phase is approximately 490℃, but the melting point can be shifted upwards by extremely slow heating to 500℃.

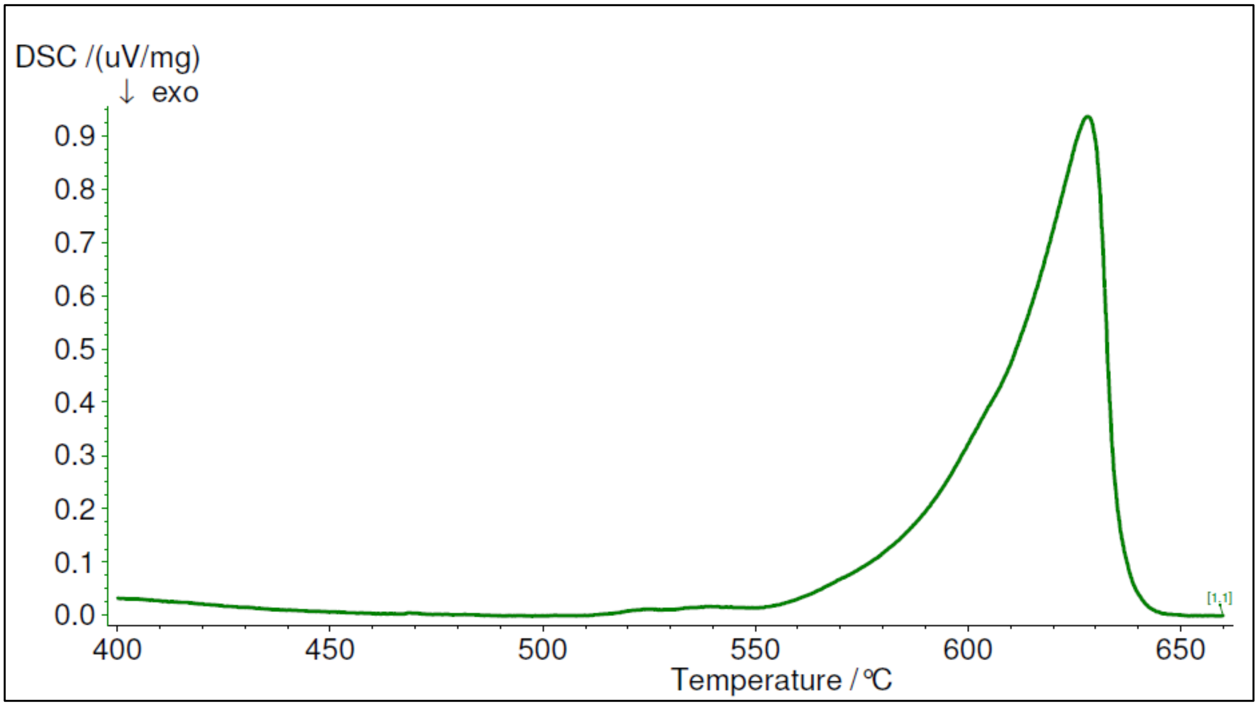

Figure 7.2: *DSC trace for SSM cast AA7075 alloy after homogenisation for 48 hours at 460℃.*

Figure 7.2 shows the DSC plot for a SSM cast AA7075 alloy after a homogenisation treatment. The removal of the incipient melting peak was achieved through homogenisation at 460 °C for 48 hours for the AA7075 alloy. No other peaks are present at the 490℃ range, as discussed by Xigang Fan *et al*[87].

Homogenisation at low temperatures does not result in the required supersaturated solid solution that is a necessary precursor for age hardening. The diffusion rate of solute into the bulk will increase with temperature, therefore, homogenising at a lower temperature, in order to avoid the occurrence of incipient melting, results in reduced diffusion rates. For this reason, it is important to include a solution treatment step in the multi-stage homogenisation practice. As mentioned previously, during the dissolution of the incipient melting phase, there is the concurrent formation of other phases, whose melting temperatures are below that of the traditional solution treatment temperature of 500°C.

With the removal of the incipient melting temperature peak, the structure could undergo a solution treatment step prior to ageing, while avoiding the negative impact of melting on the porosity within the structure.

In situ heating was used to evaluate the evolution of the microstructure during heating. The technique produced insight into the interaction between porosity and the eutectic, both during diffusion at lower temperatures and after incipient melting, at higher temperatures. The extent of incipient melting was measured by the surface area of porosity present in the field of view of a particular experiment, as well as by the amount of topographical shifting seen on the free surface. It is believed that the sub-surface changes in volume that are associated with a transformation from solid to liquid would result in topographical shifting that was visible on the surface of the sample. After *in situ* heating and cooling back to room temperature, the samples were evaluated in order to determine the extent of diffusion that took place from the interglobular solute-rich areas towards the centres of the large globular grains. The A713 alloy had a more homogeneous second phase distribution after heating than the AA7075 alloy. This was a result of the complexity of the AA7075 alloy composition when compared to the A713. The more complex alloy would have a slower diffusion rate.

The A713 alloy exhibited a high incidence of the lamellar substructure configuration, which is made up of arrangements of LAGBs. The presence of these boundaries may have acted to provide pathways for the diffusion of the solute as accelerated diffusion is seen along pathways such as grain boundaries and dislocation cores.

7.6. DISTINCTIVE FEATURES OF THE SSM CAST MICROSTRUCTURE

SSM casting produces a globular microstructure. The morphology and distribution of the grains is directly related to the solidification path through the different steps of this casting process. The solidification path was discussed in detail in **Chapter 5**.

The SSM casting process, as with all casting processes, results in the presence of shrinkage porosity. This porosity is a feature of the as-cast microstructure, and is affected deleteriously by the occurrence of incipient melting of the Zn-rich second phases. This can be seen in the progression of SEM images taken during the *in situ* heating experiments.

SEM imaging revealed the presence of a substructure (or a contrast pattern) within a number of the globular grains within the structure. EDS analysis revealed that the substructure was not as a result of obvious compositional variations within the grains. The EDS technique has limited resolution and sensitivity because of the interaction volume of the x-ray beam with the sample, a higher resolution technique may add insight into the link between the substructure and composition distribution. There were two general substructure configurations identified within the grains, firstly, a circular configuration, and secondly a lamellar configuration, resembling striation across the grain.

EBSD orientation analysis of the internal substructure revealed the coincidence of grain boundaries with the contrast pattern identified in the SEM images. The EBSD maps were viewed in Euler colours. Variation in the colour within the bulk of individual grains was also seen to coincide with the pattern, and areas of different colour, or merely slight variations in colour, were, in most cases, surrounded by grain boundaries. The misorientations associated with these boundaries were configuration specific. The lamellar substructure configuration was characterised by LAGBs. While the circular configuration comprised a combination of LAGBs and HAGBs, the arrangement of these exhibited a seemingly randomised configuration. The presence of these misorientations has been attributed to the mechanisms involved in the globularisation of the microstructure during slurry production. Two theories about the globularisation mechanisms were explored: dendritic deformation and cellular growth. The investigation into the two theories revealed that there was an absence of entrapped liquid, this suggesting that dendritic growth had not occurred and therefore dendritic deformation could not be the mechanism causing the formation of the globular grain structure. The globularisation effect and the presence of the regularly paired misorientations were attributed to the fluctuating stabilising and de-stabilising effect on the solid-liquid interface as a result of the fluid flow conditions experienced during SSM casting. The resulting morphological effects were the growth of protrusions on the interface and the occurrence of cellular growth, where the growth of the protrusion tips and the valley interfaces were alternately favoured, with the net growth front having a planar growth appearance.

CHAPTER 8: CONCLUSIONS

If semi-solid metal rheocasting is to be considered as an alternative processing route to the machining of parts, the maximum attainable properties of the final part need to be comparable to the wrought equivalents. Maximum properties can be attained through tailor-designed heat treatments practices, where the focus is on the homogenisation of the solute segregation identified in the SSM as-cast microstructure.

8.1. SEGREGATION IN THE SSM CAST MICROSTRUCTURE

The extent of the segregation associated with the SSM casting process was interrogated, using SEM, EDS analysis and EDS mapping, as well as DSC thermal analysis.

- The presence of the segregation was verified by the incipient melting peak identified in the DSC analysis for both the AA7075 and A713 alloys. The composition of the phases associated with these peaks was determined using JMatPro. The phases for the AA7075 alloy were α-Al and $Mg(Zn,Cu,Al)_2$, and for the A713 alloy were α-Al, HCP-Zn and Al_2Cu.

- Micro-segregation was identified within the individual grains, in the form of a distinct coring ring at the edges of the grains, and there was a further composition variation that extended into the cellular protrusions at the edges of these grains. The composition variations were determined by EDS analysis.

8.2. KEY FEATURES OF THE SSM MICROSTRUCTURE

Microstructural evaluation of the SSM as-cast structure revealed key features that are associated with the SSM rheocasting technique:

- The primary globular grains are surrounded by an interglobular region that is made up of smaller globular grains and eutectic.

- Shrinkage porosity is located within the interglobular regions and is surrounded by eutectic.

- The primary grains exhibit a distinct coring ring, which is clearly evident in the BSE images, and this indicates composition variations within the grains. The composition variations across the ring were determined using EDS analysis.

- The edges of the primary grains, which were not impinged by neighbouring grains during solidification, exhibit the presence of cellular protrusions that extend from the edges of the grains into the interglobular regions. The cellular growth morphology indicates that the solid-liquid interface was unstable during the final stages of solidification.

- The cellular protrusions do not have secondary arms. This indicates that there was no transition from cellular to dendritic growth morphology.

- There is no evidence of entrapped inter-dendritic liquid within the primary globular grains.

- Many of the primary grains exhibit an internal substructure, which is identified in SEM imaging and EBSD orientation mapping. The substructure is characterised by the presence of internal misorientations ranging from 5-25°, but does not correspond to any observed composition changes.

- There are two distinct substructure configurations: firstly, a circular configuration, comprising HAGBs (>15° misorientation) and LAGBs (between 2 and 15° misorientation), and secondly, a lamellar configuration, comprising LAGBs in striations.

- The lamellar substructure configuration is more prevalent in the SSM cast A713 alloy than in the AA7075 alloy.

- The analysis of the misorientation profiles across the above configurations revealed that the internal misorientations have regular (non-random) arrangements, and that the misorientations are reversed several times across the primary grains.

8.3. MECHANISMS FOR GLOBULAR EVOLUTION

The morphology of the grains, the composition distribution within the grains, the arrangement of the internal substructure and the presence of other key features within the microstructure are all evidence of the process history. This evidence was used to determine a solidification path for SSM casting and to investigate the mechanisms involved in the evolution of the globular microstructure during the slurry production step of SSM casting.

Evidence showed that the growth pattern during the turbulent fluid flow experienced during stirring is cellular and that the growth morphology is not dendritic at any stage during the slurry production stage. This is supported by the following conclusions:

- There is no evidence of entrapped inter-dendritic liquid in the primary globular grains.

- A number of grains exhibit the presence of internal low angle grain boundaries and misorientations that form where cells converge in the absence of entrapped inter-cellular liquid.

- The cellular growth mode progresses by alternating stabilisation and de-stabilisation of arrayed protrusions on the solid-liquid interface. This alternating effect is caused by the thermal gradient and constitutional supercooling conditions experienced during stirring. The extent of these conditions is insufficient to cause a transformation from cellular to dendritic growth, but rather results in a planar growth mode that borders on cellular in many areas.

- The composition distribution within the grains gives the impression of a planar growth mode on a macro (grain to grain) scale.

8.4. SEGREGATION COMPARISON BETWEEN AA7075 AND A713 ALLOYS

The AA7075 alloy is a complex composition designed for wrought applications, whereas, the A713 alloy is a casting alloy with a less complex composition. Both alloys rely on the Al, Zn and Mg to form the precipitates responsible for strengthening during ageing. The level of segregation in the as-cast condition and the ability to homogenise the segregation, directly affect the ability to strengthen the part after processing. Compositional analysis was used to investigate the segregation levels associated with the two alloys. The following observations were made:

- The Zn is less segregated in the A713 alloy, showing a more even distribution across the primary grains in the as-cast condition.

- During heating, the Zn in the A713 alloy diffuses more rapidly than is the case with the AA7075 alloy. During *in situ* heating experiments, the Zn in the AA7075 alloy diffuses to only a limited distance from the solute rich areas within the interglobular region towards the centres of the grains, while for the A713 alloy, the diffusion is such that the resulting structure is appreciably more homogeneous.

8.5. EFFECT OF HEAT TREATMENT ON POROSITY

Semi-solid metal casting reduces the amount of porosity within the final part owing to the lower casting temperatures and the non-turbulent filling of the die during casting. However, porosity is an inherent casting defect, and shrinkage porosity associated with this type of casting is located within the interglobular regions. The following observations were made during *in situ* heating experiments:

- The irregularly shaped porosity is surrounded by low-melting temperature eutectic.
- During heating, where diffusion of the solute and melting of the phases occurs, the morphology of the porosity is affected, and there is an appearance of an increase in porosity, as porosity coalesces during heat treatments at high temperatures.
- There is a significant increase in porosity surface area, owing to pore coalescence during *in situ* heating experiments, this increase corresponding to the incipient melting temperatures established by DSC thermal analysis experiments, namely, between 465-475℃.

Therefore;

- It is necessary to avoid the occurrence of incipient melting of the solute rich eutectic, as incipient melting has a negative impact on the homogenisation of the structure and on the morphology of the porosity within the structure.

8.6. T6 HEAT TREATMENT AND HOMOGENISATION

The characterisation of the as-cast structure and investigations into the heat treatment of the SSM cast structure showed that homogenisation and solution treatment practices must be tailor-made for each alloy after SSM casting. After following the standard T6 heat treatment practice, these conclusions were drawn:

- Neither the SSM cast samples of the AA7075 alloy nor the SSM cast samples of the A713 alloy achieved strengths comparable to those of the wrought AA7075 alloy. This was attributed to insufficient homogenisation of the as-cast segregation, which resulted in an ineffective solution treatment step.

- The solution treatment temperature was above the incipient melting temperature for both alloys. The occurrence of incipient melting has negative effects on the homogenisation process.

- Incipient melting was eliminated by homogenisation at 460℃ for 48 hours for the AA7075 alloy.

- The maximum achievable strengths for the A713 alloy were much lower than those for the AA7075 alloy after the T6 heat treatments.

- The success of the strengthening of these castings relies on the homogenisation of the segregation that is associated with the SSM casting process.

Therefore:

- The homogenisation process must be a multistep homogenisation process that includes a solution treatment step at higher temperatures, once the incipient melting peak has been removed through effective homogenisation.

CHAPTER 9: FUTURE WORK

9.1. GLOBULARISATION MECHANISMS

The presence of an internal substructure emerged in this research and investigations into the misorientation profiles and configurations aided in determining a mode of evolution by cellular growth. Further investigations should include 3D SEM and EBSD analysis on grains exhibiting the internal substructure. This would give insight into the true mechanisms responsible for the evolution of the globular microstructure and the formation of the substructure configurations.

.

9.2. ALLOY SELECTION

The aim of this investigation was to use an aluminium alloy that could be heat treated to a maximum strength. The Al-Zn-Mg-Cu alloys are considered as the high-strength series of alloys. For this reason the AA7075 alloy was selected. The segregation that resulted from the semi-solid casting of this complex alloy, which was designed for wrought processing, was large, and could not be removed through simple homogenisation treatments. The A713 alloy was investigated as an alternative to the AA7075 alloy but, although it produced a lower degree of segregation, the maximum achievable mechanical properties remained well below those of the AA7075 alloy. Therefore, future work should include investigations into the identification of an alloy composition more suited to SSM casting, which would have a low degree of segregation and would yield mechanical properties closer to those of a wrought AA7075 part.

In the selection of the composition, the following criteria must be considered:

- The degree of segregation
- The diffusion properties of all the alloying elements
- The formation of internal substructure
- The homogenisation kinetics
- The age hardenability

9.3. HEAT TREATMENT

The focus of this investigation was on the homogenisation of the incipient melting peak seen on the DSC plots. Therefore, further investigation into the homogenisation kinetics is needed in order to design appropriate heat treatment plans for the strengthening of the semi-solid cast parts. This should involve:

- Investigation into the diffusion kinetics of the alloying elements.
- Evaluation of the effect of the internal substructure on the homogenisation process, and whether the presence of this substructure aids diffusion during heat treatment.
- The design of multi-step homogenisation and solution treatment processes, to form the first step in a T6-type heat treatment.
- Investigation into the temperature and time profiles that are required to maximise the precipitation hardening process during age hardening of the semi-solid metal cast samples.
- Transmission electron microscopy (TEM) should be used to analyse the progression of precipitation during ageing in order to establish the presence and morphology of the ή phase required for strengthening and the role played by the GP(I) and GP(II) phases during the natural ageing step.

9.4. MECHANICAL PROPERTIES

Mechanical testing did not form part of this investigation. The evolution of the microstructure was investigated during heating and this would have an effect on the mechanical strength of the parts. Therefore, further investigation should focus on:

- The effect of the coalescing of the porosity in the SSM castings during heating and the resulting effect on the structural integrity of the part.
- The effect of the occurrence of incipient melting on the porosity morphology should be compared to the change in morphology when different temperatures are used for homogenisation and heat treatments. These effects on mechanical property need to be evaluated.

- The segregation of Zn in the SSM casting of these AL-Zn-Mg-Cu alloys forms a brittle eutectic which is found at the more highly segregated surfaces of the castings. Investigations into the effect of this phase on the mechanical and surface properties in the as-cast condition and in the post heat treatment conditions would offer insight into the effect of the macro-segregation across the sample.

REFERENCES

---

[1] F. Czerwinski, **The basics of modern SSM processing**, *Journal of Metals (JOM)*, Vol. 58, Issue 6, June 2006, pp. 17-20

[2] I. J. Polmear, **Light Alloys – Metallurgy of the Light Metals: 3rd Edition**, *Edward Arnold (Publishers) Ltd.*, 1995

[3] Z. Fan, **Rheo-forming of Mg- and Al-alloys** (a presentation), BCAST (Brunel Centre for Advanced Solidification Technology), Brunel University, UK

[4] **Aluminium components for automobiles: Casting low-cost, high quality parts**, *e-lab* (Energy Laboratory research and related activities at MIT), April-June 1998

[5] W. Kurz and D. J. Fisher, **Fundamentals of Solidification – 3rd Edition**, *Trans Tech Publications*, Switzerland, 1989

[6] R. L. Timings, **Engineering materials, Volume 1** (2nd Edition), *Addison Wesley Longman*, England, 1998

[7] A. S. Sabau, **Predicting interdendritic cavity defects during casting solidification**, *Journal of Metal (JOM)*, March 2004, pp.54-56

[8] D. B. Spencer, R. Mehrabian, M. C. Flemings, **Rheological behaviour of Sn-15%Pb in the crystallization range**, *Metallurgical Transactions*, Vol. 3, July 1972, pp. 1925-1932

[9] M. C. Flemings, R. G. Riek, K. P. Young, **Rheocasting**, *Materials Science and Engineering*, Vol. 25, 1976, pp. 103-117

[10] H.A. Barnes, **Thixotropy – a review**, *Journal of Non-Newtonian Fluid Mechanics*, Vol. 70, pp. 1-33, 1997

[11] M. C. Flemings, **Semi-solid forming: the process and the path forward**, *Metallurgical Science and Technology*, Vol. 18, Issue 2, 2000, pp. 2-4

[12] O. Lashkari, R. Ghomashchi, **The implication of rheology in semi-solid metal processes: An overview**, *Journal of Materials Processing Technology*, Vol. 182, 2007, pp.229-240

---

[13] P. A. Joly, R. Mehrabian, **The Rheology of a partially solid alloy**, *Journal of Materials Science*, Vol. 11, 1976, pp. 1393-1418

[14] M. C. Flemings, **Behavior of metal alloys in the semisolid state**, *Metallurgical and Materials Transactions A*, Vol. 22, 1991, pp.957-981

[15] S. Ji, Z. Fan, **Solidification of Sn-15wt% Pb alloy under a high shear rate and high intensity of turbulence during semisolid processing**, *Metallurgical and Materials Transactions A*, Vol. 33A, November 2002, pp. 3511-3520

[16] G. Govender, L. Ivanchev, **Near Net Shape Forming Using Semi-Solid Metal Forming**, *International Conference on Competitive Manufacturing*, 2004

[17] Z. Fan, **Semi-solid metal processing**, *International Materials Review*, Vol. 47, No. 2, pp.1-37, 2002

[18] L. Ivnachev, D. Wilkins, S. Govender, W.Du Preez, R. Bean, **Rheo-processing of semi-solid metal alloys – A new technology for manufacturing automotive and aerospace components**, *Presented at the CSIR Research and Innovation Conference*, 27 February 2006

[19] H. Fredriksson, U. Åkerlind, **Materials Processing during casting**, *John Wiley & Sons Ltd.*, England, 2006, Ch. 6

[20] D. A. Porter, K. E. Easterling, **Phase transformations in metals and alloys**, *Chapman and Hall*, Great Britain, 1981, Ch. 4

[21] http://www.matter.org.uk/solidification/cells/constitutional_undercooling.htm (16 December 2009)

[22] M. C. Flemings, **Solidification processing**, *McGraw-Hill Book Company*, USA, 1974

[23] S. Nafisi and R. Ghomashchi, **Effect of stirring on the solidification pattern and alloy distribution during semi-solid-metal casting**, *Materials Science and Engineering A*, Vol. 437, 2006, pp. 388-395

[24] M. Wu and A. Ludwig, **Modeling equiaxed solidification with melt convection and grain sedimentation – I: Model description**, *Acta Materialia*, Vol. 57, 2009, pp. 5621-5631

[25] M. Rappaz and W. J. Boettinger, **On dendritic solidification of multi-component alloys with unequal liquid diffusion coefficients**, *Acta Materialia*, Vol. 47, No. 11, 1999, pp.3205-3219

---

[26] M. Rappaz, P. H. Thévos, **Solute diffusion model for equiaxed dendritic growth**, *Acta Metallurgica*, Vol. 35, No. 7, 1987, pp. 1487-1497

[27] C. Y. Wang and C. Beckermann, **A multiphase solute diffusion model for dendritic alloy solidification**, *Metallurgical Transactions A*, Vol. 24, 1993, pp. 2787-2802

[28] M. Wu and A. Ludwig, **Modeling equiaxed solidification with melt convection and grain sedimentation – II: Model verification**, *Acta Materialia*, Vol. 57, 2009, pp. 5632-5644

[29] Z. Fan, G. Lui, M. Hitchcock, **Solidification behaviour under intensive forced convection**, *Materials Science and Engineering A*, Vol. 413-414, 2005, pp. 229-235

[30] A. Vogel and B. Cantor, **Stability of a spherical particle growing from a stirred melt**, *Journal of Crystal Growth*, Vol. 37, 1977, pp. 309-316

[31] A. Das, S. Ji, Z. Fan, **Morphological development of solidification structures under forced fluid flow: a Monte-Carlo simulation**, *Acta Materialia*, Vol. 50, 2002, pp. 4571-4585

[32] Z. Fan, G. Lui, **Solidification behaviour of AZ91D alloy under intensive forced convection in the RDC process**, *Acta Materialia*, Vol. 53, 2005, pp. 4345-4357

[33] M. C. Flemings, **Behavior of metal alloys in the semisolid state**, *Metallurgical Transactions A*, Vol. 22A, May 1991, pp. 957-981

[34] A. Vogel, R. D. Doherty and B. Cantor, **Stir-cast microstructure and slow crack growth**, *Solidification and Casting of Metals : Proceedings of an international conference on solidification,* Sheffield Metallurgical and Engineering Association, University of Sheffield, 1977, pp.518-525

[35] R. D. Doherty, H-I. Lee, E. A. Feest, **Microstructure of stir-cast metals**, *Materials Science and Engineering*, Vol. 65, 1984, pp.181-189

[36] E. A. Vieira, A. M. Kliauga and M. Ferrante, **On the formation of spheroidal microstructures in a semi-solid Al-Si alloy by thermomechanical processing**, *Scripta Materialia*, Vol.57. 2007, pp. 1165-1168

[37] R. D. Doherty, Comments on "Mechanical deformation of dendrites by fluid flow during solidification of undercooled melts", *Scripta Materialia*, Vol. 49, 2003, pp. 1219-1222

---

[38] S. Ananiev, P. Nikrityuk, K. Eckert, **Dendrite fragmentation by catastrophic elastic re-melting**, *Acta Materialia*, Vol. 57, 2009, pp. 657-665

[39] J. Pilling and A. Hellawell, **Mechanical deformation of dendrites by fluid flow**, *Metallurgical and Materials Transactions A*, Vol. 27A, January 1996, pp. 229-232

[40] A. Hellawell, **Grain evolution in conventional and rheo-castings**, *Proceedings of the fourth international conference on semi-solid processing of alloys and composites,* University of Sheffield, UK, 1996, p. 60-65

[41] T. Campanella, C. Charbon, M. Rappaz, **Grain refinement induced by electromagnetic stirring: A dendrite fragmentation criterion**, *Metallurgical and Materials Transactions A*, Vol. 35A, October 2004, pp. 3201-3210

[42] D. Ruvalcaba, R. H. Mathiesen, D. G. Eskin, L. Arnberg, L. Katgerman, **In situ observations of dendritic fragmentation due to local solute-enrichment during directional solidification of an aluminium alloy**, *Acta Materialia*, Vol. 55, 2007, pp. 4287-4292

[43] A. Hellawell, S. Liu and S. Z. Lu, **Dendrite fragmentation and the effects of fluid flow in castings**, *Journal of Metals (JOM)*, March 1997, pp. 18-20

[44] A. M. Mullis, **Growth induced dendritic bending and rosette formation during solidification in a shearing flow**, *Acta Materialia*, Vol. 47, No. 6, 1999, pp. 1783-1789

[45] J. M. M. Molenaar, F. W. H. C Salemans and L. Katgerman, **The structure of stircast Al-6Cu**, *Journal of Materials Science,* Vol. 20, 1985, pp. 4335-4344

[46] J. M. M. Molenaar, L. Katgerman, W. H. Kool, **On the formation of the stircast structure**, *Journal of Materials Science*, Vol. 21, 1986, pp. 389-394

[47] A. Das and Z. Fan, **A Monte Carlo simulation of solidification formation under melt shearing**, *Materials Science and Engineering A*, Vol. 365, 2004, pp. 330-335

[48] B. Niroumand and K. Xia, **3D study of the structure of primary crystals in a rheocast Al-Cu alloy**, *Materials Science and Engineering A*283, 2000, pp. 70-75

---

[49] M. Hitchcock, Y. Wang, Z. Fan, **Secondary solidification behaviour of the Al-Si-Mg alloy prepared by the rheo-diecasting process**, *Acta Materialia*, Vol. 55, 2007, pp. 1589-1598

[50] M. Reisi, B. Niroumand, **Growth of primary particles during secondary cooling of a rheocast alloy**, *Journal of Alloys and Compounds*, Vol. 475, 2009, pp. 643-647

[51] S. P. Ringer and K, Hono, **Microstructural evolution and age hardening in aluminium alloys: Atom probe field-ion microscopy and transmission electron microscopy studies**, *Materials Characterisation*, Vol. 44, 2000, pp. 101-131

[52] X. Fan, D. Jiang, Q. Meng, L. Zhong, **Microstructural evolution of an Al-Zn-Mg-Cu alloy during homogenisation**, *Materials Letters*, Vol. 60, 2006, pp.1475-1479

[53] C. Mondal, A. K. Mukhopadhyay, **On the nature of T($Al_2Mg_3Zn_3$) and S(Al_2CuMg) phases present in as-cast and annealed 7055 aluminium alloy**, *Materials Science and Engineering A*, Vol. 391, 2005, pp. 367-376

[54] N. A. Belov, D. G. Eskin, A. A. Aksenov, **Multicomponent phase diagrams: Applications for commercial aluminium alloys**, *Elsevier Ltd.*, United Kingdom, 2005, pp.199-202

[55] O. N. Senkov, R. B. Bhat, S. V. Senkova, J. D. Schloz, **Microstructure and properties of cast ingots of AL-Zn-Mg-Cu alloys modified with Sc and Ti**, *Metallurgical and Materials Transactions A*, Vol. 36A, 2005, pp. 2115-2126

[56] J. Gilbert Kaufman, **Introduction to Aluminium Alloys and Tempers**, ASM International, November 2000

[57] http://www.key-to-nonferrous.com, Article: **Heat Treatable Aluminium Alloys**

[58] D. Scott MacKenzie, **Heat Treatment of Aluminium Alloys**, *IndustrialHeating.com*, Thermal Processing, December 2004, pp.29-37

[59] M. J. Starink, **Analysis of aluminium based alloys by calorimetry: quantitative analysis of reactions and reaction kinetics**, *International Materials Review*, Vol. 49, No. 3-4, 2004, pp. 191-226

[60] I. J. Polmear, **Light Alloys – Metallurgy of the Light Metals: 3rd Edition**, *Edward Arnold (Publishers) Ltd.*, 1995

---

[61] M. J. Starink and S. C. Wang, **A model for the yield strength of overaged Al-Zn-Mg-Cu alloys**, *Acta Materialia*, Vol/ 51, 2003, pp. 5131-5150

[62] H. Löffler, I. Kovács, J. Lendvai, **Review: Decomposition processes in Al-Zn-Mg alloys**, *Journal of Materials Science*, Vol. 18, 1983, pp. 2215-2240

[63] Z. Zhao and G. S. Frankel, **The effect of temper on the first breakdown in AA7075**, *Corrosion Science*, Vol. 49, 2007, pp. 3089-3111

[64] P. Archambault and D. Godard, **High temperature precipitation kinetics and TTT curve of a 7XXX alloy by in-situ electrical resistivity measurements and differential calorimerty**, *Scripta Materialia*, Vol. 42, 2000, pp. 675-680

[65] J. Gilbert Kaufman, **Introduction to Aluminium Alloys and Tempers**, ASM International, November 2000

[66] K. P. Rao, Y. K. D. V. Prasad, E. B. Hawbolt, **Study of fractional softening in multi-stage hot deformation**, *Journal of Materials Process Technology*, Vol. 77, 1998, pp. 166-174

[67] ASM, Metals Handbook, 9th edition, Volume 9: Metallography and microstructures, pp.89-102

[68] http://www.ebsd.com/ebsd-explained/ebsdexplained.htm (13 November 2009)

[69] J. Humphreys, **VMAP 8 Handbook**, University of Manchester, 2002

[70] http://www.calphad.com/ (18 November 2009)

[71] P. J. Spencer, **A brief history of CALPHAD**, *Computer Coupling of Phase Diagrams and Thermodynamics*, Vol. 32, 2008, pp. 1-8

[72] N. Saunders, X. Li, A. P. Miodownik, J-Ph. Schillé, **Modelling of the Thermo-Physical and Physical Properties Relevant to Solidification**, *Advanced Solidification Processes X*, (Eds.: D. Stefanescu, J. A. Warren, M. R. Jolly and M. J. M. Krane), TMS, Warrendale, PA, 2003, 669

[73] N. Saunders, Z. Guo, X. Li, A. P. Miodownik, J. –Ph. Schillé, **Using *JMatPro* to model materials properties and behaviour**, *Journal of Metals (JOM)*, December 2003, pp. 60-65

---

[74] M. Reisi, B. Niroumand, **Effects of stirring parameters on Rheo-cast structure of Al-7.1wt%Si alloy**, *Journal of Alloys and Compounds*, Vol. 470, 2009, pp.414

[75] X. Fan, D. Jiang, Q. Meng, B. Zhang, T. Wang, **Evolution of eutectic structures in Al-Zn-Mg-Cu alloys during heat treatment**, *Transactions of Nonferrous Metals Society of China*, Vol. 16, 2006, pp. 577-581

[76] A. Deschamps, Y. Brechet, F. Livet, **Influence of copper addition on precipitation kinetics and hardening in AL-Zn-Mg alloys**, *Journal of Materials Science and Technology*, Vol. 15, 1999, pp. 993-1000

[77] X. Fan, D. Jiang, Q. Meng, B. Zhang, T. Wang, **Evolution of eutectic structures in Al-Zn-Mg-Cu alloys during heat treatment**, *Transactions of Nonferrous Metals Society of China*, Vol. 16, 2006, pp. 577-581

[78] D. Yang, **Role of Mg addition on the occurrence of incipient melting in experimental and commercial Al-Si-Cu alloys and its influence on the alloy microstructure and tensile properties**, *PhD Thesis,* University of Quabec, March 2006

[79] Z. Fan, G. Liu, **Solidification behaviour of AZ91D alloy under intensive forced convection in the RDC process**, *Acta Materialia*, Vol.53, 2005, pp. 4345-4357

[80] A. Semoroz, Y. Durandet, M. Rappaz, **EBSD characterisation of dendritic growth directions, texture and misorientations in hot-dipped Al-Zn-Si coatings**, *Acta Materialia*, Vol. 49, 2001, pp.529-541

[81] M. A. Salgado-Ordorica, M. Rappaz, **Twinned dendrite growth in binary aluminium alloys**, *Acta Materialia*, Vol. 56, 2008, pp. 5708-5718

[82] M. Li, T. Tamura, K. Miwa, **Controlling microstructures of AZ31 magnesium alloys by an electromagnetic vibration technique during solidification: From experimental observation to theoretical understanding**, *Acta Materialia*, Vol. 55, 2007, pp. 4635-4643

[83] J. Zhang, D. Shu, Q. Rao, B. Sun, G. Chen, **Nucleation and growth of high purity aluminium grains in directional solidification bulk sample without electromagnetic stirring**, *Transactions of Nonferrous Metals Society of China*, Vol. 16, 2006, pp.1-7

[84] J. M. M. Molenaar, L. Katgerman, W. H. Kool, R. J. Smeulers, **On the formation of the stircast structure**, *Journal of Materials Science*, Vol. 21, 1986, pp. 389-394

---

[85] K. Chena, H. Liu, Z. Zhang, S. Li, R. I. Todd, **The improvement of constituent dissolution and mechanical properties of 7055 aluminium alloy by stepped heat treatments,** *Materials Processing Technology*, Vol. 142, 2003, pp. 190-196

[86] G. Feng-hua, L. Nian-kui, T. Ni, S. Qiang, L. Xian-dong, Z. Gang, **Overheating temperature of 7B04 high strength aluminium alloy**, *Transactions of Nonferrous Metals Society of China*, Vol. 18, 2008, pp. 321-326

[87] X. Fan, D. Jiang, Q. Meng, L. Zhong, **The microstructural evolution of an Al–Zn–Mg–Cu alloy during homogenisation**, *Materials Letters*, Vol. 60, 2006, pp. 1475–1479